

**NONLINEAR IMPAIRMENTS AND MITIGATION TECHNOLOGIES  
FOR THE NEXT GENERATION FIBER-WIRELESS MOBILE  
FRONTHAUL NETWORKS**

A Dissertation  
Presented to  
The Academic Faculty

By

Jing Wang

In Partial Fulfillment  
of the Requirements for the Degree  
Doctor of Philosophy in the  
School of Georgia Institute of Technology

Georgia Institute of Technology

May 2017

Copyright © Jing Wang 2017

**NONLINEAR IMPAIRMENTS AND MITIGATION TECHNOLOGIES  
FOR THE NEXT GENERATION FIBER-WIRELESS MOBILE  
FRONTHAUL NETWORKS**

Approved by:

Dr. Gee-Kung Chang, Advisor  
School of Electrical and Computer  
Engineering  
*Georgia Institute of Technology*

Dr. Xiaoli Ma  
School of Electrical and Computer  
Engineering  
*Georgia Institute of Technology*

Dr. John R. Barry  
School of Electrical and Computer  
Engineering  
*Georgia Institute of Technology*

Dr. Geoffrey Y. Li  
School of Electrical and Computer  
Engineering  
*Georgia Institute of Technology*

Dr. Yao Xie  
School of Industrial and Systems  
Engineering  
*Georgia Institute of Technology*

Date Approved: February 20,  
2017

A late thesis to the memory of my beloved father

## ACKNOWLEDGEMENTS

I am deeply indebted to many people for years of support, inscription and encouragement. It is a pleasure to express my sincere gratitude to those who made this dissertation possible.

First of all, I owe my greatest debt of gratitude to my advisor, Prof. Gee-Kung Chang, who has shaped and inspired my years at Georgia Tech with his exceptional intellectual scope, technical acumen, and uncompromising effort for excellence. When I transferred from MIT to Georgia Tech in 2011, the sudden passing of my father kept me in deep depression for a long time. It is his continuous guidance, patience, and extraordinary thoughtfulness that made my PhD study back to its correct track. He has set an example of exemplary scholarship, whose enthusiasm and energy in both research and life are motivational to all the students in his group. It is my great honor and pleasure to be one of his students.

Another person I am also deeply indebted to is our post-doc, Dr. Junwen Zhang. I appreciate all his contributions of innovative ideas, insightful discussions, and extraordinary experimental skills. His perpetual energy and passion to research always motivate and inspire me.

The next thanks go to my thesis committee members, Prof. Xiaoli Ma, Prof. John R. Barry, Prof. Geoffrey Y. Li, all from School of Electrical and Computer Engineering, and Prof. Yao Xie from School of Industrial and Systems Engineering, for their valuable time, suggestions, and approval of my research work.

I am also appreciative to all my fellow students in Prof. Chang's group, whose advice, collaboration, and friendship supported my research during my study. Thanks to Dr. Shu Hao Fan, Dr. Yu-Ting Hsueh, Dr. Cheng Liu, Dr. Ming Zhu, Lin Cheng, Mu Xu, Feng Lu, Shuyi Shen, Hyunwoo Cho, and Hyung Joon Cho, and many other graduate students in our lab. I feel so lucky and proud that I can work in such a



talented group.

Finally, I owe thanks to my mother, who had selflessly tolerated my long absence from home, and her endless love, support, and encouragement were the most important driving force throughout my study. Thanks to Yurou Zhong, who shared my joy in making discoveries, listened to my frustrations, and saw me through the completion of my Ph.D. program with patience, tolerance and love.

This thesis is dedicated to the memory of my beloved father. Thank you for everything.

This work was supported by National Science Foundation (NSF) Center for Optical Wireless Applications (COWA) and Fiber-Wireless Integration and Networking (FiWIN). I would like to take this opportunity to express my gratitude to NSF industrial advisory board members, including, but not limited to, Dr. Anthony Ng'Oma of Corning, Dr. Xiang Liu of Futurewei, Dr. Jianjun Yu and Dr. Hungchang Chien of ZTE, Dr. Zhensheng Jia of CableLabs, Dr. Neda Cvijetic and Dr. Konstantinos Kanonakis of NEC Labs America, for their in-depth discussion, helpful advice and steering of my research.

## TABLE OF CONTENTS

<b>Acknowledgments</b> . . . . .	v
<b>List of Tables</b> . . . . .	xii
<b>List of Figures</b> . . . . .	xiii
<b>List of Acronyms</b> . . . . .	xvii
<b>Summary</b> . . . . .	xxi
<b>Chapter 1 Introduction</b> . . . . .	1
1.1 Mobile Fronthaul Network . . . . .	2
1.2 Analog Mobile Fronthaul . . . . .	4
1.2.1 Radio-over-Fiber Technologies . . . . .	4
1.2.2 Nonlinearities of Analog Mobile Fronthaul Network . . . . .	6
1.2.3 Orthogonal Frequency Division Multiplexing (OFDM) . . . . .	9
1.2.4 Nonlinear Impairments of OFDM Signals . . . . .	11
1.3 Linearization Technologies . . . . .	13
1.3.1 Feedforward . . . . .	15
1.3.2 Dual-Parallel Modulation . . . . .	16
1.3.3 Mixed-Polarization . . . . .	17

1.3.4	Cascaded SOA and MZM . . . . .	18
1.3.5	Light Injection Cross-Gain Modulation . . . . .	18
1.3.6	Predistortion . . . . .	19
1.4	Digital Mobile Fronthaul . . . . .	21
1.4.1	Common Public Radio Interface . . . . .	22
1.4.2	Delta-Sigma Modulation . . . . .	24
1.5	Thesis Objectives and Organization . . . . .	25
 <b>Chapter 2 Nonlinear Cross-Modulations of Single-Carrier Signals in Analog Mobile Fronthaul . . . . .</b>		 27
2.1	Introduction . . . . .	27
2.2	Operation Principles . . . . .	29
2.3	Experimental Setup . . . . .	30
2.4	Theoretical Analysis . . . . .	33
2.5	Simulation Results . . . . .	40
2.5.1	16-QAM/QPSK . . . . .	40
2.5.2	OOK+OOK . . . . .	41
2.5.3	QPSK+OOK . . . . .	42
2.5.4	16-QAM+16-QAM . . . . .	43
2.6	Experimental Results . . . . .	43
2.6.1	16-QAM/QPSK . . . . .	45
2.6.2	OOK+OOK . . . . .	49
2.6.3	QPSK+OOK . . . . .	49
2.6.4	16-QAM+16-QAM . . . . .	50

2.7	Summary . . . . .	53
 <b>Chapter 3 Nonlinear Subcarrier Intermodulations of OFDM Signals in Analog Mobile Fronthaul . . . . .</b>		
3.1	Introduction . . . . .	56
3.2	Operation Principles . . . . .	57
3.3	Experimental Setup and Theoretical Analysis . . . . .	60
3.4	Experimental Design . . . . .	64
3.5	Experimental Results . . . . .	70
3.5.1	Case I . . . . .	70
3.5.2	Case II . . . . .	72
3.5.3	Case III and IV . . . . .	75
3.5.4	Case V . . . . .	78
3.5.5	Case VI and VII . . . . .	81
3.5.6	Case VIII . . . . .	89
3.6	Summary . . . . .	91
 <b>Chapter 4 Linearization Technology based on Digital Predistortion . . . . .</b>		
4.1	Introduction . . . . .	94
4.2	Operation Principles . . . . .	96
4.3	Experimental Setup . . . . .	100
4.4	Experimental Results . . . . .	101
4.4.1	Mitigation of Cross-Modulations . . . . .	101
4.4.2	Mitigation of Subcarrier Intermodulations . . . . .	104

4.5	Summary . . . . .	108
<b>Chapter 5 Digital Mobile Fronthaul based on Delta-Sigma Modulation</b>		<b>109</b>
5.1	Introduction . . . . .	109
5.2	Operation Principles . . . . .	110
5.2.1	Common Public Radio Interface . . . . .	112
5.2.2	Delta-Sigma Modulation . . . . .	114
5.3	Experimental Setup . . . . .	118
5.4	Experimental Results . . . . .	120
5.4.1	Case I . . . . .	122
5.4.2	Case II . . . . .	125
5.4.3	Case III . . . . .	127
5.4.4	Case IV . . . . .	129
5.4.5	BER Tolerance . . . . .	129
5.4.6	Case V . . . . .	132
5.5	Summary . . . . .	134
<b>Chapter 6 Conclusion . . . . .</b>		<b>135</b>
6.1	Nonlinear Impairments of Analog MFH . . . . .	136
6.1.1	Cross-Modulations of Single-Carrier Signals . . . . .	136
6.1.2	Subcarrier Intermodulations of Multi-carrier Signals . . . . .	137
6.1.3	Linearization Technology based on Digital Predistortion . . . . .	139
6.2	Digital MFH based on Delta-Sigma Modulation . . . . .	140
6.3	Future Works . . . . .	141

6.3.1	New Multi-carrier Waveforms . . . . .	141
6.3.2	Improved Delta-Sigma Modulation for Digital MFH . . . . .	141
	<b>References . . . . .</b>	<b>160</b>
	<b>Publications . . . . .</b>	<b>161</b>
	<b>Vita . . . . .</b>	<b>167</b>

## LIST OF TABLES

1.1	OFDM parameters in popular wireless communication standards . . .	10
1.2	Nonlinear impairments of OFDM signals in optical/wireless communication scenarios . . . . .	12
1.3	Summary of linearization technologies . . . . .	14
1.4	CPRI data rate options . . . . .	23
2.1	Theoretical analysis of intra-band and inter-band XMs . . . . .	38
2.2	Summary of nonlinear XMs of single-carrier signals . . . . .	54
3.1	OFDM parameters in popular wireless communication standards . . .	66
3.2	Eight experimental cases to evaluate subcarrier IMs in multi-RAT multi-service analog MFH . . . . .	69
3.3	Summary of experimental results . . . . .	93
5.1	CPRI data rate options . . . . .	113
5.2	Comparison of three MFH technologies . . . . .	117
5.3	Experimental designs of delta-sigma modulation-based digital MFH .	121
5.4	3GPP EVM specifications . . . . .	122
6.1	Summary of nonlinear impairments in analog MFH networks . . . . .	138

## LIST OF FIGURES

1.1	C-RAN schematic architecture, consisting of MBH from core network to BBUs, and MFH from BBUs to RRHs. . . . .	2
1.2	The next generation MFH networks support multiple bands of mobile services from multiple radio access technologies. . . . .	3
1.3	Two different MFH architectures. (a) Analog MFH. (b) Digital MFH	4
1.4	Nonlinear impairments in analog MFH networks. (a) Carrier inter-modulation. (b) Cross-modulation. . . . .	7
1.5	Objective and organization of this thesis. . . . .	26
2.1	Operation principles of nonlinear XMs of single-carrier signals. (a) Intra-band XM between I and Q components of a vector signal. (b) Inter-band XM between two scalar signals. (c) Intra-band and inter-band XMs between two vector signals. . . . .	29
2.2	(a) Experimental setup. (b) Optical spectra at point i-iv. . . . .	31
2.3	Intra-band XM of a vector 16-QAM/QPSK signal (simulation w/o noise). (a) EVM as a function of normalized input amplitude. (b) 16-QAM constellations. (c) QPSK constellations. . . . .	41
2.4	Inter-band XM between two OOK signals (simulation w/o noise). $Q_1$ decreases monotonically with $V_2$ . Ch. 1 eye diagrams are shown in insets.	42
2.5	Inter-band XM between a QPSK and an OOK signals (simulation w/o noise). (a) $EVM_1$ (QPSK) increases monotonically with $V_2$ (OOK). (b) Scaling distortion of QPSK constellation. . . . .	43
2.6	Inter-band XM between two 16-QAM signals (simulation w/o noise). (a) $EVM_1$ as a function of $V_1, V_2$ . (b) Ch. 1 constellations. . . . .	44



2.7	Intra-band XM of a 16-QAM signal. (a) EVM as a function of normalized input amplitude. (b) 16-QAM constellations. . . . .	45
2.8	Intra-band XM of a QPSK signal. (a) EVM as a function of normalized input amplitude. (b) QPSK constellations. . . . .	46
2.9	Inter-band XM between two OOK signals. (a, b) Simulation w/ noise. (c, d) Experiments. (a) Simulated $Q_1$ as a function of $V_1$ , $V_2$ . (b) Simulated eye diagrams. (c) Measured $Q_1$ . (d) Measured eye diagrams. . . . .	48
2.10	Inter-band XM between a QPSK and an OOK signals. (a) $EVM_1$ (QPSK) increases monotonically with $V_2$ (OOK). (b) Measured scaling distortion of QPSK constellation. . . . .	50
2.11	Inter-band XM between two 16-QAM signals. (a, b) Simulation w/ noise. (c, d) Experiments. (a) Simulated $EVM_1$ as a function $V_1$ , $V_2$ . (b) Simulated constellations. (c) Measured $EVM_1$ . (d) Measured constellations. . . . .	52
3.1	Operation principles of subcarrier IMs. (a) In-band interferences and (b) out-of-band emission induced by intra-band IMs. (c) In-band interferences and (d) out-of-band emission induced by inter-band IMs among one subcarrier of Ch. 1 and two subcarriers of Ch. 2. . . . .	58
3.2	Nonlinear impairments of single-band and multiband OFDM signals. (a) Interference induced by intra-band IMs. (b) Interference induced by inter-band IMs. . . . .	59
3.3	(a) Experimental setup. (b) Optical spectra at point i-iv. . . . .	61
3.4	Experimental results of Case I. (a) EVM as a function of RMS amplitude of input signal. (b) Constellations and PSDs at points i-iv. . . .	71
3.5	Experimental results of Case II. (a) $EVM_2$ as a function of $V_1$ , $V_2$ . (b) Ch. 2 constellations. (c) Ch. 2 PSDs. . . . .	74
3.6	Experimental results of Case III and IV (identical EVM performance). (a) $EVM_2$ in Case III and IV. (b) Ch. 1 constellations in Case III. (c) Ch. 2 constellations in Case III. . . . .	77
3.7	Experimental results of Case V. (a) $EVM_1$ . (b) Ch. 1 constellations. (c) $EVM_2$ . (d) Ch. 2 constellations. . . . .	80

3.8	PSDs at point i ( $V_1 = 45$ mV, $V_2 = 9$ mV), ii ( $V_1 = 9$ mV, $V_2 = 45$ mV), and iii ( $V_1 = 45$ mV, $V_2 = 27$ mV) in Case V. At point i, Ch. 1 is impaired by intra-band IMs (a), and Ch. 2 impaired by inter-band IMs (d). At point ii, Ch. 1 is impaired by inter-band IMs (b) and Ch. 2 by intra-band IMs (c). At point iii, the impairments of Ch. 1 is a combination of both intra-band and inter-band IMs (e). . . . .	81
3.9	Experimental results of Case VI. (a) $\text{EVM}_1$ . (b) Ch. 1 constellations. (c) $\text{EVM}_2$ . (d) Ch. 2 constellations. . . . .	83
3.10	PSDs at point i ( $V_1 = 45$ mV, $V_2 = 9$ mV) and ii ( $V_1 = 9$ mV, $V_2 = 45$ mV) in Case VI. At point i, Ch. 1 is impaired by intra-band IMs (a), and Ch. 2 impaired by inter-band IMs, which degenerate to inter-band XM (d). At point ii, Ch. 1 is immune from inter-band interferences (b), and Ch. 2 is impaired by intra-band IMs (c). . . . .	85
3.11	Experimental results of Case VII. (a) $\text{EVM}_1$ . (b) Ch. 1 constellations. (c) $\text{EVM}_2$ . (d) Ch. 2 constellations. . . . .	88
3.12	Experimental results of Case VIII. (a, b) Constellations of Ch. 2-4 without/with Ch. 1. (c, d) PSDs of Ch. 2-4 without/with Ch. 1. (e, f) Constellation and PSD of Ch. 1. . . . .	90
4.1	Linearization based on digital predistortion for analog MFH. . . . .	97
4.2	Memory polynomial model of analog MFH channel with memory depth of $M$ and nonlinearity order of $K$ . . . . .	98
4.3	Experimental setup of digital predistortion. . . . .	100
4.4	Digital predistortion to mitigate intra-band XM for a 16-QAM signal. (a) Input constellation. (b) After predistortion. (c) After MFH w/o predistortion. (d) After MFH w/ predistortion. . . . .	102
4.5	Digital predistortion to mitigate inter-band XM between two OOK signals. (a) Input eye diagrams. (b) After predistortion. (c) After MFH w/o predistortion. (d) After MFH w/ predistortion. . . . .	103
4.6	Digital predistortion to mitigate both intra-band and inter-band XMs between two 16-QAM signals. (a) Input constellations. (b) After predistortion. (c) After MFH w/o predistortion. (d) After MFH w/ predistortion. . . . .	104

4.7	Digital predistortion to mitigate intra-band IMs (Case I). (a) Constellation after predistortion. (b) After MFH w/o predistortion. (c) After MFH w/ predistortion. . . . .	105
4.8	Digital predistortion to mitigate inter-band IMs (Case II). (a) Constellations after predistortion. (b) After MFH w/o predistortion. (c) After MFH w/ predistortion. . . . .	106
4.9	Digital predistortion to mitigate inter-band IMs (Case VI). (a) Constellations after predistortion. (b) After MFH w/o predistortion. (c) After MFH w/ predistortion. . . . .	107
5.1	Three MFH architectures. (a) C-RAN. (b) RoF-based analog MFH. (c) CPRI-based digital MFH. (d) Delta-sigma modulation-based digital MFH. . . . .	111
5.2	Operation principles of two digitization interfaces. (a) CPRI. (b-e) Delta-sigma modulation. (b) Only one-bit or two-bit quantization. (c) Oversampling to extend Nyquist zone. (d) Noise transfer function to push quantization noise out of signal band. (e) Low-pass filtering to eliminate noise and retrieve signal. . . . .	112
5.3	(a) Experimental setup. (b, c) Signal waveforms and eye-diagram of one/two-bit digitization: input analog signal at point i (red); 10-Gbaud OOK/PAM4 at point ii (blue); retrieved analog signal at point iii (green). . . . .	119
5.4	Second-order delta-sigma modulator based on CRFF structure (Case I and II). (a) Z-domain block diagram. (b) Zeroes and poles of noise transfer function. . . . .	123
5.5	Experimental results of Case I. (a) Electrical spectra of 32 aggregated LTE carriers. (b) zoom-in of (a). (c) EVMs of 32 carriers. (d) Best/worst constellations of 64-QAM and 16-QAM. . . . .	124
5.6	Experimental results of Case II. (a) Electrical spectra of 30 aggregated FBMC carriers. (b) zoom-in of (a). (c) EVMs of 30 carriers. (d) Best/worst constellations of each modulation format. . . . .	126
5.7	Fourth-order delta-sigma modulator based on CRFF structure (Case III and IV). (a) Z-domain block diagram. (b) Zeroes and poles of noise transfer function. . . . .	127

5.8	Experimental results of Case III. (a) Electrical spectra of 32 aggregated LTE carriers. (b) zoom-in of (a). (c) EVMs of 32 carriers. (d) Best/worst constellations of 256-QAM and 64-QAM. . . . .	128
5.9	Experimental results of Case IV. (a) Electrical spectra of 32 aggregated LTE carriers. (b) zoom-in of (a). (c) EVMs of 32 carriers. (d) Best/worst constellations of 1024-QAM and 256-QAM. . . . .	130
5.10	BER tolerance of delta-sigma modulation. (a) EVMs of Case I under different BERs. (b) Constellations of CC 8, 18, 19, and 31 at BER threshold $1 \times 10^{-4}$ . (c) EVMs of Case III under different BERs. (d) Constellations of CC 12, 17, 6, and 32 at BER threshold $3 \times 10^{-5}$ . . .	131
5.11	Experimental results of Case V. (a) Average EVM of 24 carriers as a function of input $V_{pp}$ before power amplifier. (b) Best constellations for two power amplifiers with NF of 5.8 and 11 dB. . . . .	133

## List of Acronyms

3GPP	3rd Generation Partnership Project
ADC	Analog-to-digital convertor/conversion
ADSL	Asynchronous digital subscriber line
AM-AM	Amplitude modulation to amplitude modulation
AM-PM	Amplitude modulation to phase modulation
ASE	Amplified spontaneous emission
AWG	Arbitrary waveform generator
BBU	Baseband processing unit
BER	Bit-error ratio
BPF	Band-pass filter
BS	Base station
BTB/B2B	Back-to-back
BW	Bandwidth
CA	Carrier aggregation
CATV	Community antenna television
CC	Component carrier
CD	Chromatic dispersion
CIFB	Cascaded-integrator feedback
CIFF	Cascaded-integrator feedforward
CNR	Carrier-to-noise ratio
CO	Central office
CoMP	Coordinated multi-point
CO-OFDM	Coherent optical orthogonal frequency division multiplexing
CP	Cyclic prefix
CPRI	Common Public Radio Interface
C-RAN	Cloud radio access network
CRFB	Cascaded-resonator feedback
CRFF	Cascaded-resonator feedforward
CTB	Composite triple beat
CW	Continuous wave
DAB	Digital audio broadcasting
DAC	Digital-to-analog converter/conversion
DC	Direct current
DEMZM	Dual-electrode Mach-Zehnder modulator
DFB	Distributed feedback
DML	Directly modulated laser
DSB	Double sideband
DSP	Digital signal processing
DVB	Digital video broadcasting
ECL	External cavity laser

EDFA	Erbium-doped fiber amplifier
ENOB	Effective number of bits
E/O	Electro-optic
E-UTRA	Evolved universal terrestrial radio access
EVM	Error vector magnitude
FBMC	Filter bank multi-carrier
FEC	Forward error correction
FPGA	Field programmable gate array
FWM	Four-wave mixing
FDM	Frequency division multiplexing
FP	Fabry-Perot
GFDM	Generalized frequency division multiplexing
HDSL	High-bit-rate digital subscriber line
HDTV	High-definition television
Het-Net	Heterogeneous network
ICI	Inter-channel interference
IF	Intermediate frequency
IL	Interleaver
IM	Intensity modulation/Intermodulation
IM/DD	Intensity modulation and direct detection
IP3	Third-order intercept point
IQ-MZM	In-phase and quadrature Mach-Zehnder modulator
ISI	Inter-symbol interference
LD	Laser diode
LED	Light emitting diode
LO	Local oscillator
LPF	Low-pass filter
LTE	Long term evolution
LTE-A	Long Term Evolution-Advanced
MBH	Mobile backhaul
MFH	Mobile fronthaul
MIMO	Multiple-input and multiple-output
MME	Mobile management entity
MMW	Millimeter wave
Multi-RAT	Multiple radio access technologies
Multi-service	Multiple services
MZM	Mach-Zehnder modulator
NF	Noise figure
O/E	Opto-electrical
OFDM	Orthogonal frequency-division multiplexing
OFDM-PON	Orthogonal frequency-division multiplexing passive optical network
OFDMA	Orthogonal frequency division multiple access

OLT	Optical line terminal
ONU	Optical network unit
OOK	On-off keying
OSNR	Optical signal-to-noise ratio
PA	Power amplifier
PAM	Pulse Amplitude Modulation
PAM4	Quaternary Pulse Amplitude Modulation
PAPR	Peak-to-average power ratio
PC	Polarization controller
PD	Photodetector
PHY	Physical layer
PM	Phase modulation/modulator
PON	Passive optical network
PRBS	Pseudo random binary sequence
PSD	Power spectral density
PSK	Phase shift keying
QAM	Quadrature amplitude modulation
QPSK	Quaternary phase-shift keying
RAN	Radio access network
RAT	Radio access technology
RF	Radio frequency
RMS	Root-mean-square
RoF	Radio-over-fiber
RRH	Remote radio head
RX	Receiver
SCM	Subcarrier multiplexing
SFDR	Spurious free dynamic range
S-GW	Service gateway
SMF	Single-mode fiber
SNR	Signal-to-noise ratio
SSB	Single sideband
SSMF	Standard single-mode fiber
TDM	Time-division multiplexing
TX	Transmitter
UFMC	Universal filtered multi-carrier
VOA	Variable optical attenuator
VLC	Visible light communication
WDM	Wavelength-division multiplexing
Wi-Fi	Wireless Internet for Frequent Interface
WiGig	Wireless Gigabit Alliance
WiMAX	Worldwide interoperability for microwave access
XM	Cross-modulation
X-talk	Crosstalk

## SUMMARY

The proliferation of Internet-connected mobile devices and the emerging video-intensive services are driving the growth of mobile data traffic in an explosive way, making the last mile of access networks, mobile fronthaul (MFH) networks, become the data rate bottleneck of user experience. To enhance the capacity and coverage of mobile data networks, the next generation MFH is expected to support the coexistence of multiple mobile services from various radio access technologies (RATs), such as LTE, Wi-Fi, WiGig, etc..

According to the signal waveforms employed for fiber-optic transmissions, MFH networks can be divided into analog MFH and digital MFH. Analog MFH transmits mobile signals in their analog waveforms using radio over fiber (RoF) technologies. It features simple low-cost implementations and high spectral efficiency, but suffers from the vulnerability of nonlinear impairments, especially given the factors of continuous envelope and high peak-to-average power ratio of multi-carrier mobile signals. So far as we know, there has been meager effort to investigate the nonlinear impairments of analog MFH networks. Most existing works only focus on the distortions of each individual signal, and inter-channel interferences have not been reported yet.

Digital MFH, on the other hand, digitizes mobile signals and transmits the digitized bit streams via digital optical communication links. It is robust against nonlinear impairments and can be accommodated by existing passive optical networks (PON). However, the most popular MFH digitization interface, common public radio interface (CPRI), features low spectral efficiency and requires tremendous bandwidth after digitization, which makes it become the data rate bottleneck of next generation mobile data networks. Furthermore, as a Nyquist analog-to-digital converter (ADC), CPRI exploits time division multiplexing (TDM) for carrier aggregation, which makes synchronization channeling for mobile services from different RATs.



**The objective and contribution of this research are two-fold.** For analog MFH, nonlinear interferences among multiple mobile signals in a multi-RAT multi-service RoF-based MFH system are investigated for the first time. The nonlinear impairments of both single-carrier and multi-carrier signals are investigated, and it is experimentally demonstrated that inter-channel interferences play a more important role in the MFH performance degradation than distortions of each individual signal. In order to mitigate nonlinear impairments, a linearization technique based on digital predistortion is demonstrated. For digital MFH, we experimentally demonstrate a novel digitization interface based on delta-sigma modulation to replace the state-of-the-art CPRI. Compared with CPRI, it provides improved spectral efficiency and enhanced fronthaul capacity, and can accommodate both 4G-LTE and 5G mobile services.

To investigate the nonlinear impairments of mobile signals, we experimentally demonstrated a millimeter wave (MMW) analog MFH testbed, and proposed a closed-form theoretical analysis to model the nonlinear behavior of single-carrier and multi-carrier signals. Both numerical simulations and experimental measurements are carried out, and consistent results are obtained. The dominant impairments of single-carrier signals are nonlinear cross-modulations (XMs), which include both intra-band and inter-band XMs. Intra-band XM comes from the crosstalk between I and Q components of a vector signal, which induces compression distortion to its constellation. Inter-band XM originates from inter-channel interference between multiple signals, where the data modulation of one channel is imprinted on onto others, and introduce either eye diagram degradation to scalar signals or constellation scaling distortion to vector signals. It is experimentally verified that scalar signals only suffer from inter-band XM; whereas vector signals can be impaired by both intra-band and inter-band XMs. XMs are baseband effect, which only depend on data modulation, but have no dependency on carrier frequencies of mobile signals, and therefore, XMs cannot be

eliminated by filtering or increasing channel spacing.

The dominant impairments of multi-carrier OFDM signals, on the other hand, are subcarrier intermodulations (IMs), which are mainly contributed by third-order beat among three subcarriers. These three subcarriers can come from the same OFDM signal, forming intra-band IMs, or from different signals, forming inter-band IMs. Most existing studies of OFDM nonlinearities only focus on the intra-band IMs within each individual signal, and there is meager effort to evaluate the inter-band interferences among different OFDM signals. In this thesis, inter-band IMs among multiple signals in a multi-RAT multi-service analog MFH are investigated for the first time. Eight experimental scenarios are designed and carried out to evaluate the IMs among mobile services from various RATs, and it is experimentally verified that inter-band IMs play a much more important role in performance degradation than the well-known intra-band IMs. Subcarrier IMs only depend on the frequency difference between participating subcarriers, but have no dependence on the central frequencies of OFDM signals. Therefore, similar with XMs, IMs can not be eliminated by filtering either.

To mitigate the nonlinear impairments, a digital predistortion technique based on memory polynomial model is also demonstrated. Thanks to the static and highly predictable channel response of analog MFH, digital predistortion is considered as one of the simplest and most cost-effective solutions, which can be implemented in electrical domain without expensive optical devices. In experiments, a digital predistorter based on a 5th order polynomial is designed, and successful mitigation of both XMs and IMs for single-carrier and multi-carrier signals are demonstrated.

For digital MFH networks, we first demonstrate a novel digitization interface based on delta-sigma modulation to replace the conventional CPRI with improved spectral efficiency. Compared with CPRI, which consumes 10 Gb/s MFH capacity to accommodate 8 LTE carriers, delta-sigma modulation increases the fronthaul capacity by four times without significant penalty of signal qualities. 32 LTE carriers are aggre-

gated, digitized, and transmitted over a 25-km single- $\lambda$  10-Gbaud optical intensity modulation/direct detection (IM/DD) link. Both one-bit and two-bit digitization are demonstrated, and transported over 10-Gbaud OOK/PAM4 links. Error vector magnitude (EVM) less than 5% or 2.1% are achieved for one-bit and two-bit digitization, respectively, and high-order modulations, such as 256-QAM, 1024-QAM, can be supported. As a waveform-agnostic digitization interface, delta-sigma modulation can work with not only 4G-LTE signals, but also 5G multi-carrier waveforms, and its 5G compatibility is verified by filter bank multi-carrier (FBMC) signals. Compared with analog MFH, digital MFH based on delta-sigma modulation significantly improves the channel robustness against nonlinear impairments; while compared with CPRI, it provides enhanced spectral efficiency and increased MFH capacity without significant performance penalty.

# CHAPTER 1

## INTRODUCTION

The proliferation of Internet-connected mobile devices, and the emerging video-intensive services, e.g., virtual reality, immerse applications, are driving the growth of mobile data traffic in an explosive way, making the last-mile access networks become the bottleneck of user bandwidth [1, 2]. The emergence of 5G new radio technologies [3–7], is leading to a paradigm shift of cellular networks from traditional macro cells with tower-mounted base stations (BS) towards multi-tier heterogeneous networks [8–11] with densely deployed small cells [12, 13]. With smaller coverage and reduced number of users in each cell, this shift not only enhances the available bandwidth for each user, but also presents opportunities to other new radio technologies, such as millimeter wave (MMW) [14–19], carrier aggregation (CA) [20–24], massive multiple-input multiple-output (MIMO) [25–27], and coordinate multiple point (CoMP) [28, 29]. LTE carrier aggregation was initially standardized by 3GPP release 10 [20], allowing five aggregated component carriers (CCs), and then quickly extended to 32 aggregated CCs in [21].

In order to enhance the capacity and coverage of the next generation mobile data networks, a new cloud-radio access network (C-RAN) architecture has been proposed to separate the baseband signal processing functions from different base stations, and consolidate them together in a shared baseband processing unit (BBU) pool to enable advanced inter-cell processing and cloud management. A schematic architecture of C-RAN is shown in Fig. 1.1, where the tower-mounted base stations are divided into two function blocks, BBU for baseband processing, and remote radio head (RRH) for radio frequency processing and wireless transmission. In Fig. 1.1, the radio access network (RAN) is divided into two segments by the BBU pool, i.e., mobile backhaul

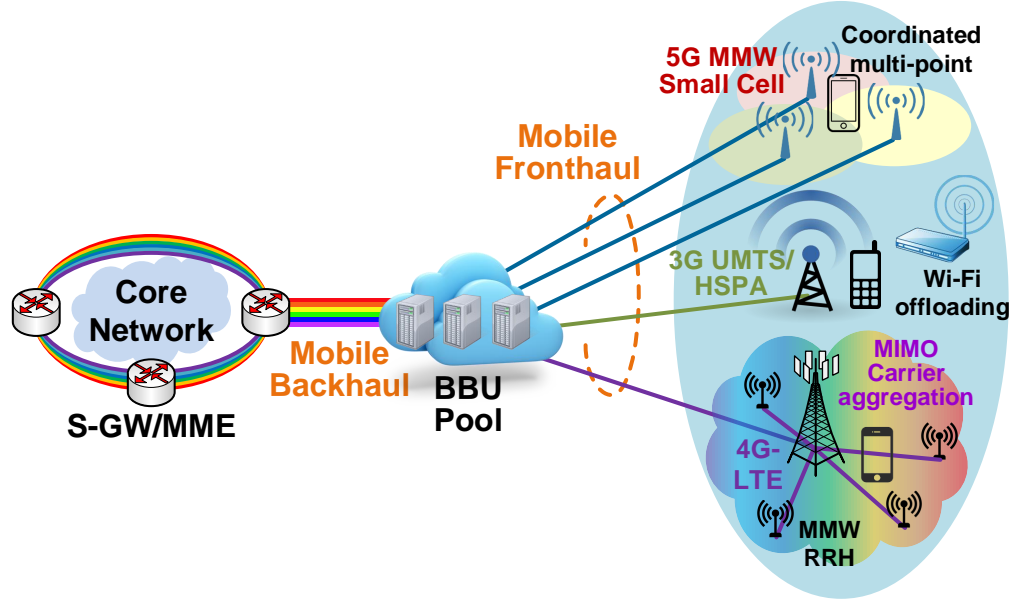


Figure 1.1: C-RAN schematic architecture, consisting of MBH from core network to BBUs, and MFH from BBUs to RRHs.

(MBH) from service gateway (S-GW) or mobile management entity (MME) of the core network to BBUs, and mobile fronthaul (MFH) from BBUs to RRHs [30–32]. To support the coexistence of multiple wireless services, MFH networks are expected to accommodate various radio access technologies (RATs), such as LTE, Wi-Fi, WiMAX, and WiGig. As shown in Fig. 1.2, multiple bands of services from multiple radio access technologies (multi-RAT) are aggregated in BBUs, and then transported to different RRHs via a converged optical wireless network.

### 1.1 Mobile Fronthaul Network

According to the different signal waveforms employed for optical fiber transmission, MFH networks can be divided into two categories, analog MFH and digital MFH, with their architectures presented in Fig. 1.3(a) and (b), respectively [33–35]. In analog MFH networks, mobile signals are transmitted over optical fiber in their analog waveforms without digitization by radio-over-fiber (RoF) technology. It features

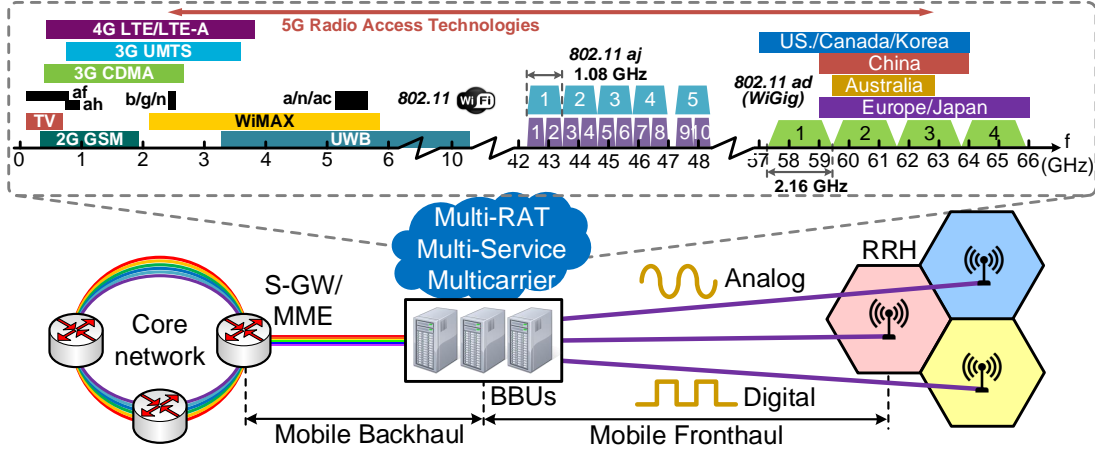


Figure 1.2: The next generation MFH networks support multiple bands of mobile services from multiple radio access technologies.

very high spectral efficiency, but suffers from transmission impairments like other analog systems do. In the following discussion, we will reveal that nonlinear signal impairments are the dominant factor limiting the performance of analog MFH. On the other hand, a digital MFH network digitizes mobile signals into 0/1 bit streams, and transmit the digitized bits via an digital fiber link based on intensity modulation and direct detection (IM/DD). Since mobile signals are transmitted in digital waveforms, such as on-off keying (OOK) and pulse amplitude modulation (PAM), which are inherently robust against noise or nonlinearities, the transmission impairments of MFH links are isolated from the quality of received signals as soon as error-free transmission is achieved. Meanwhile, optical IM/DD links can easily achieve error-free transmission, and have been widely employed as a mature technology in metro and access optical networks. Current passive optical networks (PONs) are mainly based on optical IM/DD links. However, due to the tremendous bandwidth generated by digitization, digital MFH networks suffer from low spectral efficiency and limited data rate. A popular digitization interface for Long Term Evolution (LTE) signals is common public radio interface (CPRI), which digitizes each 20-MHz LTE signal using

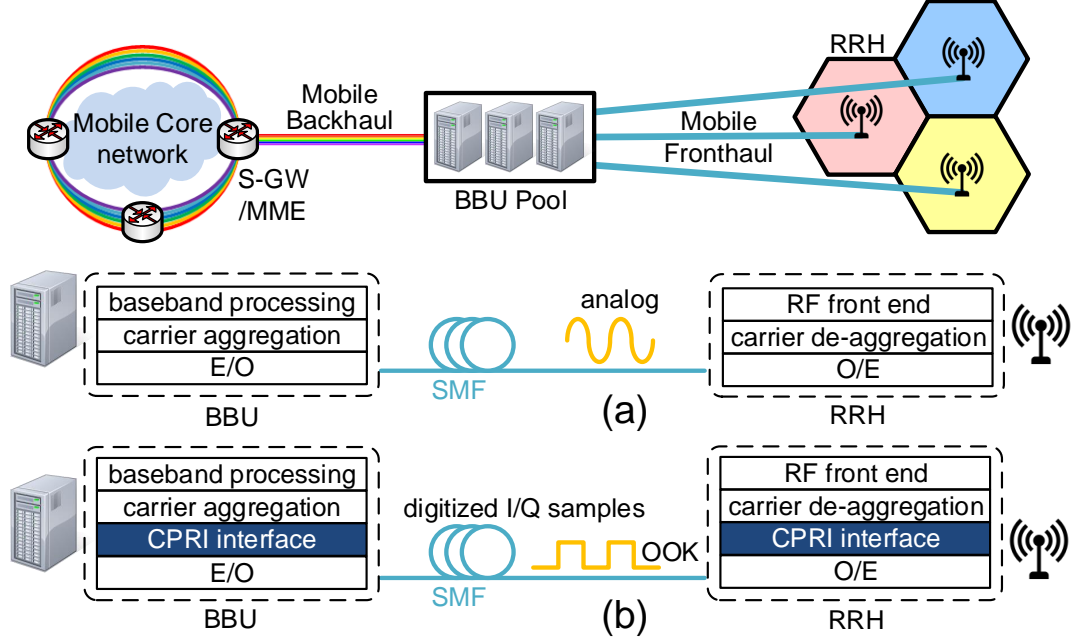


Figure 1.3: Two different MFH architectures. (a) Analog MFH. (b) Digital MFH

a Nyquist analog-to-digital converter (ADC) with sampling rate of 30.72-MSa/s and 15 quantization bits [36]. Due to its huge bandwidth requirement and lack of scalability, CPRI becomes the data rate bottleneck of MFH networks, and it would be technically challenging and cost-prohibitive to support the future carrier aggregation, massive MIMO, and CoMP using CPRI-based digital MFH.

## 1.2 Analog Mobile Fronthaul

### 1.2.1 Radio-over-Fiber Technologies

The key enabling technology for analog MFH networks is radio-over-fiber (RoF), which can transmit radio frequency (RF) signals [37–39], including MMW signals [40–42], over optical fibers in the analog waveforms. Compared with CPRI-based digital MFH architecture, RoF-based analog MFH features several advantages and one disadvantage:

1. RoF-based analog MFH uses analog signal transmission over optical fiber, which has high spectral efficiency and is able to circumvent the data rate bottleneck of CPRI.
2. Due to its transparency to signal waveforms and modulation formats, RoF technology can support the coexistence of multiple bands of wireless services from different RATs, e.g. Wi-Fi, WiGig, LTE, aggregate and convey them together via a shared fiber link, which is a promising aspect for the next generation multi-service converged access networks to enable software defined traffic offloading and resource sharing among coexistent RATs.
3. Most signal processing functions are centralized in BBU with a further simplified RRH, leaving only RF air interface, i.e., power amplifier and antenna, in the RRH. Due to the tree architecture of MFH networks, and the large number of RRHs, network deployment cost can be reduced significantly.
4. Like any other analog system, RoF-based analog MFH suffers from transmission impairments, and the received signal quality is limited by both noise and nonlinear distortions. In this thesis, we will reveal how nonlinear signal distortions limit the performance of RoF-based analog MFH networks.

Due to its simple system design, high spectral efficiency, and transparency to various RATs and signal waveforms, analog MFH technology can support multiple mobile services from various RATs, e.g. Wi-Fi, WiGig, LTE, aggregate and deliver them together via a shared fiber-optic link. There have been quite a few demonstrations of analog MFH supporting multi-RAT multi-service coexistence. In [43–46], for example, multiple bands of 60-GHz services were multiplexed in the frequency domain and delivered together by a MMW-over-fiber fronthaul system. Multi-RAT coexistence of cellular and Wi-Fi was reported [47, 48], and more importantly, resource sharing and traffic offloading between Wi-Fi and LTE-U were demonstrated [49, 50]. Multi-RAT



aggregation of LTE, Wi-Fi, WiMAX, and MMW services was also demonstrated using optical band mapping technique [45, 46, 51, 52]. In recent years, RoF technologies also attracted increasing research interest as it provides a promising solution to deliver large numbers of carrier aggregated LTE signals. Efficient MFH based on RoF technologies was proposed, where carrier aggregation can be implemented either by digital signal processing (DSP) [53–55] or by analog processing [56]. Intermediate frequency over fiber technologies were also reported [57, 58].

### 1.2.2 Nonlinearities of Analog Mobile Fronthaul Network

Besides the opportunities of high spectral efficiency and large fronthaul capacity, analog MFH technology also presents the challenge of nonlinear interferences among the coexistent multiple services from various RATs. Due to its analog nature, the received signal quality of an analog MFH system may be degraded by several factors, such as chromatic dispersion [59, 60], fiber nonlinearities [61], and imperfect electro-optical interface of optical modulators [62–70]. Due to the limited optical launch power and short fiber distance in MFH networks, the nonlinear electro-optic interface of optical modulators becomes the dominant factor that limits the performance of MFH networks. Based on the electro-optic Pockels effect, most Mach-Zehnder modulators (MZM) have an interferometric architecture and sinusoidal transfer function, e.g., intensity modulator, dual-electrode MZM (DEMZM), and in-phase quadrature MZM (IQ-MZM).

As shown in Fig. 1.4, there are two distinct nonlinear impairments in analog MFH networks, carrier intermodulation (IM) and data-dependent cross-modulation (XM). In Fig. 1.4(a), carrier IM indicates the generation of harmonic and beat frequency components among different RF carriers. For example, third-order IMs include composite triple beat (CTB)  $f_1 + f_2 - f_3$  and two-tone third-order IMs  $2f_1 - f_2$ ; second-order IMs include sum or difference frequency components  $f_1 \pm f_2$ . Carrier

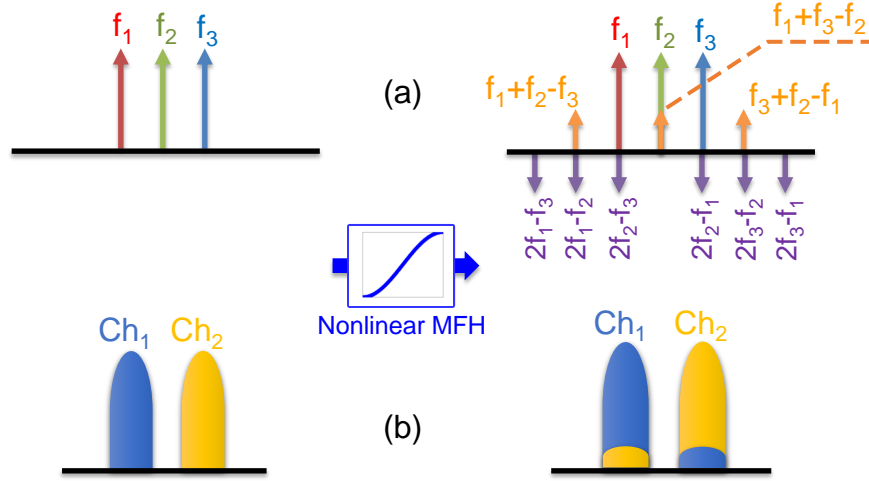


Figure 1.4: Nonlinear impairments in analog MFH networks. (a) Carrier intermodulation. (b) Cross-modulation.

IM is a frequency-dependent effect, and usually only odd-order IMs are of interest since they have large probabilities to overlap with existing carriers, especially for equally spaced multi-carrier systems such as cable TV (CATV) or orthogonal frequency division multiplexing (OFDM) systems; whereas even-order IMs are usually out-of-band and can be eliminated by filtering. On the other hand, as shown in Fig. 1.4(b), data-dependent XM is a baseband effect, which takes the data modulation into consideration and focuses on the signal distortions induced by modulation crosstalk (X-talk) between different channels. Due to their different behaviors, carrier IMs are characterized in the frequency domain in terms of carrier-to-noise ratio (CNR), third-order intercept point (IP3), spurious free dynamic range (SFDR), etc.; whereas data-dependent XMs are characterized in the time domain by eye-diagram degradations and constellation distortions. Out-of-band IMs can be eliminated by filtering or avoided by increasing channel spacing; while XM effects are always in-band, and cannot be alleviated by filtering. In this thesis, we will reveal that carrier IMs dominate the nonlinear impairments of multi-carrier signals; whereas data-dependent XMs are

the dominant impairments of single-carrier signals. So far as we know, carrier IMs have been studied extensively in various analog RoF systems, but there has been no report about data-dependent XMs.

Transmission impairments induced by optical intensity modulators were investigated by both theory [62] and experiments [63]. Carrier IMs caused by DEMZM among multiple RF tones were studied experimentally [64], and their interaction with fiber chromatic dispersion was analyzed in a subcarrier multiplexed (SCM) RoF system [65]. Nonlinear IMs of both double-sideband (DSB) [66, 67] and single-sideband (SSB) modulations [67–69] were also investigated. The impairments of single-carrier and OFDM signals were compared by both simulations [62] and experiments [63], and it was found that given the same channel response, OFDM signals experience more distortions due to their continuous envelope and high peak-to-average power ratio (PAPR).

There are two major limitations in these existing works. First, many of them simplify mobile signals as single-frequency tones without data modulation, i.e., each signal is pure sinusoidal with infinitely small bandwidth, and only carrier IMs were evaluated. Multi-tone test was widely used as a standard method to evaluate the linearity of optical modulators, but it can only characterize the out-of-band IMs. In real systems, however, each mobile signal has a certain bandwidth due to data modulation, and the out-of-band IMs should not be a concern since they are eventually filtered out by receivers. Secondly, in most of these works, only one signal was considered, and the impairments of each signal were evaluated individually. There is no effort to investigate the inter-channel interferences among multiple bands of signals, which turn out to be the most important factor limiting the system performance of multi-RAT multi-service MFH networks.

Therefore, in multi-RAT multi-service analog MFH networks, the dominant nonlinear impairments of single-carrier signals are data-dependent XMs. This is because

for single-carrier signals, most IMs are out-of-band and will be blocked by receivers; whereas XM is a baseband effect, which is always in-band and cannot be eliminated by filtering. On the other hand, for multi-carrier signals, the dominant impairments are carrier IMs. But different from conventional studies that only focus on single band of signals, this research will investigate the nonlinear inter-channel interferences among multiple bands of multi-carrier signals, which turn out to be the most important factor limiting the performance of multi-RAT multi-service MFH networks.

### 1.2.3 Orthogonal Frequency Division Multiplexing (OFDM)

Due to its high spectral efficiency, simple equalization in the frequency domain, and robustness against inter-symbol interference [71, 72], orthogonal frequency division multiplexing (OFDM) signals have been adopted widely by both wired and wireless access networks, such as asynchronous digital subscriber line (ADSL) [75], high-bit-rate digital subscriber line (HDSL) [76], digital audio broadcasting (DAB) [73], digital video broadcasting (DVB) [74], Wi-Fi (802.11), WiGig (802.11ad), WiMAX, and LTE (3GPP). Due to its simple equalization in the frequency domain, OFDM signals can easily handle multipath induced frequency selective fading, and have been widely adopted by wireless communication standards. Table 1.1 summarizes the OFDM parameters used by most popular RATs. Meanwhile, thanks to its capability to deal with chromatic dispersion and polarization mode dispersion in the frequency domain, OFDM also found its applications in optical communications, including both transmission and access networks, such as coherent optical OFDM (CO-OFDM) [77–79], and orthogonal frequency division multiple access passive optical networks (OFDMA-PON) [80–83].

Table 1.1: OFDM parameters in popular wireless communication standards

	Protocol	Subcarrier Spacing (kHz)	Frequency band (GHz)	FFT size	# of data subc. + pilots	BW (MHz)	Data BW (MHz)	Modulation Format
Wi-Fi <sup>1</sup> (802.11)	802.11 a/g	312.5	5.15-5.875 (a) 2.4-2.497 (g)	64	48+4	20	16.25	a/g/n/af/aj: BPSK /QPSK /16QAM /64QAM
	802.11 n		5.15-5.875 2.4-2.497	64	52+4	20	17.5	
				128	108+6	40	35.625	
	802.11 ac/ax		5.15-5.875	64	52+4	20	17.5	
				128	108+6	40	35.625	
				256	234+8	80	75.625	
				512	468+16	160	151.25	
	802.11 af	US 41.67	54-698MHz	144	108+6	6	4.75	ac/ax/ah: BPSK /QPSK /16QAM /64QAM /256QAM
		Europe 55.56	470-790MHz	144	108+6	8	6.33	
	802.11 ah	31.25	Sub 1-GHz ~900 MHz <sup>2</sup>	32	24+2	1	0.8125	
				64	52+4	2	1.75	
				128	108+6	4	3.5625	
				256	234+8	8	7.5625	
	802.11 ad (WiGig)	5156.25	57-64 <sup>3</sup>	512	336+16	2640	1815	ad: QPSK /16QAM /64QAM
		802.11 aj	2578.125	42.3-47 47.2-48.4	256	168+8	660	
WiMAX	802.16 e	10.94	2.1-5.9	128	114	1.4	1.25	QPSK /16QAM /64QAM
				512	456	5.6	5	
				1024	912	11.2	10	
				2048	1824	22.4	20	
LTE <sup>4</sup>	3GPP release 8	15	0.7-2.6	128	75	1.140	1.92	QPSK /16QAM /64QAM
				256	150	2.265	3.84	
				512	300	4.515	7.68	
				1024	600	9.015	15.36	
				1536	900	13.515	23.04	
UWB <sup>5</sup>	802.15.3 a	4125	3.168-10.56	128	100+12	528	462	QPSK

1. IEEE 802.11 wireless LANs standard <http://standards.ieee.org/about/get/802/802.11.html>
2. Frequency bands of 802.11 ah: South Korea 917.5-923.5 MHz, Europe 863-868 MHz, Japan 916.5-927.5 MHz, China 755-787 MHz, Singapore 866-869 MHz and 920-925 MHz, US 902-928 MHz.
3. Frequency bands of 802.11 ad (WiGig): US/Canada 57.05-64 GHz, European Union 57-66 GHz, South Korea 57-64 GHz, Japan 57-66 GHz, Australia 59.4-62.9 GHz, China 59-64 GHz.
4. 3GPP LTE standard <http://www.3gpp.org/technologies/keywords-acronyms/98-lte>
5. IEEE 802.15 standard <http://www.ieee802.org/15/>

#### 1.2.4 Nonlinear Impairments of OFDM Signals

On the other hand, OFDM signals are sensitive to nonlinear impairments due to their large number of subcarriers, continuously varying envelope, and high peak-to-average power ratio (PAPR) [84–87]. Nonlinear IMs among subcarriers are the dominant nonlinear impairments of OFDM signals, which produce both in-band interferences and out-of-band spectral emission. According to the central limit theorem [88], in-band interferences can be modeled as a zero-mean Gaussian noise [89]; whereas out-of-band spectral emission, which is also known as out-of-band spectral regrowth, lead to inter-channel interferences among neighboring signal bands, which can be alleviated by filtering or increasing channel spacing. Note that OFDM signals have equally spaced subcarriers. Third-order IMs among three subcarriers ( $f_1 \pm f_2 \pm f_3$ ) are of particular interest, since they have large probabilities to overlap with existing subcarriers. Even-order IMs ( $f_1 \pm f_2$ ) are usually out-of-band and can be filtered out easily.

Nonlinear impairments of OFDM signals have been studied extensively in various optical and wireless communication scenarios, such as CO-OFDM [90–92], RoF [93–96], power amplifier (PA) [97–99], visible light communications (VLC) [100–103], and RF front end [104]. Table 1.2 summarizes the nonlinear transmission impairments of OFDM signals in various communication scenarios.

In CO-OFDM systems, the nonlinear impairments of OFDM signals originate from four-wave mixing (FWM) induced by Kerr effect in optical fibers, which essentially is the counterpart of subcarrier IMs in the optical domain. For RoF and VLC systems, nonlinear distortions are caused by the imperfect transfer functions of electro-optic interfaces, such as MZM or light emitting diode (LED). For power amplifiers (PAs), the nonlinear impairments are induced by amplitude-to-amplitude (AM-AM) or amplitude-to-phase (AM-PM) conversions, where the amplitude of input signal leads to the amplitude/phase variations of the amplifier gain.

Table 1.2: Nonlinear impairments of OFDM signals in optical/wireless communication scenarios

Scenarios	CO-OFDM	RoF	Power amplifier	VLC
Nonlinearity Origin	FWM in fiber	Modulator transfer function	AM-AM <sup>1</sup> , AM-PM <sup>2</sup> conversions	LED transfer function
Domain	Optical	Electro-optic interface	Electrical	Electro-optic interface
Signal bands	WDM	Multiple RF bands	Single RF band	Single baseband
Nonlinearity Orders	Odd <sup>3</sup>	Odd <sup>4</sup>	Even and odd	Even and odd
References	[90–92]	[93–96]	[97–99]	[100–103]

1. Amplitude to amplitude (AM-AM) conversion.
2. Amplitude to phase (AM-PM) conversion.
3. Kerr effect in optical fibers only has odd-order nonlinearities due to the centro-symmetry of fiber.
4. Only odd-order nonlinearities produce in-band interferences, even-order interferences are usually out-of-band, and can be filtered out.

Most existing studies only focus on the impairments of each individual OFDM signal, e.g., PA and VLC systems only concern the intra-band IMs among subcarriers from the same OFDM signal. CO-OFDM systems can support multiple OFDM signals by exploiting wavelength-division-multiplexing (WDM) technology, but the interferences among different OFDM signals are negligible, since different signals are carried by different wavelengths, and the FWM conversion efficiency is very low due to the large k-vector difference and strong phase mismatching caused by fiber dispersion. In RoF-based MFH systems, however, nonlinear interferences among multiband OFDM signals become of particular interest, since most RATs, e.g., Wi-Fi, LTE, WiGig, support multiband/multichannel operations, and in 5G MFH, multiband OFDM services from different RATs will be aggregated in the frequency domain and delivered together via a shared fiber-optic link, whose nonlinear channel response makes the subcarrier IMs among different OFDM signals inevitable. Although the nonlinear

impairments of OFDM signals have been studied extensively, most existing works only focused on the nonlinear distortions of each individual OFDM signal. There has been meager effort spent on the inter-band interferences among multiple OFDM signals, which, however, will become the most common scenarios in the next generation multi-RAT multi-service MFH networks.

### 1.3 Linearization Technologies

In order to mitigate the nonlinear transmission impairments of OFDM signals in MFH networks, two different strategies could be exploited. One method is to modify the signal waveform to enhance its robustness against nonlinear distortions; whereas the other strategy is to linearize the channel response of MFH links to minimize the nonlinear impairments after transmission. The first strategy is also known as a waveform-specific method, since it changes the signal waveforms to increase the nonlinearity tolerance. For example, clipping techniques was proposed to reduce the PAPR of multi-carrier signals to improve their nonlinearity resilience [105, 106]. Digital MFH can also be considered as an extreme case of waveform-specific strategy, where the continuous envelopes of mobile signals are sampled and quantized into discrete bits by analog-to-digital converters (ADC), and then transmitted in digital communication systems, which are inherently robust against nonlinear impairments.

On the other hand, the other strategy is to keep the signal waveforms intact, but modify the nonlinear channel response of analog MFH. Since the linearized channel response is transparent to different signal waveforms, this method is considered as waveform-agnostic. Due to their wide applications in analog RoF, MFH, and many other optical/wireless access networks, waveform-agnostic linearization technologies have attracted intensive research interests and various implementation have been reported in either electrical or optical domain. Table 1.3 gives a summary of different linearization technologies, listing pros and cons of each implementation.



Table 1.3: Summary of linearization technologies

Linearization Technologies	Domain	Operation principle	Pros	Cons	References
Feedforward	Hybrid	Two electro-optical loops One for signal cancellation One for error cancellation	Suppress both nonlinearity and RIN	Two different wavelengths Only intensity modulation Complicated circuit design	[107–116]
Dual-parallel modulation	Optical	Static form of feedforward Distortions from two parallel MZMs cancel out	All-optical No bandwidth limit Applicable to coherent system	Lack of adaptivity Small tolerance Precise control Complicated MZM design	[117–122]
Mixed-polarization	Optical	Static form of feedforward Distortions from two polarizations cancel out	All-optical No bandwidth limit Applicable to coherent system	Lack of adaptivity Small tolerance Precise control Complicated setup	[123–130]
Cascaded SOA and MZM	Optical	Use nonlinear gain curve of a saturated SOA to compensate MZM	Gain and negative chirp of SOA compensate loss and positive chirp of MZM	Only intensity modulation SNR limited by ASE Bandwidth limited by SOA Require precise match	[131, 132]
Light injection XGM	Optical	Distortions from two DMLs cancel each other One generates signal One generates distortions	Simple Low-cost	Only intensity modulation Bandwidth limited by DML Stability issue Precise bias control	[133–136]
Analog predistortion	Electrical (analog)	Predistort signal before transmission	Simple Low-cost	Limited nonlinear response Difficult to handle memory	[137–154]
Digital predistortion	Electrical (digital)	Predistort signal before transmission	Versatile for arbitrary nonlinear response and memory effect	Speed limited by AD/DA Expensive AD/DA	[155–167]

### 1.3.1 Feedforward

Feedforward technique was first proposed as an effective way to suppress the nonlinear distortions of directly modulated lasers (DML) [107–111], including both distributed feedback (DFB) and Fabry-Perot (FP) lasers. It was widely used in analog amplitude-modulated subcarrier multiplexing (AM-SCM) video systems [112], such as cable TV and multiband wireless-over-fiber systems [113–116]. In a feedforward linearization setup, there are two electro-optical loops used in the transmitter side. One loop is for signal cancellation, in which there is a modulated DML and a photodetector (PD), which detects the modulated laser output and compares it with the original RF signal, so that the modulation error can be extracted. The other loop is for error cancellation, which modulates the extracted error signal to a second laser and combines its output with the first laser, so that the error signals from both lasers cancel out. Since the error signal of first laser contains both nonlinear distortions and relative intensity noise (RIN), one promising feature of the feedforward technique is that it can suppress nonlinearities and RIN simultaneously, which significantly enhances the spurious free dynamic range (SFDR) of CATV systems. On the other hand, feedforward technique suffers from complicated circuit design on the transmitter side, which exploits both optical and electrical components and requires precise adjustment of amplitude, delay, and phase shift, making it difficult to use. Meanwhile, since two lasers have different wavelengths, feedforward technique can only deal with the imperfectness of intensity modulation, and is incompatible with coherent systems with heterodyne or homodyne detections. Furthermore, fiber transmission distance is limited by chromatic dispersion, caused by the wavelength difference of two lasers; or in other words, for a given fiber length, fine tuning and accurate matching of signal amplitude and phase in both loops are required.

### 1.3.2 Dual-Parallel Modulation

All-optical linearization technologies were also developed, including dual-parallel modulation [117–122], mixed-polarization [123–130], cascaded semiconductor optical amplifier (SOA) and MZM [131, 132], and light injection cross-gain modulation (XGM) [133–136]. Most of these methods use two cascaded or parallel devices with similar or opposite nonlinear characteristics, so that the distortions generated by two devices can cancel each other. For instance, the dual-parallel modulation technique exploits two parallel modulators, one for signal generation and the other for distortion compensation. The first modulator has large optical input power and small modulation depth, so that it works in the linear region; whereas the other modulator has small optical input power and strong driving voltage, and works in the severely nonlinear region. By carefully adjusting their bias, the output from two parallel modulators have the same amount of nonlinear distortions, but with opposite phase, so that they cancel each other when the output of two modulators are combined together. Since the linearization is realized in the optical domain, dual-parallel modulation technique has no bandwidth limitation. Meanwhile, it essentially is a static form of feedforward technique implemented in the optical domain without adaptive control [117]. Due to its lack of adaptivity, the optimum operation conditions of a dual-parallel modulation setup are dependent on optical launch power and modulation indices. Once the optical input power or RF driving signal changes, the power splitting ratio, delay and phase all need to be re-calibrated. Thanks to its complicated system design and doubled hardware cost, and small tolerance to bias mismatching, it is difficult to make dual-parallel modulation work stably with discrete devices and can only be realized by integrated photonic circuits [118].

### 1.3.3 Mixed-Polarization

The linearization technology based on mixed-polarization is actually a special case of dual-parallel modulation, where the two parallel modulators are replaced by two orthogonal polarizations of an optical modulator, i.e., ordinary (o) and extraordinary (e) light, or transverse electric (TE) and transverse magnetic (TM) modes. Since  $\text{LiNbO}_3$  crystal has anisotropic electro-optic coefficients, and most electro-absorption modulator (EAMs) are polarization-dependent, in a mixed-polarization setup, the two orthogonal polarizations experience different modulation characteristics. A linear polarizer is placed before the modulator to adjust the optical power of two polarizations by rotating the angle of the polarizer; and a second polarizer is placed after the modulator to combine the two polarizations. By carefully adjusting the angles of two polarizers and exploiting the unequal electro-optic modulation characteristics, the nonlinear distortions of two polarizations can compensate each other. This method was initially proposed to linearize interferometric modulators [123, 124] and phase modulators [125], and then extended to compensate the nonlinear distortions of MZMs and EAMs in RoF systems [126–130]. It has been reported that mixed-polarization method can linearize x-cut intensity modulator, z-cut phase modulator, z-cut dual-electrode MZM (DEMZM), as well as EAM. Due to the all-optical implementation, mixed-polarization technology has no modulation bandwidth penalty and can be applied to broadband MMW scenarios. On the other hand, the two optical polarizers and DC bias of the modulator require precise control, making this method difficult to use in real-world deployment. Moreover, the cancellation between two polarizations not only suppress nonlinear distortions, but also sacrifices modulated signals and reduces the modulation efficiency.

#### 1.3.4 Cascaded SOA and MZM

Another optical-domain linearization technique is to cascade an SOA with a MZM, make the SOA working in saturated region, and use its nonlinear gain curve to compensate the nonlinear transfer function of the MZM [131, 132]. There are two side benefit of this method, one is that SOA can compensate the insertion loss of MZM, and save the necessity of a EDFA at the transmitter side; the other benefit is that SOA provides negative chirp, which can cancel out the positive chirp of MZM, and increase the fiber transmission distance limited by chromatic dispersion. The amplified spontaneous emission (ASE) noise of SOA, however, limits the achievable optical signal-to-noise ratio (OSNR) of linearized signals to less than 15 dB; and the SOA carrier relaxation process limits the modulation bandwidth to less than 10-20 GHz. This technique can only linearize intensity-modulated signals, and not applicable for optical field modulation in coherent communication systems. The nonlinear gain curve of SOA has to accurately match the nonlinear transfer function of MZM, so precise tuning of the input optical power and DC bias of SOA are required.

#### 1.3.5 Light Injection Cross-Gain Modulation

Light injection XGM technique was first proposed by [133], and then used to linearize directly modulated DFB lasers [134–136]. It exploits the XGM between two DFB lasers, making one laser works in the linear region to generate signal components and another biased at low current to generate distortion components due to the clipping effect. By carefully adjusting the DC bias of two lasers, it is possible to make the distortion components from two lasers cancel each other. By feeding the second laser into the first one, signal components from two laser do not affect each other because of the large difference in magnitude, but the distortion components cancel each other. This optical domain technique can only linearize intensity modulation, and the modulation bandwidth is limited by the bandwidth of DFB lasers. Sophisti-

cated design and stability issue of light injection make it difficult to use in real MFH systems.

### 1.3.6 Predistortion

Feedforward and other optical-domain linearization technologies all suffer from high cost optical devices, complicated system design, and more importantly, precise control and small tolerance of amplitude/phase/bias mismatching, which severely prevent these technologies from wide application in real MFH networks. Predistortion technique, on the other hand, only needs a predistorter block inserted before the transmitter to compensate the nonlinear channel response of MFH links, which can be implemented in the pure electrical domain. With a predistorter included, an overall linear channel can be obtained, which is transparent to different signal waveforms. The predistorter can be realized in the analog domain using low-cost analog circuits [137–154], or in the digital domain using digital signal processing (DSP) [155–167]. In MFH networks, due to the static and highly predictable nature of channel response, as well as the limited system budget, predistortion technique is considered as one of the simplest and most cost-effective solution for nonlinearity compensation.

Predistortion technique was first implemented in the analog domain using diodes or bipolar transistors, exploiting their exponential transfer characteristics to compensate odd-order nonlinearities. It was used to deal with the nonlinearities of DMLs in amplitude-modulated subcarrier multiplexing (AM-SCM) video systems [137–140], and then also applied to EAMs [141] and MZMs [142]. A multipath configuration of analog predistorter was demonstrated in [143], including direct feed-through (linear), second-order and third-order paths, where the nonlinear paths were used to generate different orders of distortion components. In the circuit design of predistorters, field effect transistors (FET), such as CMOS, were initially not used due to their square-law behaviors. As the FET technology advanced, increasing research interests have

been attracted due to their low-cost, small power consumption, compact integration and advanced signal processing capabilities. CMOS-based predistortion circuits were demonstrated [144–147], where feedback controls were developed to adjust the gain and phase coefficients of the predistorter according to the input signal amplitude, so that adaptive broadband linearization was demonstrated. Since the linearization was carried out in the electrical domain, analog predistortion can be applied in both intensity modulated and coherent communication systems. In recent years, it was also used in long-haul [148], RoF [149–153], and MFH systems [154].

In general, any transmission impairments can be modeled as nonlinear distortion with memory effect, where the nonlinear distortion captures the dependence of channel transfer function on input amplitudes in the time domain; whereas memory effect is contributed by the bandwidth limitation in the frequency domain. For analog predistortion, the main technical challenges are the difficulties to synthesize arbitrary transfer functions in the time domain, and to compensate arbitrary bandwidth limitation in the frequency domain. Some transfer functions are difficult or even impossible to achieve with analog diodes or transistors, e.g., in [143], simultaneous correction of both second and third-order distortions cannot be achieved due to the coupling between different paths of different orders of nonlinearities. In the frequency domain, broadband predistortion is also challenging to realize, and analog predistortion with 5-GHz bandwidth was not reported until 2012 [150].

On the other hand, thanks to the advancement of DSP technologies, predistortion can also be carried out in the digital domain, where the input analog signals are first transformed to the digital domain by analog-to-digital conversion (ADC), and after digital processing, the processed signals are transformed back to analog waveform by digital-to-analog conversion (DAC). Enabled by DSP technologies, challenges of analog predistortion can be easily addressed. In the time domain, DSP can synthesize arbitrary transfer functions; in the frequency domain, DSP can address arbitrary

memory effects by frequency equalization exploiting FFT/IFFT. Some functions that are difficult or even impossible to achieve with analog predistortion can be easily realized by DSP. For example, digital predistortion of OFDM signals with dynamic adaptivity was demonstrated [155–157], and memory effect was taken into account using memory-polynomial models [158, 159]. Digital predistortion has been widely used for multi-carrier signals, where the predistortion function can be integrated with other DSP blocks in the transmitter, for example, it has been used in coherent optical OFDM [160–163], OFDMA-PON [164], and analog MFH systems [165–167]. Meanwhile, the only constraint of digital predistortion is processing speed, which is mainly limited by the speed and power consumption of input/output ADC/DAC. Table 1.3 gives a summary of various linearization technologies.

#### 1.4 Digital Mobile Fronthaul

In the next generation mobile data networks, in order to accommodate different mobile services from various RATs, both analog and digital MFH architectures have been investigated. Analog MFH based on RoF technologies features simple, low-cost implementations, high spectral efficiency, and transparency to different RATs and signal waveforms, but it is susceptible to nonlinear transmission impairments due to the continuous waveforms of multi-carrier mobile signals, especially given the factor of multi-RAT multi-service coexistence in 5G networks. This thesis will investigate the nonlinear signal impairments and mitigation technologies of analog MFH networks, but it is not easy to dynamically track the channel response of MFH links, especially given the factor of highly time-varying broadband data traffic in access networks.

Digital MFH, on the other hand, sample and quantize the continuous envelopes of mobile signals using a digitization interface, and transport the digitized bit streams by leveraging mature digital optical communication technologies. For 5G mobile data networks, it is of interest to digitize mobile signals from different RATs and deliver



them together via digital fiber-optic links of existing passive optical networks (PON). With the help of digitization, digital MFH offers high signal fidelity and excellent tolerance against transmission impairments with the penalty of relatively low spectral efficiency. Once error-free transmission is achieved, the received signal quality can be isolated from transmission performance.

#### 1.4.1 Common Public Radio Interface

The most popular digitization interface, CPRI, digitizes each LTE signal using a Nyquist ADC with sampling rate of 30.72 MSa/s and 15 quantization bits (plus one control bit) per sample, which leads to very low spectral efficiency and requires tremendous bandwidth after digitization [36], making CPRI become the data rate bottleneck of digital MFH. Table 1.4 lists the standard data rate options of CPRI. Line coding of 8b/10b or 64b/66b is used for DC balance, disparity check, and to ensure sufficient 0/1 transitions for clock recovery. In option 1, each I or Q component of a 20-MHz LTE CC consumes fronthaul capacity of  $30.72\text{MSa/s} \times 16\text{bit/Sa} \times 10/8 = 614.4\text{Mb/s}$ ; in option 2, to support one 20-MHz LTE component carrier (CC), CPRI consumes 1.23 Gb/s fronthaul capacity, including both I and Q components; in option 7, to support eight LTE CCs, it takes up to 9.83-Gb/s, so a 10-Gb/s PON can only accommodate 8 LTE CCs. Meanwhile, the rapidly growing LTE carrier aggregation (CA) makes it challenging to use CPRI to support 5G digital MFH networks. LTE CA was initially standardized by 3GPP release 10, allowing 5 CCs [20], and then quickly expanded to 32 CCs by 3GPP release 13 [21], consuming up to 40-Gb/s fronthaul capacity if fully digitized by CPRI, which cannot be supported by any existing optical/wireless access networks. Therefore, it would be technically challenging and cost-prohibitive to use CPRI as the digitization interface for the next generation digital MFH. To overcome the CPRI bottleneck, I/Q compression with compression ratio of  $\sim 50\%$  has been demonstrated [168]. Compressed CPRI over

Table 1.4: CPRI data rate options

Option	Line coding	LTE carriers	Examples	Bit rate (Mb/s)
1	8b/10b	0.5	Only I or Q component	614.4 $491.52 \times 10/8$
2	8b/10b	1	One 20-MHz LTE CC	1228.8 $491.52 \times 10/8 \times 2$
3	8b/10b	2	2 CA / 2x2 MIMO	2457.6 $491.52 \times 10/8 \times 4$
4	8b/10b	2.5	Only I or Q, 5 CA	3072 $491.52 \times 10/8 \times 5$
5	8b/10b	4	4x4 MIMO or 2 CA + 2x2 MIMO	4915.2 $491.52 \times 10/8 \times 8$
6	8b/10b	5	5 CA	6144 $491.52 \times 10/8 \times 10$
7	8b/10b	8	8x8 MIMO or 2 CA + 4x4 MIMO	9830.4 $491.52 \times 10/8 \times 16$
7A	64b/66b	8	8x8 MIMO or 4 CA + 2x2 MIMO	8110.08 $491.52 \times 66/64 \times 16$
8	64b/66b	10	5 CA + 2x2 MIMO	10137.6 $491.52 \times 66/64 \times 20$
9	64b/66b	12	3 CA + 4x4 MIMO	12165.12 $491.52 \times 66/64 \times 24$

- CPRI: common public radio interface.
- CA: carrier aggregation.
- CC: component carrier.
- MIMO: multiple input multiple output.
- CPRI uses a sampling rate of 30.72 MSa/s to samples each 20-MHz LTE carrier and 16 bits for each sample (15 quantization bits and one control bit), so each I or Q component consumes  $30.72\text{MSa/s} \times 16\text{bits/Sa} = 491.52\text{Mb/s}$  fronthaul capacity before line coding.

time-division-multiplexed PON (TDM-PON) [169, 170], uncompressed CPRI over wavelength-division-multiplexed PON (WDM-PON) [171], as well as split physical layer functions (split-PHY) [172, 173] have been reported.

#### 1.4.2 Delta-Sigma Modulation

To circumvent the data rate bottleneck of CPRI and increase the capacity of MFH networks, one promising solution is to replace the digitization interface from CPRI to delta-sigma modulation, which trades the quantization bits for sampling rate so that both the spectral efficiency and capacity of MFH networks can be improved. Different from the Nyquist ADC of CPRI, a delta-sigma modulator uses an oversampling ADC with sampling rate much higher than the Nyquist rate of LTE signals [174, 175], but only needs few (one or two) quantization bits. A Nyquist ADC has its quantization noise evenly distributed in the Nyquist zone [176], which is the reason why CPRI needs a large number of quantization bits to reduce the noise. A delta-sigma modulator, on the other hand, has much wider Nyquist zone due to oversampling, and can exploit uneven noise distribution enabled by noise shaping technique. The quantization noise is pushed out of the signal band, so that the signal and noise are essentially separated in the frequency domain, and in-band signal-to-noise ratio (SNR) can be optimized [177–180]. It should be noted that noise shaping technique is only allowed for delta-sigma modulators due to their wide Nyquist zones enabled by oversampling. Compared with CPRI, delta-sigma modulator-based digitization interface provide higher spectral efficiency and enhanced fronthaul capacity.

Delta-sigma modulation has been employed by RF transmitters [181–190], power amplifiers [191–193], wireless receivers [194–200], radio-over-fiber systems [201–204], and visible light communications [205–207]. There have been quite a few works reported about high speed delta-sigma modulators with sampling rate up to several GSa/s [185–190].

## 1.5 Thesis Objectives and Organization

Fig. 1.5 shows the objectives and organization of this research. The objective of this thesis is two-fold. In order to support multi-RAT multi-service coexistence in the next generation MFH networks, high linearity requirement is placed on the channel response of MFH links. One objective of this research is to understand and mitigate the nonlinear transmission impairments of analog MFH, and the nonlinear distortions of mobile signals in a RoF-based multi-RAT MFH system will be investigated. We will start from signal-carrier signals, and then extend to multi-carrier OFDM signals, both with emphasis on the inter-channel interferences among multiple bands of mobile services from various RATs. Linearization technique will also be studied for nonlinearity mitigation, and there are two different linearization strategies. The waveform-agnostic strategy linearizes the MFH channel response without modifying signal waveforms, and we will choose digital predistortion technology due to its low-cost, simplicity, and versatility to deal with various nonlinearity orders and memory effects. On the other hand, waveform-specific strategy modifies the signal waveforms from continuous envelope to discrete levels and enhance their robustness against nonlinear impairments by transforming the MFH link from analog to digital. Therefore, the other objective of this research is to develop a new digital MFH architecture to replace the state-of-the-art CPRI with improved spectral efficiency and scalability. In this works, we will develop a novel digitization interface based on delta-sigma modulation, which can increase the capacity of next generation digital MFH by four times.

This thesis is organized as follows. In Chapter 2, we present the investigation of nonlinear impairments of single-carrier signals, which are dominantly contributed by nonlinear XMs, including both intra-band and inter-band XMs. In Chapter 3, we will extend our investigation to multi-carrier OFDM signals, whose impairments are

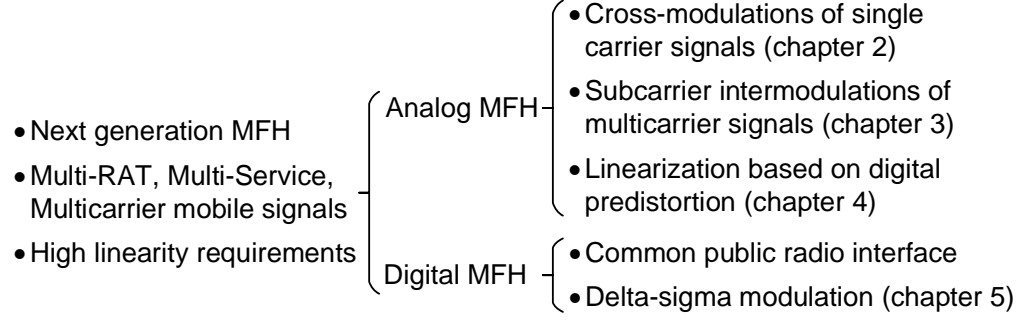


Figure 1.5: Objective and organization of this thesis.

mainly caused by nonlinear subcarrier IMs, also both intra-band and inter-band IMs will be evaluated. For both single-carrier and multi-carrier signals, both theoretical analysis and experimental measurements are carried out, and consistent results from simulation and experiments are obtained. It is experimentally verified that although the nonlinear distortions of each individual signal, i.e., intra-band XMs and intra-band IMs, have been studied extensively, it is the inter-channel interferences among different bands of signals, i.e., inter-band XMs and inter-band IMs, that dominate the nonlinear transmission impairments of multi-RAT analog MFH. Chapter 4 discusses the linearization technology based on digital predistortion for nonlinearity mitigation, which can compensate both XMs and IMs, including intra-band and inter-band effects. Chapter 5 proposes and experimentally demonstrates a novel digitization interface based on delta-sigma modulation to replace CPRI for the next generation digital MFH network. The thesis is concluded in Chapter 6.

## CHAPTER 2

### NONLINEAR CROSS-MODULATIONS OF SINGLE-CARRIER SIGNALS IN ANALOG MOBILE FRONTHAUL

#### 2.1 Introduction

In this chapter, we investigate the nonlinear impairments of single-carrier signals in a multi-RAT multi-service analog MFH network. Based on RoF technology, analog MFH features simple system design, high spectral efficiency, and large fronthaul capacity; but at the same time, it also presents the challenge of nonlinear transmission impairments due to its analog nature. There are several factors that might contribute to the signal quality degradation in an analog MFH network, chromatic dispersion [59, 60], fiber nonlinearities [61], and imperfect electro-optical interface of optical modulators [62–70]. Due to the limited optical launch power and short fiber distance in MFH networks, the nonlinear transfer function of optical modulators becomes the dominant factor that limits the MFH performance. Based on the electro-optic Pockels effect, most Mach-Zehnder modulators (MZM) have an interferometric architecture and sinusoidal transfer function, e.g., intensity modulator, dual-electrode MZM (DEMZM), and in-phase quadrature MZM (IQ-MZM). As we discussed in Chapter 1, there are two distinct nonlinear impairments in analog MFH networks, carrier IM and data-dependent XM, and for single-carrier signals, the dominant impairments are data-dependent XMs, because most carrier IMs are out-of-band and will be blocked by receivers; whereas XM is a baseband effect, which is always in-band and cannot be eliminated by filtering.

There have been many reports about the nonlinear impairments of analog RoF systems. For example, transmission impairments induced by optical intensity modulators

are investigated by theory [62] and experiments [63]. Carrier IMs caused by DEMZM were studied experimentally [64], and their interaction with fiber chromatic dispersion was analyzed in a SCM-RoF system [65]. Nonlinear IMs in both DSB [66, 67] and SSB modulations [67–69] were also evaluated. There are two major limitations of these works. First, most mobile signals are simplified as single-frequency tones without data modulation and only carrier IMs were evaluated. But in real systems, each mobile signal has a certain bandwidth due to data modulation, and it is the data-dependent XM that plays the dominant role, since it is a baseband effect which is always in-band and cannot be filtered out by receivers. Secondly, most existing works only consider one signal, and the impairments of each signal were evaluated individually. There is no effort to investigate the inter-channel interferences among multiple bands of signals, which turn out to be the most important factor limiting the system performance of multi-RAT multi-service MFH networks.

In this chapter, nonlinear XMs of single-carrier signals in a multi-RAT multi-service analog MFH network will be investigated by both theory and experiments. Intra-band XM between the in-phase (I) and quadrature (Q) components of vector signals, as well as the inter-band XMs between multiple bands of scalar and/or vector signals are studied by a closed-form analysis, and validated by experimental measurements. Both theoretical and experimental investigations give consistent results. It is observed that scalar signals only suffer from inter-band XM; whereas vector signal suffer from both intra-band and inter-band XMs. Intra-band XM induces constellation compression distortion to vector signals; while inter-band XM induces eye diagram degradation to scalar signals and constellation scaling distortion to vector signals.

This chapter is organized as follows. Section II explains the operation principles of nonlinear XMs. Section III presents the experimental setup followed by a closed-form theoretical analysis in Section IV. The simulation results are presented in Section V; and experimental results in Section VI. Section VII concludes the chapter.

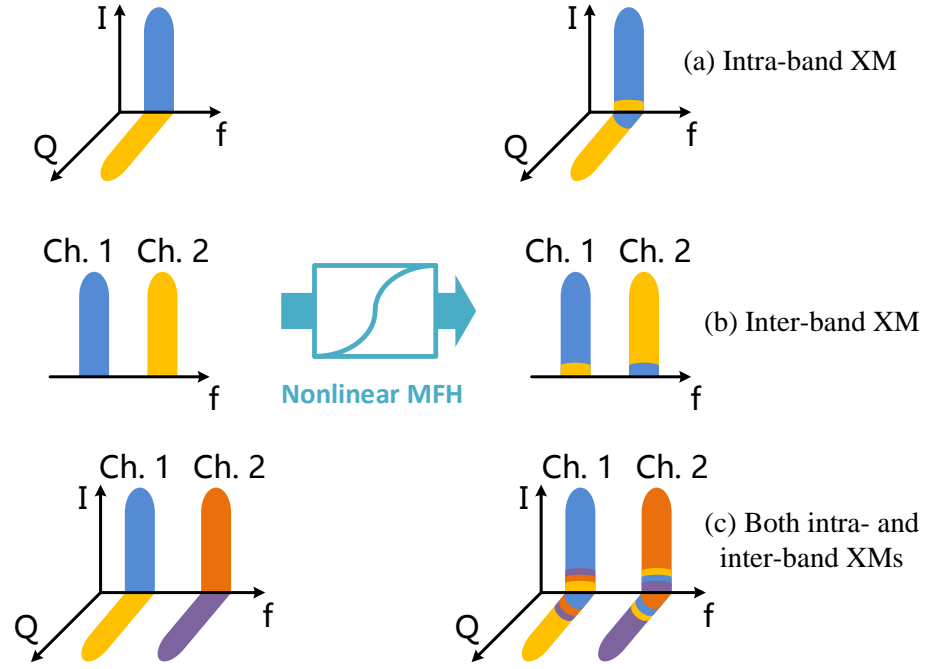


Figure 2.1: Operation principles of nonlinear XMs of single-carrier signals. (a) Intra-band XM between I and Q components of a vector signal. (b) Inter-band XM between two scalar signals. (c) Intra-band and inter-band XMs between two vector signals.

## 2.2 Operation Principles

Nonlinear XM is a baseband effect, which is independent on signal carrier frequencies but dependent on data modulation. It takes data modulation into consideration and focuses on the signal distortions caused by modulation crosstalk between different signal channels. Its operation principles are shown in Fig. 2.1. The input and output signals after propagation through a nonlinear analog MFH system are listed on the left and right sides, respectively. Fig. 2.1(a) illustrates a vector signal, e.g., a quadrature amplitude modulated (QAM) signal, whose in-phase (I) and quadrature (Q) components cross-modulate each other and introduce constellation distortions to the QAM signal. Since this XM effect occurs between the I and Q components of the same vector signal, it is defined as intra-band XM.



Fig. 2.1(b) shows two scalar signals. Scalar signals are amplitude modulated signals with only in-phase component, e.g., on-off keying (OOK) and 4-level pulse-amplitude-modulation (PAM4). After a nonlinear MFH system, the data modulation of two scalar signals crosstalk with each other, making the modulations of two signals imprint onto each other and degrade both eye diagrams. Since this XM effect occurs between two different signals, it is defined as inter-band XM. In Fig. 2.1(c), considering the nonlinear interferences between two vector signals. Besides the intra-band XMs between I and Q components from the same signal, I/Q components from different signals also cross-modulate each other, and introduce inter-band XMs. Taking Channel (Ch.) 1 as an example, it is degraded not only by the intra-band XM between I and Q components of its own, but also suffers from inter-band XMs from the I and Q components of Ch. 2. In Fig. 2.1, contributions made by different components are labeled in different colors. In a multi-service analog MFH network, scalar signals only suffer from inter-band XMs; whereas vector signals experience both intra-band and inter-band XMs. It is worth to note that nonlinear XMs are baseband effects and have no dependence on signal carrier frequencies; they are always in-band and cannot be eliminated by filtering.

### 2.3 Experimental Setup

The experimental setup of a multi-RAT multi-service analog MFH system is shown in Fig. 2.2(a). The optical spectra at points i-iv are presented in Fig. 2.2(b). A continuous wave (CW) distributed feedback (DFB) laser at 1554.5 nm with linewidth of  $\sim 10$  MHz is used in the BBU as a light source, followed by a dual-electrode Mach-Zehnder modulator (DEMZM) for both data modulation and RF sidebands generation. The half-wave voltage of DEMZM is  $V_\pi = 4.95$  V. Multiple bands of mobile signals are generated by an arbitrary waveform generator (AWG) with 2.6-GSa/s sampling rate and 1-GHz analog bandwidth. The AWG output is followed by

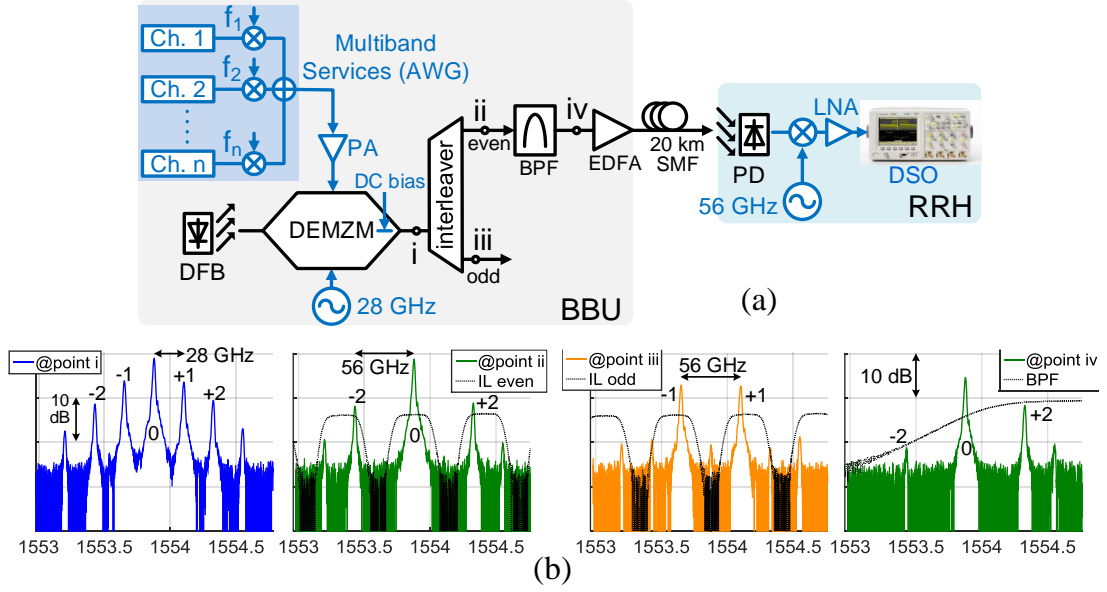


Figure 2.2: (a) Experimental setup. (b) Optical spectra at point i-iv.

a power amplifier (PA) to drive the upper arm of DEMZM. The PA has a small signal gain of 26 dB and noise figure of 11 dB. In the experiments, it is verified that the PA is the major source of noise in the MFH system; whereas the DEMZM dominates the nonlinear signal impairments. For best linearity, the DEMZM is DC biased to have a phase shift of  $\pi/2$  between its two arms.

A sinusoidal RF signal at 28 GHz is applied to the lower arm of the DEMZM to generate multiple RF sidebands with frequency spacing of 28 GHz, as shown by the optical spectrum at point i in Fig. 2.2(b). After the DEMZM, only the central optical carrier (0th-order) is modulated by the data. All other odd ( $\pm 1$ , orange) and even ( $\pm 2$ , green) sidebands are pure sinusoidal tones without data modulation. A 33/66 GHz interleaver (IL) is used to separate the even and odd orders of sidebands, so at point ii, the central (0th) and second-order ( $\pm 2$ ) sidebands are filtered out, and at point iii, two first-order ( $\pm 1$ ) sidebands are filtered out and reserved for upstream transmission. The optical spectrum at point ii shows a double sideband (DSB) modu-

lation, where both  $+2$  and  $-2$  sidebands are present. Both can beat with the central carrier to generate 56-GHz MMW signal. Due to chromatic dispersion, the phase difference between  $+2$  and  $-2$  sidebands rotates continuously as the signal propagates along the fiber, which causes periodic power fading of the generated 56-GHz signal. In order to eliminate the periodic power fading of the MMW signal, an optical band pass filter (BPF) with 3-dB bandwidth of 1.3 nm is used to suppress the  $-2$  sideband to implement single-sideband (SSB) modulation. At point iv, only 0 and  $+2$  sidebands are selected out and delivered to the RRH.

After 20-km single-mode fiber (SMF), the central and  $+2$  sidebands beat in a u2t (now Finisar) photodetector (PD) with 3-dB bandwidth of 60 GHz, and up-convert the multiband mobile signals to 56 GHz. A 56-GHz local oscillator and a mixer are used to down-convert the MMW signal to baseband, which is captured by a real-time digital storage oscilloscope (DSO) with 10-GSa/s sampling rate. Since XM effects are independent on the frequencies of participating signals, although our experiments are carried out at MMW, the experimental results are generic and can also be applied to other MFH systems operating at different frequencies. Since data-dependent XM is phase insensitive, which allows us to isolate the nonlinear impairments from chromatic dispersion, and use a back-to-back model in theoretical analysis.

In any analog optical communication systems, transmission impairments can be contributed by fiber nonlinearities, chromatic dispersion, and modulator nonlinearities. In the case of analog MFH networks, due to the limited optical launch power, short fiber distance, and narrow bandwidth of mobile services (less than GHz), the effects of fiber nonlinearities and chromatic dispersion can be neglected, and the transmission impairments of MFH network are dominated by the nonlinear electro-optic interface of optical modulators. In the experiments, 20-km single mode fiber is inserted between BBU and RRH, and no fiber penalty is observed, which enables us to use a back-to-back model in the theoretical analysis without loss of generality. As we

will see in the following discussion, the nonlinear impairments of mobile signals are independent on their carrier frequencies. Although our experiments are carried out at 60 GHz MMW frequencies, the theoretical analysis and experimental results are generic and can also be applied to other analog MFH systems operating at different frequencies, such as the intermediate frequency-over-fiber (IFoF) systems in [53–58].

## 2.4 Theoretical Analysis

The multiband mobile signal driving the upper arm of the DEMZM can be expressed by (2.1), which consist of multiple bands of scalar and vector signals, e.g.,  $V_i(t) \sin(\omega_i t)$  represents a scalar signal carried by an intermediate frequency  $f_i$ , and  $I_j(t) \cos(\omega_j t) + Q_j(t) \sin(\omega_j t)$  represents a vector signal carried by intermediate frequency  $f_j$ .

$$V_S(t) = \sum_i V_i(t) \sin(\omega_i t) + \sum_j [I_j(t) \cos(\omega_j t) + Q_j(t) \sin(\omega_j t)] \quad (2.1)$$

The sinusoidal RF signal driving the lower arm of the DEMZM can be written as  $V_{RF}(t) = V_{RF} \sin(\omega_{RF} t)$ . The nonlinear electro-optic interface of the DEMZM is shown in (2.2),

$$\begin{aligned} T &= \frac{1}{2} \left[ \exp(j\phi_{DC}) \cdot \exp\left(j\frac{\pi V_{RF}(t)}{V_\pi}\right) + \exp\left(j\frac{\pi V_S(t)}{V_\pi}\right) \right] \\ &= \frac{1}{2} \left[ \exp(j\phi_{DC}) \cdot \sum_{k=-\infty}^{+\infty} J_k(m_{RF}) \exp(jk\omega_{RF} t) + \exp\left(j\frac{\pi V_S(t)}{V_\pi}\right) \right] \end{aligned} \quad (2.2)$$

where  $m_{RF} = \pi V_{RF}/V_\pi$  is the modulation index of the RF signal.  $\phi_{DC} = \pi V_{DC}/V_\pi$  is the static phase shift between two arms induced by DC bias, and in experiments,  $\pi/2$  phase shift is used for best linearity.  $J_k(\cdot)$  is the first kind Bessel function of order  $k$ . After PD, the multiband mobile signal is up-converted to MMW frequency at  $2\omega_{RF}$ ,

and the photocurrent can be expressed by (2.3).

$$I_{ph} \propto J_2(m_{RF}) \cos(2\omega_{RF}t) \left[ J_0(m_{RF}) + \cos\left(\frac{\pi V_S(t)}{V_\pi} - \phi_{DC}\right) \right] \quad (2.3)$$

After the mixer in RRH, the up-converted MMW signal is down-converted to base-band. Due to the interferometric architecture of DEMZM, the received signal experiences a sinusoidal nonlinear transfer function. In (2.3), the cosine function in the brackets originates from DEMZM. Taking a QAM signal as an example, by substituting (2.1) into (2.3), we obtain the received signal shown in (2.4).

$$\begin{aligned} E_{QAM} \propto & \cos(\omega_1 t) J_1(m_I) [J_0(m_Q) + J_2(m_Q)] \\ & + \sin(\omega_1 t) J_1(m_Q) [J_0(m_I) + J_2(m_I)] \end{aligned} \quad (2.4)$$

where  $m_I = \pi I(t)/V_\pi$  and  $m_Q = \pi Q(t)/V_\pi$  are modulation indices of I and Q components. With DC bias of  $V_\pi/2$ , only odd-order harmonics of  $\omega_1$  are generated. In (2.4), only the fundamental term is kept since high order harmonics are blocked by the receiver filter. For small modulation depths, Bessel functions  $J_k(m)$  reduce rapidly with the increase of  $k$ , so high order Bessel functions with  $k > 3$  can be neglected. In (2.4), the first term represents the received I component, which is cross-modulated by an intra-band XM factor of  $J_0(m_Q) + J_2(m_Q)$  from the Q component; the second term represents received Q component, also cross-modulated by  $J_0(m_I) + J_2(m_I)$  from the I component. Both XM factors are smaller than the unity, leading to a compression distortion to the constellation of QAM signal. Furthermore, these XM factors will only approach the unity with infinitely small modulation index, indicating that intra-band XMs between the I and Q components always exist unless the input amplitude is reduced to zero. Meanwhile, it is worth noting that the compression effect is symbol-dependent. Outer symbols have larger I/Q magnitudes than the inner ones, and also experience smaller XM factors, which lead to more severe compression. With outer symbols experience more compression than inner ones, the QAM

constellation is squeezed from a square to a circle. Higher order QAM formats, such as 16-QAM, 64-QAM, suffer more from intra-band XMs since they have more distinct I/Q levels. For QPSK, however, there is only one magnitude for I and Q components, the XM factors in (2.4) converge to a constant, i.e., all four symbols experience the same amount of compression, and no net constellation distortion will be observed. Therefore, it is expected that QPSK has superior resilience against intra-band XM than high order QAM formats.

We can also extend the proposed analysis to multiple bands. Three combinations of scalar and vector signals are investigated, including OOK+OOK, QAM+OOK, and QAM+QAM, shown in (2.5), (2.6), and (2.7), respectively. For two OOK signals in (2.5),  $J_1(m_1)$  in the first term represents the received Ch. 1 at intermediate frequency  $\omega_1$ , which is modulated by a inter-band XM factor of  $J_0(m_2)$  from Ch. 2. Since  $J_0(m_2)$  is a positive number smaller than 1, it imposes a suppression distortion to the eye diagram of Ch. 1. Moreover,  $J_0(m_2)$  only degenerates to the unity when  $m_2$  reduces to zero, so the inter-band XM from Ch. 2 to Ch. 1 always exists unless Ch. 2 becomes infinitesimal. Due to the symmetry of two channels, the analysis of Ch. 2 is similar.

$$E_{OOK} \propto J_0(m_2) J_1(m_1) \sin(\omega_1 t) + J_0(m_1) J_1(m_2) \sin(\omega_2 t) \quad (2.5)$$

In (2.6), we consider the interferences between one vector (QAM) and one scalar (OOK) signal. The first term represents the received QAM signal, and the second term is the received OOK signal. The QAM signal suffers from both intra-band and inter-band XMs, where  $J_0(m_2)$  is the inter-band XM factor contributed by OOK, and  $J_0(m_{I/Q}) + J_2(m_{I/Q})$  are the intra-band XMs between I and Q components. Since the inter-band XM factor  $J_0(m_2)$  is imposed on all the symbols of the QAM signal, it acts as a time-varying scaling factor to the constellation with its magnitude dependent on the data pattern of OOK. On the other hand, the OOK signal only suffers from inter-band XM. In the second term of (2.6), it is modulated by an inter-band XM

factor of  $J_0(m_I)J_0(m_Q) - 2J_2(m_I)J_2(m_Q)$  from the QAM signal. Note that both I and Q components make symmetric contributions to the eye diagram suppression of OOK.

$$E_{QAM+OOK} \propto J_0(m_2) \cdot \left\{ \begin{array}{l} \cos(\omega_1 t) J_1(m_I) [J_0(m_Q) + J_2(m_Q)] \\ + \sin(\omega_1 t) J_1(m_Q) [J_0(m_I) + J_2(m_I)] \end{array} \right\} \quad (2.6)$$

$$+ [J_0(m_I)J_0(m_Q) - 2J_2(m_I)J_2(m_Q)] J_1(m_2) \sin(\omega_2 t)$$

$$E_{QAM+QAM} \propto [J_0(m_{I2})J_0(m_{Q2}) - 2J_2(m_{I2})J_2(m_{Q2})]$$

$$\times \left\{ \begin{array}{l} \cos(\omega_1 t) J_1(m_{I1}) [J_0(m_{Q1}) + J_2(m_{Q1})] \\ + \sin(\omega_1 t) J_1(m_{Q1}) [J_0(m_{I1}) + J_2(m_{I1})] \end{array} \right\} \quad (2.7)$$

$$+ [J_0(m_{I1})J_0(m_{Q1}) - 2J_2(m_{I1})J_2(m_{Q1})]$$

$$\times \left\{ \begin{array}{l} \cos(\omega_2 t) J_1(m_{I2}) [J_0(m_{Q2}) + J_2(m_{Q2})] \\ + \sin(\omega_2 t) J_1(m_{Q2}) [J_0(m_{I2}) + J_2(m_{I2})] \end{array} \right\}$$

Eq (2.7) shows the case of two vector (QAM) signals. Each of them suffers from both intra-band and inter-band XMs. The intra-band factors are represented by  $J_0(m_{I/Q}) + J_2(m_{I/Q})$ ; while the inter-band factor is  $J_0(m_I)J_0(m_Q) - 2J_2(m_I)J_2(m_Q)$ . Intra-band XM introduces compression distortion to each QAM signal; whereas inter-band XMs between two signals introduce scaling distortions to both signals. We summarize the theoretical results in Table 2.1 with intra-band XMs labeled in red, and inter-band XMs in blue.

- (a) Both intra-band and inter-band XMs are baseband effects. They are always in-band and cannot be eliminated by filtering.
- (b) As a baseband effect, XMs are independent on carrier frequencies, but dependent on data modulations.
- (c) All XM factors are positive real-valued scalars. They only induce compression

or stretching distortions in the radial direction of constellations, but no phase rotation.

- (d) XM factors are always smaller than 1, and they only approach 1 for infinitesimal modulation indices. So XMs always exist unless input signals reduce to zero.
- (e) Scalar signals only suffer from inter-band XMs; vector signals suffer from both intra-band and inter-band XMs.
- (f) Intra-band XM introduces compression distortion to vector signals.
- (g) Inter-band XM introduces eye diagram degradation to scalar signals, and scaling distortion to vector signals.



Table 2.1: Theoretical analysis of intra-band and inter-band XMs

Band #	Scalar/Vector		Input	Ch.	Modulation index	Output	XM	Distortion
Single-band	Vector	QAM	$I(t)\cos(\omega_1 t) + Q(t)\sin(\omega_1 t)$	I	$m_I(t) = \pi I(t)/V_\pi$	$J_1(m_I)[J_0(m_Q) + J_2(m_Q)]$	Intra-band	Constellation compression
				Q	$m_Q(t) = \pi Q(t)/V_\pi$	$J_1(m_Q)[J_0(m_I) + J_2(m_I)]$		
Two-band	Scalar+Scalar	OOK+OOK	$V_1(t)\sin(\omega_1 t) + V_2(t)\sin(\omega_2 t)$	OOK <sub>1</sub>	$m_1(t) = \pi V_1(t)/V_\pi$	$J_0(m_2)J_1(m_1)$	Inter-band	Eye-diagram degradation
				OOK <sub>2</sub>	$m_2(t) = \pi V_2(t)/V_\pi$	$J_0(m_1)J_1(m_2)$		
	Vector+Scalar	QAM+OOK	$I(t)\cos(\omega_1 t) + Q(t)\sin(\omega_1 t) + V_2(t)\sin(\omega_2 t)$	I	$m_I(t) = \pi I(t)/V_\pi$	$J_0(m_2)J_1(m_I)[J_0(m_Q) + J_2(m_Q)]$	Intra-band +Inter-band	Constellation compression & scaling
				Q	$m_Q(t) = \pi Q(t)/V_\pi$	$J_0(m_2)J_1(m_Q)[J_0(m_I) + J_2(m_I)]$		
				OOK	$m_2(t) = \pi V_2(t)/V_\pi$	$[J_0(m_I)J_0(m_Q) - 2J_2(m_I)J_2(m_Q)] \times J_1(m_2)$	Inter-band	Eye-diagram degradation
	Vector+Vector	QAM+QAM	$I_1(t)\cos(\omega_1 t) + Q_1(t)\sin(\omega_1 t) + I_2(t)\cos(\omega_2 t) + Q_2(t)\sin(\omega_2 t)$	I <sub>1</sub>	$m_{I1}(t) = \pi I_1(t)/V_\pi$	$[J_0(m_{I2})J_0(m_{Q2}) - 2J_2(m_{I2})J_2(m_{Q2})] \times J_1(m_{I1})[J_0(m_{Q1}) + J_2(m_{Q1})]$	Intra-band +Inter-band	Constellation compression & scaling
				Q <sub>1</sub>	$m_{Q1}(t) = \pi Q_1(t)/V_\pi$	$[J_0(m_{I2})J_0(m_{Q2}) - 2J_2(m_{I2})J_2(m_{Q2})] \times J_1(m_{Q1})[J_0(m_{I1}) + J_2(m_{I1})]$		
				I <sub>2</sub>	$m_{I2}(t) = \pi I_2(t)/V_\pi$	$[J_0(m_{I1})J_0(m_{Q1}) - 2J_2(m_{I1})J_2(m_{Q1})] \times J_1(m_{I2})[J_0(m_{Q2}) + J_2(m_{Q2})]$		
				Q <sub>2</sub>	$m_{Q2}(t) = \pi Q_2(t)/V_\pi$	$[J_0(m_{I1})J_0(m_{Q1}) - 2J_2(m_{I1})J_2(m_{Q1})] \times J_1(m_{Q2})[J_0(m_{I2}) + J_2(m_{I2})]$		

- Intra-band XMs are labeled in red.
- Inter-band XMs are labeled in blue.

It should be noted that XMs have no phase effect, and there is no interaction between XMs and fiber dispersion, which enables us to perform the theoretical analysis in a back-to-back model without loss of generality. This is a unique feature and very different from carrier IMs, which are frequency dependent, and have phase rotation due to dispersion as the signal propagate along the fiber. The power of carrier IM products fluctuates periodically along the fiber [59, 62, 65]; whereas XM effects have no dependence on transmission distance.

In this work, a DEMZM is used as an example to investigate the nonlinear XMs caused by optical modulators. But the proposed methodology and results are generic, and can be applied to other analog MFH systems based on intensity or phase modulation. Intensity modulation has the same nonlinear sinusoidal transfer function due to its interferometric architecture; phase modulation has linear phase response, but requires homodyne or heterodyne detection, which eventually forms an interferometer transforming the phase modulation to intensity modulation with a sinusoidal transfer function.

In order to focus on XMs, only two signals are considered in this work, so any beat frequency components generated by IMs are out of band. For analog MFH systems with more than two signals, both XMs and carrier IMs exist, and it will be expected that carrier IMs dominate the nonlinear impairments of multi-carrier signals, since the beat frequency components have large probabilities to overlap with existing carriers; whereas XMs take the dominance of single-carrier signals, especially in cases when there are a few signal bands unequally spaced in the frequency domain. The proposed closed-form analysis is generic, and can be applied to both single-carrier and OFDM signals without significant modification. In Chapter 3, we apply the same analysis to OFDM signals.

## 2.5 Simulation Results

This section presents simulation results based on the theoretical analysis. Single-band vector signals, such as 16-QAM and QPSK, as well as two-band combinations of scalar/vector signals, including OOK+OOK, QPSK+OOK, and 16-QAM+16-QAM, are investigated. To characterize the nonlinear distortions induced by XMs, quality factor (Q-factor) and error vector magnitude (EVM) are used to evaluate the degradation of eye diagrams and constellations for scalar and vector signals, respectively. In this section, noise is intentionally excluded from the simulation, so that nonlinear impairments can be revealed explicitly even for very small input signals. The other consideration is that there are several different noise sources in analog MFH networks, e.g., amplified spontaneous emission (ASE) of erbium doped fiber amplifier (EDFA), shot noise of photodetector, thermal noise of RF power amplifiers, etc.. Since different systems may suffer from different source of noise, rather than adopting a specific type of noise but sacrificing the generality of the model, we exclude noise in the simulation for this section; but in the next section, experimental results will be presented and compared with simulation results with noise taken into account. It will be observed that with noise taken into account, good consistency has been achieved between the results from simulation and experiments.

### 2.5.1 16-QAM/QPSK

The simulation results of intra-band XMs are shown in Fig. 2.3, where the EVMs of QPSK and 16-QAM signals are plotted as a function of input signal amplitude. The input amplitude is normalized with respect to the half-wave voltage of the DEMZM, which is  $V_\pi = 4.95$  V. The constellations of 16-QAM and QPSK signals are presented in Fig. 2.3(b) and (c), respectively. Consistent with the prediction in Section III, the EVM of 16-QAM increases monotonically due to intra-band XM between the I and Q

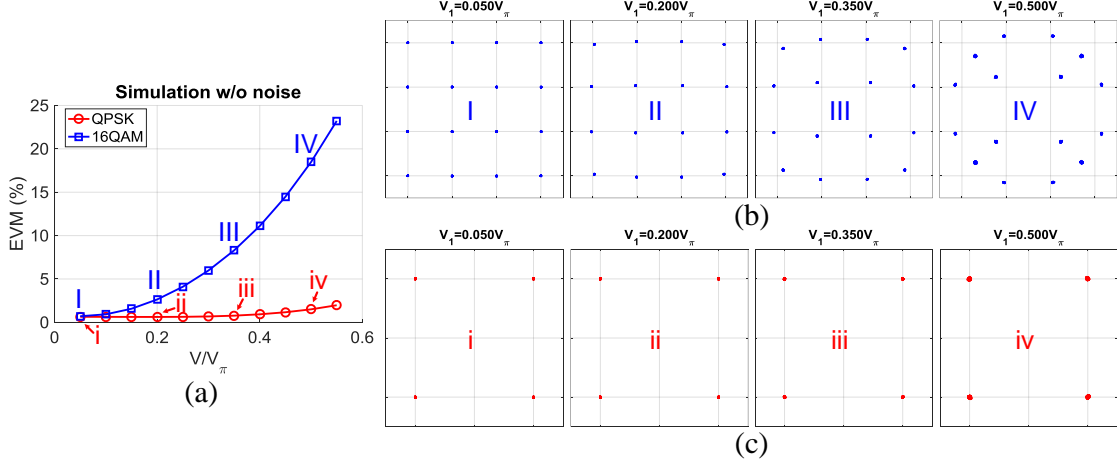


Figure 2.3: Intra-band XM of a vector 16-QAM/QPSK signal (simulation w/o noise). (a) EVM as a function of normalized input amplitude. (b) 16-QAM constellations. (c) QPSK constellations.

components, and compression distortion is observed in 16-QAM constellations in Fig. 2.3(b). This is because the outer symbols of 16-QAM have larger I/Q magnitudes and smaller intra-band XM factors, which experience more severe compression. With the outer symbols pushed inward, the 16-QAM constellation is squeezed from square to circle. On the other hand, the EVM of QPSK signal keeps constant with different input amplitudes, and there is no distortion observed in Fig. 2.3(c). This is because QPSK has only one I/Q magnitude, and the intra-band XM factors converge to a constant, i.e., with all four symbols experience the same amount of compression, there is no observable distortion. In the experiments, it will be shown that QPSK has superior resilience than high order QAM signals.

### 2.5.2 OOK+OOK

Fig. 2.4 shows the inter-band XM between two OOK signals. Due to the symmetry of two channels, we only show the results of Ch. 1. With noise not taken into account, the Q-factor of Ch. 1 ( $Q_1$ ) only depends on the input amplitude of Ch. 2 ( $V_2$ ). This is because the input amplitude of Ch. 1 ( $V_1$ ) determines the signal-to-noise ratio (SNR)

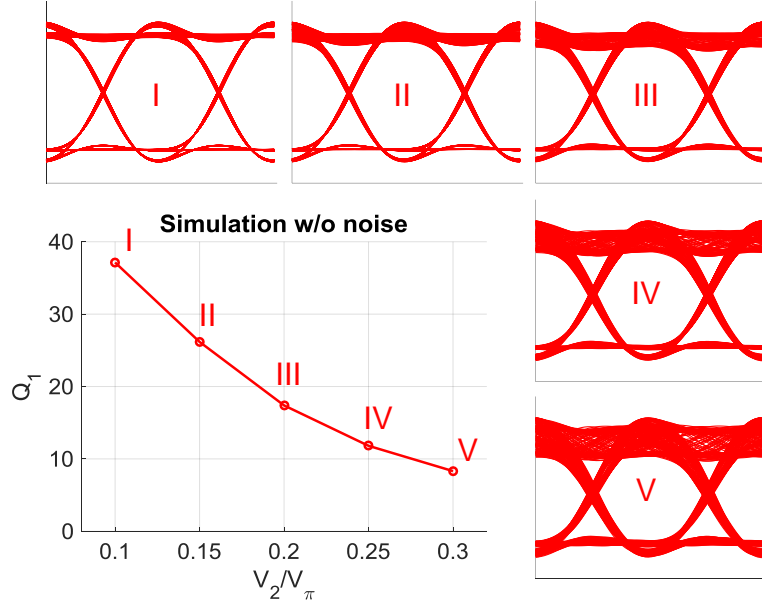


Figure 2.4: Inter-band XM between two OOK signals (simulation w/o noise).  $Q_1$  decreases monotonically with  $V_2$ . Ch. 1 eye diagrams are shown in insets.

of Ch. 1, and with the assumption of infinite SNR,  $Q_1$  becomes independent on  $V_1$ . As  $V_2$  increases,  $Q_1$  decreases monotonically due to inter-band XM. In the insets of Fig. 2.4, it is shown that inter-band XM from Ch. 2 to Ch. 1 suppresses the eye diagram of Ch. 1 and thickens its eye lid (one-level). According to the definition of Q-factor,  $Q = (I_1 - I_0) / (\sigma_1 + \sigma_0)$ , inter-band XM not only suppresses the eye opening by reducing  $I_1$ , but also increases the deviation of one-level ( $\sigma_1$ ). These two effects work together to diminish the Q-factor of Ch. 1 significantly.

### 2.5.3 QPSK+OOK

Fig. 2.5 shows the inter-band XM between a vector (QPSK) and a scalar (OOK) signal. Since QPSK has intrinsic resistance to intra-band XM, only inter-band XM is concerned here. It is observed that the EVM of QPSK increases monotonically due to the scaling distortion induced by the inter-band XM from OOK, and the scaled constellations are presented in Fig. 2.5(b). On the other hand, the inter-band XM

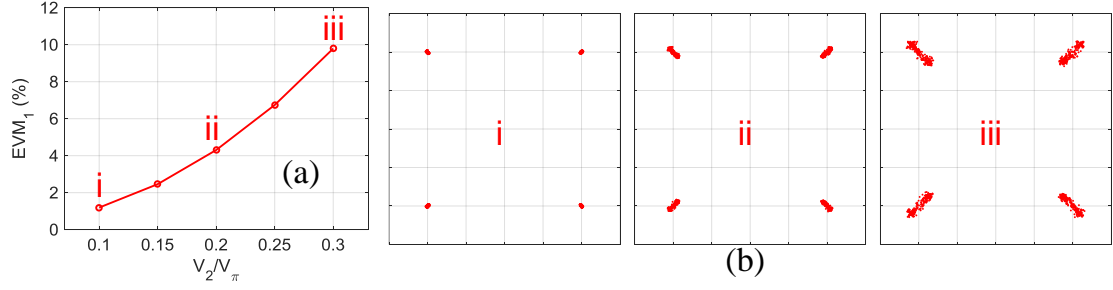


Figure 2.5: Inter-band XM between a QPSK and an OOK signals (simulation w/o noise). (a)  $\text{EVM}_1$  (QPSK) increases monotonically with  $V_2$  (OOK). (b) Scaling distortion of QPSK constellation.

from QPSK to OOK generates similar results as in Fig. 2.4, which are not presented to save some space.

#### 2.5.4 16-QAM+16-QAM

Fig. 2.6 shows the inter-band XM between two vector (16-QAM) signals, where each signal suffers from both intra-band and inter-band XMs, so there are two dimensions of nonlinearities. Due to the symmetry of two signals, only the results of Ch. 1 are presented here. In Fig. 2.6(a), for a given  $V_2$ ,  $\text{EVM}_1$  increases with  $V_1$  due to intra-band XM; whereas for a given  $V_1$ ,  $\text{EVM}_1$  increases with  $V_2$  monotonically due to inter-band XM. The corresponding constellations are shown in Fig. 2.6(b). In the horizontal direction, constellations experience compression distortion caused by intra-band XM; whereas in the vertical direction, they have scaling distortion contributed by inter-band XM.

## 2.6 Experimental Results

In this section, experiments are carried out to validate the theoretical predictions. Simulation results with noise taken into account are presented as a reference to the experimental measurements and good consistency is achieved.

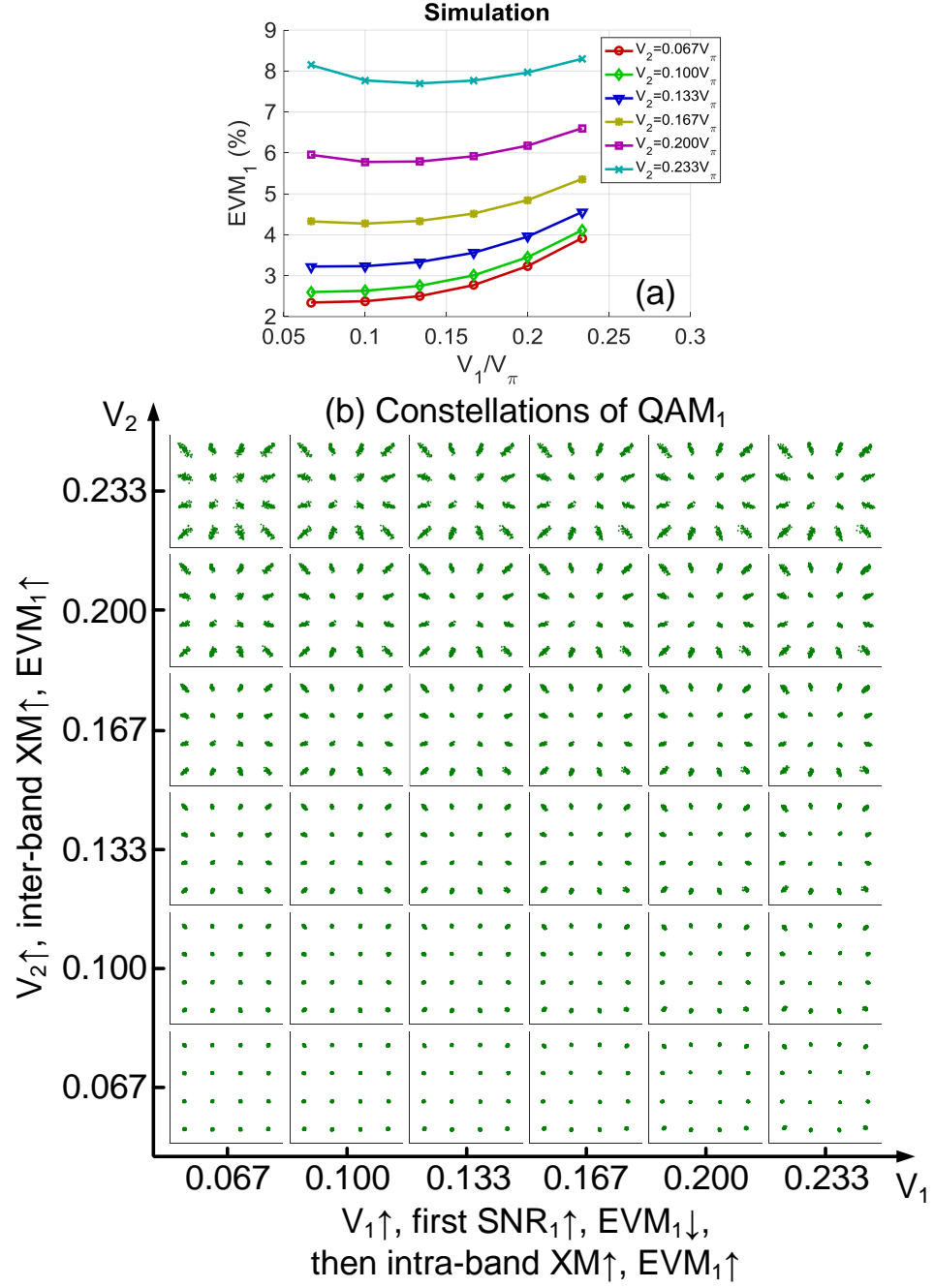


Figure 2.6: Inter-band XM between two 16-QAM signals (simulation w/o noise). (a) EVM<sub>1</sub> as a function of  $V_1$ ,  $V_2$ . (b) Ch. 1 constellations.

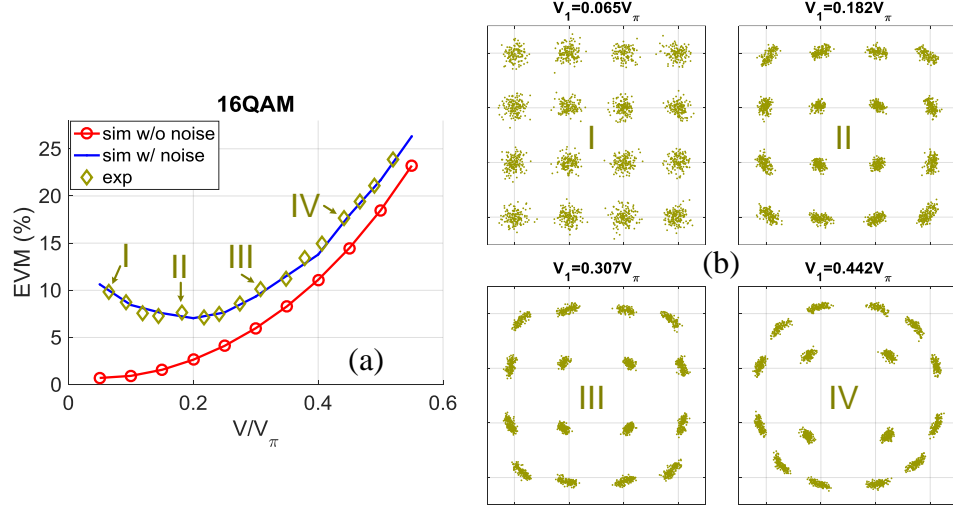


Figure 2.7: Intra-band XM of a 16-QAM signal. (a) EVM as a function of normalized input amplitude. (b) 16-QAM constellations.

### 2.6.1 16-QAM/QPSK

Fig. 2.7 shows the experimental results of intra-band XMs for a 16-QAM signal, and simulation results with and without noise are both plotted as references. The yellow scattered dots are from experimental measurements; the blue and red lines are from simulations with and without noise, respectively. The experimental results are very close to the blue line. With noise taken into account, both blue line and experimental dots are higher than the red line for larger EVMs, and major discrepancies are observed for small input amplitudes. As the input signal increases, EVM of the red line increases monotonically due to intra-band XM; whereas the EVMs of blue line and experimental dots first decrease due to the improvement of signal-to-noise (SNR), and then increase due to the constellation compression induced by intra-band XM. 16-QAM constellations at four input voltages are illustrated in Fig. 2.7. As  $V$  increases, the constellation first becomes clearer due to SNR improvement, and then compression distortions appear due to intra-band XM. For small input  $V < 0.15V_\pi$ , EVM is dominated by noise; for large input  $V > 0.25V_\pi$ , EVM is limited by nonlin-



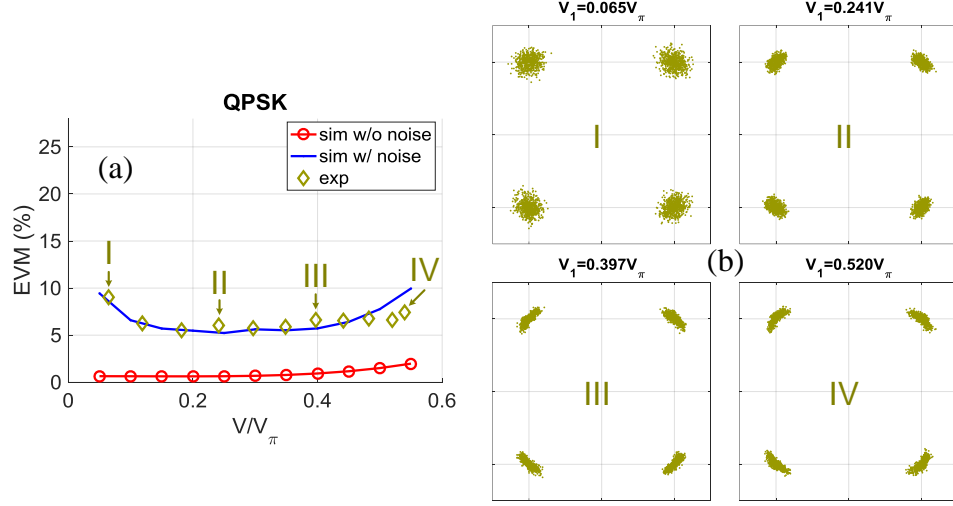
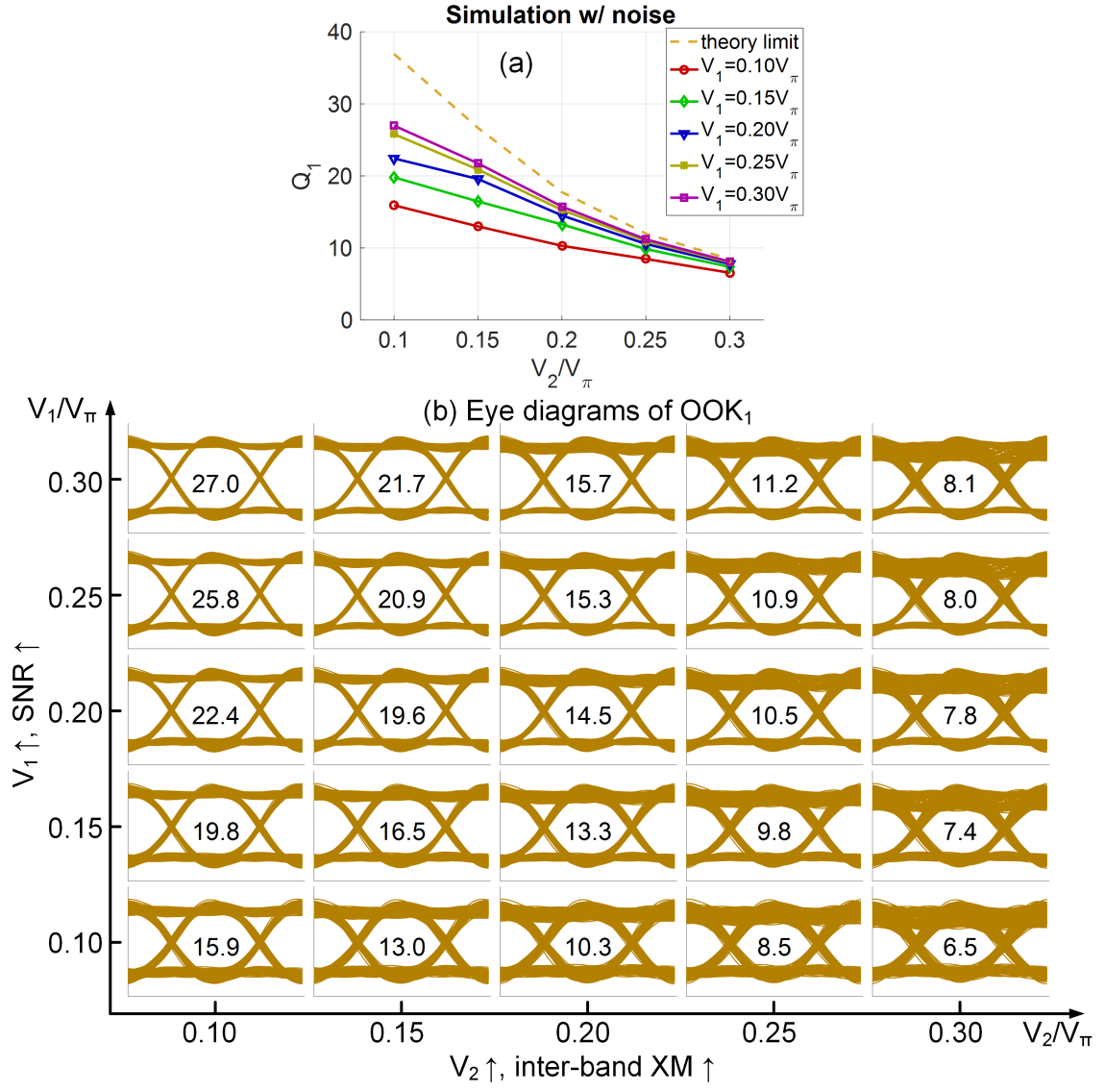


Figure 2.8: Intra-band XM of a QPSK signal. (a) EVM as a function of normalized input amplitude. (b) QPSK constellations.

earity. In order to reduce EVM, a trade-off between noise and nonlinearity has to be made, and the optimum operation range of input voltage is  $0.15V_\pi < V < 0.25V_\pi$ .

Fig. 2.8 shows the experimental results of intra-band XMs of a QPSK signal, and the constellations of four different input voltages are shown in Fig. 2.8(b). Experimental results are illustrated by yellow scattered dots; simulation results with and without noise are labeled by blue and red lines. Both EVMs of the blue line and yellow dots are larger than the EVM of red line due to inclusion of noise. As  $V$  increases, the EVM of QPSK first decreases due to SNR improvement, and then keeps constant due to its intrinsic resilience to intra-band XM. In Fig. 2.8(b), as  $V$  increases, the QPSK constellations first become clearer, and then keep constant without noticeable distortion. In constellations of both 16-QAM and QPSK, radial noise is suppressed by the nonlinear compression distortion; whereas the tangential noise is contributed by frequency offset or phase jittering in the MMW receiver.



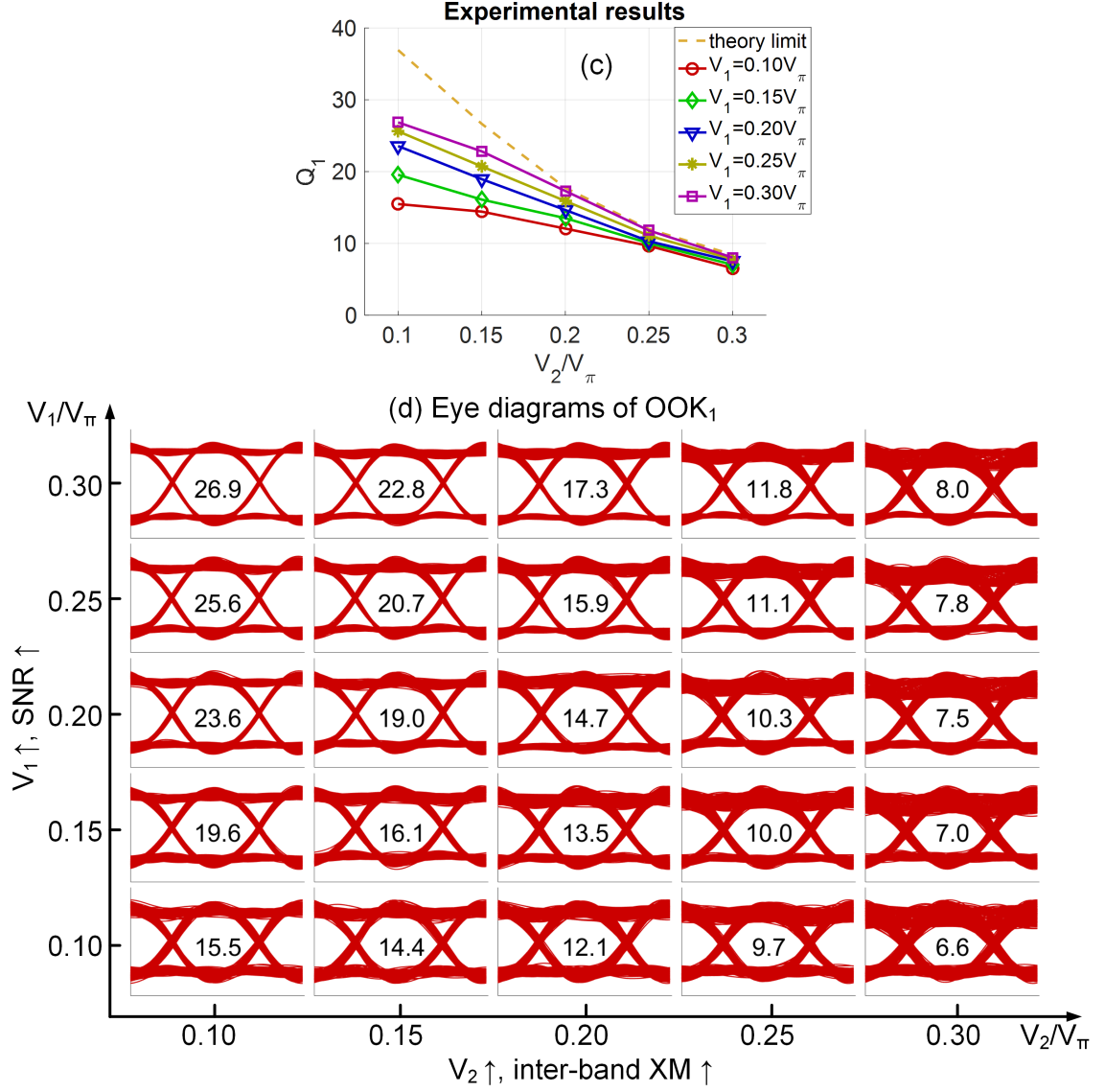


Figure 2.9: Inter-band XM between two OOK signals. (a, b) Simulation w/ noise. (c, d) Experiments. (a) Simulated  $Q_1$  as a function of  $V_1$ ,  $V_2$ . (b) Simulated eye diagrams. (c) Measured  $Q_1$ . (d) Measured eye diagrams.

### 2.6.2 OOK+OOK

Fig. 2.9 shows the inter-band XMs between two scalar (OOK) signals. Due to the symmetry of two channels, only the results of Ch. 1 are illustrated. The simulation results including noise are presented in (a) and (b); whereas experimental results in (c) and (d). The simulation result excluding noise is also shown as a theoretical limit, which is labeled by a yellow dashed line. With noise taken into account, the Q-factor of Ch. 1 from simulation (a) and experiments (c) are both less than the theoretical limit. Note that in Fig. 2.4,  $Q_1$  only depends on  $V_2$  due to the assumption of infinite SNR, but in Fig. 2.9  $Q_1$  becomes a function of both  $V_1$  and  $V_2$ , where  $V_1$  determines the SNR, and  $V_2$  determines inter-band XM.

For a given  $V_1$ , inter-band XM grows as  $V_2$  increases, leading to the degradation of  $Q_1$ , therefore, for a fixed  $V_1$ ,  $Q_1$  reduces with  $V_2$  monotonically. For a given  $V_2$ , increased  $V_1$  leads to improved SNR, so  $Q_1$  increases with  $V_1$  monotonically. If both channels have large input amplitudes (large  $V_1$  and  $V_2$ ), Ch. 1 has sufficient SNR, while at the same time experiences strong inter-band XM from Ch. 2, which makes nonlinear XM becomes the dominant limitation of  $Q_1$ . In Fig. 2.9(a) and (c), both the simulation and experimental results approach the theoretical limit when  $V_1$  and  $V_2$  are large. The corresponding eye diagrams from simulation and experiments are presented in Fig. 2.9(b) and (d) respectively. In the horizontal direction, as  $V_2$  increases, eye diagrams of Ch. 1 are suppressed by inter-band XM; in the vertical direction, as  $V_1$  increases, eye diagram becomes clearer with improved SNR.

### 2.6.3 QPSK+OOK

Fig. 2.10 shows the inter-band XM between a vector (QPSK) and a scalar (OOK) signals, with experimental results plotted by scatted dots, simulation results labeled by green and red dashed lines for including and excluding noise, respectively. EVM of the QPSK signal ( $EVM_1$ ) increases monotonically with the input amplitude of OOK

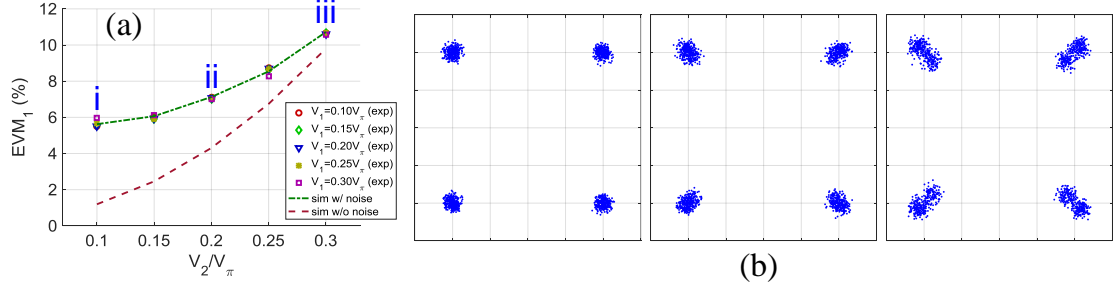
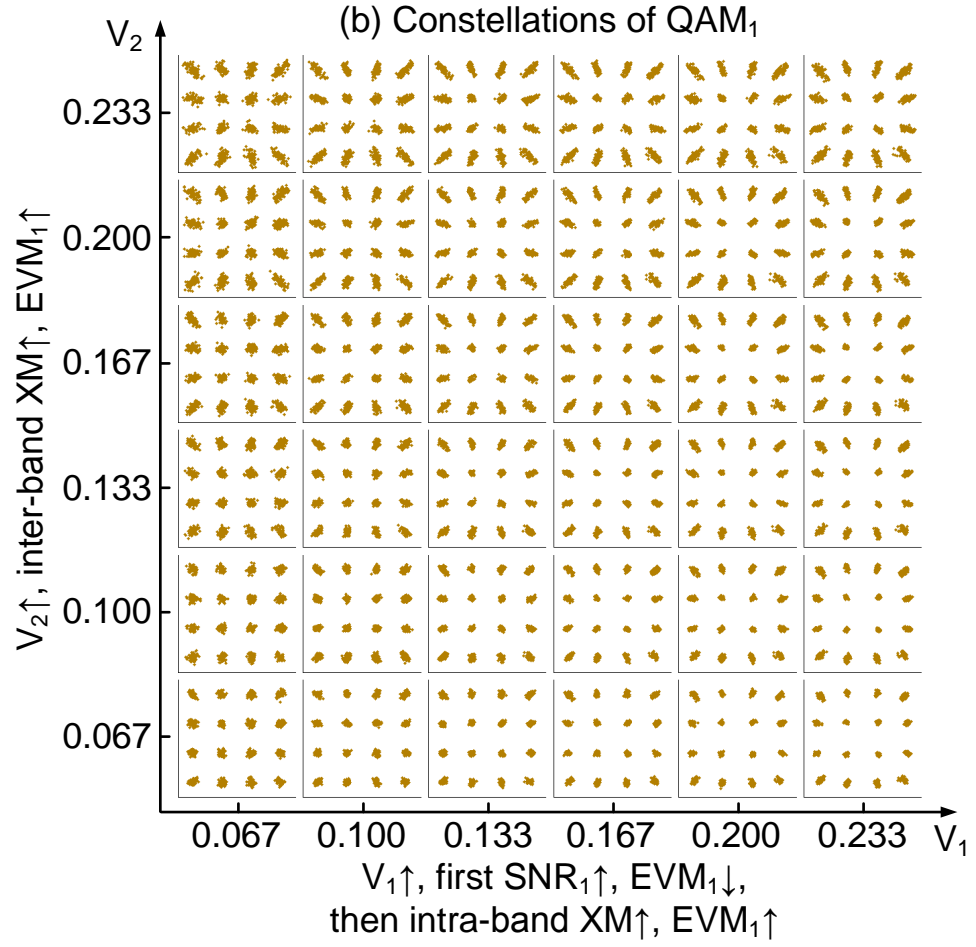
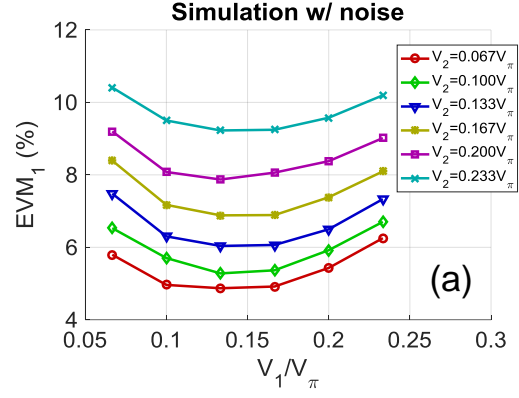


Figure 2.10: Inter-band XM between a QPSK and an OOK signals. (a)  $\text{EVM}_1$  (QPSK) increases monotonically with  $V_2$  (OOK). (b) Measured scaling distortion of QPSK constellation.

signal ( $V_2$ ) due to the inter-band XM from Ch. 2 (OOK) to Ch. 1 (QPSK), and scaling distortion of QPSK constellation are presented in Fig. 2.10(b). In both simulation and experiments,  $\text{EVM}_1$  has no dependence on  $V_1$  since QPSK has intrinsic resilience against intra-band XM. With noise taken into account, the experimental (scattered dots) and simulation (green dashed line) EVMs are higher than the theoretical limit (red line), and good consistency is achieved between simulation and experiments. The inter-band XM from QPSK to OOK generates same eye diagram suppression as shown in Fig. 2.9, which is omitted here.

#### 2.6.4 16-QAM+16-QAM

The inter-band interferences between two vector (16-QAM) signals are shown in Fig. 2.11. Due to the symmetry of two channels, only the results of Ch. 1 are presented. Fig. 2.11(a) and (b) are simulation results with noise taken into account; (c) and (d) are from experiments. In (a) and (c),  $\text{EVM}_1$  is plotted as a function of  $V_1$  and  $V_2$ , and the corresponding 16-QAM constellations from simulation and experiments are shown in (b) and (d), respectively. Since 16-QAM suffers from both intra-band and inter-band XMs, there are two dimensions of nonlinearities. Comparing Fig. 2.11(a), (c) with Fig. 2.6(a), discrepancy is observed for small  $V_1$  because of the noise



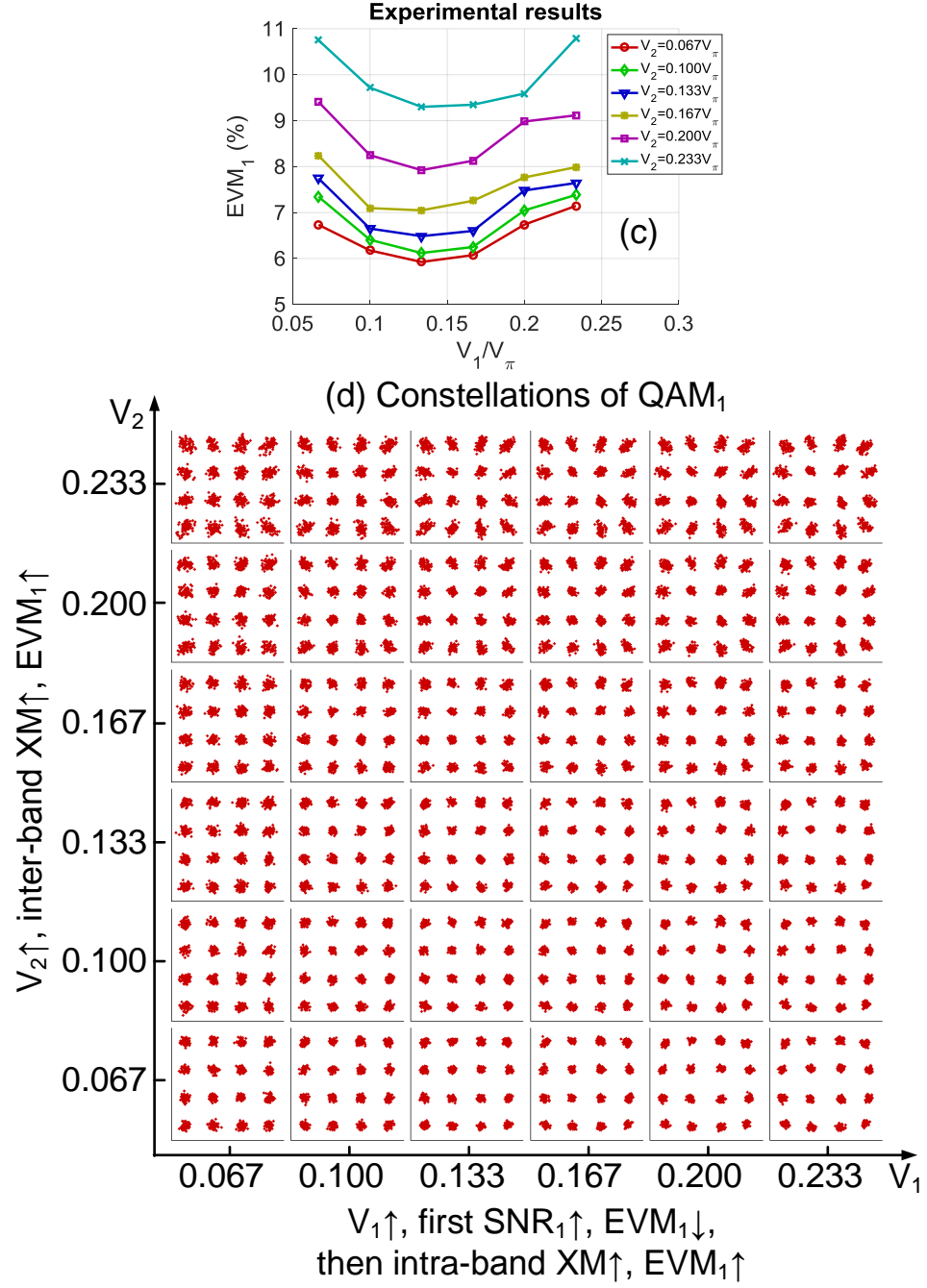


Figure 2.11: Inter-band XM between two 16-QAM signals. (a, b) Simulation w/ noise. (c, d) Experiments. (a) Simulated  $EVM_1$  as a function  $V_1$ ,  $V_2$ . (b) Simulated constellations. (c) Measured  $EVM_1$ . (d) Measured constellations.

effect. In Fig. 2.6(a),  $\text{EVM}_1$  increases monotonically with both  $V_1$  and  $V_2$  due to intra-band and inter-band XMs, respectively. But in Fig. 2.11(a) and (c), for a given  $V_2$ , as  $V_1$  increases,  $\text{EVM}_1$  first decreases due to the SNR improvement of Ch. 1, and then increases due to intra-band XM. This tendency is consistent with our previous observation of a single channel 16-QAM signal shown in Fig. 2.7. For a given  $V_1$ ,  $\text{EVM}_1$  increases monotonically with  $V_2$  due to the inter-band XM. In Fig. 2.11(b) and (d), in the horizontal direction, as  $V_1$  increases, the constellation first becomes clearer due to SNR improvement, and then experience compression distortion caused by intra-band XM; in the vertical direction, as  $V_2$  increases, the constellation experiences scaling distortion contributed by inter-band XM. Although the simulation results (a, b) do not exactly match with experiments, identical tendency of intra-band XM and inter-band XM are observed.

## 2.7 Summary

In this chapter, nonlinear impairments of single-carrier signals in a multi-RAT multi-service analog MFH network are investigated. The dominant impairments of single-carrier signals are XMs, which include both intra-band and inter-band XMs. Intra-band XM comes from the crosstalk between I and Q components of a vector signal; inter-band XM originates from inter-channel interferences among different signals, where the data modulation of one channel is imprinted onto others. A millimeter wave analog MFH testbed is demonstrated, and a closed-form theoretical model is proposed to evaluate the XM behaviors. Both numerical simulations and experimental measurements are carried out, and consistent results are obtained. According to the theoretical analysis in Table 2.1, all XMs are imposed as a positive real valued multiplicative factor, which indicates that all XMs are baseband effects. They only depend on the data modulation, but have no dependency on the carrier frequencies of mobile signals. Therefore, XMs cannot be eliminated by filtering or alleviated



Table 2.2: Summary of nonlinear XMs of single-carrier signals

		Intra-band XM	Inter-band XM
Operation principles		Crosstalk between I/Q components of vector signals	Data modulation imprints from one channel onto others
Nonlinear impairments	Scalar signals	N/A <sup>1</sup>	Eye diagram degradation
	Vector signals <sup>2</sup>	Constellation compression (except PSK <sup>3</sup> )	Constellation scaling
Math explanation		All XMs factors are positive real-valued Only radical distortions, no phase rotation	
Frequency dependency		Baseband effects, independent on carrier frequencies	

1. Scalar signals only suffer from inter-band XMs, since they only have in-phase components.
2. Vector signals suffer from both intra-band and inter-band XMs except PSK signals.
3. PSK signals are immune from intra-band XM due to their constant envelope, but can still be impaired by inter-band XM.

by increasing channel spacing. Furthermore, positive real valued XM factors only introduce radical distortions to signal eye diagrams or constellations, and there is no phase rotation induced. It is experimentally verified that scalar signals only suffer from inter-band XM since they only have in-phase component; vector signals can be impaired by both intra-band and inter-band XMs except PSK signals. Due to their constant envelope, PSK signals are immune from intra-band XM, but can still be impaired by inter-band XM. Intra-band XM induces compression distortion to the constellation of vector signals; inter-band XM induces eye diagram degradation to scalar signals, and scaling distortion to vector signals. The operation principles and impairments induced by XMs are summarized in Table 2.2.

In the next chapter, we will investigate the nonlinear impairments of OFDM signals, since most popular RATs all use OFDM as their multi-carrier waveforms. Although nonlinear XMs are baseband effects, which exist in any nonlinear system with any signal waveform, the dominant impairments of OFDM signals are subcarrier IMs, which refer to the beat among three subcarriers to generate a fourth frequency

component located within the signal band. OFDM signals have both XM and IM impairments, but as will be discussed in Chapter 3, the multiplication of XM factors contributed by large number of subcarriers converge to a constant, making the effect of XMs negligible.

# CHAPTER 3

## NONLINEAR SUBCARRIER INTERMODULATIONS OF OFDM SIGNALS IN ANALOG MOBILE FRONTHAUL

### 3.1 Introduction

Due to its high spectral efficiency, simple equalization in the frequency domain, and robustness against inter-symbol interference, OFDM has been widely adopted by most radio access technologies, e.g., Wi-Fi (802.11), WiGig (802.11ad), and LTE (3GPP). On the other hand, OFDM signals are sensitive to nonlinear impairments due to their continuously varying waveforms and high PAPR [84–86]. Subcarrier intermodulation (IM) is the dominant nonlinear impairment of OFDM signals, which can produce both in-band interferences and out-of-band spectral emission. According to the central limit theorem, in-band interferences can be modeled as an additive Gaussian noise with zero mean [84,89]; whereas out-of-band spectral emission leads to inter-channel interferences, which can be alleviated by filtering or increasing channel spacing. Third-order IMs among three subcarriers ( $f_1 \pm f_2 \pm f_3$ ) are of particular interest, since they have large probabilities to overlap with existing subcarriers. Even-order IMs ( $f_1 \pm f_2$ ) are usually out-of-band and can be filtered out easily.

Carrier aggregation of LTE/E-UTRA signals in Analog MFH networks has been studied extensively [53–58], but the nonlinear interferences among aggregated LTE component carriers (CCs) have not been reported. Although the nonlinear impairments of OFDM signals have been studied extensively in various optical and wireless communication scenarios, such as CO-OFDM [90–92], RoF [93–96], power amplifier (PA) [97–99], visible light communications (VLC) [100–103], and RF front end [104], most works only focus on the distortions of each individual OFDM signal, i.e., intra-

band subcarrier IMs, and there has been meager effort spent on the inter-band interferences among multiple OFDM signals. These existing research are summarized in Table 1.2. In a multi-RAT multi-service analog MFH network, nonlinear interferences among different OFDM services become the most important factor that limits the fronthaul performance, because there are several coexistent RATs, such as Wi-Fi, WiGig, LTE, and each RAT supports multiband/multichannel operations.

In this chapter, we propose and investigate the inter-band subcarrier IMs among different OFDM services in a multi-RAT multi-service analog MFH network. A MMW RoF-based MFH testbed is used to evaluate the nonlinear interferences among multiple OFDM signals, and it will be revealed that inter-band IMs among different signals play a more important role in fronthaul performance degradation than the well-known intra-band IMs of each individual signal. Both theoretical analysis and experimental validation will be carried out, and the close-form analysis proposed in Chapter 2 will be extended to multiband OFDM signals to identify the contributions of both intra-band and inter-band IMs. This chapter is organized as follows. Section II explains the operation principles of subcarrier IMs. Section III presents the experimental setup followed by theoretical analysis. Section IV presents experimental design, and Section V discusses the experimental results. Section VI concludes the chapter.

### 3.2 Operation Principles

The operation principles of subcarrier IMs are illustrated in Fig. 3.1. IM among three subcarriers from the same OFDM signal bands are defined as intra-band IMs, and IMs among subcarriers from different OFDM signals are defined as inter-band IMs. Intra-band IM  $f_p \pm (f_q - f_r)$  among three subcarriers, i.e.,  $f_p$ ,  $f_q$ , and  $f_r$ , of an OFDM signal can induce both in-band interference, as shown in Fig. 3.1(a), and out-of-band emission, shown in Fig. 3.1(b). Inter-band IMs among subcarriers from two different

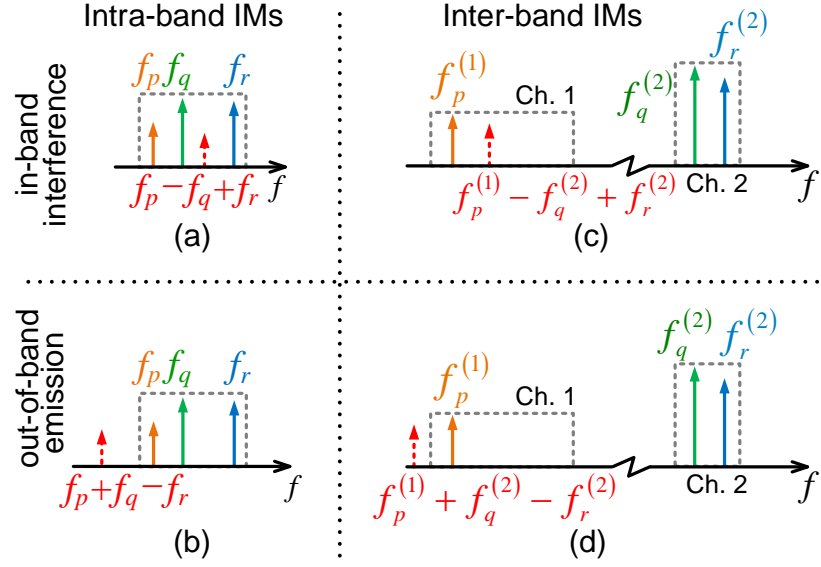


Figure 3.1: Operation principles of subcarrier IMs. (a) In-band interferences and (b) out-of-band emission induced by intra-band IMs. (c) In-band interferences and (d) out-of-band emission induced by inter-band IMs among one subcarrier of Ch. 1 and two subcarriers of Ch. 2.

OFDM signals are shown in Fig. 3.1(c) and (d). Taking third-order IMs from Ch. 2 to Ch. 1 as an example, the intermodulations among two subcarriers of Ch. 2,  $f_q^{(2)}$  and  $f_r^{(2)}$ , and one subcarrier of Ch. 1,  $f_p^{(1)}$  generate two IM products at  $f_p^{(1)} \pm (f_q^{(2)} - f_r^{(2)})$ , which locate within or near Ch. 1. It is worth to note that these IM products only depend on the frequency difference between  $f_q^{(2)}$  and  $f_r^{(2)}$ , i.e.,  $|f_q^{(2)} - f_r^{(2)}|$ , but are independent on the central frequency of Ch. 2, and cannot be alleviated by increasing the channel spacing between two signals. Similarly, IMs from Ch. 1 to Ch. 2,  $f_p^{(2)} \pm (f_q^{(1)} - f_r^{(1)})$ , only depend on the frequency difference  $|f_q^{(1)} - f_r^{(1)}|$ , but are independent on the central frequency of Ch. 1. In analog MFH networks, almost all RATs support multiband/multichannel operations, e.g. LTE supports carrier aggregation for up to 32 component carriers [20, 21]; 802.11ac supports channel bonding of two to four channels to enhance capacity. No matter the aggregated carriers or bonded channels are contiguous or non-contiguous in the frequency domain, and how

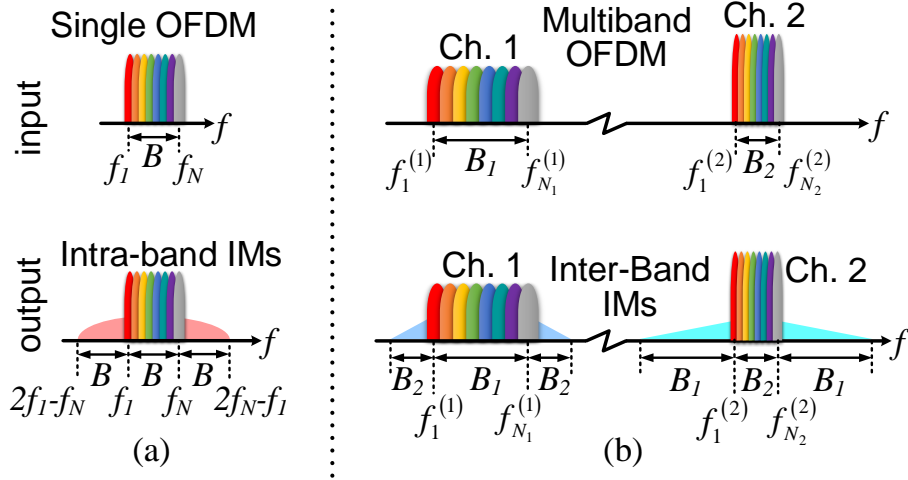


Figure 3.2: Nonlinear impairments of single-band and multiband OFDM signals. (a) Interference induced by intra-band IMs. (b) Interference induced by inter-band IMs.

much guard band are inserted in between, inter-band interferences will always exist due to their independence on central frequencies of participating signals.

Fig. 3.2 shows the nonlinear impairments of single and multiple bands of OFDM signals, induced by intra-band and inter-band IMs, respectively. The case of a single OFDM signal is shown in Fig. 3.2(a), and the case of multiband signals in (b). The input and output spectra of OFDM signals after a nonlinear MFH system are shown in the upper and lower rows, respectively. In Fig. 3.2(a), an OFDM signal has  $N$  subcarriers with the first subcarrier at  $f_1$ , and the last one at  $f_N$ . The signal bandwidth is  $B = |f_N - f_1|$ . The intra-band IM products cover a spectral range of  $3B$ , from  $2f_1 - f_N$  to  $2f_N - f_1$ . If we apply the same analysis to two OFDM signals with subcarrier numbers of  $N_1$  and  $N_2$  respectively, shown in Fig. 3.2(b). The inter-band IMs from Ch. 2 to Ch. 1, i.e.,  $f_p^{(1)} \pm (f_q^{(2)} - f_r^{(2)})$ , cover a spectral range of  $B_1 + 2B_2$  around Ch. 1, from the lowest IM product at  $f_1^{(1)} - f_{N_2}^{(2)} + f_1^{(2)} = f_1^{(1)} - B_2$  to the highest one at  $f_{N_1}^{(1)} - f_1^{(2)} + f_{N_2}^{(2)} = f_{N_1}^{(1)} + B_2$ . Similarly, inter-band IMs from Ch. 1 to Ch. 2 cover a spectral range of  $B_2 + 2B_1$  around Ch. 2, from  $f_1^{(2)} - B_1$  to  $f_{N_2}^{(2)} + B_1$ . It is worth to note that these inter-band interferences have no dependence

on the central frequencies of two signals, and they always exist no matter Ch. 1 and Ch. 2 are contiguous or non-contiguous to each other, or how much guard band is inserted in between. In Fig. 3.2, we intentionally use two OFDM signals with different bandwidths ( $B_1 > B_2$ ), so that Ch. 1 experiences more in-band interferences than Ch. 2. This is because for inter-band IMs from Ch. 2 to Ch. 1, a large portion,  $B_1/(B_1 + 2B_2)$ , of them locates within the band of Ch. 1; but for inter-band IMs from Ch. 1 to Ch. 2, only a small portion,  $B_2/(B_2 + 2B_1)$ , locates within Ch. 2, most of them are out-of-band and filtered out. Now consider a general case, for a narrowband Ch.  $k$  with  $N_k$  subcarriers, the inter-band IMs from Ch.  $k$  to any other signal Ch.  $i$  would have the form of  $f_p^{(i)} \pm (f_q^{(k)} - f_r^{(k)})$ , where the frequency offset  $|f_q^{(k)} - f_r^{(k)}|$  is small due to the narrow bandwidth of Ch.  $k$ , making these IM products have large chance to locate within the band of Ch.  $i$ . Therefore, in multi-RAT multiband MFH systems, a strong narrowband service is detrimental since it introduces severe inter-band IMs to other coexistent services.

### 3.3 Experimental Setup and Theoretical Analysis

The experimental setup of a multi-RAT multi-service analog MFH system is shown in Fig. 3.3(a), and the optical spectra at points i-iv are presented in Fig. 3.3(b). A detailed explanation of the experimental setup can be found in Chapter 2. It should be note that since the nonlinear subcarrier IMs are independent on central frequencies of participating signals, although the experiments are carried out at MMW frequency, the theoretical analysis and experimental results are generic and can also be applied to other analog MFH systems operating at different frequencies, such as the intermediate frequency-over-fiber (IFoF) systems in [53–58].

In any analog optical communication systems, transmission impairments can be contributed by fiber nonlinearities, chromatic dispersion, and modulator nonlinearities. In the case of analog MFH networks, due to the limited optical launch power,

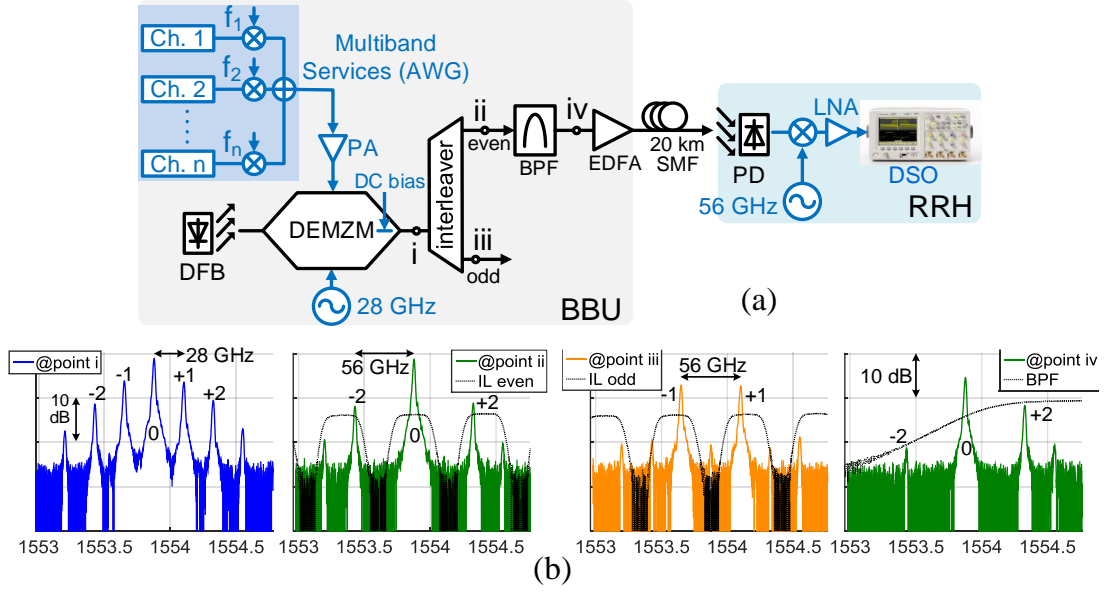


Figure 3.3: (a) Experimental setup. (b) Optical spectra at point i-iv.

short fiber distance, and narrow bandwidth of mobile services (less than GHz), transmission impairments of MFH network are dominated by the nonlinear electro-optic interface of optical modulators. In the experiments, 20-km single mode fiber is inserted between BBU and RRH, and no fiber penalty is observed, which enables us to use a back-to-back model in the theoretical analysis without loss of generality. The transfer function of the DEMZM is shown in (3.1), where  $V_{RF}(t)$  represents a sinusoidal RF signal, and  $V_S(t)$  is a multiband OFDM signal.  $\phi_{DC} = \pi V_{DC}/V_\pi$  is the static phase shift between two arms induced by DC bias, and  $\pi/2$  phase shift is used in experiments for best linearity.

$$T = \frac{1}{2} \left[ \exp(j\phi_{DC}) \cdot \exp\left(j\frac{\pi V_{RF}(t)}{V_\pi}\right) + \exp\left(j\frac{\pi V_S(t)}{V_\pi}\right) \right] \quad (3.1)$$

After the photodetector (PD), the photocurrent  $I_{ph}$  can be expressed by (3.2), where the OFDM signals were up-converted to a MMW frequency at  $2\omega_{RF}$ . After down-converted to baseband by the mixer, the OFDM signals are retrieved, but with a non-



linear sinusoidal transfer function imposed by the interferometric nature of DEMZM.

$$I_{ph} \propto J_2(m_{RF}) \cos(2\omega_{RF}t) \left[ J_0(m_{RF}) + \cos\left(\frac{\pi V_S(t)}{V_\pi} - \phi_{DC}\right) \right] \quad (3.2)$$

The input signal for a single OFDM signal is shown in (3.3), and the input for multiband OFDM signals is shown in (3.4). For the two OFDM signals in (3.4), they are differentiated by superscripts, e.g.,  $\omega_k^{(i)}$  represents the frequency of k-th subcarrier of Ch. i, which is modulated by a complex symbol of  $I_k^{(i)} + jQ_k^{(i)}$ .

$$V_S^{(one)}(t) = \sum_{k=0}^{N-1} [I_k \cos(\omega_k t) + Q_k \sin(\omega_k t)] \quad (3.3)$$

$$\begin{aligned} V_S^{(two)}(t) = & \sum_{k=0}^{N_1-1} \left[ I_k^{(1)} \cos(\omega_k^{(1)} t) + Q_k^{(1)} \sin(\omega_k^{(1)} t) \right] \\ & + \sum_{k=0}^{N_2-1} \left[ I_k^{(2)} \cos(\omega_k^{(2)} t) + Q_k^{(2)} \sin(\omega_k^{(2)} t) \right] \end{aligned} \quad (3.4)$$

Substitute (3.3) or (3.4) into (3.2), and expand using first kind Bessel functions, the received OFDM signals can be obtained in (3.5) and (3.6), for single-band and multiband input, respectively.  $Y_k^{(i)}$  is the received symbol carried by the k-th subcarrier of Ch. i, and  $A_k^{(i)}$  is a scaling factor contributed by nonlinear XM effect, as shown in (3.7).  $m_{I,k}^{(i)}$  and  $m_{Q,k}^{(i)}$  are optical modulation indices of the k-th subcarrier of Ch. i, for in-phase and quadrature components respectively.  $J_m(\cdot)$  is the m-th order Bessel function of the first kind.

In (3.5), there are two different nonlinear impairments, i.e., intra-band XMs and intra-band IMs.  $Y_k$  represents the received symbol on the k-th subcarrier, and it is scaled by a green term,  $\prod_{l \neq k} A_l$ , which is a product of  $N - 1$  XM scaling factors, contributed by all  $N - 1$  subcarriers other than the k-th subcarrier. On the other hand, there is a red term,  $Y_p Y_q \overline{Y_r}$ , which stands for an intra-band IM among three subcarriers, and their beat frequency locates at  $f_p + f_q - f_r$ , which overlaps with the

k-th subcarrier.

For two OFDM signals, in (3.6), there are four different nonlinear impairments, besides the aforementioned intra-band XMs and intra-band IMs, there are inter-band interferences. Taking the first term of (3.6) as an example, besides intra-band XM (green), there is another scaling factor (orange) imposed on the received symbol,  $\prod_{k=0}^{N_2-1} A_k^{(2)}$ , which is a product of  $N_2$  XM scaling factors contributed by all the subcarriers of Ch. 2. Moreover, besides the intra-band IMs (red), there is inter-band IMs (blue). The third term in (3.6) stands for inter-band IMs from Ch. 2 to Ch. 1, which takes two subcarriers from Ch. 2,  $f_p^{(2)}$ ,  $f_q^{(2)}$ , and one subcarrier from Ch. 1,  $f_k^{(1)}$ , and their beat frequency locates near the k-th subcarrier of Ch. 1. Similarly, the fourth term represents inter-band IMs from Ch. 1 to Ch. 2, which takes two subcarriers from Ch. 1,  $f_p^{(1)}$ ,  $f_q^{(1)}$ , and one subcarrier from Ch. 2,  $f_k^{(2)}$ , and the beat frequency locates near the k-th subcarrier of Ch. 2.

$$Rec^{(one)} \propto \sum_{k=0}^{N-1} \left[ \left( \prod_{l \neq k} A_l \right) Y_k - \sum_{\substack{p \neq q \neq r \\ p+q-r=k}} \left( \prod_{l \neq p,q,r} A_l \right) Y_p Y_q \overline{Y_r} \right] \exp(-j\omega_k t) \quad (3.5)$$

$$\begin{aligned} Rec^{(two)} \propto & \left( \prod_{k=0}^{N_2-1} A_k^{(2)} \right) \sum_{k=0}^{N_1-1} \left[ \left( \prod_{l \neq k} A_l^{(1)} \right) Y_k^{(1)} - \sum_{\substack{p \neq q \neq r \\ p+q-r=k}} \left( \prod_{l \neq p,q,r} A_l^{(1)} \right) Y_p^{(1)} Y_q^{(1)} \overline{Y_r^{(1)}} \right] e^{-j\omega_k^{(1)} t} \\ & + \left( \prod_{k=0}^{N_1-1} A_k^{(1)} \right) \sum_{k=0}^{N_2-1} \left[ \left( \prod_{l \neq k} A_l^{(2)} \right) Y_k^{(2)} - \sum_{\substack{p \neq q \neq r \\ p+q-r=k}} \left( \prod_{l \neq p,q,r} A_l^{(2)} \right) Y_p^{(2)} Y_q^{(2)} \overline{Y_r^{(2)}} \right] e^{-j\omega_k^{(2)} t} \\ & - \left[ \sum_{k=0}^{N_1-1} \left( \prod_{l \neq k} A_l^{(1)} \right) Y_k^{(1)} \right] \left[ \sum_{0 \leq p \neq q \leq N_2-1} \left( \prod_{l \neq p,q} A_l^{(2)} \right) Y_p^{(2)} \overline{Y_q^{(2)}} \right] e^{-j(\omega_k^{(1)} + \omega_p^{(2)} - \omega_q^{(2)}) t} \\ & - \left[ \sum_{k=0}^{N_2-1} \left( \prod_{l \neq k} A_l^{(2)} \right) Y_k^{(2)} \right] \left[ \sum_{0 \leq p \neq q \leq N_1-1} \left( \prod_{l \neq p,q} A_l^{(1)} \right) Y_p^{(1)} \overline{Y_q^{(1)}} \right] e^{-j(\omega_k^{(2)} + \omega_p^{(1)} - \omega_q^{(1)}) t} \end{aligned} \quad (3.6)$$

Intra-band XMs, Inter-band XMs, intra-band IMs, inter-band IMs.

$$\begin{aligned}
A_k^{(i)} &\approx J_0 \left( m_{I,k}^{(i)} \right) J_0 \left( m_{Q,k}^{(i)} \right) - 2J_2 \left( m_{I,k}^{(i)} \right) J_2 \left( m_{Q,k}^{(i)} \right) \\
Y_k^{(i)} &\approx J_1 \left( m_{I,k}^{(i)} \right) \left[ J_0 \left( m_{Q,k}^{(i)} \right) + J_2 \left( m_{Q,k}^{(i)} \right) \right] \\
&\quad + j \cdot J_1 \left( m_{Q,k}^{(i)} \right) \left[ J_0 \left( m_{I,k}^{(i)} \right) + J_2 \left( m_{I,k}^{(i)} \right) \right] \\
m_{I,k}^{(i)} &= \frac{\pi I_k^{(i)}}{V_\pi}, \quad m_{Q,k}^{(i)} = \frac{\pi Q_k^{(i)}}{V_\pi}, \quad i = 1 \text{ or } 2
\end{aligned} \tag{3.7}$$

In (3.5) and (3.6), it is worth noting that nonlinear XMs are multiplicative, which induce distortions to signal constellations or eye diagrams; whereas subcarrier IMs are additive, which can be modeled as additive Gaussian noise. As discussed in Chapter 2, nonlinear XMs refer to the modulation crosstalk among different signal carriers, which is a baseband effect and independent on signal frequencies. Nonlinear XMs are the dominant impairments of single-carrier signals, but for OFDM signals, the contribution of XMs are negligible. This is because in (3.5) and (3.6), the scaling factors  $A_k^{(i)}$  always appear in a multiplication form of  $\prod A_k^{(i)}$ , which in turn converges to a constant due to the large number of subcarriers of OFDM signals. Therefore, nonlinear impairments of a single OFDM signal mainly come from intra-band subcarrier IMs, and the dominant impairments of multiband OFDM signals are contributed by inter-band IMs among different OFDM signals. In the following experiments, we will prove that in a multi-RAT multi-service analog MFH network, inter-band IMs across different OFDM signals play a much more important role in performance degradation than the well-known intra-band IMs of each individual OFDM signal.

### 3.4 Experimental Design

Most popular radio access technologies use OFDM as the air interface waveform, and their physical layer parameters are listed in Table 3.1. For example, Wi-Fi protocol 802.11 ac operates at 5.8 GHz with subcarrier spacing of 312.5 kHz, and its channel

bandwidth can be selected from 20, 40, 80, and 160 MHz by using different number of subcarriers (64, 128, 256, 512). Many other Wi-Fi protocols are developed as variants of 802.11 ac, e.g., 802.11af, also known as White-Fi or super Wi-Fi, opportunistically exploits unused TV spectrum (54-698 MHz white space) based on cognitive radio technologies. It utilizes narrow subcarrier spacing of 41.67 kHz and small channel bandwidth of 6 MHz. 802.11ah works at sub-1 GHz license-exempt band, exploiting the improved wall-penetration property and long propagation distance of RF signals in this frequency range for large coverage low data rate applications, such as Internet of things (IoT), machine to machine (M2M) interconnect, and rural area communications. Compared with 802.11ac, 802.11ah is 10 times down-clocked. Its subcarrier spacing is reduced from 312.5 kHz to 31.25 kHz, and bandwidth shrinks to 1, 2, 4, 8, 16 MHz. WiGig (802.11ad) has  $\sim 7$  GHz license-free bandwidth at 60 GHz, containing four channels, each with 2.16 GHz bandwidth. 802.11aj is essentially a China's version of WiGig, which operates at 42.3-47 and 47.2-48.4 GHz, supporting 10 channels each with 0.54 GHz bandwidth, or 5 channels each with 1.08 GHz bandwidth.

OFDM parameters of these RATs are listed in Table 3.1. Note that each RAT has a unique subcarrier spacing, i.e., 802.11ac 312.5 kHz, af 41.67 kHz, ah 31.25 kHz, ad (WiGig) 5.156 MHz, aj 2.578 MHz, LTE 15 kHz, and UWB 4.125 MHz; and each RAT support several bandwidth options by choosing different numbers of subcarriers (FFT size) to accommodate different data rate requirements, e.g., 802.11ac supports channel bandwidths from 20 MHz (64 subcarriers) to 160 MHz (512 subcarriers); LTE supports bandwidths from 1.92 MHz (128 subcarriers) to 30.72 MHz (2048 subcarriers). Each RAT also supports several modulation formats to deal with varied channel conditions or signal-to-noise ratios. It is worth to note that 802.11ad, 802.11aj, and UWB utilize large subcarrier spacing due to their broad bandwidth and high data rate; whereas 802.11af, ah, and LTE need fine frequency granularity provided by small

Table 3.1: OFDM parameters in popular wireless communication standards

	Protocol	Subcarrier Spacing (kHz)	Frequency band (GHz)	FFT size	# of data subc. + pilots	BW (MHz)	Data BW (MHz)	Modulation Format
Wi-Fi <sup>1</sup> (802.11)	802.11 a/g	312.5	5.15-5.875 (a) 2.4-2.497 (g)	64	48+4	20	16.25	a/g/n/af/aj: BPSK /QPSK /16QAM /64QAM
	802.11 n		5.15-5.875 2.4-2.497	64	52+4	20	17.5	
				128	108+6	40	35.625	
	802.11 ac/ax		5.15-5.875	64	52+4	20	17.5	
				128	108+6	40	35.625	
				256	234+8	80	75.625	
		512		468+16	160	151.25		
	802.11 af	US 41.67	54-698MHz	144	108+6	6	4.75	ac/ax/ah: BPSK /QPSK /16QAM /64QAM
		Europe 55.56	470-790MHz	144	108+6	8	6.33	
	802.11 ah	31.25	Sub 1-GHz ~900 MHz <sup>2</sup>	32	24+2	1	0.8125	/16QAM /64QAM /256QAM
				64	52+4	2	1.75	
				128	108+6	4	3.5625	
				256	234+8	8	7.5625	
	802.11 ad (WiGig)	5156.25	57-64 <sup>3</sup>	512	336+16	2640	1815	ad: QPSK /16QAM /64QAM
802.11 aj	2578.125	42.3-47 47.2-48.4	256	168+8	660	453.75		
WiMAX	802.16 e	10.94	2.1-5.9	128	114	1.4	1.25	QPSK /16QAM /64QAM
				512	456	5.6	5	
				1024	912	11.2	10	
				2048	1824	22.4	20	
LTE <sup>4</sup>	3GPP release 8	15	0.7-2.6	128	75	1.140	1.92	QPSK /16QAM /64QAM
				256	150	2.265	3.84	
				512	300	4.515	7.68	
				1024	600	9.015	15.36	
				1536	900	13.515	23.04	
UWB <sup>5</sup>	802.15.3 a	4125	3.168-10.56	128	100+12	528	462	QPSK

1. IEEE 802.11 wireless LANs standard <http://standards.ieee.org/about/get/802/802.11.html>
2. Frequency bands of 802.11 ah: South Korea 917.5-923.5 MHz, Europe 863-868 MHz, Japan 916.5-927.5 MHz, China 755-787 MHz, Singapore 866-869 MHz and 920-925 MHz, US 902-928 MHz.
3. Frequency bands of 802.11 ad (WiGig): US/Canada 57.05-64 GHz, European Union 57-66 GHz, South Korea 57-64 GHz, Japan 57-66 GHz, Australia 59.4-62.9 GHz, China 59-64 GHz.
4. 3GPP LTE standard <http://www.3gpp.org/technologies/keywords-acronyms/98-lte>
5. IEEE 802.15 standard <http://www.ieee802.org/15/>

subcarrier spacing to combat with multipath-induced frequency selective fading. In some extreme cases, subcarrier spacing of a broadband service could be even larger than the whole bandwidth of a narrowband service, e.g., the subcarrier spacing of 802.11ad (5.156 MHz), 802.11aj (2.578 MHz), and UWB (4.125 MHz) are even larger than the whole bandwidth of a 802.11ah or LTE service, which can be as low as 1 or 1.92 MHz.

Table 3.2 lists eight cases we experimentally investigated to evaluate the nonlinear subcarrier IMs in a multi-RAT heterogeneous MFH network. Limited by our AWG and DSO, OFDM parameters in Table 3.2 do not strictly follow the standards specified in Table 3.1, but principle-proof results can still be obtained. In Case I, we first evaluate the intra-band subcarrier IMs, so only one OFDM signal was used with 50 MHz bandwidth, 2048 subcarriers, and 24.4 kHz subcarrier spacing. Case II to VII tested various scenarios of the coexistence of two OFDM services. The two services in Case II have the same subcarrier spacing (24.4 kHz), FFT size (2048), bandwidth (50 MHz), and modulation format (16-QAM), corresponding to two wireless services from the same RAT. Many RATs support multiband or multichannel operations, e.g., LTE carrier aggregation, 802.11ac channel bonding. In Case III, the two services have the same subcarrier spacing (24.4 kHz) and bandwidth (50 MHz), but with different modulation formats (QPSK, 32-QAM). They still belong to the same RAT, since most RATs support several different options of modulation formats, e.g., LTE can support modulation formats of QPSK, 16-QAM, 64-QAM, and 256-QAM. In Case IV, the two services have the same bandwidth (50 MHz) and modulation format, but different FFT sizes (4096, 256) and subcarrier spacings (12.2 kHz, 195.3 kHz). They belong to different RATs since each RAT has a unique subcarrier spacing. We designed this case because sometimes services from different RATs have very similar bandwidths, e.g., both 802.11ac and LTE support 20 MHz bandwidth, and they have plenty opportunities to be transported together in a future heterogeneous MFH net-

work. For example, in cellular data offloading, Wi-Fi is used as a complementary RAT to deliver data originally targeted for LTE; in scenarios of LTE in unlicensed spectrum (LTE-U) or license assisted access (LAA), cellular carriers use the unlicensed 5-GHz band, which is already populated by Wi-Fi, to boost the LTE coverage. In Section VI, by comparing the experimental results of Case II-IV, it will be revealed that the nonlinear behaviors of inter-band IMs are dominated by the bandwidths of participating signals, rather than their modulation formats or subcarrier numbers (FFT sizes). Case V uses two services from the same RAT, which share the same subcarrier spacing (24.4 kHz) but with different bandwidths (25, 100 MHz) by exploiting different numbers of subcarriers (1024, 4096). Real-world examples of Case V include 802.11ac channel bonding and LTE carrier aggregation. In 802.11ac, signal bandwidth can be chosen from 20/40/80/160 MHz by using FFT sizes of 64/128/256/512; in LTE, channel bandwidth ranges from 1.92 to 30.72 MHz with FFT size from 128 to 2048. Case VI and VII study extreme scenarios where two services from different RATs with drastically different bandwidths are transported together, where the subcarrier spacing of a broadband service is larger than (Case VI) or comparable with (Case VII) the whole bandwidth of a narrowband service. These extreme cases occur when narrowband services, such as 802.11ah or LTE with bandwidths of only 1-2 MHz, are transported together with broadband 802.11ad, aj or UWB services, whose subcarrier spacing could be up to 5.156, 2.578 or 4.125 MHz, respectively. Finally, Case VIII studies the coexistence of four services from the same RAT, which have the same subcarrier spacing but exploit different bandwidths by using different numbers of subcarriers. This scenario corresponds to LTE carrier aggregation with four component carriers, or 802.11ac channel bonding of four channels.

Table 3.2: Eight experimental cases to evaluate subcarrier IMs in multi-RAT multi-service analog MFH

	Case	Band #	Subc. Spacing (kHz)	FFT Size	Data Subc. #	BW (MHz)	Data BW (MHz)	Modulation Format	Description	Real-World Examples	Fig.
Intra-band IMs	I	1	24.4	2048	1200	50	29.3	QPSK /16-QAM /32-QAM	single OFDM signal	one service from one RAT	3.4
Inter-band IMs	II	2	24.4	2048	1200	50	29.3	16-QAM	same subcarrier spacing same BW	two services from same RAT LTE carrier aggregation 802.11ac channel bonding	3.5
			24.4	2048	1200	50	29.3		same modulation formats		
	III	2	24.4	2048	1200	50	29.3	QPSK	same subcarrier spacing same BW, different	two services from same RAT LTE carrier aggregation 802.11ac multichannel	3.6
			24.4	2048	1200	50	29.3	32-QAM	modulation formats		
	IV	2	12.2	4096	2400	50	29.3	16-QAM	same BW, different	two services from different RATs	3.6
			195.3	256	150	50	29.3		subcarrier spacing		
	V	2	24.4	1024	600	25	14.6	16-QAM	same subcarrier spacing	two services from same RAT but with different FFT sizes LTE 7.68MHz + 30.72MHz 802.11ac 20MHz + 80MHz	3.7, 3.8
			24.4	4096	2400	100	58.6		different FFT size (BW)		
	VI	2	78.1	64	38	5	3	16-QAM	subcarrier spacing of one service larger than or comparable with	two different RATs one broadband one narrowband 802.11af/ah or LTE + 802.11ad/aj or UWB	3.9, 3.10
			6250	16	10	100	62.5		whole BW of other service		
	VII	2	78.1	64	38	5	3	16-QAM			3.11
			1562.5	64	38	100	59.4				
	VIII	4	24.4	1024	600	25	14.6	16-QAM	four services same subcarrier spacing, but different FFT sizes (BW <sub>s</sub> )	four services from same RAT but with different FFT sizes LTE carrier aggregation 802.11ac multichannel	3.12
			24.4	4096	2400	100	58.6	QPSK			
			24.4	1024	600	25	14.6	16-QAM			
			24.4	512	300	12.5	7.3	32-QAM			



All the OFDM services in Table 3.2 are generated by an AWG with intermediate frequencies (IFs), and then up-converted to 56 GHz by optical MMW up-conversion. In Case I, a single OFDM service is generated at 301 MHz and then up-converted to 56.3 GHz; in Case II-VII, the two services are generated with IFs of 301 and 641 MHz, and then up-converted to 56.3 and 56.64 GHz, respectively. In Case VIII, the four services have IFs of 301, 633, 831, and 437 MHz. Since subcarrier IMs have no dependence on the frequencies of participating signals, the IF choices for each OFDM service have no impact on their nonlinear interferences, which has been verified by experiments. Although the experiments were carried out on a MMW testbed, the theoretical analysis and experimental results are generic and can also be applied to other MFH systems operating at different frequencies. In OFDM-based RATs, cyclic prefix (CP) is used to combat with multipath-induced inter-symbol interference, and the CP lengths are chosen according to the maximum delay spread. Since CP lengths have no impact on nonlinear signal impairments, a uniform CP ratio (1/16 of FFT size) was used for all the services in experiments.

### 3.5 Experimental Results

In experiments, subcarrier IMs of OFDM signals are characterized as a function of input signal amplitudes. Root-mean-square (RMS) amplitudes of input signals are measured before the power amplifier in Fig. 3.3, so that the nonlinear transfer functions of both power amplifier and DEMZM are taken into account. In experiments, nonlinear impairments are evaluated in terms of error vector magnitude (EVM) and power spectral density (PSD).

#### 3.5.1 Case I

Fig. 3.4 shows the experimental results of Case I. EVM as a function of the RMS amplitude of input signal is presented in Fig. 3.4(a). As the input amplitude increases,

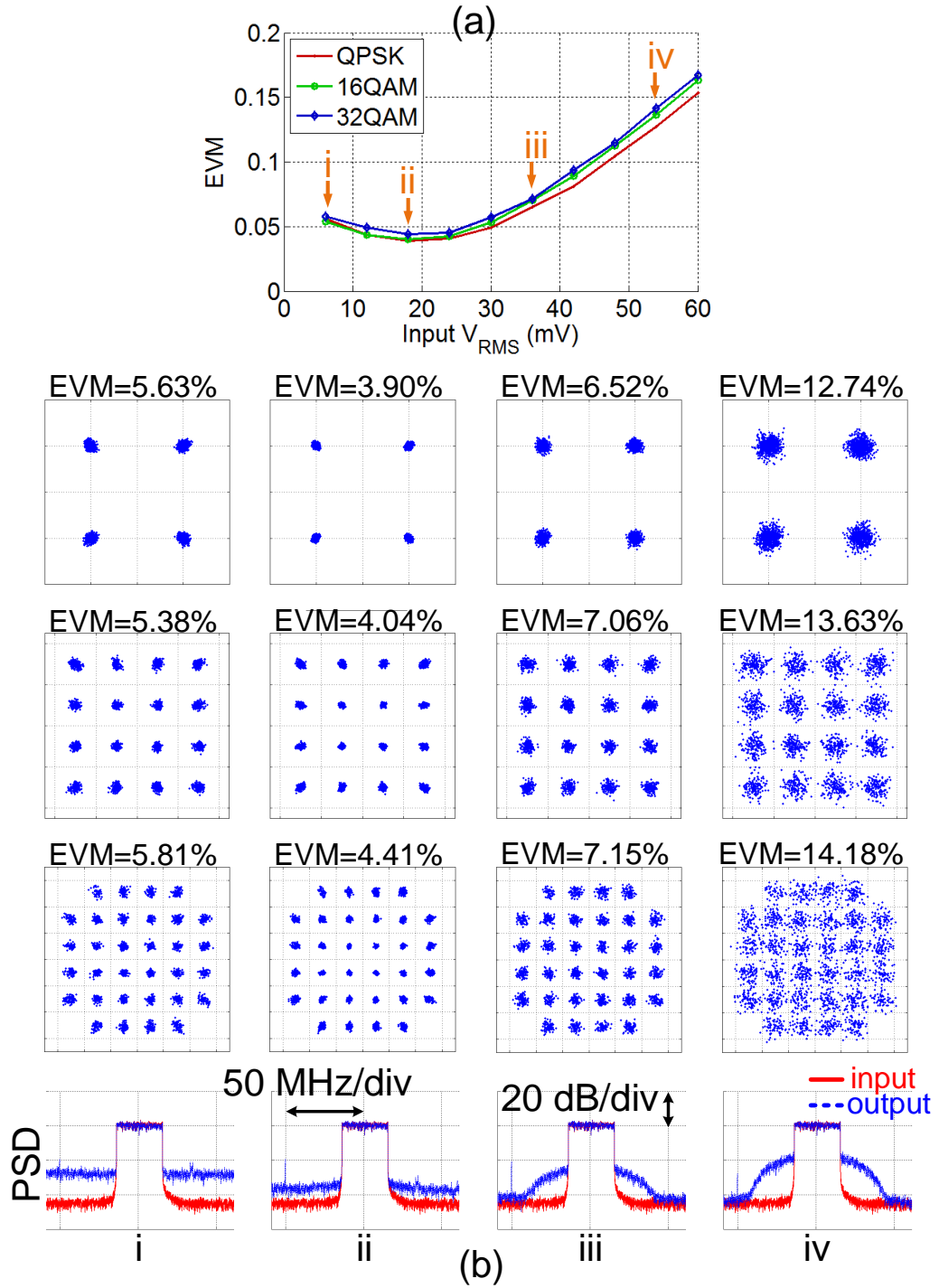
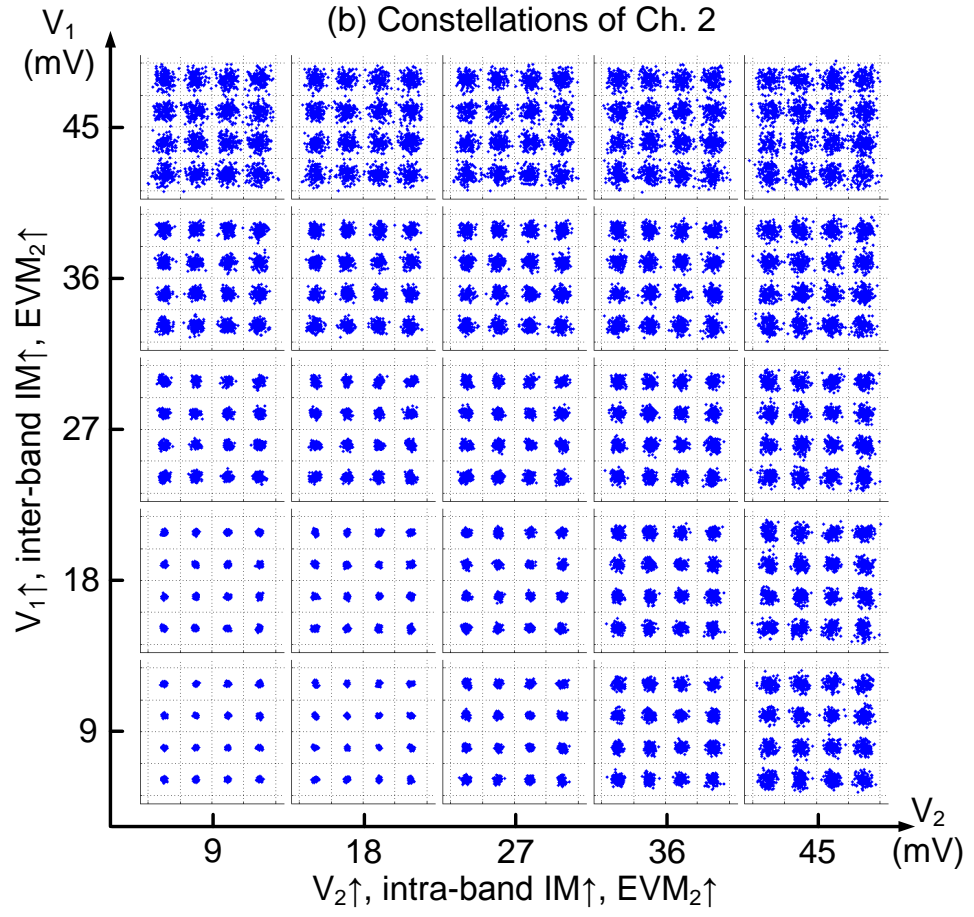
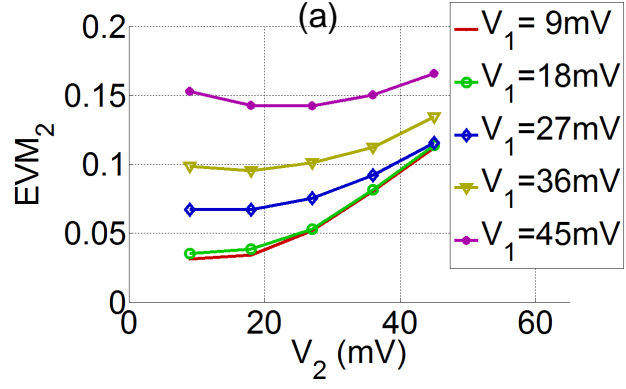


Figure 3.4: Experimental results of Case I. (a) EVM as a function of RMS amplitude of input signal. (b) Constellations and PSDs at points i-iv.

EVM first reduces and then increases. This is because the system performance is mainly limited by noise when the input signal is small, so EVM first decreases due to the improvement of signal-to-noise (SNR). But if the input signal continues increasing, nonlinear intra-band IMs start to show up and make EVM increase. The same trend is also observed in the frequency domain by PSDs, shown in the last row of Fig. 3.4(b). To facilitate comparison, PSDs of the input (red) and output (blue) signals are normalized and plotted together. At point i, the system performance is limited by noise, and a high noise pedestal is observed in the output PSD. As the input signal increases, SNR improves, so the noise pedestal is reduced at point ii. At point iii and iv, intra-band IMs start to appear and introduce both in-band interferences and out-of-band emission, revealed by constellation degradation and out-of-band PSD growth, respectively. It is also verified that intra-band IMs cover a frequency range of  $3B$  around the central frequency of the original signal. Three modulation formats were tested, all with similar performance, indicating that intra-band IMs have no dependence on the modulation formats.

### 3.5.2 Case II

Fig. 3.5 shows the experimental results of Case II, where two OFDM services from the same RAT with identical bandwidth, FFT size, subcarrier spacing and modulation format are transported together in a MFH network. A real-world example of this case is LTE carrier aggregation or 802.11ac channel bonding. Since each channel suffers from both intra- and inter-band IMs, there are two dimensions of nonlinearities. Due to the symmetry of two channels, only Ch. 2 results are presented. Fig. 3.5(a) shows  $\text{EVM}_2$  as a function of input amplitudes of Ch. 1 ( $V_1$ ) and Ch. 2 ( $V_2$ ). For a given  $V_1$ ,  $\text{EVM}_2$  increases with  $V_2$  due to intra-band IMs; for a given  $V_2$ ,  $\text{EVM}_2$  increases with  $V_1$  due to inter-band IMs. Moreover, the rate that  $\text{EVM}_2$  increases with  $V_1$  is faster than that it increases with  $V_2$ , indicating that inter-band IMs make



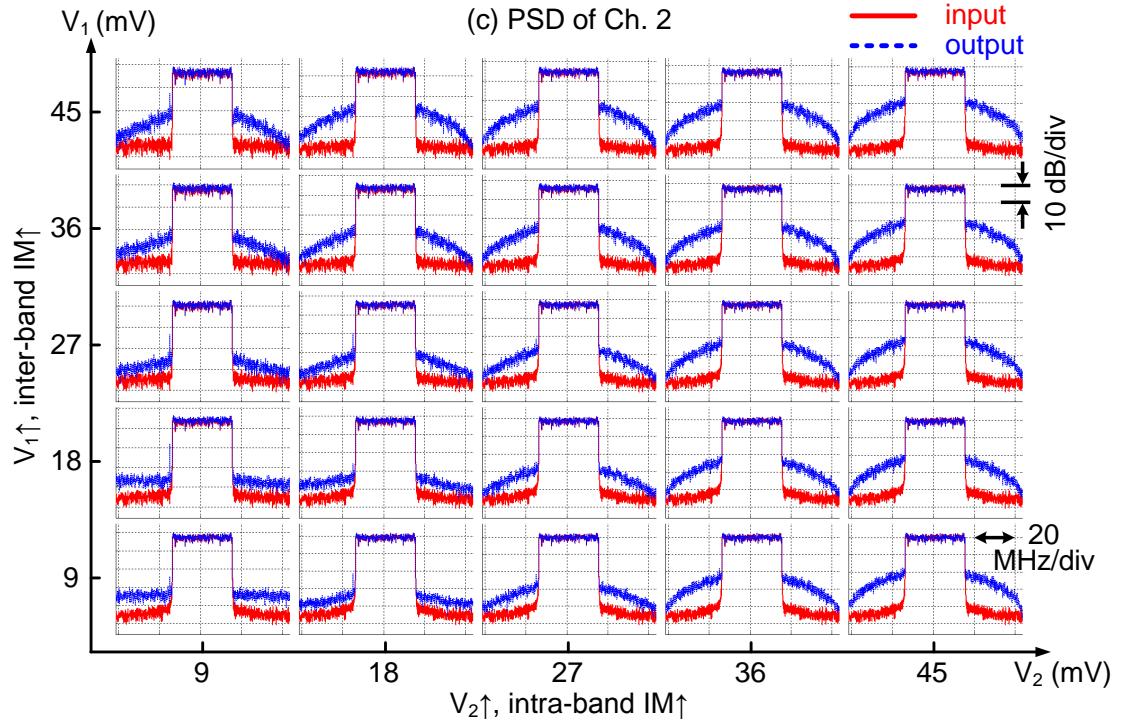
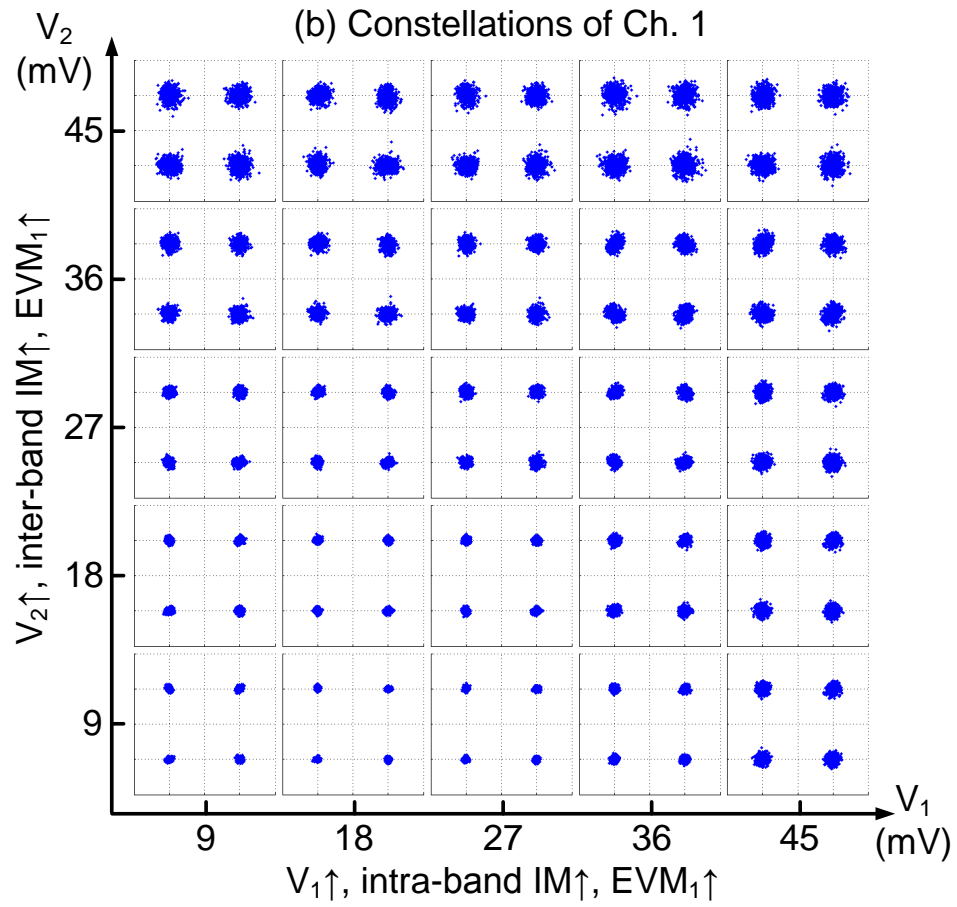
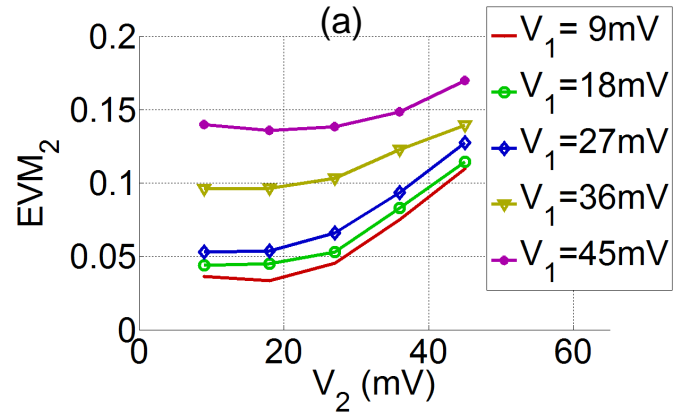


Figure 3.5: Experimental results of Case II. (a)  $\text{EVM}_2$  as a function of  $V_1$ ,  $V_2$ . (b) Ch. 2 constellations. (c) Ch. 2 PSDs.

more significant contributions to signal impairments than the well-known intra-band IMs. Constellations and PSDs of Ch. 2 are shown in Fig. 3.5(b) and (c). In the horizontal direction, intra-band IMs increase with  $V_2$ ; in vertical direction, inter-band IMs increase with  $V_1$ . Both intra- and inter-band IMs introduce in-band interferences and out-of-band emissions, leading to constellation degradation and out-of-band PSD growth.

### 3.5.3 Case III and IV

Case III and IV are variants of Case II. In Case III, the two services have the same subcarrier spacing (24.4 kHz) and bandwidth (50 MHz), but different modulation formats (QPSK, 32-QAM), corresponding to a multiband operation of the same RAT, where different services carry different modulation formats, such as two LTE component carriers or two 802.11ac channels. In Case IV, the two services have the same bandwidth (50 MHz) and modulation format, but different FFT sizes (4096, 256) and subcarrier spacings (12.2 kHz, 195.3 kHz), corresponding to two services from different RATs. In experiments, the results of Case II, III, and IV are very similar, since all the signals in these three cases have the same bandwidths of 50 MHz, despite of their various modulation formats (Case III) or subcarrier spacing (Case IV). This indicates that inter-band IMs are mainly determined by the bandwidths of participating signals, rather than their modulation formats or subcarrier spacing. Experimental results of Case III and IV are shown in Fig. 3.6, and the constellations of two signals in Case III (QPSK, 32-QAM) are shown in Fig. 3.6(b) and (c). Despite of the different modulation formats, the EVM performance in Fig. 3.6(a) is very similar to that in Fig. 3.5(a) of Case II.



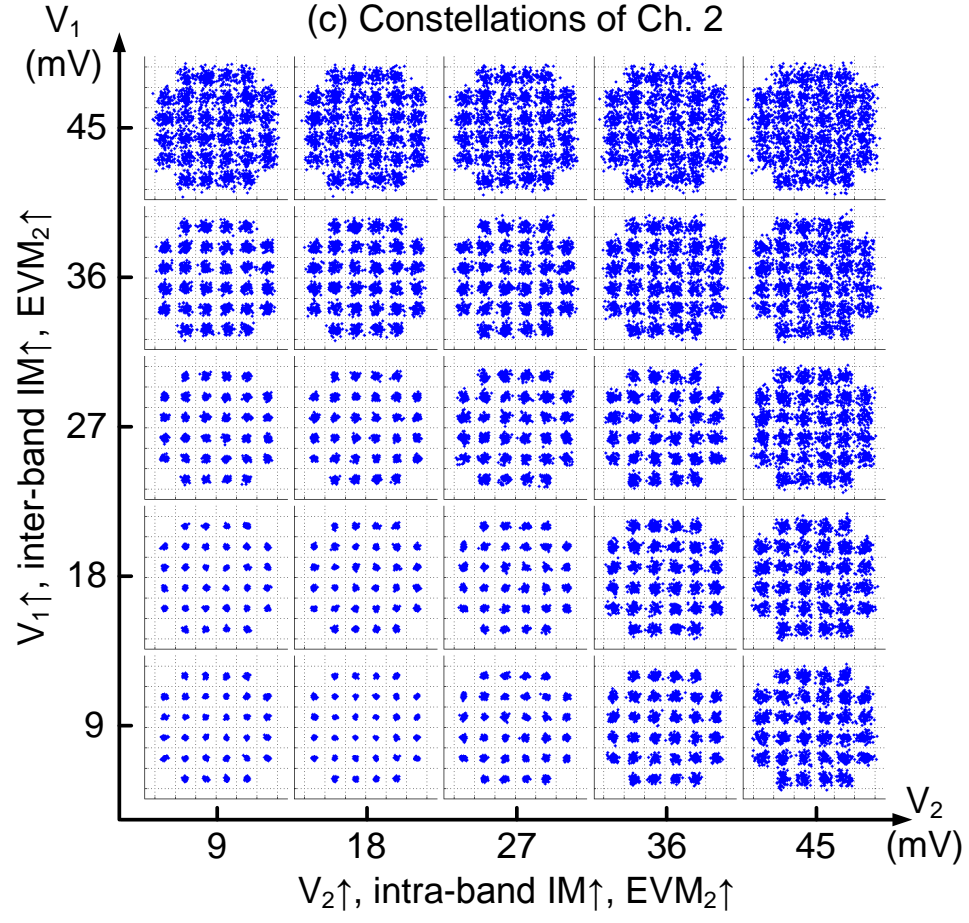


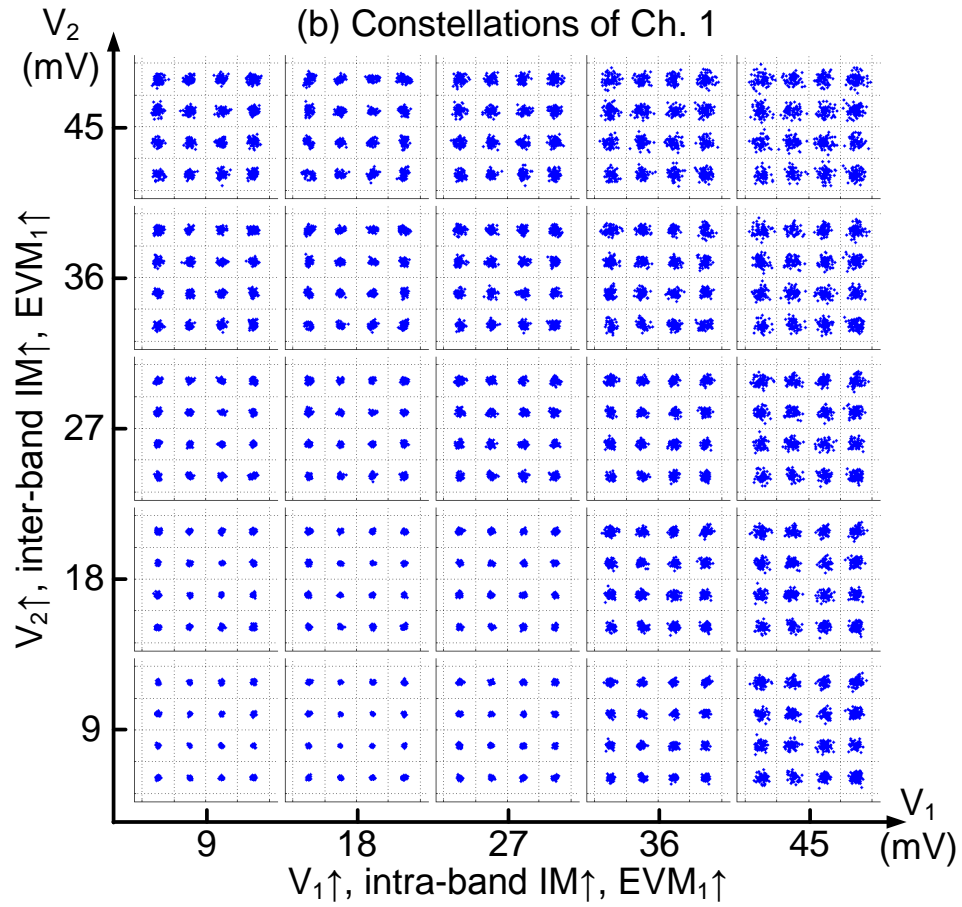
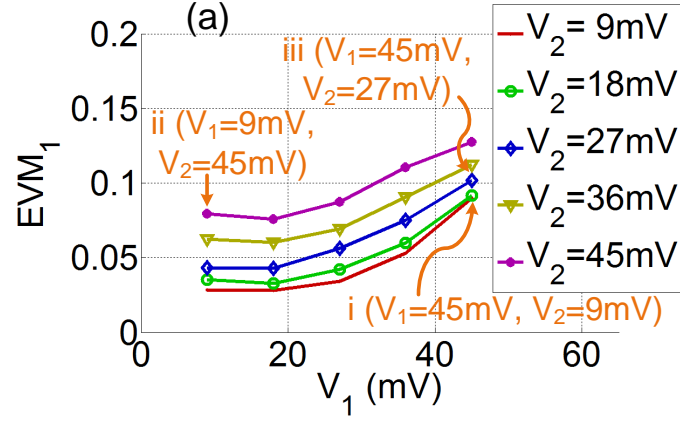
Figure 3.6: Experimental results of Case III and IV (identical EVM performance). (a) EVM $_2$  in Case III and IV. (b) Ch. 1 constellations in Case III. (c) Ch. 2 constellations in Case III.



### 3.5.4 Case V

Case V uses two services from the same RAT, which share the same subcarrier spacing but have different bandwidths and different subcarrier numbers. This case corresponds to a real-world scenario of multi-service aggregation from same RAT but with different FFT sizes, such as LTE carrier aggregation, Wi-Fi channel bonding, etc.. In Case V, two signals with bandwidths of 25 and 100 MHz were transported together to emulate two services from the same RAT. Experimental results are shown in Fig. 3.7. EVMs of two channels are presented in (a) and (c), and constellations in (b) and (d). Ch. 2 experiences more inter-band IMs than Ch. 1, since it has broader bandwidth, so  $\text{EVM}_2$  increases with  $V_1$  at a rate much faster than that  $\text{EVM}_1$  increases with  $V_2$ . This is because most inter-band IMs from Ch. 1 to Ch. 2 are in-band interferences to Ch. 2; whereas most inter-band IMs from Ch. 2 to Ch. 1 are out of Ch. 1, and can be filtered out.

This observation is consistent with previous analysis in Section II, and can also be experimentally verified in frequency domain. Fig. 3.8 shows the PSDs of both OFDM signals at points i, ii, and iii labeled in Fig. 3.7(a) and (c). At point i ( $V_1 = 45$  mV,  $V_2 = 9$  mV), Ch. 1 is strong and Ch. 2 is weak, so Ch. 1 is dominated by intra-band IMs; whereas Ch. 2 is impaired by inter-band IMs from Ch. 1. At point ii ( $V_1 = 9$  mV,  $V_2 = 45$  mV), Ch. 1 weak and Ch. 2 strong, so Ch. 1 is dominated by inter-band IMs from Ch. 2; Ch. 2 is impaired by intra-band IMs. In Fig. 3.8(b), it is observed that inter-band IMs from Ch. 2 to Ch. 1 cover a frequency range of  $B_1 + 2B_2$  around Ch. 1; in Fig. 3.8(d), inter-band IMs from Ch. 1 to Ch. 2 cover a frequency range of  $B_2 + 2B_1$  around Ch. 2. Since  $B_1 < B_2$ , Ch. 2 experiences more in-band interferences than Ch. 1. Fig. 3.8(e) shows the PSD of Ch. 1 at an intermediate state (point iii,  $V_1 = 45$  mV,  $V_2 = 27$  mV), where the out-of-band emission far away from Ch. 1 central frequency are contributed by only inter-band IMs, since intra-band IMs only cover a spectral range of  $3B_1$ .



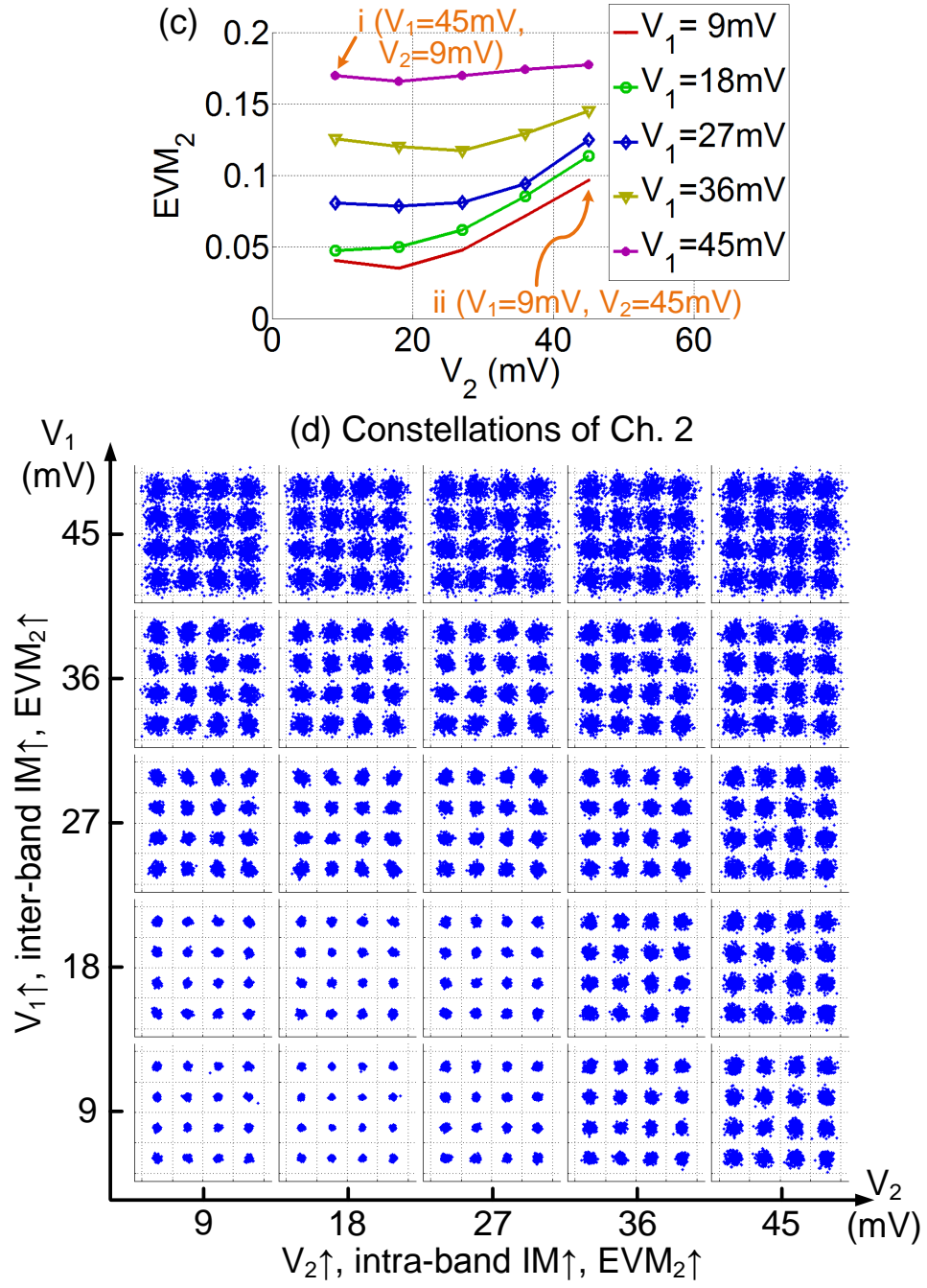


Figure 3.7: Experimental results of Case V. (a)  $EVM_1$ . (b) Ch. 1 constellations. (c)  $EVM_2$ . (d) Ch. 2 constellations.

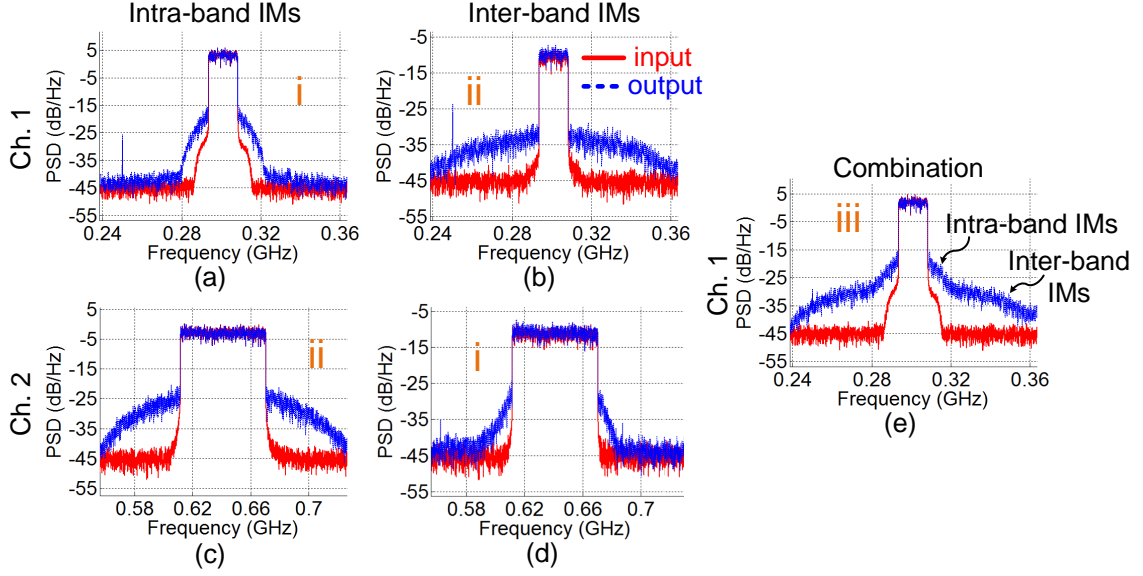
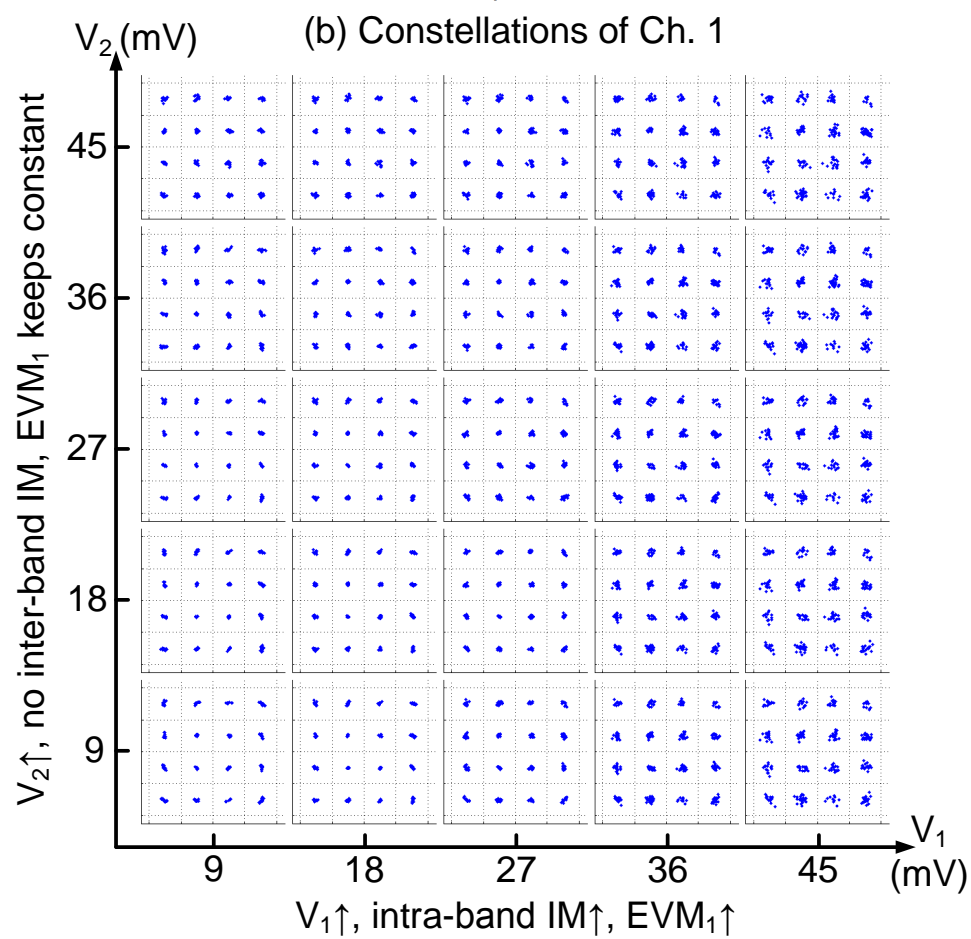
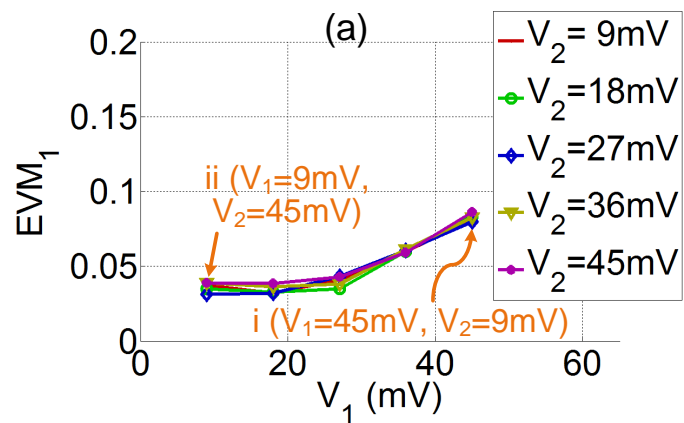


Figure 3.8: PSDs at point i ( $V_1 = 45$  mV,  $V_2 = 9$  mV), ii ( $V_1 = 9$  mV,  $V_2 = 45$  mV), and iii ( $V_1 = 45$  mV,  $V_2 = 27$  mV) in Case V. At point i, Ch. 1 is impaired by intra-band IMs (a), and Ch. 2 impaired by inter-band IMs (d). At point ii, Ch. 1 is impaired by inter-band IMs (b) and Ch. 2 by intra-band IMs (c). At point iii, the impairments of Ch. 1 is a combination of both intra-band and inter-band IMs (e).

### 3.5.5 Case VI and VII

Case VI and VII study extreme scenarios, where services from different RATs have drastically different bandwidths, so that the subcarrier spacing of a broadband service is larger than (Case VI) or comparable with (Case VII) the whole bandwidth of a narrowband service. These extreme cases would occur when a narrowband service, such as 802.11ah or LTE, with bandwidth of only 1-2 MHz, are transported together with a broadband 802.11ad, aj, or UWB service with subcarrier spacing up to 5.156, 2.578 or 4.125 MHz in a multi-RAT MFH network.

The experimental results of Case VI are shown in Fig. 3.9. Two OFDM services with bandwidths of 5 MHz and 100 MHz are transported together, with FFT size of 64 and 16, respectively. The subcarrier spacing of Ch. 2 ( $\Delta f_2 = 6.25$  MHz) is even larger than the whole bandwidth of Ch. 1 ( $B_1 = 5$  MHz). Consider inter-band IMs



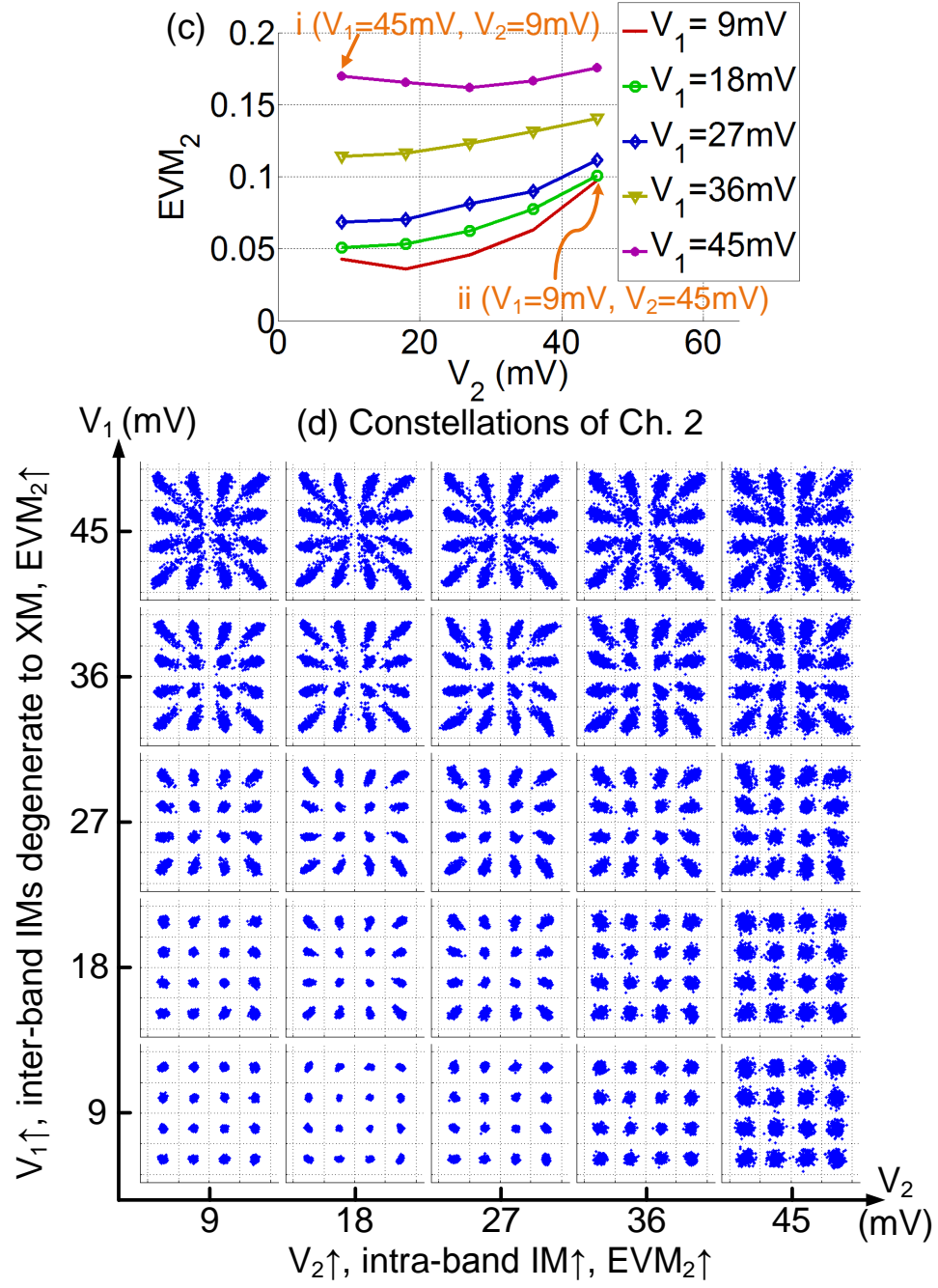


Figure 3.9: Experimental results of Case VI. (a)  $EVM_1$ . (b) Ch. 1 constellations. (c)  $EVM_2$ . (d) Ch. 2 constellations.

from Ch. 2 to Ch. 1,  $f_k^{(1)} \pm (f_p^{(2)} - f_q^{(2)})$ , since the frequency offset  $|f_p^{(2)} - f_q^{(2)}|$  is larger than the whole bandwidth of Ch. 1, i.e.  $|f_p^{(2)} - f_q^{(2)}| \geq \Delta f_2 > B_1$ , any inter-band IMs from Ch. 2 to Ch. 1 always locate out of Ch. 1, making Ch. 1 immune from inter-band interferences. In Fig. 3.9(a),  $\text{EVM}_1$  only increases with  $V_1$  due to intra-band IMs, but keeps constant as  $V_2$  increases because of the absence of inter-band IMs. The constellations of Ch. 1 are shown in Fig. 3.9(b), and there is no constellation degradation observed along the vertical direction as  $V_2$  increases. Now consider inter-band IMs from Ch. 1 to Ch. 2,  $f_k^{(2)} \pm (f_p^{(1)} - f_q^{(1)})$ . Due to the narrow bandwidth of Ch. 1,  $|f_p^{(1)} - f_q^{(1)}| \leq B_1 < \Delta f_2$ , these two IM products always locate within one subcarrier spacing from the  $k$ -th subcarrier of Ch. 2, as shown in (3.8). The combination of two conjugate IM terms, i.e.  $Y_k^{(2)} Y_p^{(1)} \overline{Y_q^{(1)}}$  at  $f_k^{(2)} + f_p^{(1)} - f_q^{(1)}$  and  $Y_k^{(2)} \overline{Y_p^{(1)}} Y_q^{(1)}$  at  $f_k^{(2)} - f_p^{(1)} + f_q^{(1)}$ , degenerate to a real-valued cross-modulation (XM) factor, which introduces a scaling distortion to the symbol of  $Y_k^{(2)}$ , as shown in (3.9). The constellations of Ch. 2 are shown in Fig. 3.9(d). In this extreme case, inter-band IMs from Ch. 2 to Ch. 1 are always out-of-band, making Ch. 1 immune from inter-band interferences; whereas inter-band IMs from Ch. 1 to Ch. 2 degenerate to XM and induce scaling distortions to Ch. 2.

$$f_{k-1}^{(2)} < f_k^{(2)} - B^{(1)} \leq f_k^{(2)} \pm (f_p^{(1)} - f_q^{(1)}) \leq f_k^{(2)} + B^{(1)} < f_{k+1}^{(2)} \quad (3.8)$$

$$\begin{aligned} & Y_k^{(2)} Y_p^{(1)} \overline{Y_q^{(1)}} \exp \left[ -j \left( \omega_k^{(2)} + \omega_p^{(1)} - \omega_q^{(1)} \right) t \right] \\ & + Y_k^{(2)} \overline{Y_p^{(1)}} Y_q^{(1)} \exp \left[ -j \left( \omega_k^{(2)} - \omega_p^{(1)} + \omega_q^{(1)} \right) t \right] \\ & \propto \text{Re} \left[ Y_p^{(1)} \overline{Y_q^{(1)}} \exp \left( -j \Delta \omega_{pq}^{(1)} t \right) \right] Y_k^{(2)} \exp \left( -j \omega_k^{(2)} t \right) \end{aligned} \quad (3.9)$$

This experimental observation is also consistent with the intuition. Since  $B_1 \ll B_2$ , from the point of view of Ch. 2, Ch. 1 can be considered as a single-carrier signal, and according to Chapter 2, a single-carrier signal introduces inter-band XM to its

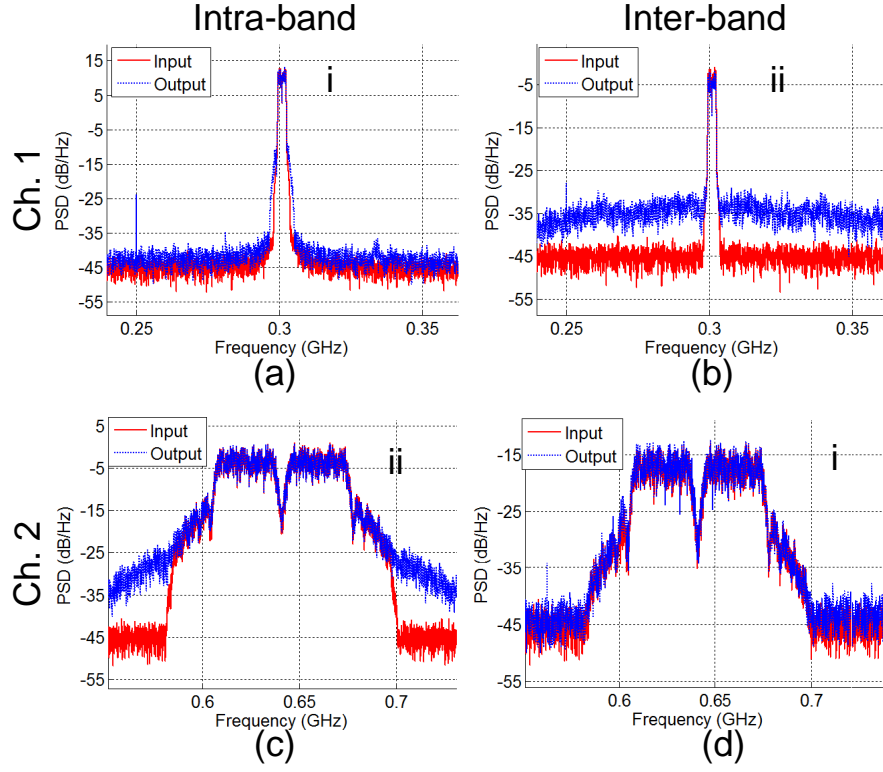
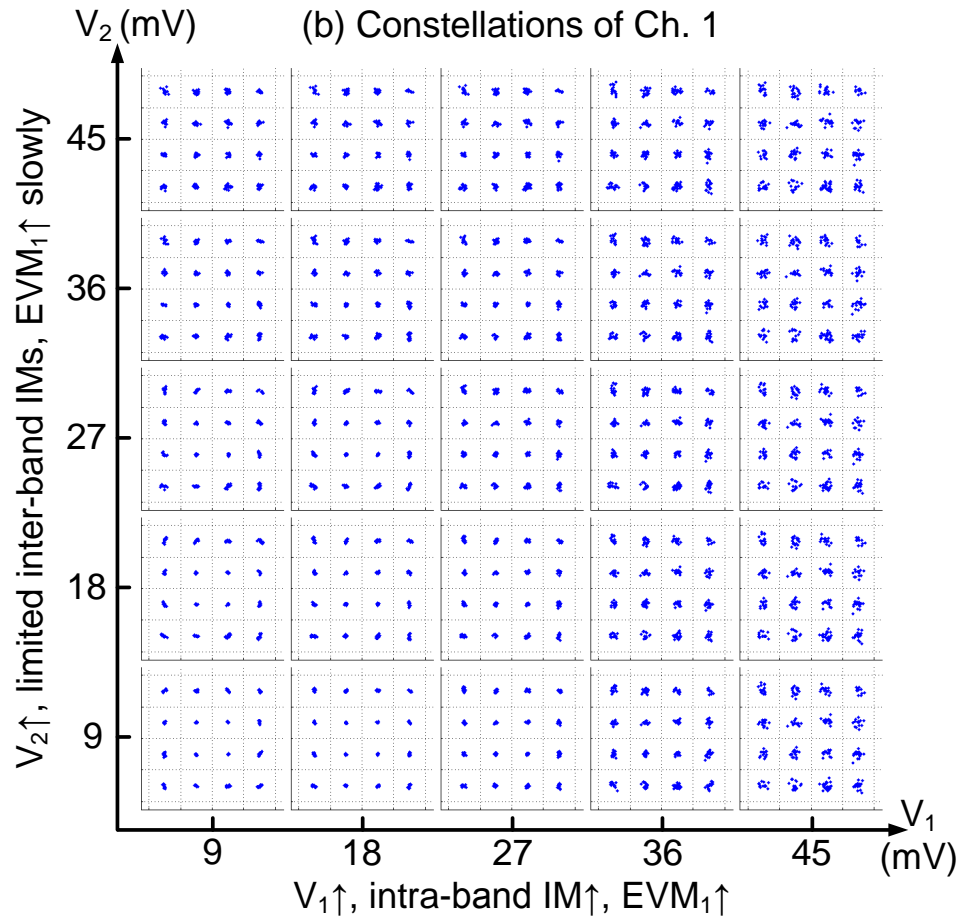
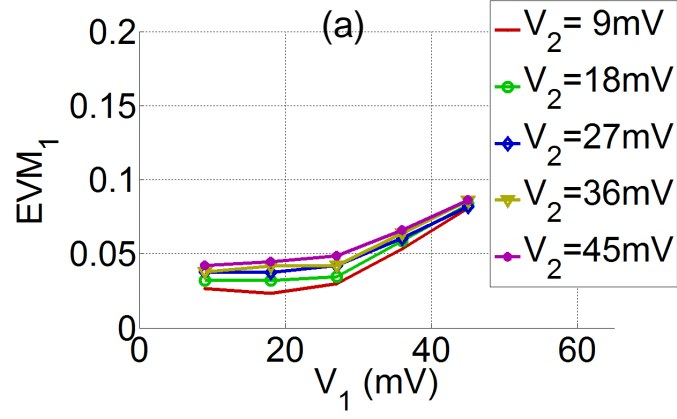


Figure 3.10: PSDs at point i ( $V_1 = 45 \text{ mV}, V_2 = 9 \text{ mV}$ ) and ii ( $V_1 = 9 \text{ mV}, V_2 = 45 \text{ mV}$ ) in Case VI. At point i, Ch. 1 is impaired by intra-band IMs (a), and Ch. 2 impaired by inter-band IMs, which degenerate to inter-band XM (d). At point ii, Ch. 1 is immune from inter-band interferences (b), and Ch. 2 is impaired by intra-band IMs (c).



coexistent signals, which evidence as a scaling distortion to their constellations. It is worth to note that given the same EVM, XM-caused scaling distortion leads to higher BER than the Gaussian noise induced by subcarrier IMs. Fig. 3.10 shows the PSDs of both signals at point i and ii in Fig. 3.9. In Fig. 3.10(b), inter-band IMs from Ch. 2 to Ch. 1 always locate out of Ch. 1. In Fig. 3.10(d), inter-band IMs from Ch. 1 to Ch. 2 always locate within Ch. 2, and there is no out-of-band emission observed. The input (red) and output (blue) PSDs almost overlap with each other, giving an illusion that there is no distortion to Ch. 2. This is another evidence that inter-band IMs have degenerated to XM, since XM is a baseband effect, which cannot be revealed in the frequency domain.

Fig. 3.11 shows the experimental results of Case VII, where the subcarrier spacing of Ch. 2 ( $\Delta f_2 = 1.56$  MHz) is smaller than but still comparable with the bandwidth of Ch. 1 ( $B_1 = 5$  MHz). A large portion of inter-band IMs from Ch. 2 to Ch. 1 locate out of Ch. 1, so Ch. 1 experiences very limited amount of inter-band IMs. In Fig. 3.11(a),  $\text{EVM}_1$  shows weak dependence on  $V_2$ , and in Fig. 3.11(b), Ch. 1 constellations only show slight degradation along the vertical direction, due to the limited inter-band IMs. On the other hand, most inter-band IMs from Ch. 1 to Ch. 2 locate within Ch. 2, making severe in-band interferences. Moreover, (3.8) no longer holds, and conjugate IMs from Ch. 1 to Ch. 2,  $f_k^{(2)} \pm (f_p^{(1)} - f_q^{(1)})$ , no longer locate within the same subcarrier spacing around  $f_k^{(2)}$ , but partially spread into neighboring subcarriers of Ch. 2. Therefore, the inter-band interferences of Ch. 2 become a combination of inter-band XM and inter-band subcarrier IM. In Fig. 3.11(d), Ch. 2 constellations experience both scaling distortion contributed by XM and additive Gaussian noise contributed by subcarrier IMs.



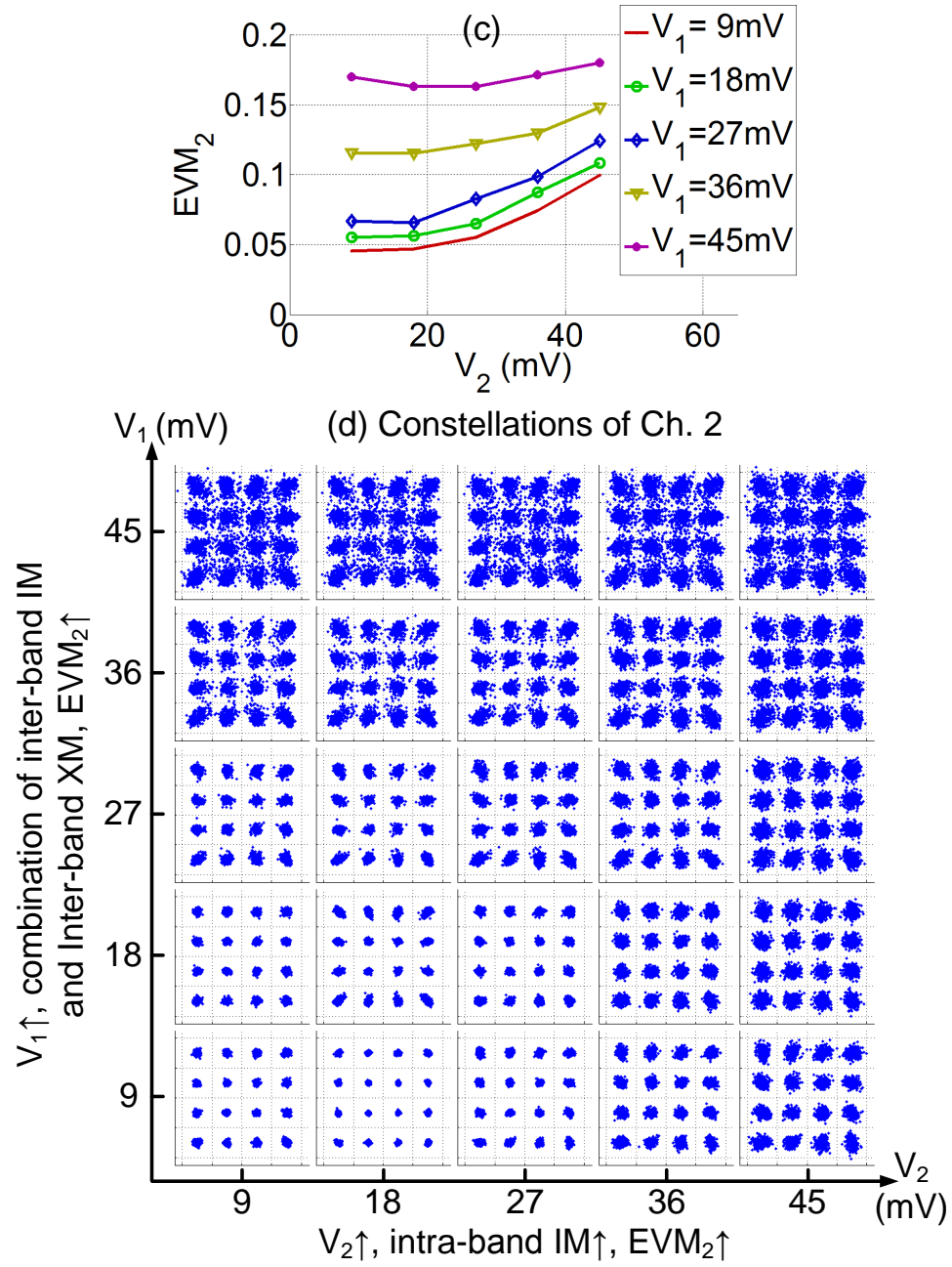


Figure 3.11: Experimental results of Case VII. (a)  $EVM_1$ . (b) Ch. 1 constellations. (c)  $EVM_2$ . (d) Ch. 2 constellations.

### 3.5.6 Case VIII

Case VIII studies the coexistence of four services from one RAT, which share the same subcarrier spacing but have different bandwidths by exploiting different subcarrier numbers. This case corresponds to a real-world example of LTE carrier aggregation with four component carriers.

Four OFDM services with bandwidth of 25, 100, 25 and 12.5 MHz are used with FFT size of 1024, 4096, 1024, and 512, respectively. To evaluate the impact of inter-band IMs from one strong service on other services, the input amplitudes of four services were chosen carefully,  $V_1 = 35$  mV,  $V_2 = V_3 = V_4 = 10$  mV, so that only one service (Ch. 1) has large enough amplitude to introduce inter-band IMs, all others (Ch. 2-4) are too small to induce either intra- or inter-band IMs. Different modulation formats are assigned to four services. Constellations of Ch. 2-4 with and without the presence of Ch. 1 are shown in Fig. 3.12(a) and (b), respectively. Without Ch. 1, clear constellations are obtained for Ch. 2-4, with EVM of 4.67%, 2.55%, and 2.35%, respectively. With Ch. 1 present, due to the strong inter-band IMs from Ch. 1, EVMs of Ch. 2-4 degrade to 10.86%, 8.88%, and 7.24%. PSDs of Ch. 2-4 with and without Ch. 1 are shown in Fig. 3.12(c), (d), where the input (red) and output (blue) PSDs are normalized and plotted together for easy comparison. In Fig. 3.12(c), there is no out-of-band emission observed due to the absence of IMs. The output PSDs have slightly increased noise pedestal due to SNR degradation after MFH transmission. In Fig. 3.12(d), however, with Ch. 1 present, significant out-of-band emissions are observed, indicating strong inter-band IMs from Ch. 1. We intentionally chose different bandwidths for Ch. 2-4, so they experience different amount of inter-band interferences. The broadband Ch. 2 has severe in-band interferences and worst EVM (10.86%); the narrowband Ch. 4 has a large portion of IMs locating out-of-band, and best EVM (7.24%). Due to their different susceptibilities to IMs, different modulation formats are assigned, 16-QAM for Ch. 1, QPSK for Ch. 2, 16-QAM for Ch. 3,

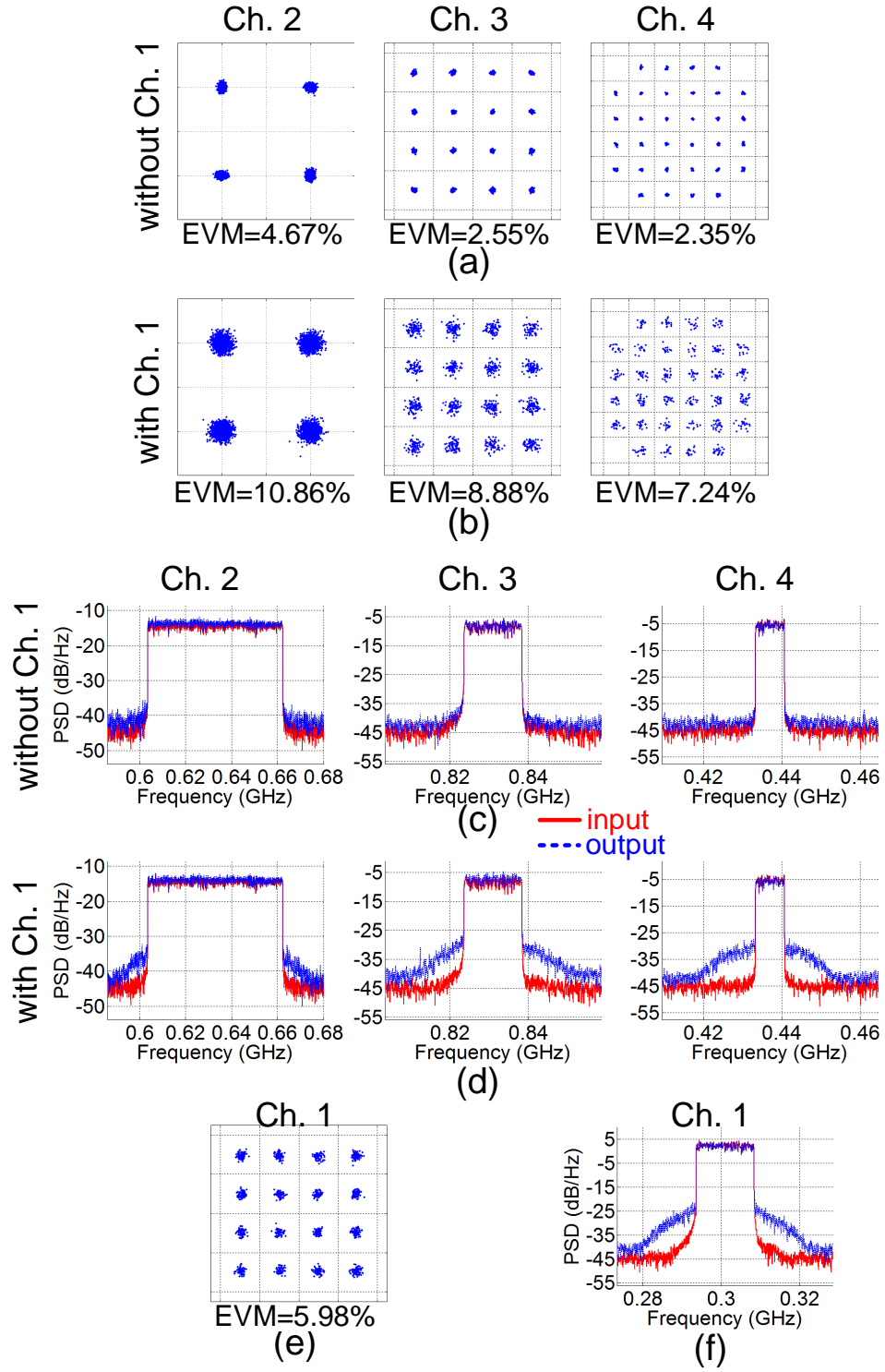


Figure 3.12: Experimental results of Case VIII. (a, b) Constellations of Ch. 2-4 without/with Ch. 1. (c, d) PSDs of Ch. 2-4 without/with Ch. 1. (e, f) Constellation and PSD of Ch. 1.

32-QAM for Ch. 4. Fig. 3.12(e) and (f) show the constellation and PSD of Ch. 1, where the out-of-band spectral growth in Fig. 3.12(f) only comes from intra-band IMs. With EVM of only 5.98%, Ch. 1 itself does not experience much impairments from intra-band IMs, but it brings significant contamination to other coexistent services via inter-band IMs. Once again, it is verified that inter-band IMs play a much more important role than intra-band IMs in a multi-RAT multiband MFH system.

### 3.6 Summary

In this chapter, nonlinear impairments of multi-carrier signals in the next generation multi-RAT multi-service analog MFH networks are investigated. The dominant impairments of multi-carrier signals are subcarrier IMs, i.e., third-order beat among subcarriers. These subcarriers can come from the same OFDM signal, forming intra-band IMs, or from different signals, forming inter-band IMs. Most existing studies only focus on the intra-band IMs with each individual OFDM signal, but there has been meager effort to study the inter-band interferences among multiple signals. In this chapter, inter-band IMs among multiple mobile signals in a multi-RAT analog MFH are investigated for the first time. Eight experimental cases are designed and the results are summarized in Table 3.3.

Both intra-band and inter-band IMs can introduce in-band interferences and out-of-band emission, and the in-band interferences can be modeled as a Gaussian noise with zero mean. It has been experimentally verified that in a multi-RAT multi-service system, inter-band IMs play a more significant role in the performance degradation of analog MFH than the well-known intra-band IMs. Inter-band IMs are mainly determined by the bandwidths of participating signals, and have weak dependency on the modulation formats and subcarrier spacing. Broadband multi-carrier services suffer more from inter-band IMs since their large bandwidth can capture more in-band interferences. In some extreme scenarios, inter-band IMs will degenerate to baseband

XMs, depending on the relative sizes of bandwidth and subcarrier spacing of mobile signals.

It is worth noting that although subcarrier IMs are not baseband effects, they only depend on the frequency difference among subcarriers, and have no dependency on the central frequencies of OFDM signals. Therefore, same as XMs of single-carrier signals, subcarrier IMs can not be eliminated by filtering. Our experiments are carried out at 60 GHz, but the theoretical analysis and experimental results are generic and can also be applied to other analog MFH systems operating at different frequencies. In the next chapter, a linearization technique based on digital predistortion will be investigated and effective mitigation of both XMs and IMs will be presented.

Table 3.3: Summary of experimental results

Case	Band #	Real-world examples	Experimental observations
I	1	One service from one RAT	Intra-band subcarrier IMs
II	2	Same RAT, same BW	Inter-band IMs play a more important role than intra-band IMs in OFDM signal degradation
III	2	Same RAT, same BW Different modulation formats	Inter-band IMs mainly determined by BWs of participating signals, but have weak dependence on modulation formats or subcarrier spacing
IV	2	Different RATs, different subcarrier spacing, same BW	
V	2	Same RAT, same subcarrier spacing Different BWs (different FFT size)	Broadband service suffers more from inter-band IMs since it captures more in-band interferences
VI	2	Different RATs Drastically different BWs and subcarrier spacing ( $\Delta f_2 > BW_1$ )	Narrowband service is immune from inter-band IMs Inter-band IMs from narrowband service to broadband service degenerate to baseband XM (scaling distortions)
VII	2	Different RATs $\Delta f_2, BW_1$ comparable	Narrowband service has slight inter-band IMs Inter-band IMs of broadband service become a combination of scaling distortion and Gaussian noise
VIII	4	Same RAT, different BWs	One strong narrowband service is detrimental to other coexistent services



## CHAPTER 4

### LINEARIZATION TECHNOLOGY BASED ON DIGITAL PREDISTORTION

#### 4.1 Introduction

In Chapter 2 and 3, we have investigated the nonlinear transmission impairments of analog MFH networks. It was experimentally demonstrated that the dominant impairments for single-carrier signals are cross-modulations (XMs), and the dominant impairments for multi-carrier signals are subcarrier intermodulations (IMs). It was also verified that electric power amplifiers and the electro-optic interface of optical modulators are major contributors of nonlinear channel response of analog MFH.

To mitigate the nonlinear impairments, two different linearization strategies can be exploited, waveform-specific and waveform-agnostic. The waveform-specific strategy modifies signal waveforms to enhance their robustness against nonlinear distortions, such as clipping technique for PAPR reduction [105, 106]. Digital MFH can also be considered as an extreme scenario of waveform-specific strategy, where the continuous envelopes of mobile signals are digitized into discrete bits, and transmitted via digital communication links, which are inherently robust against nonlinear impairments. In Chapter 5, we will discuss the digitization interface of digital MFH networks, where CPRI based on Nyquist ADC and delta-sigma modulation based on oversampling ADC will be comparatively investigated.

On the other hand, waveform-agnostic strategy keeps the signal waveforms intact, but modifies the channel response, and the linearized channel is transparent to different signal waveforms. Due to its simplicity, low-cost, and signal transparency, waveform-agnostic techniques have found wide applications in the linearization

of power amplifiers, wireless transmitters/receivers, RoF links, etc., and many implementation schemes have been reported in either electrical or optical domain. A summary of different linearization technologies are given in Table 1.3 in Chapter 1.

Most optical domain linearization technologies, such as feedforward [107–116], dual-parallel modulation [117–122], mixed polarizations [123–130], cascaded SOA and MZM [131, 132], and light injection cross gain modulation [133–136], suffer from expensive optical components, complicated system design, and more importantly, precise control/matching requirement of amplitude, phase, or bias, which severely prevent them from real application. Predistortion technique, on the other hand, features simple and low cost implementations, which only needs a block of predistorter before the transmitter to pre-compensate the nonlinear channel response, and can be realized in electrical domain without expensive optical components. Given the static and highly predictable nature of MFH networks, as well as the limited system budget of access networks, predistortion is considered as one of the most cost-effective solutions to linearize analog MFH.

Predistortion can be realized either in the analog domain using low-cost analog circuits [137–154], or in the digital domain based on digital signal processing (DSP) [155–167]. Analog predistortion exploits the exponential transfer characteristics of diodes, bipolar transistors, or CMOS circuits to synthesize desired nonlinear transfer function to compensate MFH channel response. In general, any transmission impairments can be modeled as nonlinear distortion with memory effect, where the nonlinear distortion captures the dependence of channel transfer function on input amplitudes in the time domain; whereas memory effect is contributed by the bandwidth limitation in the frequency domain. For analog predistortion, the main technical challenges are the difficulties to synthesize arbitrary transfer functions in the time domain, and to compensate arbitrary bandwidth limitation in the frequency domain. Some transfer functions are difficult or even impossible to achieve with ana-

log diodes or transistors, e.g., in [143], simultaneous correction of both second and third-order distortions cannot be achieved due to the coupling between different paths of different orders of nonlinearities. In the frequency domain, broadband predistortion is also challenging to realize, and analog predistortion with 5-GHz bandwidth was not reported until 2012 [150].

On the other hand, predistortion can also be carried out in the digital domain. Digital predistortion first transforms the input analog signals to digital domain by ADC, and after DSP the processed signals are transformed back to analog domain by DAC. Enabled by the advancement of DSP technologies, the challenges of analog predistortion can be easily addressed. In the time domain, arbitrary transfer functions can be synthesized; in the frequency domain, arbitrary memory effects can be addressed by frequency equalization enabled by FFT/IFFT. Some functions that are difficult or even impossible to achieve with analog diodes can be easily realized by DSP. The only constraint of digital predistortion is the processing speed, which is limited by the speed and power consumption of input/output ADC/DAC.

In this chapter, we demonstrate a digital predistortion technique to linearize the analog MFH channel in Chapter 2 and 3. A memory polynomial model is used to capture the nonlinear channel response of analog MFH links, and in experiments, it is verified that it can address both nonlinear XMs for single-carrier signals and subcarrier IMs for multi-carrier signals. This chapter is organized as follows. Section II explains the operation principles of memory-polynomial based digital predistortion. Section III presents the experimental setup. The experimental results are presented in Section IV. Section V concludes the chapter.

## 4.2 Operation Principles

The operation principle of digital predistortion is shown in Fig. 4.1. A baseband processing unit (BBU) is connected with remote radio heads (RRHs) with single-mode

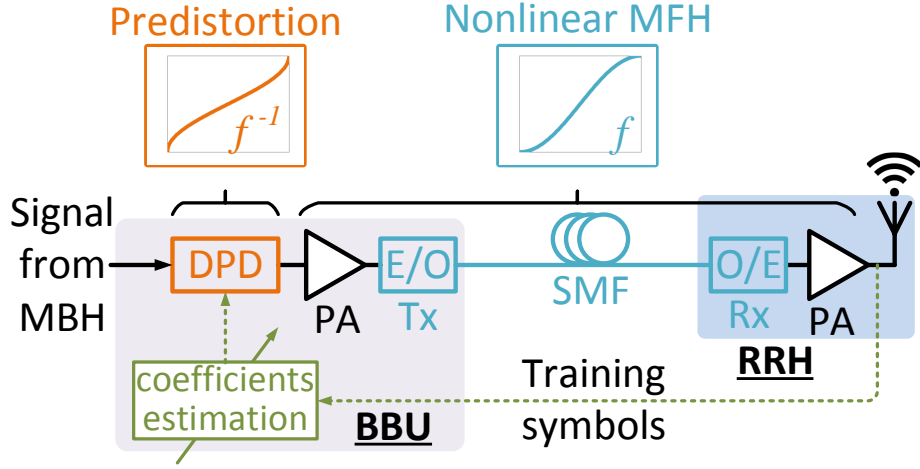


Figure 4.1: Linearization based on digital predistortion for analog MFH.

fibers (SMF). Optical wavelength division multiplexing (WDM) can be exploited to connect multiple RRHs with one BBU to enable centralized signal processing for coordinated joint transmission. The nonlinear impairments of an analog MFH link could be contributed by several devices, including the power amplifier and the electro-optic (E/O) interface of the optical modulator at BBU, and the opto-electric (O/E) interface of photodetector at RRH. A digital predistorter is inserted before the power amplifier in BBU, so that the nonlinear impairments contributed by both the power amplifier, E/O, and O/E interfaces can be compensated. It should be noted that the fiber-optic link can be based on either intensity modulation/direct detection (IM/DD) or coherent transmission, both could be addressed by a digital predistortion. The analog MFH channel response and digital predistorter have two complimentary transfer functions, shown in the insets of Fig. 4.1, whose nonlinear response cancel each other and an overall linearized MFH channel is obtained. In the following experiments, we will verify that the linearized MFH is transparent to different signal waveforms, and works for both single-carrier and multi-carrier mobile signals.

The channel model of a bandwidth-limited nonlinear analog MFH system is pre-

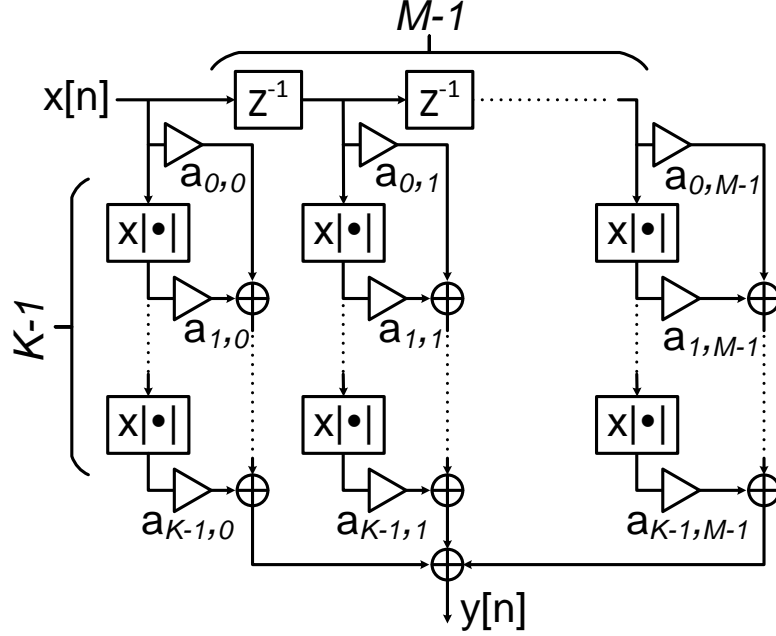


Figure 4.2: Memory polynomial model of analog MFH channel with memory depth of  $M$  and nonlinearity order of  $K$ .

sented in Fig. 4.2, with memory depth of  $M$  and nonlinearity order of  $K$ . Assuming a baseband input signal  $x[n]$ , where  $n$  is the time index, after the nonlinear analog MFH system, the received signal is  $y[n]$ , which is a distorted replica of  $x[n]$ . In general, the transfer function of any bandwidth-limited nonlinear system can be modeled by a polynomial with memory effect, shown in (4.1), where  $y[n]$  is not linearly proportional to  $x[n]$ , but also depends on several high order terms of  $x[n]$ . To keep sign consistency, high order terms are represented by  $x[n] |x[n]|^{k-1}$ , where  $k$  denotes the order of nonlinearity. Meanwhile, due to the bandwidth limitation, there is inter-symbol interference (ISI), which can be captured by the memory effect, i.e., the current output  $y[n]$  is not only determined by current input  $x[n]$ , but also depends on few previous inputs  $x[n - m + 1]$ ,  $m = 1, 2, \dots, M$ . Here  $M$  denotes the memory depth, which is equal to the number of interfering symbols consecutive in the time domain, and also represents the extent of bandwidth limitation in the frequency domain.  $a_{k,m}$  is the

polynomial coefficient of the  $k - th$  order term with memory depth of  $m$ .

$$y[n] = \sum_{k=1}^K \sum_{m=1}^M a_{k,m} \cdot x[n - m + 1] \cdot |x[n - m + 1]|^{k-1} \quad (4.1)$$

In order to compensate the nonlinear impairments of analog MFH, the objective of digital predistortion is to obtain the inverse function of (4.1). A simple solution would be to reverse the roles of input and output, and find the inverse transfer function from output  $y[n]$  to input  $x[n]$ , shown in (4.2).

$$x[n] = \sum_{k=1}^K \sum_{m=1}^M d_{k,m} \cdot y[n - m + 1] \cdot |y[n - m + 1]|^{k-1} \quad (4.2)$$

In our experiments, training symbols were used to estimate the inverse channel response and extract polynomial coefficients of  $d_{k,m}$ . Assuming  $L$  training symbols are used, by reshaping the polynomial coefficients from  $K \times M$  matrix into a  $(K \cdot M) \times 1$  vector, we can rewrite (4.2) in a matrix form  $X = YD$ , where  $X = (x[1], x[2], \dots, x[L])^T$  is a  $L \times 1$  vector,  $Y$  is a  $L \times (K \cdot M)$  matrix, and  $D$  is a  $(K \cdot M) \times 1$  vector, shown in (4.3). Since the number of training symbol  $L$  is much larger than  $K \cdot M$ , (4.3) is a overdetermined equation, polynomial coefficients can be solved in the least square sense. Due to the static and predictable nature of analog MFH, the obtained polynomial coefficients can be used for a long period of time once calibrated by training symbols.

$$\begin{aligned} D[(k-1)M + m] &= d_{k,m} \\ Y[n, (k-1)M + m] &= y[n - m + 1] \cdot |y[n - m + 1]|^{k-1} \\ k &= 1, 2, \dots, K, \quad m = 1, 2, \dots, M \end{aligned} \quad (4.3)$$

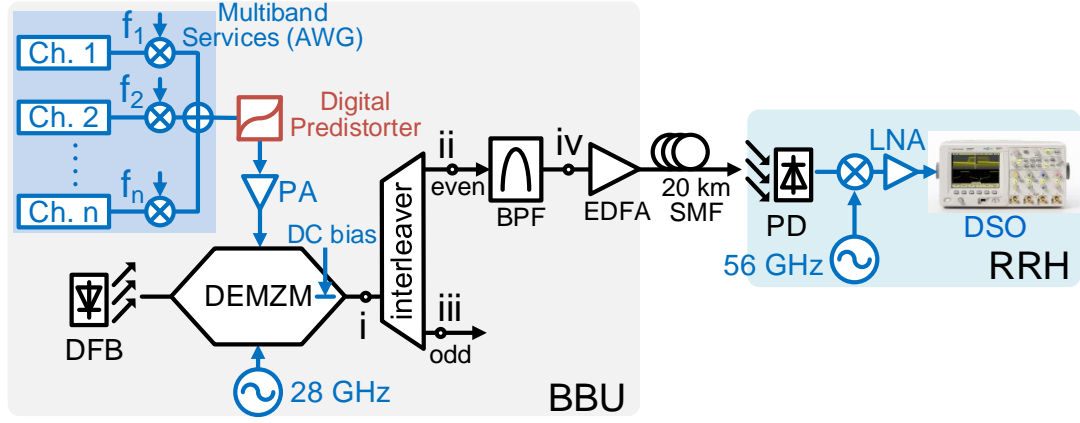


Figure 4.3: Experimental setup of digital predistortion.

### 4.3 Experimental Setup

Fig. 4.3 shows the experimental setup of digital predistortion for an analog MFH network, which is identical with the setup we discussed in Chapter 2 and 3, except that a digital predistorter is included to compensate nonlinear distortions. A detailed explanation of the experimental setup can be found in Chapter 2. A dual-electrode Mach-Zehnder modulator (DEMZM) with half-wave voltage of  $V_\pi = 4.95$  V is used in BBU for both data modulation and RF sideband generation. Multiple bands of mobile signals are generated by an arbitrary waveform generator (AWG) with 2.6-GSa/s sampling rate and 1-GHz analog bandwidth. The AWG output is followed by a power amplifier (PA) to drive one arm of DEMZM. The predistorter is implemented in the digital domain by the AWG, and virtually is inserted before the PA so that the nonlinear impairments contributed by both amplifier and optical modulator can be addressed. The PA has a small signal gain of 26 dB and noise figure of 11 dB. In the experiments, it is verified that PA is the major noise source; whereas nonlinear distortions are contributed by both PA and DEMZM.

It should be noted that digital predistortion is a generic linearization technique,

which not only works with DEMZM in our experiment, but also works for other optical modulation and detection schemes, such as coherent optical OFDM [160–163], OFDMA-PON [164], and other analog MFH systems [165–167].

In any analog optical communication systems, transmission impairments can be contributed by fiber nonlinearities, chromatic dispersion, and modulator nonlinearities. In the case of analog MFH networks, chromatic dispersion and fiber nonlinearities can be neglected due to the limited optical launch power, short fiber distance, and narrow bandwidth of mobile services (less than GHz), and the nonlinear impairments are dominated by power amplifiers and nonlinear electro-optic interfaces of optical modulators. It is worth of noting that memory polynomial can model any nonlinear bandwidth-limited system, not only amplifier and modulators, but also include fiber dispersion and nonlinearities.

#### 4.4 Experimental Results

The nonlinear channel response of analog MFH is mainly contributed by PA and DEMZM, whose nonlinear transfer functions mainly contain odd-order nonlinearities. In our experiments, it is found that an odd-order polynomial with order up to 5 is sufficient to compensate most nonlinear impairments. Furthermore, since the bandwidths of mobile signals ( $< 1$  GHz) are much smaller than the bandwidth limitation of PA (10 GHz) and DEMZM (40 GHz), only very limited memory effect is observed. In experiments, it is verified that both nonlinear XMs of single-carrier signals and subcarrier IMs of multi-carrier signals can be effectively mitigated by a digital predistorter based on 5th order polynomial without memory.

##### 4.4.1 Mitigation of Cross-Modulations

As discussed in Chapter 2, the dominant nonlinear impairments of single-carrier signals are nonlinear XMs, including both intra-band XM between I and Q components



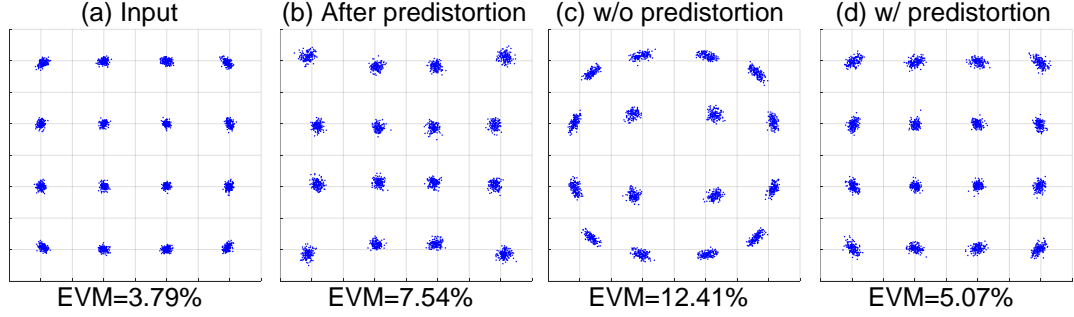


Figure 4.4: Digital predistortion to mitigate intra-band XM for a 16-QAM signal. (a) Input constellation. (b) After predistortion. (c) After MFH w/o predistortion. (d) After MFH w/ predistortion.

of a vector signal, and inter-band XMs between the data modulations of different signal channels. In experiments, we tested a single channel of 16-QAM signal, and two channels of OOK/16-QAM signals, and demonstrated that digital predistortion can mitigate both intra-band and inter-band XMs effectively.

The experimental results of intra-band XM mitigation for a single channel 16-QAM signal are shown in Fig. 4.4. The constellations before and after predistortion are shown in Fig. 4.4(a) and (b), and the constellations after MFH link without and with predistortion are shown in (c) and (d), respectively. Comparing Fig. 4.4(b) and (c), it is observed that the intra-band XM imposes a compression distortion to the constellation, which pushes the outer symbols inward; whereas the predistortion makes a stretching distortion, pulling the outer symbols outward. These two opposite effects will cancel each other as the signal propagate through the MFH link, and an overall linear channel response is obtained. Comparing (c) and (d), with the help of predistortion, the received EVM is improved from 12.41% to 5.07%, which is close to the noise limit of the experimental setup.

The experiments results of inter-band XM mitigation between two channels of OOK signals are shown in Fig. 4.5. We intentionally use two OOK signals with unequal input amplitudes ( $V_1 = 0.1V_\pi$ ,  $V_2 = 0.4V_\pi$ ), so that Ch. 2 is much stronger

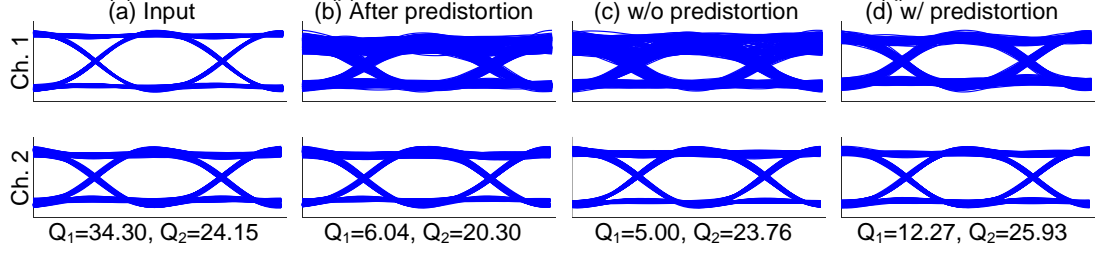


Figure 4.5: Digital predistortion to mitigate inter-band XM between two OOK signals. (a) Input eye diagrams. (b) After predistortion. (c) After MFH w/o predistortion. (d) After MFH w/ predistortion.

than Ch. 1, and there is severe inter-band XM from Ch. 2 to Ch. 1. In Fig. 4.5(c), the eye diagram of Ch. 1 is severely degraded by inter-band XM with its Q-factor reduced to  $Q_1 = 5$ . In (b), predistorter introduces an opposite inter-band XM to Ch. 1 ( $Q_1 = 6.04$ ), and when cascaded with the MFH link, an overall linear channel response is achieved. In (d), the received eye diagram of Ch. 1 is significantly improved with Q-factor enhanced to 12.27. Since Ch. 2 only experiences very limited amount of inter-band XM,  $Q_2$  remains above 20 along the MFH link, slightly improved from 23.76 to 25.93 with the help of predistortion.

To demonstrate its effectiveness to simultaneously mitigate both intra-band and inter-band XMs, digital predistortion is also applied to two channels of 16-QAM signals. The input amplitudes of two channels are intentionally chosen to be unequal ( $V_1 = 0.25V_\pi$ ,  $V_2 = 0.15V_\pi$ ), so that the strong Ch. 1 only suffers from intra-band XM, and the weak Ch. 2 is dominated by inter-band XM. The experimental results are shown in Fig. 4.6. In (c), the constellation of Ch. 1 shows a compression distortion caused by intra-band XM, and the constellation of Ch. 2 experiences a scaling distortion induced by inter-band XM. Their EVMs are degraded to 8.4% and 11.27%, respectively. In Fig. 4.6(b), predistortion stretches the constellations of both signals to compensate intra-band XM, and also imposes a scaling distortion on the constellation of Ch. 2 to cancel out the inter-band XM from Ch. 1. Thanks to predistortion,

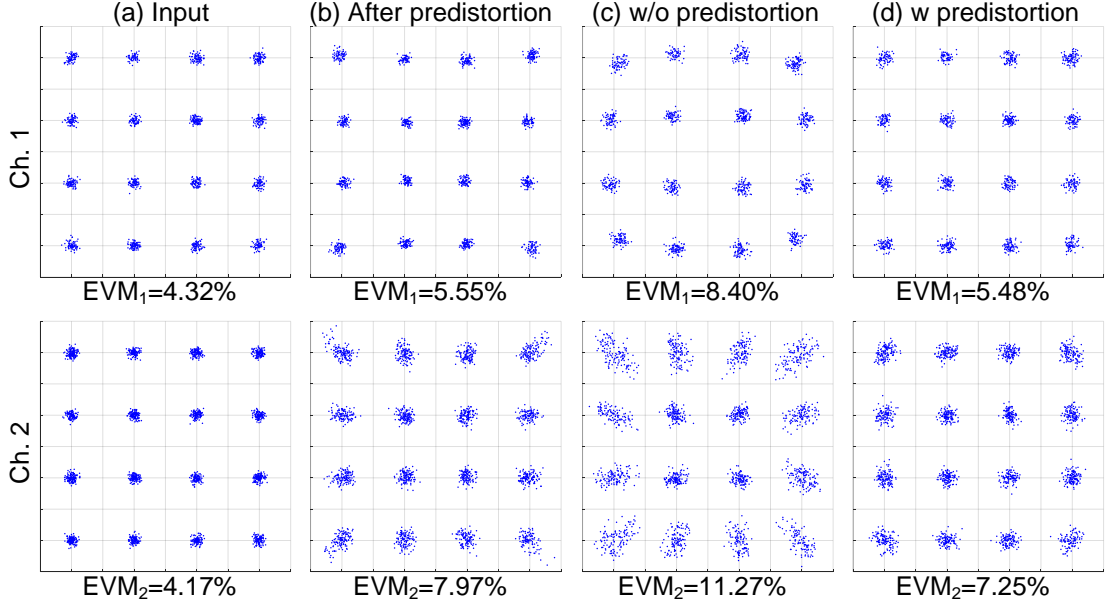


Figure 4.6: Digital predistortion to mitigate both intra-band and inter-band XMs between two 16-QAM signals. (a) Input constellations. (b) After predistortion. (c) After MFH w/o predistortion. (d) After MFH w/ predistortion.

clear constellations of both signals can be obtained in (d), and their EVMs are decreased to 5.48% and 7.25%, respectively.

#### 4.4.2 Mitigation of Subcarrier Intermodulations

Three experimental cases in Chapter 3 (Case I, II, VI) are selected as representative examples to verify the effectiveness of digital predistortion to mitigate both intra-band and inter-band subcarrier IMs. Details of these three cases can be found in Section 3.4 in Chapter 3, and their experimental parameters are listed in Table 3.2.

In Case I, there is only one OFDM channel which suffers from intra-band IMs. In Case II, there are two OFDM signals from the same radio access technology (RAT), which have the same subcarrier spacing (24.4 kHz) and bandwidth (50 MHz) and suffer from both intra-band and inter-band IMs. Case II corresponds to scenarios of multiband or multichannel operations, such as LTE carrier aggregation and 802.11ac

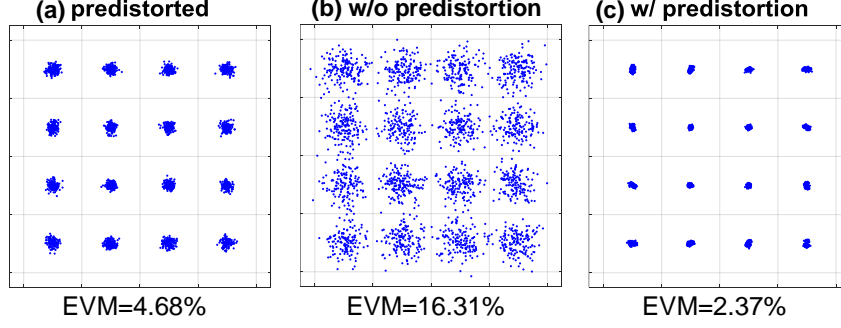


Figure 4.7: Digital predistortion to mitigate intra-band IMs (Case I). (a) Constellation after predistortion. (b) After MFH w/o predistortion. (c) After MFH w/ predistortion.

channel bonding. In Case VI, two OFDM signals from different RATs are transmitted together in a MFH network. They have drastically different subcarrier spacings and bandwidths, so that the subcarrier spacing of a broadband signal is even larger than the whole bandwidth of the narrowband signal. This extreme case occurs when narrowband signals, e.g., 802.11ah or LTE with bandwidths only 1-2 MHz, are transported together with broadband signals such as 802.11ad, aj or UWB, whose subcarrier spacing can be up to 2-5 MHz. In Case VI, inter-band IMs between two signals degenerate to XMs because from the point of view of the broadband signal, the bandwidth of the narrowband signal is even smaller than one subcarrier spacing and can be reasonably considered as a single-carrier signal, and according to Chapter 2, a single-carrier signal introduces inter-band XM to its coexistent signals.

The experimental results of Case I are shown in Fig. 4.7, where intra-band subcarrier IMs are successfully mitigated. With the input root-mean-square (RMS) amplitude of 60 mV, the OFDM signal suffers from severe intra-band IMs, and its EVM is degraded to 16.32%, as shown in Fig. 4.7(b). With the help of predistortion, clear constellation is obtained with EVM reduced to 2.37%, which approaches the noise limit of our experimental setup.

The experimental results of Case II are shown in Fig. 4.8, where both intra-band

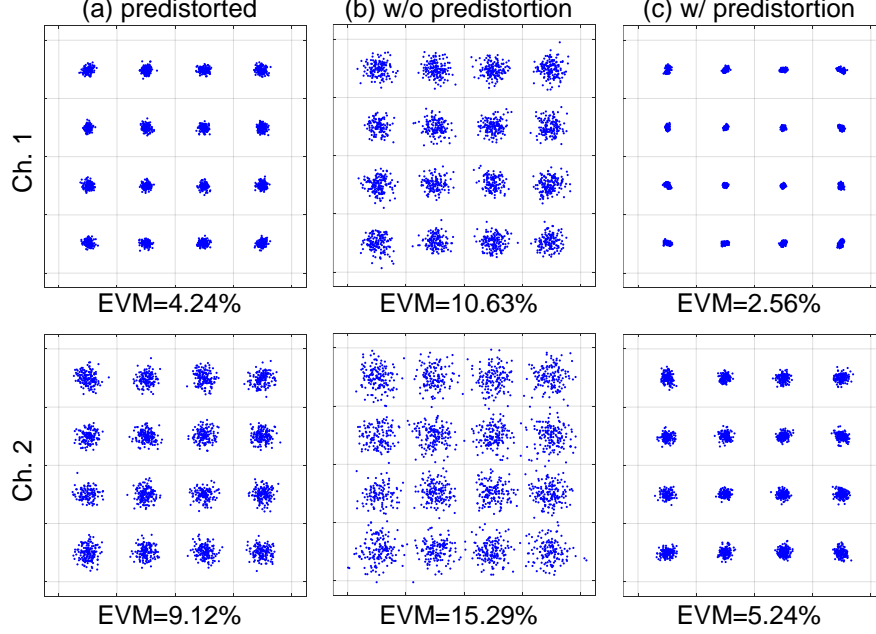


Figure 4.8: Digital predistortion to mitigate inter-band IMs (Case II). (a) Constellations after predistortion. (b) After MFH w/o predistortion. (c) After MFH w/ predistortion.

and inter-band subcarrier IMs are successfully mitigated. We intentionally use two OFDM signals from the same RAT but with unequal input power. Ch. 1 has larger input amplitude ( $V_1 = 45$  mV) than Ch. 2 ( $V_2 = 9$  mV), so the impairments of Ch. 1 are mainly contributed by intra-band IMs among its own subcarriers; whereas the impairments of Ch. 2 are dominated by inter-band IMs from Ch. 1. The constellations of both channels without and with predistortion are shown in Fig. 4.8(b) and (c). It can be observed that digital predistortion is able to mitigate both intra-band and inter-band IMs and EVMs of both channels are improved from 10.63% and 15.29% to 2.56% and 5.24%, respectively.

The experimental results of Case VI are shown in Fig. 4.9. Two OFDM signals from different RATs with drastically different bandwidths (5, 100 MHz) and subcarrier spacing are transported together with unequal input powers ( $V_1 = 45$  mV,  $V_2 = 9$  mV). Due to its narrow bandwidth, Ch. 1 is immune from inter-band IMs,

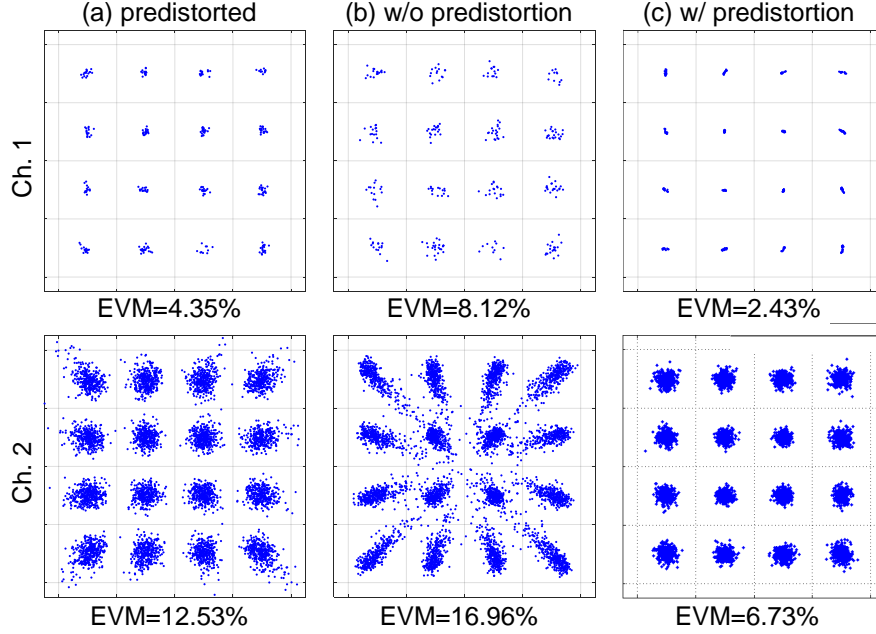


Figure 4.9: Digital predistortion to mitigate inter-band IMs (Case VI). (a) Constellations after predistortion. (b) After MFH w/o predistortion. (c) After MFH w/ predistortion.

since any inter-band subcarrier IMs from Ch. 2 are always located out of Ch. 1. Therefore we use large input amplitude for Ch. 1, so that Ch. 1 only suffers from intra-band IMs. Ch. 2 can have both intra-band and inter-band IMs, and we choose a small input amplitude of Ch. 2 to make sure its nonlinear impairments are mainly contributed by inter-band IMs. As discussed in Section 3.5.5 in Chapter 3, from the point of view of Ch. 2, Ch. 1 can be considered as a single-carrier signal since its bandwidth is smaller than the subcarrier spacing of Ch. 2. The inter-band IMs from Ch. 1 to Ch. 2 degenerate to a baseband XM effect, and introduce a scaling distortion to the constellation of Ch. 2. As shown in Fig. 4.9(b), without predistortion, the received EVM for both signals are 8.12% and 16.96%, respectively. With the help of predistortion, both intra- and inter-band IMs, and the degenerated baseband XM can be compensated. In Fig. 4.9(c), EVMs are improved to 2.43% and 6.73%.

## 4.5 Summary

In Chapter 2 and 3, we have demonstrated that the dominant nonlinear impairments of single-carrier signals are XMs; whereas the dominant impairments of multi-carrier signals are IMs. In this chapter, we demonstrated a digital predistorter based on memory polynomial model, which can compensate both XMs and IMs with a simple predistorter inserted before the transmitter in BBUs. In experiments, both intra-band and inter-band XMs and IMs are effectively mitigated by a 5th order polynomial predistorter, and the received signal qualities after analog MFH are significantly improved. As a waveform-agnostic linearization technology, digital predistortion is transparent to different RATs and signal waveforms. It can be applied to both single-carrier and multi-carrier signals, and can work with not only 4G-LTE but also 5G new radio waveforms.

## CHAPTER 5

### DIGITAL MOBILE FRONTHAUL BASED ON DELTA-SIGMA MODULATION

#### 5.1 Introduction

In the next generation mobile data networks, to accommodate mobile services from various RATs, both analog and digital MFH architectures have been investigated. Analog MFH based on RoF technologies features simple, low-cost implementations, high spectral efficiency, and transparency to different RATs and signal waveforms, but it is susceptible to nonlinear transmission impairments due to the continuous waveforms of multi-carrier mobile signals, especially given the factor of multi-RAT multi-service coexistence in 5G mobile data networks. The nonlinear impairments of analog MFH have been investigated in Chapter 2 and 3, and linearization techniques based on digital predistortion have been demonstrated in Chapter 4. However, it is not easy to dynamically track the MFH channel response and compensate its nonlinear distortions, especially given the factor of time-varying broadband data traffic from various RATs.

Digital MFH, on the other hand, sample and quantize the continuous envelopes of mobile signals using a digitization interface, and transport the digitized bit streams by leveraging mature digital optical communication technologies. For 5G mobile data networks, it is of interest to digitize mobile signals from different RATs and deliver them together via digital fiber-optic links of existing passive optical networks (PONs). With the help of digitization, digital MFH offers high signal fidelity and excellent tolerance against transmission impairments with the penalty of relatively low spectral efficiency. Once error-free transmission is achieved, the received signal



quality can be isolated from transmission performance.

The most popular digitization interface, CPRI, has low spectral efficiency and requires tremendous bandwidth after digitization [36], and has become the data rate bottleneck of the next generation digital MFH networks, especially given the fact of rapidly growing LTE carrier aggregation (CA). Standardized by 3GPP release 10, LTE CA initially allows aggregation of 5 component carriers (CCs) [20], and then quickly expanded to 32 CCs by 3GPP release 13 [21], which consumes up to 40-Gb/s fronthaul capacity if digitized by CPRI and cannot be supported by any existing optical/wireless access networks. To circumvent the data rate bottleneck of CPRI and increase MFH capacity, in this chapter, we demonstrate a promising solution to replace the digitization interface from CPRI to delta-sigma modulation, which trades the quantization bits for sampling rate so that both the spectral efficiency and capacity of digital MFH can be improved. This chapter is organized as follows. Section II explains the operation principles of digitization interfaces for digital MFH networks, including both CPRI and delta-sigma modulation. Section III presents the experimental setup. Section IV presents the experimental design and results. Finally, Section V concludes the chapter.

## 5.2 Operation Principles

A cloud-radio access network (C-RAN) is shown in Fig. 5.1(a) with three different MFH implementations presented in (b-d). (b) shows an analog MFH architecture based on RoF technologies, where mobile signals are aggregated in BBU and delivered to RRH in their analog waveforms without digitization. (c) and (d) show two digital MFH architectures using different digitization interfaces based on CPRI and delta-sigma modulation, respectively, and both of them digitize mobile signals into bits in the BBU, and transport digitized bit streams from BBU to RRHs via mature digital optical communication technologies.

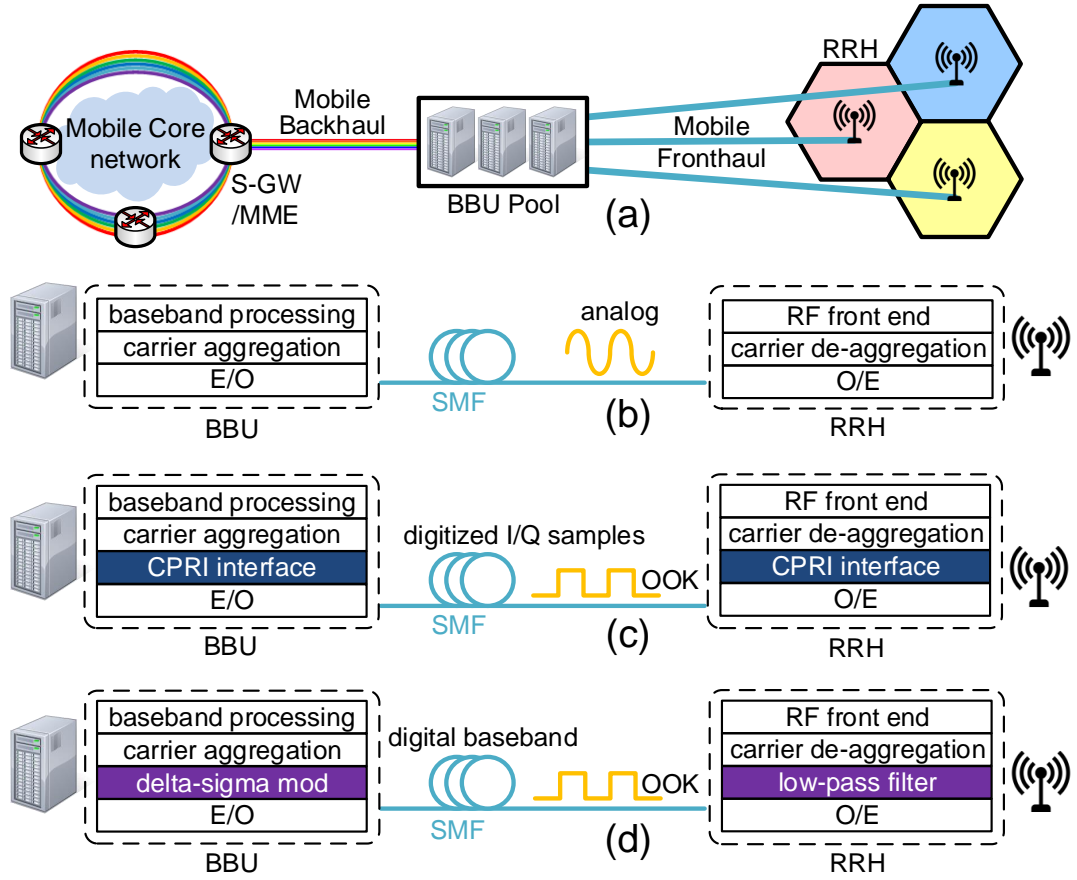


Figure 5.1: Three MFH architectures. (a) C-RAN. (b) RoF-based analog MFH. (c) CPRI-based digital MFH. (d) Delta-sigma modulation-based digital MFH.

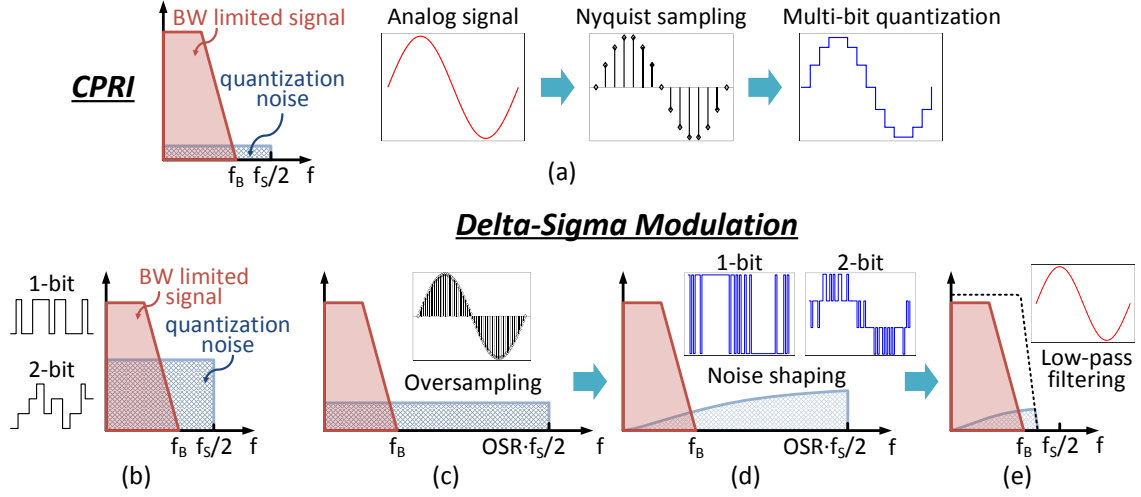


Figure 5.2: Operation principles of two digitization interfaces. (a) CPRI. (b-e) Delta-sigma modulation. (b) Only one-bit or two-bit quantization. (c) Oversampling to extend Nyquist zone. (d) Noise transfer function to push quantization noise out of signal band. (e) Low-pass filtering to eliminate noise and retrieve signal.

### 5.2.1 Common Public Radio Interface

The operation principles of two digitization interfaces are illustrated in Fig. 5.2. CPRI exploits a Nyquist ADC with sampling rate of 30.72 MSa/s, and uses 15 quantization bits and one control bit per sample, as shown in Fig. 5.2(a). The quantization noise of a Nyquist ADC is evenly distributed in the Nyquist zone in frequency domain, which can be approximated by Gaussian white noise [176]. To reduce the quantization noise and increase SNR of digitized signal, large number of quantization bits are exploited, leading to low spectral efficiency and tremendous bandwidth after digitization, making CPRI become the data rate bottleneck of 5G digital MFH networks.

The standard data rate options are listed in Table 5.1. Line coding of 8b/10b or 64b/66b is used for DC balance, disparity check, and to ensure sufficient 0/1 transitions for clock recovery. In option 1, each I or Q component of a 20-MHz LTE CC consumes fronthaul capacity of  $30.72\text{MSa/s} \times 16\text{bit/Sa} \times 10/8 = 614.4\text{Mb/s}$ ; in option 2, each 20-MHz LTE CC consumes 1.23 Gb/s (include both I and Q); for 10-

Table 5.1: CPRI data rate options

Option	Line coding	LTE carriers	Examples	Bit rate (Mb/s)
1	8b/10b	0.5	Only I or Q component	614.4 $491.52 \times 10/8$
2	8b/10b	1	One 20-MHz LTE CC	1228.8 $491.52 \times 10/8 \times 2$
3	8b/10b	2	2 CA / 2x2 MIMO	2457.6 $491.52 \times 10/8 \times 4$
4	8b/10b	2.5	Only I or Q, 5 CA	3072 $491.52 \times 10/8 \times 5$
5	8b/10b	4	4x4 MIMO or 2 CA + 2x2 MIMO	4915.2 $491.52 \times 10/8 \times 8$
6	8b/10b	5	5 CA	6144 $491.52 \times 10/8 \times 10$
7	8b/10b	8	8x8 MIMO or 2 CA + 4x4 MIMO	9830.4 $491.52 \times 10/8 \times 16$
7A	64b/66b	8	8x8 MIMO or 4 CA + 2x2 MIMO	8110.08 $491.52 \times 66/64 \times 16$
8	64b/66b	10	5 CA + 2x2 MIMO	10137.6 $491.52 \times 66/64 \times 20$
9	64b/66b	12	3 CA + 4x4 MIMO	12165.12 $491.52 \times 66/64 \times 24$

- CPRI: common public radio interface.
- CA: carrier aggregation.
- CC: component carrier.
- MIMO: multiple input multiple output.
- CPRI uses a sampling rate of 30.72 MSa/s to samples each 20-MHz LTE carrier and 16 bits for each sample (15 quantization bits and one control bit), so each I or Q component consumes  $30.72\text{MSa/s} \times 16\text{bits/Sa} = 491.52\text{Mb/s}$  fronthaul capacity before line coding.

Gb/s PON, only 8 LTE CCs can be accommodated (option 7). In order to support 32 CA of 3GPP release 13, up to 40-Gb/s fronthaul capacity is required, which cannot be supported by existing optical/wireless access networks. It is worth noting that CPRI digitizes each LTE carrier individually, and it works in a symmetric way for downstream and upstream. Both BBU and RRH are equipped with a Nyquist ADC as the CPRI interface. CPRI has a fixed chip clock rate 3.84 MHz, and by choosing different integer multiples of chip clock, it can accommodate several different RATs, such as UMTS (CPRI V1 and V2), WiMAX (V3), LTE (V4), and GSM (V5).

### 5.2.2 Delta-Sigma Modulation

Delta-sigma modulation, on the other hand, trades the quantization bits with sampling rate, which exploits a high sampling rate but only needs few (one or two) quantization bits. Due to the limited number of quantization bits, Nyquist sampling would lead to significant quantization noise, as shown in Fig. 5.2(b). So oversampling is needed for delta-sigma modulation to extend the Nyquist zone, so that the quantization noise is spread over a wide frequency range and in-band noise can be reduced, as shown in Fig. 5.2(c). Moreover, noise shaping technique is exploited to push the quantization noise out of the signal band, so that signal and noise are essentially separated in the frequency domain. For example, in Fig. 5.2(d), the noise transfer function of a low-pass delta-sigma modulator acts as a low-pass filter to signal and a high-pass filter to noise, so after digitization, the output of the delta-sigma modulator becomes a high speed bit stream at the oversampling rate, whose low frequency components duplicate the analog input, while high frequency components are contributed by quantization noise, as shown in 5.2(d). One-bit quantization generates a digital output of OOK signal (0/1), where the density of “1”s is proportional to the amplitude of analog input. When the input amplitude is close to the maximum, the output OOK signal contains almost all “1”s; when the input close to minimum, the output

contains all “0”s. For intermediate input amplitude, there are equal populations of “0”s and “1”s.

This feature is very different from Nyquist ADC, which samples analog signals at their Nyquist frequencies and each sample is quantized individually. Oversampling ADC, on the other hand, uses a sampling rate much higher than the Nyquist frequency of analog input, and samples are digitized consecutively. The output of an oversampling ADC is a high data rate bit stream, whose amplitude follows the input amplitude after a weighted moving average. Since averaging is essentially a low-pass filtering, a LPF can smooth out the high frequency oscillation of the bit stream, and retrieve the original analog input. This can be explained intuitively in the frequency domain, as shown in Fig. 5.2(e). In RRH, a low-pass filter eliminates the out-of-band noise, which essentially smooth out the oscillation of bit stream, and filters out the original signal. Note that the retrieved signal has an uneven noise floor due to the noise shaping.

In our experiments, we use a 10-GSa/s delta-sigma modulator to digitize 32 LTE CCs into a 10-Gb/s OOK or 10-Gbaud PAM4 signal, and transmitted it over a single- $\lambda$  optical IM/DD link. Compared with CPRI option 7 (10 Gb/s for 8 LTE CCs), the MFH capacity is increased by four times. As a waveform agnostic interface, delta-sigma modulator can work with not only OFDM signals, such as 4G-LTE, Wi-Fi, WiMAX, but also 5G multi-carrier waveforms. In Section III, its 5G compatibility will be verified by filter bank multi-carrier (FBMC) signals. A detailed comparison of three MFH technologies is summarized in Table 5.2.

CPRI works in a symmetric way for downstream and upstream, and both BBU and RRH are equipped with a Nyquist ADC interface. Delta-sigma modulation, however, digitizes mobile signals after carrier aggregation, and is able to work in an asymmetric way by leveraging the asymmetric bandwidth requirements for downstream and upstream. Due to the tree architecture of MFH and large number of RRHs, each

BBU is shared by multiple RRHs, so the downstream bandwidth from BBU to RRHs is much wider than the upstream bandwidth from each RRH to BBU. Therefore, for downstream, a high speed oversampling ADC is exploited in BBU, and each RRH only needs a low-cost filter as DAC to retrieve the desired mobile signals; for upstream, each RRH is equipped with a low speed delta-sigma modulator thanks to the small upstream bandwidth. Given the large number of RRHs, by leveraging the simplified DAC design based on low-cost filters and asymmetric downstream/upstream bandwidths, delta-sigma modulation can significantly reduce the system cost of the next generation digital MFH networks.

Moreover, CPRI digitizes each mobile signal individually, and multiplexes digitized signals using time-division-multiplexing (TDM). Although it can accommodate several RATs by choosing different multiples of chip clock rate (3.84 MHz), synchronization will still be an issue to multiplex services from different RATs. On the other hand, delta-sigma modulation uses frequency division multiplexing (FDM) to aggregate services from different RATs before digitization, and the synchronization problem for multi-RAT multi-service coexistence could be circumvented.

Table 5.2: Comparison of three MFH technologies

	Analog MFH	Digital MFH	
Interface	RoF	CPRI	Delta-sigma modulation
ADC	N/A	Nyquist ADC	Oversampling ADC
Sampling rate		30.72 MSa/s	10 GSa/s
Quantization bits		15	1 or 2
DAC		Nyquist DAC	Filter
Fronthaul capacity per 20-MHz LTE CC	18.02-30.72 MHz <sup>1</sup>	1.23 Gb/s <sup>2</sup>	312.5 Mb/s <sup>3</sup>
Carrier aggregation	Analog FDM	TDM after digitization	FDM before digitization
Multi-RAT compatibility	RAT transparent	UMTS, WiMAX, LTE, GSM Synchronization issue	RAT transparent
Pros	Simple Low cost High spectral efficiency	Digital IM/DD, PON-compatible Robust against nonlinearities Low-cost	Digital IM/DD, PON-compatible Robust against nonlinearities MFH capacity $\times 4$
Cons	Susceptible to nonlinear impairments	Data rate bottleneck Fixed chip rate 3.84MHz	Expensive high sampling rate DSP
References	[53–58]	[36, 168–171]	[201–204]

1. Each 20-MHz LTE CC has 2048 subcarriers with subcarrier spacing of 15 kHz (total bandwidth  $15\text{kHz} \times 2048 = 30.72\text{MHz}$ ), within which there are 1201 active subcarriers carrying data (data bandwidth  $15\text{kHz} \times 1201 = 18.02\text{MHz}$ ), others are set to zeroes for guard band.
2. See CPRI data rate option 2 in Table 5.1.
3. 32 LTE CCs are accommodated with a 10-Gb/s MFH link, each CC consumes  $10\text{Gb/s} \div 32 = 312.5\text{Mb/s}$ .



There have been quite a few works demonstrated about high speed delta-sigma modulators with sampling rates in the range of 3-8 GSa/s [185–190], however, there is no 10-GSa/s delta-sigma modulator reported. For proof-of-concept experiments, we use a 10-GSa/s modulator which is realized by an arbitrary waveform generator (AWG). But for real implementations, to alleviate the ADC speed limit, a 10-GSa/s delta-sigma modulator can be replaced by four parallel 2.5-GSa/s modulators, or eight 1.25-GSa/s modulators, and the output bit streams from multiple modulators are interleaved together in the time domain by time-division-multiplexing (TDM) technology. In this way, the sampling rate of each modulator is reduced by four/eight times, while keeping the overall fronthaul capacity unchanged. A 10-GSa/s modulator with oversampling ratio (OSR) of 8 can digitize 32 LTE CCs with the signal band ranging from 0 to 625 MHz; a 2.5-GSa/s modulator with the same OSR is able to digitize 8 LTE CCs with signal band of 0-156.25 MHz, so four modulators in total still support 32 LTE CCs.

### 5.3 Experimental Setup

The experimental setup is shown in Fig. 5.3(a). We use a 10G-PON compatible architecture with BBU located in the optical line terminal (OLT) and RRHs in optical network units (ONUs). In BBU, 32 LTE CCs are aggregated by DSP with sampling rate at 1.25 GSa/s, then fed into a delta-sigma modulator with OSR of 8, where the analog input is first oversampled to 10 GSa/s, and then digitized into a 10-Gb/s OOK or 10-Gbaud PAM4 signal by one-bit or two-bit quantization, respectively. With  $\text{OSR} = 8$ , in order to keep the analog input signal real, the available bandwidth to accommodate LTE signals is 625 MHz. A 1554 nm DFB laser is used in OLT, followed by a Mach-Zehnder modulator (MZM). After 25-km single-mode fiber (SMF), a 10-GHz photodetector in ONU receives the OOK or PAM4 signal, captured by a real-time digital storage oscilloscope (DSO). In our experiments, delta-sigma modulation was

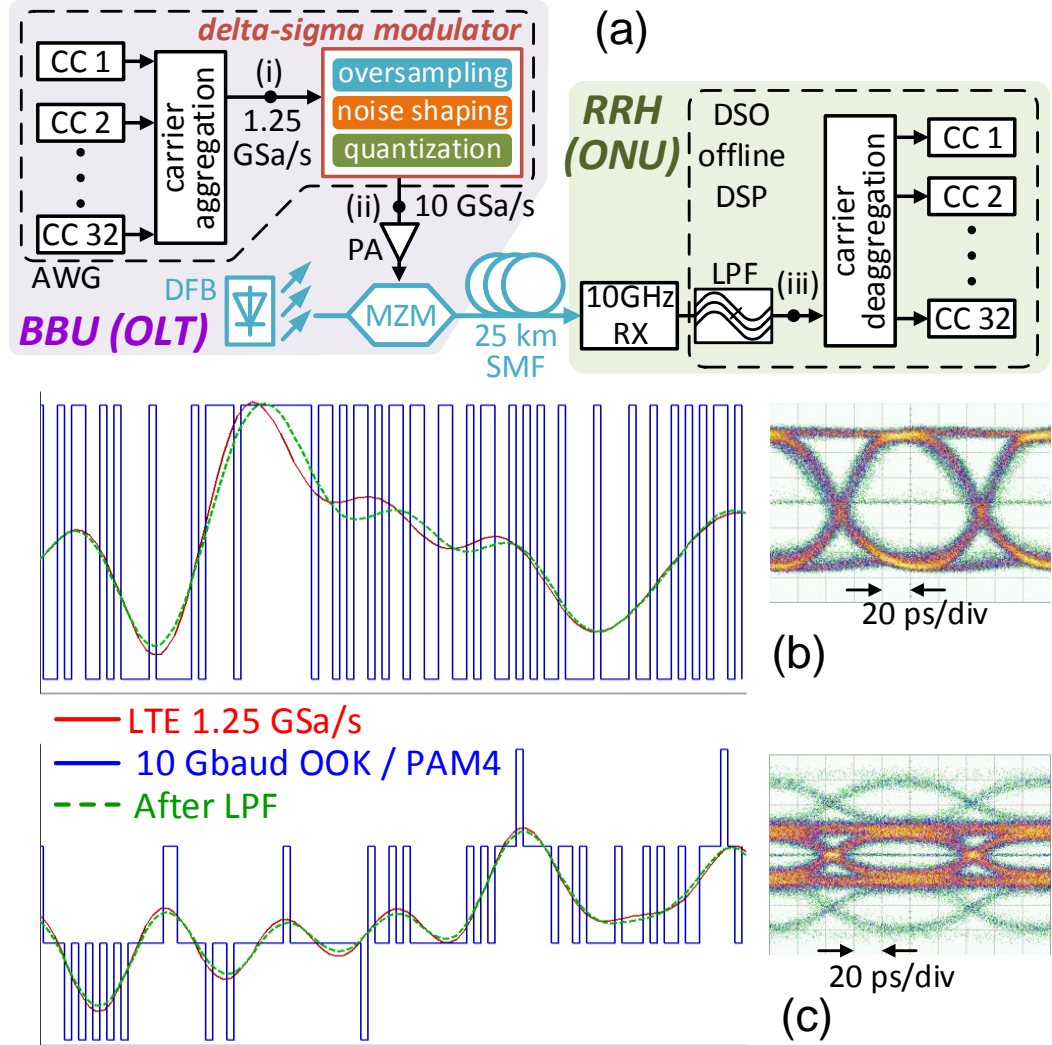


Figure 5.3: (a) Experimental setup. (b, c) Signal waveforms and eye-diagram of one/two-bit digitization: input analog signal at point i (red); 10-Gbaud OOK/PAM4 at point ii (blue); retrieved analog signal at point iii (green).

realized by a Tektronix 7122C AWG.

The measured waveform and eye diagrams of one-bit quantization are shown in Fig. 5.3(b). At point i, the input analog signal before delta-sigma modulator is plotted in red; at point ii, the output OOK signal after delta-sigma modulator is plotted in blue; at point iii, the retrieved LTE signal after LPF in RRH is plotted in green. The difference between the original (red) and retrieved (green) signals is caused by quantization noise. Results of two-bit quantization are shown in Fig. 5.3(c), where the difference between the original (red) and retrieved (green) waveforms are much smaller than Fig. 5.3(a) due to the reduced quantization noise contributed by the additional quantization bit. The eye diagrams of OOK and PAM4 are shown in the insets, where the central dots are caused by zero-padding of AWG between successive data patterns. The PAM4 eye diagram has unequal intensities of  $\pm 1$  and  $\pm 3$  levels, which is because OFDM-based signal has Gaussian distribution, so after digitization, there are much more  $\pm 1$  samples than  $\pm 3$  samples.

## 5.4 Experimental Results

Table 5.3 lists five experimental cases we designed to evaluate the performance of delta-sigma modulation to replace CPRI as a new digitization interface of digital MFH networks. By definition, the order of a delta-sigma modulator is the number of cascaded integrators, resonators or feedback loops used in the modulator [179], which also equals to the number of zeroes or poles of the noise transfer function. After noise shaping, there is a quantizer at the output of the delta-sigma modulator, whose output levels are determined by the number of quantization bits, e.g., a  $\log_2 N$ -bit quantizer outputs  $N$  levels, so an one-bit quantizer outputs an OOK signal, and a two-bit quantizer outputs a PAM4 signal.

In experiments, Case I and II use a simple second-order one-bit delta-sigma modulator based on a cascade-of-resonators feedforward (CRFF) structure, whose noise

Table 5.3: Experimental designs of delta-sigma modulation-based digital MFH

Case	I	II	III	IV	V
Order	2	2	4	4	RoF-based analog MFH
Noise transfer function	$\frac{(z-1)^2}{(z^2-1.23z+0.44)}$		$\frac{(z^2-1.98z+1)(z^2-1.88z+1)}{(z^2-1.27z+0.42)(z^2-1.50z+0.69)}$		
Bit number	1	1	1	2	
Digital waveform	OOK	OOK	OOK	PAM4	
Applications	32 LTE 64-QAM x 18 16-QAM x 14	30 FBMC 256-QAM x 10 64-QAM x 8 16-QAM x 6 QPSK x 6	32 LTE 256-QAM x 16 64-QAM x 16	32 LTE 1024-QAM x 10 256-QAM x 22	24 LTE 64-QAM x 24
Figures	Fig. 5.5	Fig. 5.6	Fig. 5.8	Fig. 5.9	Fig. 5.11

transfer function is shown in Table 5.3. It has two degenerated zeroes both located at DC ( $f = 0, z = 1$ ). By using this modulator, digitization of 32 carrier aggregated LTE signals and 30 FBMC signals is demonstrated in Case I and II, respectively. Due to low modulation order and unoptimized noise shaping, Case I and II suffer from uneven noise floor and large EVM penalty at high-frequency component carriers (CCs) due to severe quantization noise at these frequencies. Pre-emphasis technique is used to improve the performance of high-frequency CCs by boosting their signal powers, but leading to unequal wireless transmission power.

In Case III and IV, a fourth-order CRFF delta-sigma modulator is designed with zero-spreading technique to move the zeroes away from DC, so that quantization noise is more evenly distributed in the signal band. Both one-bit and two-bit digitization are realized in Case III and IV, respectively. With the help of increased modulation order, EVM performance of all 32 LTE CCs are improved, and high order modulation formats, such as 256 and 1024-QAM, can be supported. Using delta-sigma modulation as the digitization interface of digital MFH networks, carrier aggregation of 32 LTE CCs within a 10G-PON optical IM/DD link was implemented, so 3GPP release 13

Table 5.4: 3GPP EVM specifications

Modulation formats	QPSK	16-QAM	64-QAM	256-QAM	1024-QAM
EVM (%)	17.5	12.5	8	3.5	1*

\* EVM requirement of 1024-QAM has not been specified by 3GPP yet.

can be supported in a 10G-PON system. Compared with CPRI, which only supports 8 LTE CCs within a 10-Gb/s MFH link, the MFH capacity is increased by four times without significant EVM penalty.

EVM requirements of four LTE modulation formats (QPSK, 16-QAM, 64-QAM, and 256-QAM) has been specified by 3GPP release 12 [208], as listed in Table 5.4. 3GPP has not specified the EVM requirement of 1024-QAM yet, and we use 1% as a temporary criterion. It should be noted that these EVM specifications are performance criterion of MFH links from BBU up to RRH, excluding the wireless air transmission of LTE signals [209].

Low-pass delta-sigma modulation are used in Case I-IV, where signals are located in the low-frequency end and quantization noise at high-frequency end. At RRH, a LPF eliminates the out-of-band noise and retrieves the original analog signal, and an IF/RF conversion is needed to up-convert the mobile signals to their wireless transmission frequencies before feeding to air interface. To make a fair comparison with analog MFH, we design Case V where 24 LTE CCs each carrying 64-QAM are aggregated together and transmitted in their analog waveform using RoF technology. The experimental setup of Case V is similar to Fig. 5.3 without the delta-sigma digitization interface.

#### 5.4.1 Case I

In Case I and II, we use a simple second-order one-bit delta-sigma modulator based on CRFF structure. Its noise transfer function is shown in Table 5.3, and the Z-domain

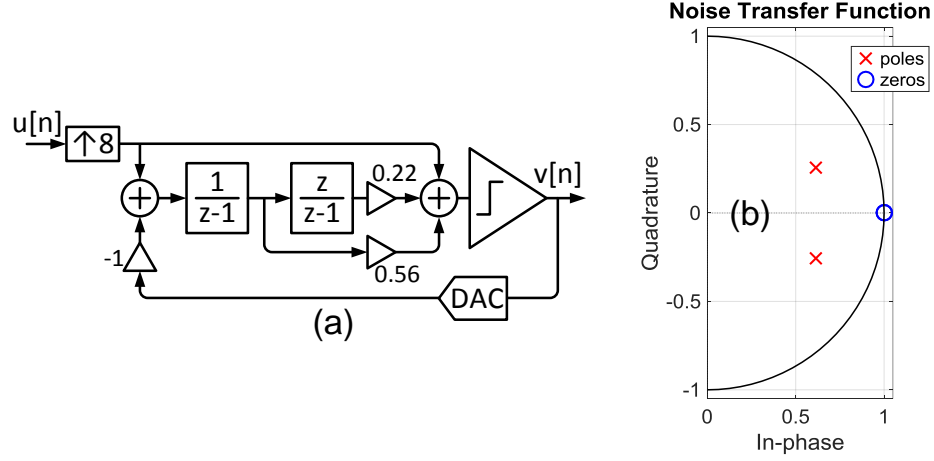


Figure 5.4: Second-order delta-sigma modulator based on CRFF structure (Case I and II). (a) Z-domain block diagram. (b) Zeroes and poles of noise transfer function.

block diagram is presented in Fig. 5.4(a). Fig. 5.4(b) illustrates the zeroes and poles of the noise transfer function. There are two degenerated zeroes both located at DC ( $f = 0, z = 1$ ). Since quantization noise achieve their minimum at zeroes of the noise transfer function, LTE CCs close to DC have smaller quantization noise than those at high frequencies.

The experimental results of Case I are shown in Fig. 5.5. 32 LTE CCs are aggregated within a single- $\lambda$  10-Gb/s OOK link, with 18 CCs carrying 64-QAM, and 14 CCs carrying 16-QAM. Electrical spectra of 32 CCs after delta-sigma modulation are shown in Fig. 5.5(a) and (b), where LTE CCs are aggregated in the low-frequency end and quantization noise pushed to the high-frequency end. (b) is a zoom-in of (a). Each LTE CC has 20-MHz bandwidth with 1200 data-carrying subcarriers. Subcarrier spacing of 15.26-kHz is used to accommodate the sampling rate of our AWG, and 763 kHz guard band is inserted between neighboring CCs. Thanks to the digitization, 32 LTE CCs can be aggregated closely without severe inter-carrier interferences. EVMs of all 32 CCs are shown in Fig. 5.5(c), where 18 CCs have  $\text{EVM} < 8\%$  to support 64-QAM and the rest 16 CCs have  $\text{EVM} < 12.5\%$  to support 16-QAM. EVMs of all

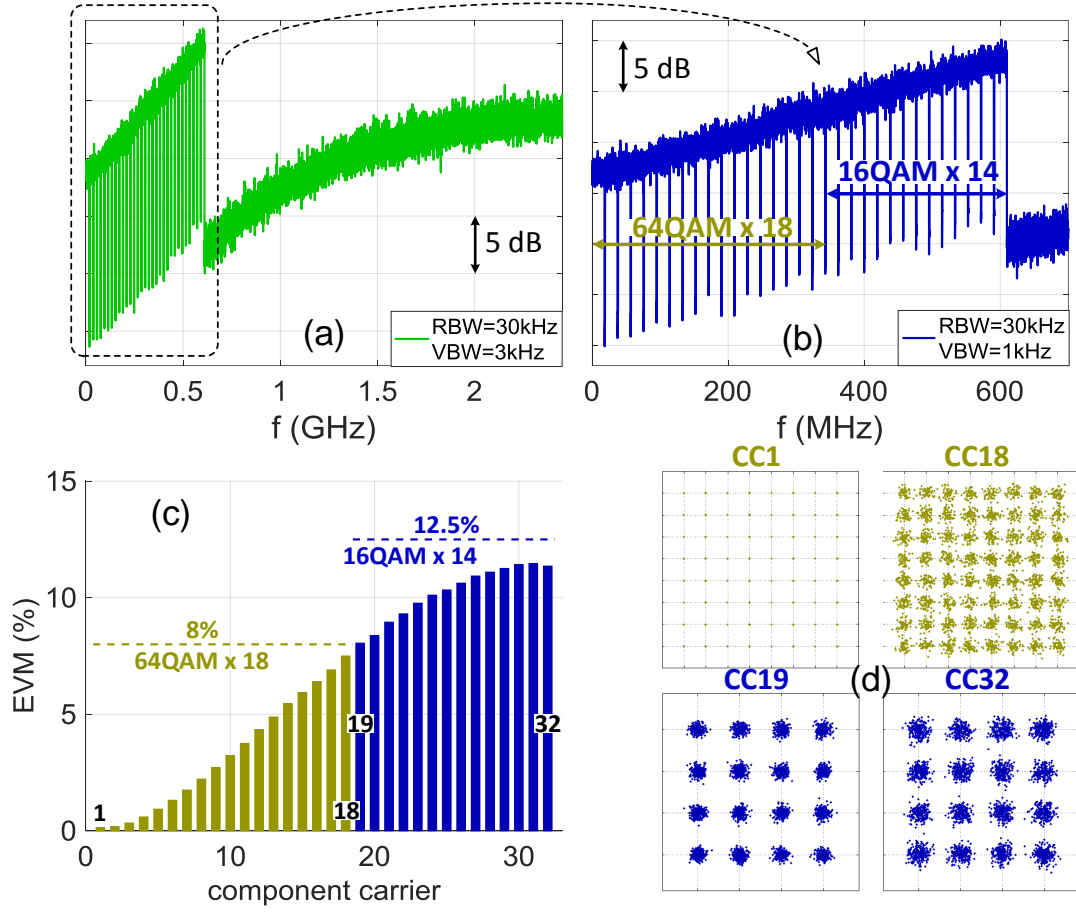


Figure 5.5: Experimental results of Case I. (a) Electrical spectra of 32 aggregated LTE carriers. (b) zoom-in of (a). (c) EVMs of 32 carriers. (d) Best/worst constellations of 64-QAM and 16-QAM.

CCs comply with the 3GPP specifications listed in Table 5.4. Constellations of CC1, 18, 19, and 32 are shown in Fig. 5.5(d), corresponding to the best and worst cases of 64-QAM and 16-QAM, respectively.

Due to the uneven noise floor, high-frequency CCs suffer from severe EVM penalties. The motivation of pre-emphasis is to improve the performance of high-frequency CCs by boosting up their signal power. However, since the second-order noise transfer function used in Case I and II has two degenerated zeroes, both located at DC ( $f = 0, z = 1$ ), low-frequency CCs, which are closer to the zeroes, have much smaller quantization noise than high-frequency ones. Pre-emphasis technique can only increase the signal power, but is not able to eliminate the residual quantization noise left in the signal band due to the imperfect noise shaping. The performance of high-frequency CCs is improved, but still not as good as low-frequency ones.

Moreover, pre-emphasis makes the aggregated LTE CCs have unequal power, which needs to be re-equalized before feeding to the air interface for wireless transmission. In Case III and IV, a fourth-order noise transfer function is used to realize a steeper high-pass filter for quantization noise, and push more noise out of the signal band. Zero-spreading technique is exploited to separate the zeroes and move them away from DC, so that the quantization noise is more evenly distributed across all LTE CCs, rather than concentrated in the high-frequency CCs.

#### 5.4.2 Case II

As a waveform agnostic digitization interface, delta-sigma modulation can digitize not only OFDM signals, but also 5G multi-carrier waveforms. We verify its 5G compatibility by FBMC signals. In Fig. 5.6(a) and (b), 30 FBMC CCs are aggregated within a single- $\lambda$  10-Gb/s OOK link. Each FBMC CC is filtered by a Nyquist filter with coefficients of  $H = [0, 0.972, 0.707, 0.235]$  and has an overlap factor of 4. EVMs of all 30 CCs are shown in Fig. 5.6(c). According to the 3GPP specifications in Table



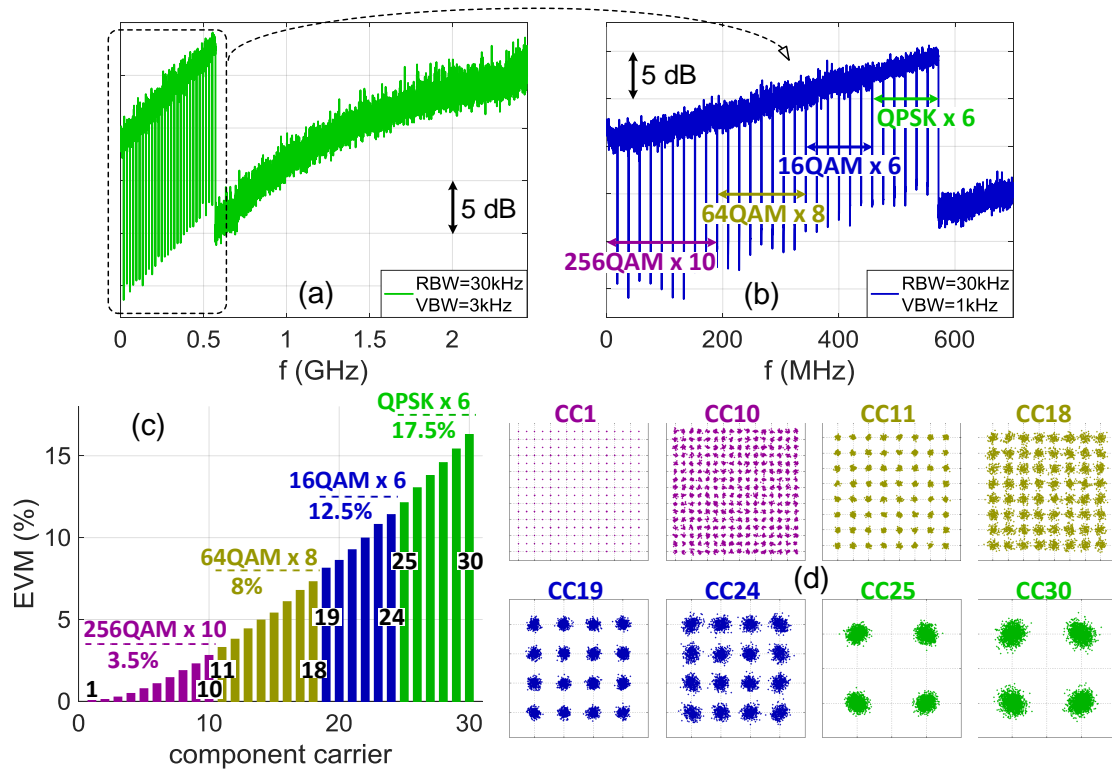


Figure 5.6: Experimental results of Case II. (a) Electrical spectra of 30 aggregated FBMC carriers. (b) zoom-in of (a). (c) EVMs of 30 carriers. (d) Best/worst constellations of each modulation format.

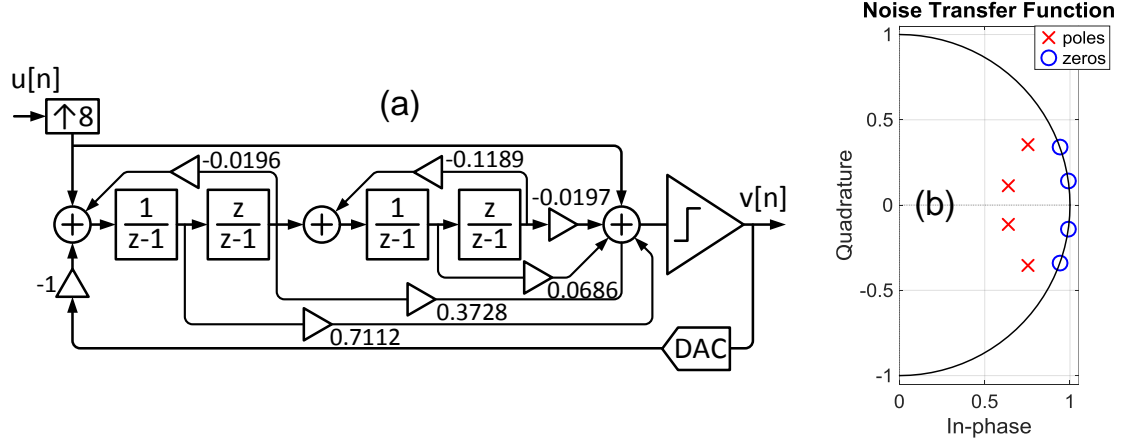


Figure 5.7: Fourth-order delta-sigma modulator based on CRFF structure (Case III and IV). (a) Z-domain block diagram. (b) Zeroes and poles of noise transfer function.

5.4, there are 10 CCs with  $\text{EVM} < 3.5\%$ , which can support 256-QAM, 8 CCs with  $\text{EVM} < 8\%$ , which can support 64-QAM, 6 CCs with  $\text{EVM} < 12.5\%$  for 16-QAM, and 6 CCs with  $\text{EVM} < 17.5\%$  for QPSK. It should be noted that the carrier aggregation number is limited to 30 due to the imperfect noise transfer function and high PAPR of FBMC signals.

#### 5.4.3 Case III

In Case I and II, high-frequency CCs suffer from severe EVM penalty due to the uneven distribution of quantization noise caused by the non-ideal noise transfer function. In Case III and IV, a fourth-order noise transfer function is designed to form a steeper high-pass filter for quantization noise and push more noise out of the signal band, as shown in Table 5.3. The Z-domain block diagram and the zeroes and poles of the noise transfer function are presented in Fig. 5.7(a) and (b), respectively. Zero-spreading technique is used to move zeroes away from DC. There are four separated zeroes (two conjugated pairs), and the quantization noise is evenly distributed across all 32 CCs, rather than concentrated on high-frequency ones.

The experimental results of Case III are presented in Fig. 5.8. 32 LTE CCs are

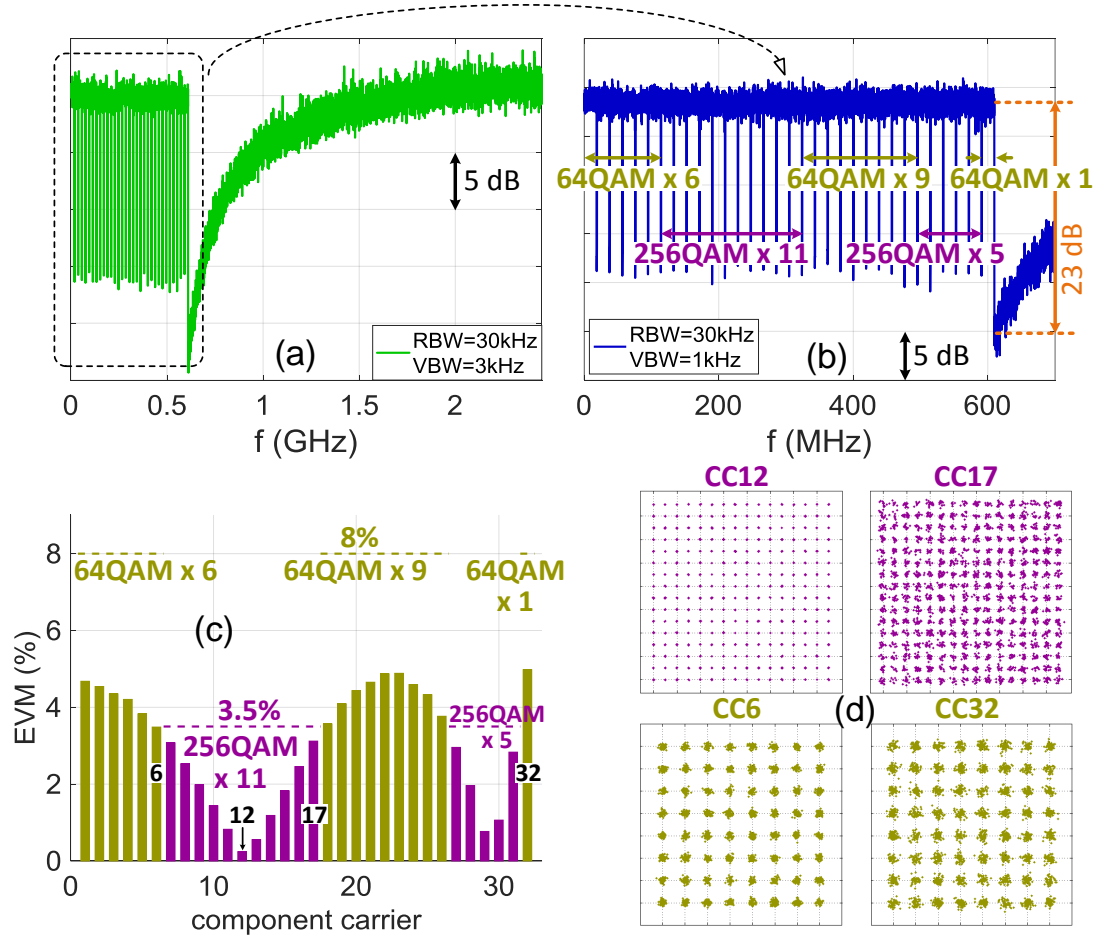


Figure 5.8: Experimental results of Case III. (a) Electrical spectra of 32 aggregated LTE carriers. (b) zoom-in of (a). (c) EVMs of 32 carriers. (d) Best/worst constellations of 256-QAM and 64-QAM.

aggregated within a single- $\lambda$  10-Gb/s OOK link, with 16 CCs carrying 64-QAM, and 14 CCs carrying 16-QAM. The electrical spectra of 32 LTE CCs are shown in Fig. 5.8(a, b). (b) is a zoom-in of (a). In Fig. 5.8(c), EVMs of all 32 CCs are reduced to less than 5%, where 16 CCs carry 256-QAM with  $\text{EVM} < 3.5\%$ , and the other 16 carry 64-QAM with  $\text{EVM} < 5\%$ . Constellations of CC12, 17, 6, and 32 are shown in (d), which correspond to the best and worst cases of 256-QAM and 64-QAM, respectively.

#### 5.4.4 Case IV

In order to further reduce the EVM penalty of digitization interface, leaving more EVM budget to the analog RF link (include amplifier chain and antenna), Case IV is designed using a fourth-order two-bit delta-sigma modulator. 32 LTE CCs are aggregated within a single- $\lambda$  10-Gbaud PAM4 (20-Gb/s) IM/DD link. In recent years, Gbaud multilevel (e.g. PAM4, PAM8) transmission over short distance of fiber ( $< 100$  km) have attracted intensive research interested for data center interconnect, where the application scenarios are very similar to MFH networks. With the help of the additional one bit, quantization noise is significantly reduced compared with Case III. In Fig. 5.3(b) and (c), this improvement can be observed by comparing the input analog signal before delta-sigma modulation (red) with the retrieved signal after LPF (green). Experimental results of Case IV are shown in Fig. 5.9, with EVMs of all CCs reduced to less than 2.1%. 10 CCs with  $\text{EVM} < 1\%$  can support modulation format up to 1024-QAM, and the rest 22 CCs with  $\text{EVM} < 2.1\%$  support 256-QAM. Constellations of CC12, 28, 16, and 22 are shown in Fig. 5.9(d), corresponding to best and worst cases of 1024-QAM and 256-QAM, respectively.

#### 5.4.5 BER Tolerance

In experiments, error-free transmissions were achieved for both 10-Gbaud OOK and PAM4 over 25-km fiber. The BER tolerance of EVM performance in a delta-sigma

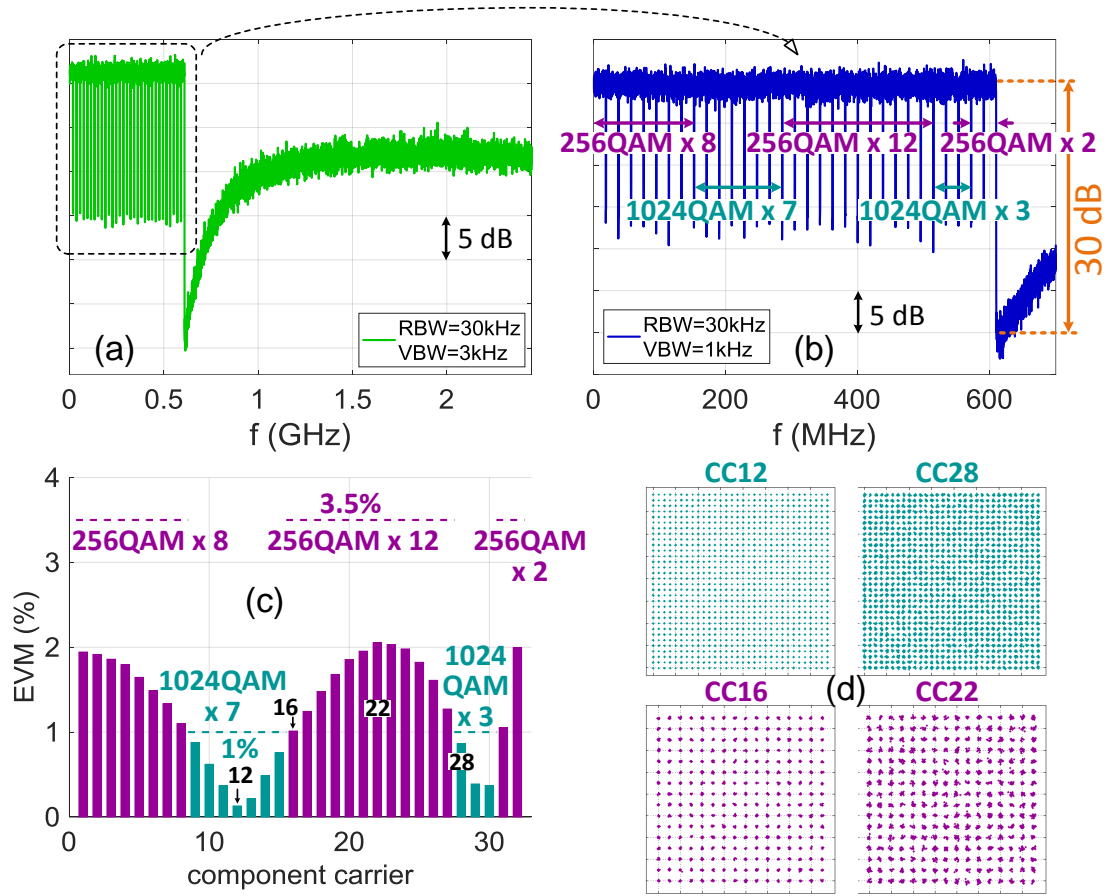


Figure 5.9: Experimental results of Case IV. (a) Electrical spectra of 32 aggregated LTE carriers. (b) zoom-in of (a). (c) EVMs of 32 carriers. (d) Best/worst constellations of 1024-QAM and 256-QAM.

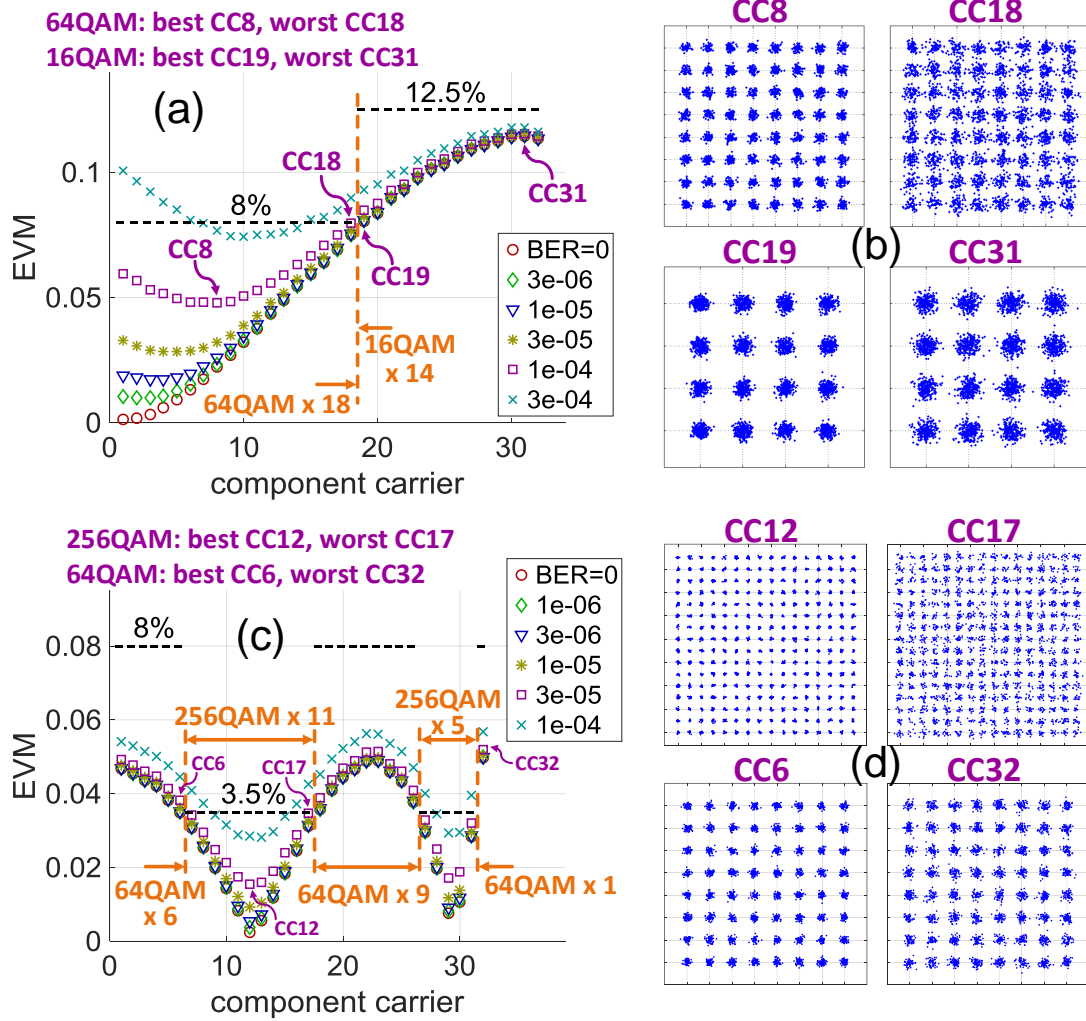


Figure 5.10: BER tolerance of delta-sigma modulation. (a) EVMs of Case I under different BERs. (b) Constellations of CC 8, 18, 19, and 31 at BER threshold  $1 \times 10^{-4}$ . (c) EVMs of Case III under different BERs. (d) Constellations of CC 12, 17, 6, and 32 at BER threshold  $3 \times 10^{-5}$ .

modulation-based digital MFH link is also investigated. In Case I and III, EVMs of all 32 LTE CCs are evaluated under different BER conditions, and the results are shown in Fig. 5.10.

For Case I, the EVM performance as a function of BER of the 10-Gb/s OOK link is shown in Fig. 5.10(a), and EVM has weak dependence on BER for BER up to  $1 \times 10^{-4}$ . This BER insensitivity is due to the operation principle of delta-sigma modulation, where the digitized signal only follows the low-frequency components of analog input; and random error bits will be smoothed out by the LPF in RRH and have weak impact on the received signal quality. In Fig. 5.10(a), the BER threshold is  $1 \times 10^{-4}$ , i.e., for BER below this value, the digital MFH can support 32 CCs without exceeding 3GPP specifications. The constellations at BER threshold are shown in (b), where CC8, 18, 19 and 31 correspond to the best and worst cases of 64-QAM and 16-QAM, respectively. Fig. 5.10(c) shows the EVM performance in Case III as a function of BER with threshold at  $3 \times 10^{-5}$ . Constellations of 256-QAM and 64-QAM at the threshold are shown in Fig. 5.10(d).

Due to the limited memory depth of our real-time oscilloscope, there is only  $10^6$  bits transmitted, and the minimum achievable BER granularity is  $10^{-6}$ . We experimentally tested BER around  $1e-6$ ,  $1e-5$ ,  $1e-4$ , and found that simulation results have very good consistency with experiments. Since it is difficult to control BER precisely in experiments, the results we shown in Fig. 5.10 are based on simulations by flipping a desired number of bits.

#### 5.4.6 Case V

To make a comparison with analog MFH, Case V was designed to evaluate the performance of analog MFH with 24 aggregated LTE CCs all carrying 64-QAM. The experimental setup is almost same with Fig. 5.3 except the digitization interface. In Case V, 24 LTE CCs are transmitted in their analog waveform without digitization.

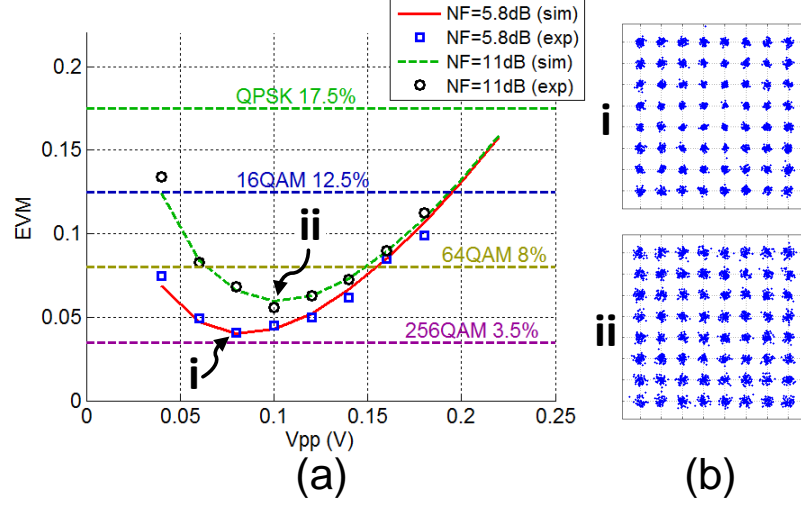


Figure 5.11: Experimental results of Case V. (a) Average EVM of 24 carriers as a function of input  $V_{pp}$  before power amplifier. (b) Best constellations for two power amplifiers with NF of 5.8 and 11 dB.

As discussed in Chapter 3, the performance of an analog MFH is limited by both noise and nonlinear impairments. The dynamic range of input signals is constrained by noise in the small signal end, and by nonlinear distortions in the large signal end. Fig. 5.11 shows the average EVM of 24 CCs as a function of the peak-to-peak amplitude ( $V_{pp}$ ) of input signal before the power amplifier in Fig. 5.3. The best achievable EVM is limited by the trade-off between noise and nonlinear impairments. Two power amplifiers (PA) with different noise figures (NF) of 5.8 dB and 11 dB are tried respectively. In Fig. 5.11, square and circle dots represent experimental results; red and green curves are from simulations. The minimum achievable EVMs are 4% and 5.6% for both PAs, satisfying the 3GPP specification of 64-QAM (8%). The PA with smaller NF provides smaller EVM and wider dynamic range due to the improved SNR. The best constellations at point i and ii are shown in the insets. Since the best EVM is limited to 4%, it would be challenging to support higher-order modulation formats such as 256 or 1024-QAM using this analog MFH without nonlinear compensation. In contrast, the proposed digital MFH based on delta-sigma modulation can



easily support 16 LTE CCs of 256-QAM in Case III, and up to 22 CCs of 256-QAM and 10 CCs of 1024-QAM in Case IV.

## 5.5 Summary

In this chapter, we propose and demonstrate a novel digitization interface based on delta-sigma modulation to replace conventional CPRI for the next generation digital MFH with improved spectral efficiency and scalability. 32 LTE carrier aggregation is implemented within a 25-km single- $\lambda$  10-Gbaud optical IM/DD link to support 3GPP release 13. Compared with CPRI, which consumes 10 Gb/s to accommodate 8 LTE carriers, the MFH capacity is increased by four times without significant EVM penalty. Both one-bit and two-bit delta-sigma modulations are demonstrated, and transmitted over OOK/PAM4 optical IM/DD links, with EVM less than 5% or 2.1%, respectively, supporting high order modulation formats, up to 256-QAM and 1024-QAM. As a waveform-agnostic digitization interface, delta-sigma modulation not only works with 4G-LTE signals, but can also digitize 5G mobile signals, and its 5G compatibility is verified by FBMC signals. BER tolerance of delta-sigma modulation-based digital MFH is also evaluated, and with BER up to  $3 \times 10^{-5}$ , there is no significant EVM degradation observed. Compared with analog MFH, delta-sigma modulation-based digital MFH offer significantly improved robustness against nonlinear impairments; while compared with CPRI, it provides enhanced spectral efficiency and increases MFH capacity by four times without significant EVM penalty.

## CHAPTER 6

### CONCLUSION

The proliferation of Internet-connected mobile devices and the emerging video-intensive services are driving the growth of mobile data traffic in an explosive way. The paradigm shift of the next generation cellular network from tower-based macro cells towards multi-tier heterogeneous small cells is making the last mile of access networks, mobile fronthaul, become the data rate bottleneck of user experience. To enhance the capacity and coverage of mobile data networks, next generation MFH is expected to support multi-RAT multi-service coexistence with enhanced spectral efficiency.

There are two MFH architectures proposed, analog MFH and digital MFH. Analog MFH transmits mobile signals in their analog waveforms using radio over fiber technologies. It features simple low-cost implementations and high spectral efficiency, but suffers from the vulnerability to nonlinear impairments. So far as we know, there have been meager effort to investigate the nonlinear impairments of analog MFH, and most works only focus on the distortion of each individual signal. In this research, for the first time as we know, nonlinear inter-channel interferences in a multi-RAT multi-service analog MFH are investigated. Digital MFH, on the other hand, digitizes mobile signals before MFH transmission, and is inherently robust against nonlinear impairments. But digital MFH suffers from low spectral efficiency and requires tremendous bandwidth after digitization. CPRI-based digitization interface has become the data rate bottleneck of the next generation mobile data networks.

In order to address the challenges to both analog and digital MFH networks, the contribution of this research is two-fold. For analog MFH, we investigate the nonlinear impairments of both single-carrier and multi-carrier signals, with the emphasis on inter-channel interferences among multiple signals from different RATs. To mitigate

the nonlinear impairments, a linearization technique based on digital predistortion is demonstrated. For digital MFH, we demonstrate a novel digitization interface based on delta-sigma modulation to replace CPRI with improved spectral efficiency and increased fronthaul capacity, which can accommodate not only 4G-LTE but also 5G mobile services.

## 6.1 Nonlinear Impairments of Analog MFH

### 6.1.1 Cross-Modulations of Single-Carrier Signals

The dominant nonlinear impairments of single-carrier signals are cross-modulations (XMs). In Chapter 2, both intra-band and inter-band XMs are investigated. Intra-band XM comes from the crosstalk between I and Q components of a vector signal; inter-band XM originates from the inter-channel interference among different signals, where the data modulation of one channel is imprinted onto others. A millimeter wave analog MFH testbed is demonstrated, and closed-form theoretical analysis is proposed to evaluate the XM behaviors. Both simulation and experiments are carried out with consistent results.

It is experimentally verified that scalar signals only suffer from inter-band XM since they only have the in-phase component; vector signals could be impaired by both intra-band and inter-band XMs except PSK signals. PSK signals are immune from intra-band XM due to their constant envelope, but may still be impaired by inter-band XM. Intra-band XM causes compression distortion to constellations of vector signals; inter-band XM induces eye diagram degradation to scalar signals, and scaling distortion to vector signals. The operation principles and impairments caused by XMs are summarized in Table 6.1. All XM effects are imposed as a multiplicative factor with positive real value, indicating that XMs are baseband effects, which only cause radical distortions to eye diagrams or constellations, but no phase rotation. Since XMs only depend on data modulation and have no dependence on signal frequencies,

they cannot be eliminated by filtering or alleviated by increasing channel spacing.

### 6.1.2 Subcarrier Intermodulations of Multi-carrier Signals

The dominant impairments of multi-carrier signals are subcarrier intermodulations (IMs), i.e., third-order beat among subcarriers. These subcarriers can come from the same OFDM signal, forming intra-band IMs, or from different signals, forming inter-band IMs. Most existing studies of OFDM nonlinearities only focus on the intra-band IMs of each individual signal, and there has been meager effort to study the inter-channel interferences among multiple OFDM signals. In Chapter 3, for the first time as we know, inter-band IMs among multiple OFDM signals in a multi-RAT analog MFH are investigated. Eight experimental scenarios are designed to evaluate IMs across services from different RATs, and consistent results are obtained with simulation.

As summarized in Table 6.1, both intra-band and inter-band IMs can introduce in-band interferences and out-of-band emission, and the in-band interferences can be modeled as a Gaussian noise with zero mean. It is experimentally verified that inter-band IMs play a more important role in performance degradation of analog MFH than the well-known intra-band IMs. Inter-band IMs are mainly determined by the bandwidths of participating signals, but have weak dependence on modulation formats or subcarrier spacing. Broadband services suffer more from inter-band IMs since there are more interference beat products located in their large bandwidth. In some extreme scenarios, inter-band IMs degenerate to baseband XMs, depending on the relative size of bandwidth and subcarrier spacing of mobile signals. Although subcarrier IMs are not baseband effects, they only depend on the frequency difference among subcarriers, and have no dependence on the central signal frequencies. Therefore, same as XMs of single-carrier signals, subcarrier IMs can not be eliminated by filtering either.

Table 6.1: Summary of nonlinear impairments in analog MFH networks

Nonlinearities	Cross-modulation (XM)		Intermodulation (IM)	
	Intra-band	Inter-band	Intra-band	Inter-band
Operation principles	Crosstalk between I/Q components	Data modulation imprints from one service onto others	Beat among subcarriers from same signal	Beat among subcarriers from different signals
Impairments	Constellation compression except PSK	Eye diagram degradation Constellation scaling	In-band interferences and out-of-band spectral emission	
Math explanation	Positive real-valued multiplicative factors Only radical distortions, no phase rotation		Additive Gaussian noise	
Frequency dependency	Baseband effects Independent on carrier frequency		Dependent on subcarrier frequency difference Independent on signal central frequencies	
Single-band single-carrier	Dominant if vector signal	N/A	N/A	N/A
Multiband single-carrier	Yes if vector signal	Dominant	N/A	N/A
Single-band multi-carrier	Negligible <sup>1</sup>	Converge to constant <sup>2</sup>	Dominant	N/A
Multiband multi-carrier	Negligible <sup>1</sup>	Converge to constant <sup>2</sup>	Yes	Dominant <sup>3</sup>

1. Compared with the impairments induced by subcarrier IMs, the contribution of intra-band XM is negligible.
2. Each subcarrier contributes a XM factor. The multiplication of large number of XM factors converges to a constant.
3. Inter-band IMs are dependent on the bandwidths of participating signals, and can degenerate to baseband XMs (scaling distortion) in extreme scenarios.

For both single-carrier and multi-carrier signals, although nonlinear distortions of each individual signal (intra-band XMs and IMs) have been studied extensively, it is the inter-channel interferences (inter-band XMs and IMs) that dominate the transmission impairments of multi-RAT multi-service analog MFH. For different communication scenarios in analog MFH, e.g., single-band/multiband, single-carrier/multi-carrier, the dominant nonlinear impairments are listed in Table 6.1. Single-carrier signals only suffer from XMs, since they only have one carrier, and any carrier IM will be out-of-band and can be eliminated by filtering. Multi-carrier signals could be impaired by both XMs and IMs, but IMs take the dominance, since the multiplication of XM factors contributed by all subcarriers converge to a constant due to the large number of subcarriers.

### 6.1.3 Linearization Technology based on Digital Predistortion

To mitigate the nonlinear impairments of analog MFH networks, a linearization technology based on digital predistortion is demonstrated in Chapter 4. Thanks to the static and highly predictable nature of analog MFH, digital predistortion is one of the simplest and most cost-effective solutions which can be implemented in electrical domain without expensive optical devices. It is experimentally demonstrated that both intra-band and inter-band XMs and IMs are effectively mitigated by the digital predistorter based on 5th order polynomial, and the received signal qualities after analog MFH transmission are significantly improved. As a waveform-agnostic technology, digital predistortion is transparent to different signal waveforms and RATs. It can be used for both single-carrier and multi-carrier signals, not only 4G-LTE but also 5G new radio waveforms.

## 6.2 Digital MFH based on Delta-Sigma Modulation

Other than the waveform-agnostic linearization technologies, waveform-specific strategy modifies signal waveforms to enhance their robustness against nonlinear impairments. Digitization can be considered as an extreme scenario of waveform-specific strategy. In a digital MFH, mobile signals are digitized into discrete bits before fronthaul transmission, trading spectral efficiency for the robustness against nonlinear impairments. In Chapter 5, we experimentally demonstrate a novel digitization interface based on delta-sigma modulation to replace the conventional CPRI with reduced system cost and improved spectral efficiency for the next generation digital MFH networks.

In experiments, 32 LTE carrier aggregation is realized to support 3GPP release 13, and transmitted via a 25-km single- $\lambda$  10-Gbaud optical IM/DD link. Compared with CPRI, which consumes 10 Gb/s to accommodate 8 LTE carriers, the MFH capacity is increased by four times without significant EVM penalty. Both one-bit and two-bit delta-sigma modulations are demonstrated, and transmitted over OOK/PAM4 links with EVM less than 5% or 2.1%, respectively, and high order modulation formats, up to 256-QAM and 1024-QAM, can be supported. Delta-sigma modulation can digitize not only 4G-LTE signals, but also 5G mobile signals, and its 5G compatibility is verified by FBMC signals. BER tolerance of delta-sigma modulation-based digital MFH is also evaluated. With BER up to  $3 \times 10^{-5}$ , there is no significant EVM degradation observed. Compared with analog MFH, delta-sigma modulation offers significantly improved robustness against nonlinear impairments; while compared with CPRI, it provides enhanced spectral efficiency and increases MFH capacity without significant penalty of signal quality.

## 6.3 Future Works

### 6.3.1 New Multi-carrier Waveforms

Recently, there have been quite a few 5G multi-carrier waveforms proposed as OFDM successors for the next generation air interface of wireless communications, e.g., filtered orthogonal frequency division multiplexing (F-OFDM), generalized frequency division multiplexing (GFDM), universal filtered multi-carrier (UFMC), and filter bank multi-carrier (FBMC). They feature low latency, free cyclic prefix, increased spectral efficiency, and low out-of-band leakage, but there have been little effort to investigate their nonlinear impairments. To enable multi-RAT multi-service MFH networks, it is of importance to understand the transmission impairments of these new 5G waveforms, and their interferences with legacy OFDM services. Digitization of these new multi-carrier waveforms, including both CPRI and delta-sigma modulation will also be of interest.

### 6.3.2 Improved Delta-Sigma Modulation for Digital MFH

For digital MFH, on the other hand, it is observed in Chapter 5 that delta-sigma modulation is limited by large quantization noise due to its limited quantization bits. Since most multi-carrier waveforms, including both 4G OFDM and new 5G waveforms, have high PAPR and Gaussian distribution, there are more samples with small amplitudes than those with large amplitudes. Few-bit (one or two) quantization, even with the help of noise shaping technique, will inevitably lead to large amount of quantization noise. One interesting step for the next research is to add a statistical DSP function before the digitization interface to modify the input signal distribution, so that the quantization noise can be reduce. This method has been proven effective for OFDM signal with Nyquist ADC in CPRI, and we believe it can significantly reduce the quantization noise of delta-sigma modulation as well.



## REFERENCES

- [1] Cisco Visual Networking Index, “Global mobile data traffic forecast update, 2012-2017,” white paper 2013.
- [2] Cisco Visual Networking Index, “Global mobile data traffic forecast update, 2013-2018,” white paper 2014.
- [3] P. Demestichas, A. Georgakopoulos, D. Karvounas, K. Tsagkaris, V. Stavroulaki, J. Lu, C. Xiong, and J. Yao, “5G on the horizon: key challenges for the radio-access network,” *IEEE Vehicular Technology Magazine*, vol. 8, no. 3, pp. 47-53, 2013.
- [4] J. G. Andrews, S. Buzzi, W. Choi, S. V. Hanly, A. Lozano, A. C. K Soong, and J. C. Zhang, “What will 5G be?,” *IEEE Journal on Selected Areas in Communications*, vol. 32, no. 6, pp. 1065-1082, 2014.
- [5] F. Boccardi, R. W. Heath, A. Lozano, T. L. Marzetta, P. Popovski, “Five disruptive technology directions for 5G,” *IEEE Communications Magazine*, vol. 52, no. 2, pp. 74-80, 2014.
- [6] C.-X. Wang, F. Haider, X. Gao, X.-H. You, Y. Yang, D. Yuan, H. Aggoune, H. Haas, S. Fletcher, E. Hepsaydir, “Cellular architecture and key technologies for 5G wireless communication networks,” *IEEE Communications Magazine*, vol. 52, no. 2, pp. 122-130, 2014.
- [7] V. Jungnickel, K. Manolakis, W. Zirwas, B. Panzner, V. Braun, M. Lossow, M. Sternad, R. Apelfrojd, T. Svensson, “The role of small cells, coordinated multipoint, and massive MIMO in 5G,” *IEEE Communications Magazine*, vol. 52, no. 5, pp. 44-51, 2014.
- [8] A. Damnjanovic, J. Montojo, Y. Wei, T. Ji, T. Luo, M. Vajapeyam, T. Yoo, O. Song, D. Malladi, “A survey on 3GPP heterogeneous networks,” *IEEE Wireless Communications*, vol. 18, no. 3, pp. 10-21, 2011.
- [9] A. Ghosh, N. Mangalvedhe, R. Ratasuk, B. Mondal, M. Cudak, E. Visotsky, T. A. Thomas, J. G. Andrews, P. Xia, H. S. Jo, H. S. Dhillon, T. D. Novlan, “Heterogeneous cellular networks: from theory to practice,” *IEEE Communications Magazine*, vol. 50, no. 6, pp. 54-64, 2012.
- [10] S. Yeh, S. Talwar, G. Wu, N. Himayat, K. Johnsson, “Capacity and coverage enhancement in heterogeneous networks,” *IEEE Wireless Communications*, vol. 18, no. 3, pp. 32-38, 2011.
- [11] M. Jo, T. Maksymyuk, R. L. Batista, T. F. Maciel, A. L. F. de Almeida, M. Klymash, “A survey of converging solutions for heterogeneous mobile networks,” *IEEE Wireless Communications*, vol. 21, no. 6, pp. 54-62, 2014.

- [12] V. Chandrasekhar, J. G. Andrews, A. Gatherer, "Femtocell networks: a survey," *IEEE Communications Magazine*, vol. 46, no. 9, pp. 59-67, 2008.
- [13] J. G. Andrews, H. Claussen, M. Dohler, S. Rangan, M. C. Reed, "Femtocells: past, present, and future," *Journal on Selected Areas in Communications*, vol. 30, no. 3, pp. 497-508, 2012.
- [14] P. Smulders, "Exploiting the 60 GHz band for local wireless multimedia access: prospects and future directions," *IEEE Communications Magazine*, vol. 40, no. 1, pp. 140-147, Jan 2002.
- [15] C. Park and T. S. Rappaport, "Short-range wireless communications for next-generation networks: UWB, 60 GHz millimeter-wave WPAN, and ZigBee," *IEEE Wireless Communications*, vol. 14, no. 4, pp. 70-78, 2007.
- [16] T. S. Rappaport, F. Gutierrez, E. Ben-Dor, J. N. Murdock, Y. Qiao and J. I. Tamir, "Broadband millimeter-wave propagation measurements and models using adaptive-beam antennas for outdoor urban cellular communications," *IEEE Transactions on Antennas and Propagation*, vol. 61, no. 4, pp. 1850-1859, 2013.
- [17] T. S. Rappaport, S. Sun, R. Mayzus, H. Zhao, Y. Azar, K. Wang, G. N. Wong, J. K. Schulz, M. Samimi, and F. Gutierrez, "Millimeter wave mobile communications for 5G cellular: it will work!," *IEEE Access*, vol. 1, pp. 335-349, 2013.
- [18] W. Roh, J.-Y. Seol, J. Park, B. Lee, J. Lee, Y. Kim, J. Cho, and K. Cheun, F. Aryanfar, "Millimeter-wave beamforming as an enabling technology for 5G cellular communications: theoretical feasibility and prototype results," *IEEE Communications Magazine*, vol. 52, no. 2, pp. 106-113, 2014.
- [19] A. Ghosh, T. A. Thomas, M. C. Cudak, R. Ratasuk, P. Moorut, F. W. Vook, T. S. Rappaport, G. R. MacCartney, S. Sun, and S. Nie, "Millimeter-wave enhanced local area systems: a high-data-rate approach for future wireless networks," *IEEE Journal on Selected Areas in Communications*, vol. 32, no. 6, pp. 1152-1163, 2014.
- [20] 3GPP TR 36.808, V10.1.0, "Evolved Universal Terrestrial Radio Access (E-UTRA); Carrier Aggregation; Base Station (BS) radio transmission and reception," Release 10, 2013-07.
- [21] 3GPP RP142286, "New WI proposal: LTE Carrier Aggregation Enhancement Beyond 5 Carriers," 2014-12.
- [22] G. Yuan, X. Zhang, W. Wang, and Y. Yang, "Carrier aggregation for LTE-advanced mobile communication systems," *IEEE Communications Magazine*, vol. 48, no. 2, pp. 88-93, 2010.
- [23] A. Ghosh, R. Ratasuk, B. Mondal, N. Mangalvedhe, T. Thomas, "LTE-advanced: next-generation wireless broadband technology," *IEEE Wireless Communications*, vol. 17, no. 3, pp. 10-22, 2010.

- [24] Y. Rui, P. Cheng, M. Li, Q. T. Zhang, M. Guizani, "Carrier aggregation for LTE-advanced: uplink multiple access and transmission enhancement features," *IEEE Wireless Communications*, vol. 20, no. 4, pp. 101-108, 2013.
- [25] E. Larsson, O. Edfors, F. Tufvesson, and T. Marzetta, "Massive MIMO for next generation wireless systems," *IEEE Communications Magazine*, vol. 52, no. 2, pp. 186-195, 2014.
- [26] L. Lu, G. Y. Li, A. L. Swindlehurst, A. Ashikhmin, and R. Zhang, "An overview of massive MIMO: benefits and challenges," *IEEE Journal of Selected Topics in Signal Processing*, vol. 8, no. 5, pp. 742-758, 2014.
- [27] B. Panzner, W. Zirwas, S. Dierks, M. Lauridsen, P. Mogensen, K. Pajukoski, D. Miao, "Deployment and implementation strategies for massive MIMO in 5G," *Globecom Workshops 2014*, pp. 346-351, 2014.
- [28] X. Tao, X. Xu, Q. Cui, "An overview of cooperative communications," *IEEE Communications Magazine*, vol. 50, no. 6, pp. 65-71, 2012.
- [29] R. Irmer, H. Droste, P. Marsch, M. Grieger, and G. Fettweis, S. Brueck, H.-P. Mayer, L. Thiele and V. Jungnickel, "Coordinated multipoint: concepts, performance, and field trial results," *IEEE Communications Magazine*, vol. 49, no. 2, pp. 102-111, 2011.
- [30] China Mobile, "C-RAN the road towards green RAN (version 2.5)," White Paper, Oct 2011.
- [31] A. Checko, H.L. Christiansen, Y. Yan, L. Scolari, G. Kardaras, M.S. Berger, L. Dittmann, "Cloud RAN for mobile networks - a technology overview," *IEEE Communications Surveys & Tutorials*, vol.17, no.1, pp.405-426, 2015.
- [32] K. Tanaka, A. Agata, "Next-generation optical access networks for C-RAN," *Optical Fiber Communication Conference (OFC) 2015*, paper Tu2E.1.
- [33] T. Pfeiffer, "Next generation mobile fronthaul architectures," *Optical Fiber Communication Conference (OFC) 2015*, paper M2J.7.
- [34] T. Pfeiffer, "Next generation mobile fronthaul and midhaul architectures," *Journal of Optical Communications and Networking*, vol. 7, no. 11, pp. B38-B45, 2015.
- [35] A. Pizzinat, P. Chanclou, F. Saliou, T. Diallo, "Things you should know about fronthaul," *Journal of Lightwave Technology*, vol.33, no.5, pp.1077-1083, 2015.
- [36] Common Public Radio Interface (CPRI) Specification V7.0 (2015-10-09), [http://www.cpri.info/downloads/CPRI\\_v7\\_0\\_2015-10-09.pdf](http://www.cpri.info/downloads/CPRI_v7_0_2015-10-09.pdf)
- [37] C. Lim, A. Nirmalathas, M. Bakaul, P. Gamage, K.-L. Lee, Y. Yang, D. Novak, R. Waterhouse, "Fiber-wireless networks and subsystem technologies," *Journal of Lightwave Technology*, vol. 28, no. 4, pp. 390-405, 2010.

- [38] C. Liu, L. Zhang, M. Zhu, J. Wang, L. Cheng, and G. K. Chang, "A novel multi-service small-cell cloud radio access network for mobile backhaul and computing based on radio-over-fiber technologies," *Journal of Lightwave Technology*, vol. 31, no. 17, pp. 2869-2875, 2013.
- [39] C. Liu, J. Wang, L. Cheng, M. Zhu, and G. K. Chang, "Key microwave-photonics technologies for next-generation cloud-based radio access networks," *Journal of Lightwave Technology*, vol. 32, no. 20, pp. 3452-3460, 2014.
- [40] Z. Jia, J. Yu, G. Ellinas, and G.-K. Chang, "Key enabling technologies for optical-wireless networks: optical millimeter-wave generation, wavelength reuse, and architecture," *Journal of Lightwave Technology*, vol. 25, no. 11, pp. 3452-3471, 2007.
- [41] G.-K. Chang, A. Chowdhury, Z. Jia, H.-C. Chien, M.-F. Huang, J. Yu, and G. Ellinas, "Key technologies of WDM-PON for future converged optical broadband access networks," *Journal of Optical Communications and Networking*, vol. 1, no. 4, pp. C35-C50, 2009.
- [42] J. Yu, G.-K. Chang, Z. Jia, A. Chowdhury, M.-F. Huang, H.-C. Chien, Y.-T. Hsueh, W. Jian, C. Liu, and Z. Dong, et al., "Cost-effective optical millimeter technologies and field demonstrations for very high throughput wireless-over-fiber access systems," *Journal of Lightwave Technology*, vol. 28, no. 16, pp. 2376-2397, 2010.
- [43] A. Chowdhury, H.-C. Chien, S.-H. Fan, J. Yu, and G.-K. Chang, "Multi-band transport technologies for in-building host-neutral wireless over fiber access systems," *Journal of Lightwave Technology*, vol. 28, no. 16, pp. 2406-2415, 2010.
- [44] Y.-T. Hsueh, C. Liu, S.-H. Fan, J. Yu, and G.-K. Chang, "A novel full-duplex testbed demonstration of converged all-band 60-GHz radio-over-fiber access architecture," *Optical Fiber Communication Conference (OFC) 2012*, paper OTu2H.5.
- [45] M. Zhu, A. Yi, Y.-T. Hsueh, C. Liu, J. Wang, S.-C. Shin, J. Yu, and G.-K. Chang, "Demonstration of 4-band millimeter-wave radio-over-fiber system for multi-service wireless access networks," *Optical Fiber Communication Conference (OFC) 2013*, paper OM3D.4.
- [46] M. Zhu, L. Zhang, J. Wang, L. Cheng, C. Liu, and G. K. Chang, "Radio-over-fiber access architecture for integrated broadband wireless services," *Journal of Lightwave Technology*, vol. 31, no. 23, pp. 3614-3620, 2013.
- [47] R. Wang, H. Hu, X. Yang, "Potentials and challenges of C-RAN supporting Multi-RATs toward 5G mobile networks," *IEEE Access*, vol. 2, pp. 1187-1195, 2014.

- [48] F. M. Abinader, E. P. L. Almeida, F. S. Chaves, A. M. Cavalcante, R. D. Vieira, R. C. D. Paiva, A. M. Sobrinho, S. Choudhury, E. Tuomaala, K. Doppler, V. A. Sousa, "Enabling the coexistence of LTE and Wi-Fi in unlicensed bands," *IEEE Communications Magazine*, vol. 52, no. 11, pp. 54-61, 2014.
- [49] H. Zhang, X. Chu, W. Guo, and S. Wang, "Coexistence of Wi-Fi and heterogeneous small cell networks sharing unlicensed spectrum," *IEEE Communications Magazine*, vol. 53, no. 3, pp. 158-164, 2015.
- [50] Signals Research Group, "The prospect of LTE and Wi-Fi sharing unlicensed spectrum," White Paper developed for Qualcomm, 2015.  
<https://www.qualcomm.com/documents/prospect-lte-and-wi-fi-sharing-unlicensed-spectrum-srg-white-paper>
- [51] A. Chowdhury, H.-C. Chien, Y.-T. Hsueh, G.-K. Chang, "Advanced system technologies and field demonstration for in-building optical-wireless network with integrated broadband services," *Journal of Lightwave Technology*, vol. 27, no. 12, pp. 1920-1927, 2009.
- [52] J. Zhang, M. Xu, J. Wang, F. Lu, L. Cheng, M. Zhu, I. Khalil, J. Yu, G.-K. Chang, "Carrier aggregation for MMW inter-RAT and intra-RAT in next generation heterogeneous mobile data network based on optical domain band mapping," *European Conference on Optical Communication (ECOC) 2015*, paper We.4.4.5.
- [53] X. Liu, F. Effenberger, N. Chand, L. Zhou, and H. Lin, "Demonstration of bandwidth-efficient mobile fronthaul enabling seamless aggregation of 36 E-UTRA-like wireless signals in a single 1.1-GHz wavelength channel," *Optical Fiber Communication Conference (OFC) 2015*, paper M2J.2.
- [54] X. Liu, H. Zeng, N. Chand, F. Effenberger, "Experimental demonstration of high-throughput low-latency mobile fronthaul supporting 48 20-MHz LTE signals with 59-Gb/s CPRI-equivalent rate and 2-s processing latency," *European Conference on Optical Communication (ECOC) 2015*, paper We.4.4.3.
- [55] X. Liu, H. Zeng, N. Chand and F. Effenberger, "Efficient mobile fronthaul via DSP-based channel aggregation," *Journal of Lightwave Technology*, vol. 34, no. 6, pp. 1556-1564, 2016.
- [56] M. Zhu, X. Liu, N. Chand, F. Effenberger, and G. K. Chang, "High-capacity mobile fronthaul supporting LTE-advanced carrier aggregation and 8x8 MIMO," *Optical Fiber Communication Conference (OFC) 2015*, paper M2J.3.
- [57] S. Cho, H. Park, H. Chung, K. Doo, S. Lee, and J. H. Lee, "Cost-effective next generation mobile fronthaul architecture with multi-IF carrier transmission scheme," *Optical Fiber Communication Conference (OFC) 2014*, paper Tu2B.6.

- [58] S. Cho, H. S. Chung, C. Han, S. Lee, and J. H. Lee, "Experimental demonstrations of next generation cost-effective mobile fronthaul with IFoF technique," Optical Fiber Communication Conference (OFC) 2015, paper M2J.5.
- [59] J. Ma, C. Yu, J. Yu, G.-K. Chang, X. Sang, "Transmission performance of the optical mm-wave signals generated by optical carrier suppression," IEEE Annual Meeting of Lasers and Electro-Optics Society (LEOS) 2006, paper TuE3, pp.197-198.
- [60] J. Ma, J. Yu, C. Yu, X. Xin, J. Zeng, L. Chen, "Fiber dispersion influence on transmission of the optical millimeter-waves generated using LN-MZM intensity modulation," Journal of Lightwave Technology, vol. 25, no. 11, pp. 3244-3256, 2007.
- [61] X. Qi, J. Liu, X. Zhang, L. Xie, "Fiber dispersion and nonlinearity influences on transmissions of AM and FM data modulation signals in radio-over-fiber system," IEEE Journal of Quantum Electronics, vol. 46, no. 8, pp. 1170-1177, 2010.
- [62] J. James, P. Shen, A. Nkansah, X. Liang and N. J. Gomes, "Nonlinearity and noise effects in multi-level signal millimeter-wave over fiber transmission using single and dual wavelength modulation," IEEE Transactions on Microwave Theory and Techniques, vol. 58, no. 11, pp. 3189-3198, 2010.
- [63] H. Yang, J. Zeng, Y. Zheng, H. D. Jung, B. Huiszoon, J. H. C. van Zantvoort, E. Tangdiongga and A. M. J. Koonen, "Evaluation of effects of MZM nonlinearity on QAM and OFDM signals in RoF transmitter," International topical meeting on Microwave photonics (MWP) 2008, pp. 90-93.
- [64] C. Lim, A. Nirmalathas, K. L. Lee, D. Novak and R. Waterhouse, "Intermodulation distortion improvement for fiber-radio applications incorporating OSSB+C modulation in an optical integrated-access environment," Journal of Lightwave Technology, vol. 25, no. 6, pp. 1602-1612, 2007.
- [65] W. H. Chen and W. I. Way, "Multichannel single-sideband SCM/DWDM transmission systems," Journal of Lightwave Technology, vol. 22, no. 7, pp. 1679-1693, 2004.
- [66] T.-S. Cho and K. Kim, "Optimization of radio-on-fiber systems employing ODSB signals by utilizing a dual-electrode Mach-Zehnder modulator against IM3," Photonics Technology Letters, vol. 18, no. 9, pp. 1076-1078, 2006.
- [67] T.-S. Cho and K. Kim, "Effect of third-order intermodulation on radio-over-fiber systems by a dual-electrode Mach-Zehnder modulator with ODSB and OSSB signals," Journal of Lightwave Technology, vol. 24, no. 5, pp. 2052-2058, 2006.

- [68] C. Wu and X. Zhang, "Impact of nonlinear distortion in radio over fiber systems with single-sideband and tandem single-sideband subcarrier modulations," *Journal of Lightwave Technology*, vol. 24, no. 5, pp. 2076-2090, 2006.
- [69] L. Cheng, S. Aditya, Z. Li and A. Nirmalathas, "Generalized analysis of subcarrier multiplexing in dispersive fiber-optic links using Mach-Zehnder external modulator," *Journal of Lightwave Technology*, vol. 24, no. 6, pp. 2296-2304, 2006.
- [70] C.-T. Lin, J. Chen, S.-P. Dai, P.-C. Peng, and S. Chi, "Impact of nonlinear transfer function and imperfect splitting ratio of MZM on optical up-conversion employing double sideband with carrier suppression modulation," *Journal of Lightwave Technology*, vol. 26, no. 15, pp. 2449-2459, 2008.
- [71] R. W. Chang, "Synthesis of band-limited orthogonal signals for multichannel data transmission," *Bell System Technical Journal*, vol. 45, no. 10, pp. 1775-1796, 1966.
- [72] J. A. C. Bingham, "Multicarrier modulation for data transmission: an idea whose time has come," *IEEE Communications Magazine*, vol. 28, no. 5, pp. 5-14, 1990.
- [73] ETSI EN 300 401 v1.4.1, "Radio broadcasting systems: digital audio broadcasting (DAB) to mobile, portable and fixed receivers," Jan 2006.
- [74] ETSI EN 300 744 v1.5.1, "Digital video broadcasting (DVB): framing structure, channel coding and modulation for digital terrestrial television," Jun 2004.
- [75] K. Sistanizadeh, P. S. Chow, and J. M. Cioffi, "Multi-tone transmission for asymmetric digital subscriber lines (ADSL)," *IEEE International Conference on Communications (ICC)*, vol. 2, pp. 756-760, 1993.
- [76] P. S. Chow, J. C. Tu, and J. M. Cioffi, "A discrete multitone transceiver system for HDSL applications," *IEEE Journal of Selected Areas in Communications*, vol. 9, no. 6, pp. 895-908, 1991.
- [77] W. Shieh and C. Athaudage, "Coherent optical orthogonal frequency division multiplexing," in *Electronics Letters*, vol. 42, no. 10, pp. 587-589, 11 May 2006.
- [78] W. Shieh, H. Bao, and Y. Tang, "Coherent optical OFDM: theory and design," *Optics Express*, vol. 16, no. 2, pp. 841-859, 2008.
- [79] J. Armstrong, "OFDM for optical communications," *Journal of Lightwave Technology*, vol. 27, no. 3, pp. 189-204, 2009.
- [80] J. Yu, M. F. Huang, D. Qian, L. Chen and G. K. Chang, "Centralized lightwave WDM-PON employing 16-QAM intensity modulated OFDM downstream and OOK modulated upstream signals," *Photonics Technology Letters*, vol. 20, no. 18, pp. 1545-1547, 2008.

- [81] D. Qian, N. Cvijetic, J. Hu, and T. Wang, "108 Gb/s OFDMA-PON with polarization multiplexing and direct detection," *Journal of Lightwave Technology*, vol. 28, no. 4, pp. 484-493, 2010.
- [82] N. Cvijetic, "OFDM for next-generation optical access networks," *Journal of Lightwave Technology*, vol. 30, no. 4, pp. 384-398, 2012.
- [83] R. Giddings, "Real-time digital signal processing for optical OFDM-based future optical access networks," *Journal of Lightwave Technology*, vol. 32, no. 4, pp. 553-570, 2014.
- [84] D. Dardari, V. Tralli, and A. Vaccari, "A theoretical characterization of nonlinear distortion effects in OFDM systems," *IEEE Transactions on Communications*, vol. 48, no. 10, pp. 1755-1764, 2000.
- [85] P. Banelli and S. Cacopardi, "Theoretical analysis and performance of OFDM signals in nonlinear AWGN channels," *IEEE Transactions on Communications*, vol. 48, no. 3, pp. 430-441, 2000.
- [86] P. Banelli, "Theoretical analysis and performance of OFDM signals in nonlinear fading channels," *IEEE Transactions on Wireless Communications*, vol. 2, no. 2, pp. 284-293, 2003.
- [87] T. Araujo and R. Dinis, "Analytical evaluation of nonlinear effects on OFDMA signals," *IEEE Transactions on Wireless Communications*, vol. 9, no. 11, pp. 3472-3479, 2010.
- [88] A. Papoulis, *Probability, Random Variables and Stochastic Processes*, 3rd edition, New York: McGraw-Hill, 1991.
- [89] T. Araujo and R. Dinis, "On the accuracy of the Gaussian approximation for the evaluation of nonlinear effects in OFDM signals," *IEEE Transactions on Communications*, vol. 60, no. 2, pp. 346-351, 2012.
- [90] A. J. Lowery, "Fiber nonlinearity pre- and post-compensation for long-haul optical links using OFDM," *Optics Express*, vol. 15, no. 20, pp. 12965-12970, 2007.
- [91] A. J. Lowery, S. Wang, and M. Premaratne, "Calculation of power limit due to fiber nonlinearity in optical OFDM systems," *Optics Express*, vol. 15, no. 20, pp. 13282-13287, 2007.
- [92] M. Nazarathy, J. Khurgin, R. Weidenfeld, Y. Meiman, P. Cho, R. Noe, I. Shpanzter, and V. Karagodsky, "Phased-array cancellation of nonlinear FWM in coherent OFDM dispersive multi-span links," *Optics Express*, vol. 16, no. 20, pp. 15777-15810, 2008.



- [93] C. Sui, B. Hraimel, X. Zhang, L. Wu, Y. Shen, K. Wu, T. Liu, T. Xu, and Q. Nie, "Impact of electro-absorption modulator integrated laser on MB-OFDM ultra-wideband signals over fiber systems," *Journal of Lightwave Technology*, vol. 28, no. 24, pp. 3548-3555, 2010.
- [94] K. Hayasaka, T. Higashino, K. Tsukamoto, and S. Komaki, "A theoretical estimation of IMD on heterogeneous OFDM service over SCM RoF link," *International topical meeting on Microwave Photonics (MWP) 2011*, pp. 328-330.
- [95] W. P. Ng, T. Kanesan, Z. Ghassemlooy, and C. Lu, "Theoretical and experimental optimum system design for LTE-RoF over varying transmission span and identification of system nonlinear limit," *Photonics Journal*, vol. 4, no. 5, pp. 1560-1571, 2012.
- [96] H. Chen, J. Li, K. Xu, Y. Pei, Y. Dai, F. Yin, and J. Lin, "Experimental investigation on multi-dimensional digital predistortion for multi-band radio-over-fiber systems," *Optics Express*, vol. 22, no. 4, pp. 4649-4661, 2014.
- [97] J. Minkoff, "The role of AM-to-PM conversion in memoryless nonlinear systems," *IEEE Transactions on Communications*, vol. 33, no. 2, pp. 139-144, 1985.
- [98] E. Costa and S. Pupolin, "M-QAM-OFDM system performance in the presence of a nonlinear amplifier and phase noise," *IEEE Transactions on Communications*, vol. 50, no. 3, pp. 462-472, 2002.
- [99] G. T. Zhou and J. S. Kenney, "Predicting spectral regrowth of nonlinear power amplifiers," *IEEE Transactions on Communications*, vol. 50, no. 5, pp. 718-722, 2002.
- [100] S. C. J. Lee, S. Randel, F. Breyer, A. M. J. Koonen, "PAM-DMT for intensity-modulated and direct-detection optical communication systems," *Photonics Technology Letters*, vol. 21, no. 23, pp. 1749-1751, 2009.
- [101] R. Mesleh, H. Elgala, and H. Haas, "LED nonlinearity mitigation techniques in optical wireless OFDM communication systems," *Journal of Optical Communications and Networking*, vol. 4, no. 11, pp. 865-875, 2012.
- [102] S. Dimitrov and H. Haas, "Information rate of OFDM-based optical wireless communication systems with nonlinear distortion," *Journal of Lightwave Technology*, vol. 31, no. 6, pp. 918-929, 2013.
- [103] D. Tsonev, S. Sinanovic, and H. Haas, "Complete modeling of nonlinear distortion in OFDM-based optical wireless communication," *Journal of Lightwave Technology*, vol. 31, no. 18, pp. 3064-3076, 2013.
- [104] M. Ranjan and L. E. Larson, "Distortion analysis of ultra-wideband OFDM receiver front-ends," *IEEE Transactions on Microwave Theory and Techniques*, vol. 54, no. 12, pp. 4422-4431, 2006.

- [105] S. H. Han and J. H. Lee, "An overview of peak-to-average power ratio reduction techniques for multicarrier transmission," *IEEE Wireless Communications*, vol. 12, no. 2, pp. 56-65, 2005.
- [106] T. Jiang and Y. Wu, "An overview: peak-to-average power ratio reduction techniques for OFDM signals," *IEEE Transactions on Broadcasting*, vol. 54, no. 2, pp. 257-268, 2008.
- [107] L. S. Fock, R. S. Tucker, "Reduction of distortion in analogue modulated semiconductor lasers by feedforward compensation," *Electronics Letters*, vol. 27, no. 8, pp. 669-671, 1991.
- [108] L. S. Fock, R. S. Tucker, "Simultaneous reduction of intensity noise and distortion in semiconductor lasers by feedforward compensation," *Electronics Letters*, vol. 27, no. 14, pp. 1297-1299, 1991.
- [109] L. S. Fock, A. Kwan, and R. S. Tucker, "Reduction of semiconductor laser intensity noise by feedforward compensation: experiment and theory," *Journal of Lightwave Technology*, vol. 10, no. 12, pp. 1919-1925, 1992.
- [110] D. Hassin and R. Vahldieck, "Feedforward linearization of analog modulated laser diodes-theoretical analysis and experimental verification," *IEEE Transactions on Microwave Theory and Techniques*, vol. 41, no. 12, pp. 2376-2382, 1993.
- [111] B. Buxton, R. Vahldieck, "Noise and intermodulation distortion reduction in an optical feedforward transmitter," *IEEE Microwave Theory and Techniques Society (MTT-S) International Microwave Symposium (IMS) 1994*, paper WE3F-47, pp. 1105-1108.
- [112] T. Iwai, K. Sato, K. Suto, "Signal distortion and noise in AM-SCM transmission systems employing the feedforward linearized MQW-EA external modulator," *Journal of Lightwave Technology*, vol. 13, no. 8, pp. 1606-1612, 1995.
- [113] S.-H. Park and Y.-W. Choi, "Significant suppression of the third intermodulation distortion in transmission system with optical feedforward linearized transmitter," *Photonics Technology Letters*, vol. 17, no. 6, pp. 1280-1282, 2005.
- [114] T. Ismail, C. P. Liu, A. J. Seeds, "Uncooled directly modulated high dynamic range source for IEEE802.11a wireless over fibre LAN applications," *Optical Fiber Communication Conference (OFC) 2004*, paper FE3.
- [115] T. Ismail, J. E. Mitchell, A. J. Seeds, "Linearity enhancement of a directly modulated uncooled DFB laser in a multi-channel wireless-over-fibre system," *IEEE Microwave Theory and Techniques Society (MTT-S) International Microwave Symposium (IMS) 2005*, pp. 7-10.

- [116] T. Ismail, C.-P. Liu, J. E. Mitchell, and A. J. Seeds, "High-dynamic-range wireless-over-fiber link using feedforward linearization," *Journal of Lightwave Technology*, vol. 25, no. 11, pp. 3274-3282, 2007.
- [117] S. K. Korotky and R. M. De Ridder, "Dual parallel modulation schemes for low-distortion analog optical transmission," *IEEE Journal of Selected Areas in Communications*, vol. 8, no. 7, pp. 1377-1381, 1990.
- [118] A. Djupsjobacka, "A linearization concept for integrated-optic modulators," *Photonics Technology Letters*, vol. 4, no. 8, pp. 869-872, 1992.
- [119] J. L. Brooks, R. A. Becker, "Implementation and evaluation of a dual parallel linearization system for AM-SCM video transmission," *Journal of Lightwave Technology*, vol. 11, no. 1, pp. 34-41, 1993.
- [120] H.-D. Jung, S.-K. Han, "Dynamic nonlinearity reduction of DFB-LD by dual parallel modulation," *IEEE Lasers and Electro-Optics Society (LEOS) Annual Meeting 2000*, vol. 1, pp. 74-75, paper MH2.
- [121] H.-D. Jung, S.-K. Han, "Nonlinear distortion suppression in directly modulated DFB-LD by dual-parallel modulation," *Photonics Technology Letters*, vol. 14, no. 7, pp. 980-982, 2002.
- [122] T. M. F. Alves and A. V. T. Cartaxo, "Transmission of OFDM-UWB radio signals in IM-DD optical fiber communication systems employing optimized dual parallel mach-zehnder modulators," *Journal of Optical Communications and Networking*, vol. 5, no. 2, pp. 159-171, 2013.
- [123] L. M. Johnson and H. V. Roussel, "Reduction intermodulation distortion in interferometric optical modulators," *Optics Letters*, vol. 13, no. 10, pp. 928-930, 1988.
- [124] L. M. Johnson and H. V. Roussel, "Linearization of an interferometric modulator at microwave frequencies by polarization mixing," *Photonics Technology Letters*, vol. 2, no. 11, pp. 810-811, 1990.
- [125] B. M. Haas and T. E. Murphy, "A simple, linearized, phase-modulated analog optical transmission system," *Photonics Technology Letters*, vol. 19, no. 10, pp. 729-731, 2007.
- [126] B. Masella and X. Zhang, "Linearized optical single-sideband Mach-Zehnder modulator for radio-over-fiber systems," *Photonics Technology Letters*, vol. 19, no. 24, pp. 2024-2026, 2007.
- [127] B. Masella, B. Hraimel, and X. Zhang, "Enhanced spurious-free dynamic range using mixed polarization in optical single sideband Mach-Zehnder modulator," *Journal of Lightwave Technology*, vol. 27, no. 15, pp. 3034-3041, 2009.

- [128] B. Hraimel, X. Zhang, W. Jiang, K. Wu, T. Liu, T. Xu, Q. Nie, K. Xu, "Experimental demonstration of mixed-polarization to linearize electro-absorption modulators in radio-over-fiber links," *Photonics Technology Letters*, vol. 23, no. 4, pp. 230-232, 2011.
- [129] B. Hraimel and X. Zhang, "Performance improvement of radio-over fiber links using mixed-polarization electro-absorption modulators," *IEEE Transactions on Microwave Theory and Techniques*, vol. 59, no. 12, pp. 3239-3248, 2011.
- [130] B. Hraimel, X. Zhang, T. Liu, T. Xu, Q. Nie, and D. Shen, "Performance enhancement of an OFDM ultra-wideband transmission-over-fiber link using a linearized mixed-polarization single-drive x-cut MachZehnder modulator," *IEEE Transactions on Microwave Theory and Techniques*, vol. 60, no. 10, pp. 3328-3338, 2012.
- [131] S.-Y. Lee, B.-J. Koo, H.-D. Jung, and S.-K. Han, "Reduction of chromatic dispersion effects and linearization of dual-drive Mach-Zehnder modulator by using semiconductor optical amplifier in analog optical links," *European Conference on Optical Communication (ECOC) 2002*, paper P3.32.
- [132] D.-H. Jeon, H.-D. Jung, and S.-K. Han, "Mitigation of dispersion-induced effects using SOA in analog optical transmission," *Photonics Technology Letters*, vol. 14, no. 8, pp. 1166-1168, 2002.
- [133] G. Yabre, J. Le Bihan, "Reduction of nonlinear distortion in directly modulated semiconductor lasers by coherent light injection," *Journal of Quantum Electronics*, vol. 33, no. 7, pp. 1132-1140, 1997.
- [134] S.-H. Lee, J.-M. Kang, Y.-Y. Won, H.-C. Kwon, and S.-K. Han, "Linearization of RoF optical source by using light-injected gain modulation," *International topical meeting on Microwave Photonics (MWP) 2005*, pp.265-268.
- [135] S.-H. Lee, J.-M. Kang, I.-H. Choi, and S.-K. Han, "Linearization of DFB laser diode by external light-injected cross-gain modulation for radio-over-fiber link," *Photonics Technology Letters*, vol. 18, no. 14, pp. 1545-1547, 2006.
- [136] C. Sun, D. Liu, B. Xiong, Y. Luo, J. Wang, Z. Hao, Y. Han, L. Wang, H. Li, "Modulation characteristics enhancement of monolithically integrated laser diodes under mutual injection locking," *Journal of Selected Topics in Quantum Electronics*, vol. 21, no. 6, pp. 628-635, 2015.
- [137] R. B. Childs and V. A. O'Byrne, "Predistortion linearization of directly modulated DFB lasers and external modulators for AM video transmission," *Optical Fiber Communication Conference (OFC) 1990*, paper WH6.
- [138] R. B. Childs, V. A. O'Byrne, V.A., "Multichannel AM video transmission using a high-power Nd:YAG laser and linearized external modulator," *Journal on Selected Areas in Communications*, vol. 8, no. 7, pp. 1369-1376, 1990.

- [139] H.-T. Lin, Y.-H. Kao, "A predistortion technique for multichannel AM-VSB lightwave CATV systems," IEEE Lasers and Electro-Optics Society (LEOS) Annual Meeting 1995, vol. 2, pp. 367-368, paper OC8.4.
- [140] H.-T. Lin, Y.-H. Kao, "Nonlinear distortions and compensations of DFB laser diode in AM-VSB lightwave CATV applications," Journal of Lightwave Technology, vol. 14, no. 11, pp. 2567-2574, 1996.
- [141] T. Iwai, K. Sato, K. Suto, "Reduction of dispersion-induced distortion in SCM transmission systems by using predistortion-linearized MQW-EA modulators," Journal of Lightwave Technology, vol. 15, no. 2, pp. 169-178, 1997.
- [142] G. C. Wilson, "Optimized predistortion of overmodulated Mach-Zehnder modulators with multicarrier input," Photonics Technology Letters, vol. 9, no. 11, pp. 1535-1537, 1997.
- [143] L. Roselli, V. Borgioni, F. Zepparelli, F. Ambrosi, M. Comez, P. Faccin, A. Casini, "Analog laser predistortion for multiservice radio-over-fiber systems," Journal of Lightwave Technology, vol. 21, no. 5, pp. 1211-1223, 2003.
- [144] Y. Chiu, B. Jalali, S. Garner, W. Steier, "Broadband linearization of externally modulated fiber-optic links," International Topical Meeting on Microwave Photonics (MWP) 1998, pp. 49-50.
- [145] Y. Chiu, B. Jalali, S. Garner, W. Steier, "Broad-band electronic linearizer for externally modulated analog fiber-optic links," Photonics Technology Letters, vol. 11, no. 1, pp. 48-50, 1999.
- [146] R. Sadhwani and B. Jalali, "Adaptive CMOS predistortion linearizer for fiber-optic links," Journal of Lightwave Technology, vol. 21, no. 12, pp. 3180-3193, 2003.
- [147] A. R. Shah and B. Jalali, "Adaptive equalisation for broadband predistortion linearisation of optical transmitters," IEE Proceedings-Optoelectronics, vol. 152, no. 1, pp. 16-32, 2005.
- [148] V. J. Urick, M. S. Rogge, P. F. Knapp, L. Swingen, F. Bucholtz, "Wide-band predistortion linearization for externally modulated long-haul analog fiber-optic links," IEEE Transactions on Microwave Theory and Techniques, vol. 54, no. 4, pp. 1458-1463, 2006.
- [149] Y. Shen, B. Hraimel, X. Zhang, G. E. R. Cowan, K. Wu, and T. Liu, "A novel analog broadband RF predistortion circuit to linearize electro-absorption modulators in multiband OFDM radio-over-fiber systems," IEEE Transactions on Microwave Theory and Techniques, vol. 58, no. 11, pp. 3327-3335, 2010.
- [150] B. Hraimel and X. Zhang, "Low-cost broadband predistortion-linearized single-drive x-cut Mach-Zehnder modulator for radio-over-fiber systems," Photonics Technology Letters, vol. 24, no. 18, pp. 1571-1573, 2012.

- [151] R. Zhu, X. Zhang, B. Hraimel, D. Shen, T. Liu, "Broadband predistortion circuit using zero bias diodes for radio over fiber systems," *Photonics Technology Letters*, vol. 25, no. 21, pp. 2101-2104, 2013.
- [152] R. Zhu, Z. Xuan, Y. Zhang, X. Zhang, D. Shen, "Novel broadband analog predistortion circuit for radio-over-fiber systems," *IEEE Microwave Theory and Techniques Society (MTT-S) International Microwave Symposium (IMS)* 2015.
- [153] A. Hekkala, M. Hiivala, M. Lasanen, J. Perttu, L. C. Vieira, and N. J. Gomes, A. Nkansah, "Predistortion of radio over fiber links: algorithms, implementation, and measurements," *IEEE Transactions on Circuits and Systems I*, vol. 59, no. 3, pp. 664-672, 2012.
- [154] C. Han, S. Cho, H. S. Chung, J. H. Lee, "Linearity improvement of directly-modulated multi-IF-over-fibre LTE-A mobile fronthaul link using shunt diode predistorter," *European Conference on Optical Communication (ECOC)* 2015, paper We.4.4.4.
- [155] W. G. Jeon, K. H. Chang, and Y. S. Cho, "An adaptive data predistorter for compensation of nonlinear distortion in OFDM systems," *IEEE Transactions on Communications*, vol. 45, no. 10, pp. 1167-1171, 1997.
- [156] H. W. Kang, Y. S. Cho, D. H. Youn, "On compensating nonlinear distortions of an OFDM system using an efficient adaptive predistorter," *IEEE Transactions on Communications*, vol. 47, no. 4, pp. 522-526, 1999.
- [157] T. Sadeghpour Ghazaany, "Design and implementation of adaptive baseband predistorter for OFDM nonlinear transmitter," Ph.D. thesis, University of Bradford, 2011.
- [158] L. Ding, G. T. Zhou, D. R. Morgan, Z. Ma, J. S. Kenney, J. Kim, and C. R. Giardina, "A robust digital baseband predistorter constructed using memory polynomials," *IEEE Transactions on Communications*, vol. 52, no. 1, pp. 159-165, 2004.
- [159] D. R. Morgan, Z. Ma, J. Kim, M. G. Zierdt, J. Pastalan, "A generalized memory polynomial model for digital predistortion of RF power amplifiers," *IEEE Transactions on Signal Processing*, vol. 54, no. 10, pp. 3852-3860, 2006.
- [160] Y. Tang, K.-P. Ho, W. Shieh, "Optimal design for coherent optical OFDM transmitter employing pre-distortion," *European Conference on Optical Communication (ECOC)* 2007.
- [161] Y. Tang, W. Shieh, Y. Xingwen, R. Evans, "Optimum design for RF-to-optical up-converter in coherent optical OFDM systems," *Photonics Technology Letters*, vol. 19, no. 7, pp. 483-485, 2007.

- [162] Y. Tang, K.-P. Ho, W. Shieh, "Coherent optical OFDM transmitter design employing predistortion," *Photonics Technology Letters*, vol. 20, no. 11, pp. 954-956, 2008.
- [163] D. J. F. Barros and J. M. Kahn, "Optical modulator optimization for orthogonal frequency-division multiplexing," *Journal of Lightwave Technology*, vol. 27, no. 13, pp. 2370-2378, 2009.
- [164] T. F. Alves, J. Morgado, and A. Cartaxo, "Linearity improvement of directly modulated PONs by digital pre-distortion of coexisting OFDM-based signals," *Advanced Photonics Congress 2012*, paper AW4A.2.
- [165] J. Zhang, J. Wang, M. Xu, F. Lu, L. Chen, J. Yu, and G.-K. Chang, "Memory-polynomial digital pre-distortion for linearity improvement of directly-modulated multi-IF-over-fiber LTE mobile fronthaul," *Optical Fiber Communication Conference (OFC) 2016*, paper Tu2B.3.
- [166] Z. Jia, H.-C. Chien, Y. Cai, J. Yu, B. Zhu, C. Ge, T. Wang, S. Shi, H. Wang, Y. Xia, and Y. Chen, "Experimental demonstration of PDM-32QAM single-carrier 400G over 1200-km transmission enabled by training-assisted pre-equalization and look-up table," *Optical Fiber Communication Conference (OFC) 2016*, paper Tu3A.4.
- [167] Y. Wang, J. Yu and N. Chi, "Demonstration of 4x128-Gb/s DFT-S OFDM signal transmission over 320-km SMF with IM/DD," *Photonics Journal*, vol. 8, no. 2, article 7903209, 2016.
- [168] B. Guo, W. Cao, A. Tao, D. Samardzija, "LTE/LTE-A signal compression on the CPRI interface," *Bell Labs Technical Journal*, vol.18, no.2, pp.117-133, 2013.
- [169] S.H. Park, O. Simeone, O. Sahin, S. Shamai, "Fronthaul compression for cloud radio access networks: signal processing advances inspired by network information theory," *IEEE Signal Processing Magazine*, vol.31, no.6, pp.69-79, 2014.
- [170] N. Shibata, T. Tashiro, S. Kuwano, N. Yuki, J. Terada, A. Otaka, "Mobile front-haul employing ethernet-based TDM-PON system for small cells," *Optical Fiber Communication Conference (OFC) 2015*, paper, M2J.1.
- [171] Y. Ma, Z. Xu, H. Lin, M. Zhou, H. Wang, C. Zhang, J. Yu, X. Wang, "Demonstration of CPRI over self-seeded WDM-PON in commercial LTE environment," *Optical Fiber Communication Conference (OFC) 2015*, paper M2J.6.
- [172] K. Miyamoto, S. Kuwano, J. Terada, and A. Otaka, "Split-PHY processing architecture to realize base station coordination and transmission bandwidth reduction in mobile fronthaul," *Optical Fiber Communication Conference (OFC) 2015*, paper M2J.4.

- [173] K. Miyamoto, S. Kuwano, J. Terada, and A. Otaka, "Analysis of mobile fronthaul bandwidth and wireless transmission performance in split-PHY processing architecture," *Optics Express*, vol. 24, no. 2, pp. 1261-1268, 2016.
- [174] R. Gray, "Oversampled sigma-delta modulation," *IEEE Transactions on Communications*, vol. 35, no. 5, pp. 481-489, 1987.
- [175] P. M. Aziz, H. V. Sorensen and J. V. der Spiegel, "An overview of sigma-delta converters," *IEEE Signal Processing Magazine*, vol. 13, no. 1, pp. 61-84, 1996.
- [176] W. R. Bennett, "Spectra of quantized signals," *Bell System Technical Journal*, vol. 27, no. 3, pp. 446-472, 1948.
- [177] J. C. Candy and G. C. Temes, *Oversampling Delta Sigma Data Converters*, ISBN 978-0-87942-285-1, 512 pages, John Wiley & Sons, Aug. 1991.
- [178] S. R. Norsworthy, R. Schreier, G. C. Temes, *Delta-Sigma Data Converters*, ISBN 978-0-7803-1045-2, 512 pages, Wiley-IEEE Press, Oct. 1996.
- [179] R. Schreier and G. C. Temes, *Understanding Delta-Sigma Data Converters*, ISBN 978-0-471-46585-0, 464 pages, Wiley-IEEE Press, Nov. 2004.
- [180] R. Schreier, High-level design and simulation of delta-sigma modulators, <http://www.mathworks.com/matlabcentral/fileexchange/19-delta-sigma-toolbox>, Jun 2016.
- [181] S. Yan and E. Sanchez-Sinencio, "A continuous-time sigma-delta modulator with 88-dB dynamic range and 1.1-MHz signal bandwidth," *IEEE Journal of Solid-State Circuits*, vol. 39, no. 1, pp. 75-86, 2004.
- [182] A. Jerng and C. G. Sodini, "A wideband  $\Delta\Sigma$  digital-RF modulator for high data rate transmitters," *IEEE Journal of Solid-State Circuits*, vol. 42, no. 8, pp. 1710-1722, 2007.
- [183] M. Helaoui, S. Hatami, R. Negra and F. M. Ghannouchi, "A novel architecture of delta-sigma modulator enabling all-digital multiband multistandard RF transmitters design," *IEEE Transactions on Circuits and Systems II: Express Briefs*, vol. 55, no. 11, pp. 1129-1133, 2008.
- [184] S. A. Bassam, W. Chen, M. Helaoui and F. M. Ghannouchi, "Transmitter architecture for CA: carrier aggregation in LTE-advanced systems," *IEEE Microwave Magazine*, vol. 14, no. 5, pp. 78-86, 2013.
- [185] A. Frappe, A. Flament, B. Stefanelli, A. Kaiser and A. Cathelin, "An all-digital RF signal generator using high-speed  $\Delta\Sigma$  modulators," *IEEE Journal of Solid-State Circuits*, vol. 44, no. 10, pp. 2722-2732, 2009.



- [186] A. Pozsgay, T. Zounes, R. Hossain, M. Boulemnaker, V. Knopik and S. Grange, "A fully digital 65nm CMOS transmitter for the 2.4-to-2.7GHz WiFi/WiMAX bands using 5.4 GHz  $\Delta\Sigma$  RF DACs," IEEE International Solid-State Circuits Conference (ISSCC) 2008, pp. 360-361, 619.
- [187] S. Chung, R. Ma, S. Shinjo, and K. H. Teo, "Inter-band carrier aggregation digital transmitter architecture with concurrent multi-band delta-sigma modulation using out-of-band noise cancellation," IEEE MTT-S International Microwave Symposium 2015.
- [188] 8.6 GSa/s S. Chung, R. Ma, S. Shinjo, H. Nakamizo, K. Parsons and K. H. Teo, "Concurrent multiband digital outphasing transmitter architecture using multidimensional power coding," IEEE Transactions on Microwave Theory and Techniques, vol. 63, no. 2, pp. 598-613, 2015.
- [189] T. Kitayabu, Y. Amano, and H. Ishikawa, "Concurrent dual-band transmitter architecture for spectrum aggregation system," IEEE Radio and Wireless Symposium (RWS) 2010, pp. 689-692.
- [190] N. V. Silva, A. S. R. Oliveira and N. B. Carvalho, "Design and optimization of flexible and coding efficient all-digital RF transmitters," IEEE Transactions on Microwave Theory and Techniques, vol. 61, no. 1, pp. 625-632, 2013.
- [191] T. P. Hung, J. Rode, L. E. Larson and P. M. Asbeck, "Design of H-bridge class-D power amplifiers for digital pulse modulation transmitters," IEEE Transactions on Microwave Theory and Techniques, vol. 55, no. 12, pp. 2845-2855, 2007.
- [192] M. Nielsen and T. Larsen, "A transmitter architecture based on delta-sigma modulation and switch-mode power amplification," IEEE Transactions on Circuits and Systems II: Express Briefs, vol. 54, no. 8, pp. 735-739, 2007.
- [193] F. M. Ghannouchi, S. Hatami, P. Aflaki, M. Helouai and R. Negra, "Accurate power efficiency estimation of GHz wireless delta-sigma transmitters for different classes of switching mode power amplifiers," IEEE Transactions on Microwave Theory and Techniques, vol. 58, no. 11, pp. 2812-2819, 2010.
- [194] J. A. Wepman, "Analog-to-digital converters and their applications in radio receivers," IEEE Communications Magazine, vol. 33, no. 5, pp. 39-45, May 1995.
- [195] M. R. Miller and C. S. Petrie, "A multibit sigma-delta ADC for multimode receivers," IEEE Journal of Solid-State Circuits, vol. 38, no. 3, pp. 475-482, 2003.
- [196] T. Kitayabu, Y. Ikeda, Y. Amano and H. Ishikawa, "Concurrent dual-band receiver for spectrum aggregation system," IEEE Radio and Wireless Symposium (RWS) 2009, paper WE2C-1, pp. 634-637.

- [197] C. Wu, E. Alon and B. Nikoli, "A wideband 400 MHz-to-4 GHz direct RF-to-digital multimode  $\Delta\Sigma$  receiver," *IEEE Journal of Solid-State Circuits*, vol. 49, no. 7, pp. 1639-1652, 2014.
- [198] L. Bettini, T. Christen, T. Burger and Q. Huang, "A reconfigurable DT  $\Delta\Sigma$  modulator for multi-standard 2G/3G/4G wireless receivers," *IEEE Journal on Emerging and Selected Topics in Circuits and Systems*, vol. 5, no. 4, pp. 525-536, 2015.
- [199] J. Arias, P. Kiss, V. Prodanov, V. Boccuzzi, M. Banu, D. Bisbal, J. San Pablo, L. Quintanilla, and J. Barbolla, "A 32-mW 320-MHz continuous-time complex delta-sigma ADC for multi-mode wireless-LAN receivers," *IEEE Journal of Solid-State Circuits*, vol. 41, no. 2, pp. 339-351, 2006.
- [200] K. B. stman, M. Englund, O. Viitala, K. Stadius, K. Koli and J. Ryyanen, "Next-generation RF front-end design methods for direct  $\Delta\Sigma$  receivers," *IEEE Journal on Emerging and Selected Topics in Circuits and Systems*, vol. 5, no. 4, pp. 514-524, 2015.
- [201] A. Kanno, T. Kawanishi, "Analog signal transmission by FPGA-based pseudo-delta-sigma modulator," *Photonics Conference (IPC) 2015*, paper WC2.3, pp.136-137.
- [202] S. Jang, G. Jo, J. Jung, B. Park, S. Hong, "A digitized IF-over-fiber transmission based on low-pass delta-sigma modulation," *Photonics Technology Letters*, vol. 26, no. 24, pp. 2484-2487, 2014.
- [203] L. M. Pessoa, J. S. Tavares, D. Coelho, and H. M. Salgado, "Experimental evaluation of a digitized fiber-wireless system employing sigma delta modulation," *Optics Express*, vol. 22, no. 14, pp. 17508-17523, 2014.
- [204] T. Maehata, S. Kameda, N. Suematsu, "A novel channel coding scheme for digital RF transmitter comprising a 1-bit band-pass delta-sigma modulator," *Asia-Pacific Microwave Conference (APMC) 2014*, paper TH3G-18, pp.932-934.
- [205] Z. Yu, A.J. Redfern, G.T. Zhou, "Using delta-sigma modulators in visible light OFDM systems," *Wireless and Optical Communication Conference (WOCC)*, paper O6.3, May 2014.
- [206] H. Qian, J. Chen, S. Yao, Z. Yu, H. Zhang, W. Xu, "One-bit sigma-delta modulator for nonlinear visible light communication systems," *Photonics Technology Letters*, vol.27, no.4, pp.419-422, 2015.
- [207] K. Kitamura, S. Sasaki, Y. Matsuya and T. Douseki, "Optical wireless digital-sound transmission system with 1-bit  $\Delta\Sigma$ -modulated visible light and spherical Si solar cells," *IEEE Sensors Journal*, vol. 10, no. 11, pp. 1753-1758, 2010.
- [208] 3GPP TS 36.104 V.12.6.0, "Base Station (BS) radio transmission and reception," Release 12, Feb 2015.

- [209] 3GPP TS 36.141 V.14.1.0, “Base Station (BS) conformance testing,” Release 14, Sep 2016.

## PUBLICATIONS

### Journal papers

#### 2017

- [1] **J. Wang**, Z. Yu, K. Ying, J. Zhang, F. Lu, M. Xu, L. Cheng, X. Ma, G.-K. Chang, “Digital mobile fronthaul based on delta-sigma modulation for 32 LTE carrier aggregation and FBMC signals,” *Journal of Optical Communications and Networking*, vol. 9, no. 2, pp. TBD, 2017. (*invited, editors’ pick*)

#### 2016

- [2] M. Xu, J.-H. Yan, J. Zhang, F. Lu, **J. Wang**, L. Cheng, D. Guidotti, and G.-K. Chang, “Bidirectional fiber-wireless access technology for 5G mobile spectral aggregation and cell densification,” *Journal of Optical Communications and Networking*, vol. 8, no. 12, pp. B104-B110, 2016.
- [3] F. Lu, M. Xu, L. Cheng, **J. Wang**, J. Zhang, and G.-K. Chang. “Non-Orthogonal Multiple Access With Successive Interference Cancellation in Millimeter-Wave Radio-Over-Fiber Systems,” *Journal of Lightwave Technology*, vol. 34, no. 17, pp. 4179-4186, 2016.
- [4] **J. Wang**, C. Liu, J. Zhang, M. Zhu, M. Xu, F. Lu, L. Cheng, and G.-K. Chang, “Nonlinear inter-band subcarrier intermodulations for multi-RAT OFDM wireless services in 5G heterogeneous mobile fronthaul networks,” *Journal of Lightwave Technology*, vol. 34, no. 17, pp. 4089-4103, 2016.
- [5] M. Xu, J. Zhang, F. Lu, **J. Wang**, L. Cheng, D. Guidott, G.-K. Chang, “Orthogonal multiband CAP modulation based on offset-QAM and advanced filter design in spectral efficient MMW RoF systems,” accepted by *Journal of Lightwave Technology*, 2016.
- [6] J. Zhang, M. Xu, **J. Wang**, F. Lu, L. Cheng, H. Cho, K. Ying, J. Yu, and G.-K. Chang, “Full-duplex quasi-gapless carrier-aggregation using FBMC in centralized radio-over-fiber heterogeneous networks,” accepted by *Journal of Lightwave Technology*, 2016. (*invited*)
- [7] L. Cheng, M. M. U. Gul, F. Lu, M. Zhu, **J. Wang**, M. Xu, X. Ma, and G.-K. Chang, “Coordinated multipoint transmissions in millimeter-wave radio-over-fiber systems,” *Journal of Lightwave Technology*, vol. 34, no. 2, pp. 653-660, 2016. (*invited*)
- [8] M. Xu, J. Zhang, F. Lu, **J. Wang**, L. Cheng, H. J. Cho, M. I. Khalil, D. Guidotti, and G.-K. Chang, “FBMC in next-generation mobile fronthaul networks with centralized pre-equalization,” *Photonics Technology Letters*, vol. 28, no. 18, pp. 1912-1915, 2016.

- [9] J. Zhang, **J. Wang**, Y. Xu, M. Xu, F. Lu, L. Cheng, J. Yu, and G.-K. Chang, "Fiber-wireless integrated mobile backhaul network based on a hybrid millimeter-wave and free-space-optics architecture with an adaptive diversity combining technique," *Optics Letters*, vol. 41, no. 9, pp. 1909-1912, 2016.
- [10] B. Wu, J.-Y. Sung, J.-H. Yan, M. Xu, **J. Wang**, F. Yan, S. Jian, and G.-K. Chang, "Polarization-insensitive remote access unit for radio-over-fiber mobile fronthaul system by reusing polarization orthogonal light waves," *Photonics Journal*, vol. 8, no. 1, article 7200108, 2016.

## 2015

- [11] B. Wu, M. Zhu, J. Zhang, **J. Wang**, M. Xu, F. Yan, S. Jian, and G.-K. Chang, "Multi-service RoF links with colorless upstream transmission based on orthogonal phase-correlated modulation," *Optics Express*, vol. 23, no. 14, pp. 18323-18329, 2015.
- [12] M. Xu, Y.-C. Chi, **J. Wang**, L. Cheng, F. Lu, M. I. Khalil, C.-T. Tsai, G.-R. Lin, and G.-K. Chang, "Wavelength sharing and reuse in dual-band WDM-PON systems employing WRC-FPLDs," *Photonics Technology Letters*, vol. 27 no. 17, pp. 1821-1824, 2015.
- [13] T. Su, J. Zheng, **J. Wang**, Z. Dong, M. Xu, M. Zhang, X. Chen, and G.-K. Chang, "Multi-service wireless transport over RoF link with colorless BS using PolM-to-IM convertor," *Photonics Technology Letters*, vol. 27, no. 4, pp. 403-406, 2015.
- [14] B. Wu, M. Zhu, M. Xu, **J. Wang**, M. Wang, F. Yan, S. Jian, and G.-K. Chang, "Flexible compensation of dispersion-induced power fading for multi-service RoF links based on a phase-coherent orthogonal lightwave generator," *Optics Letters*, vol. 40, no. 9, pp. 2103-2106, 2015.

## 2014

- [15] C. Liu, **J. Wang**, L. Cheng, M. Zhu, and G.-K. Chang, "Key microwave-photonics technologies for next-generation cloud-based radio access networks," *Journal of Lightwave Technology*, vol. 32, no. 20, pp. 3452-3460, 2014. (*invited*)
- [16] **J. Wang**, C. Liu, M. Zhu, A. Yi, L. Cheng, and G. K. Chang, "Investigation of data-dependent channel cross-modulation in multiband radio-over-fiber systems," *Journal of Lightwave Technology*, vol. 32, no. 10, pp. 1861-1871, 2014.
- [17] L. Cheng, M. Zhu, **J. Wang**, M. Xu, F. Lu, and G.-K. Chang, "Photonic precoding for millimeter-wave multicell MIMO in centralized RoF system," *Photonics Technology Letters*, vol. 26, no. 11, pp. 1116 - 1119, 2014.

- [18] J. Zheng, **J. Wang**, J. Yu, M. Zhu, Z. Dong, X. Wang, T. Su, J. Liu, N. Zhu, and G.-K. Chang, "Photonic microwave-signal-mixing technique using phase-coherent orthogonal optical carriers for radio-over-fiber application," *Optics Letters*, vol.39, no.18, pp. 5263-5266, 2014.

## 2013

- [19] C. Liu, L. Zhang, M. Zhu, **J. Wang**, L. Cheng, and G.-K. Chang, "A novel multi-service small-cell cloud radio access network for mobile backhaul and computing based on radio-over-fiber technologies," *Journal of Lightwave Technology*, vol. 31, no. 17, pp. 2869-2875, 2013.
- [20] M. Zhu, L. Zhang, **J. Wang**, L. Cheng, C. Liu, and G. K. Chang, "Radio-over-fiber access architecture for integrated broadband wireless services," *Journal of Lightwave Technology*, vol. 31, no. 23, pp. 3614-3620, 2013.
- [21] A.-L. Yi, L.-S. Yan, C. Liu, M. Zhu, **J. Wang**, L. Zhang, C.-H. Ye, G.-K. Chang, "Frequency offset compensation and carrier phase recovery for differentially encoded 16-QAM vector signal in a 60-GHz RoF system," *Photonics Journal*, vol. 5, no. 4, article 7200807, 2013.
- [22] L. Cheng, C. Liu, Z. Dong, **J. Wang**, M. Zhu, G.-K. Chang, "Real-time dual-band wireless videos in millimeter-wave radio-over-fiber system," *Optical Fiber Technology*, vol. 19, no. 6, part A, pp. 529-532, 2013.

## Conference proceedings

### 2017

- [1] **J. Wang**, Z. Jia, L. A. Campos, C. Knittle, G.-K. Chang, "Optical coherent transmission of 20x192-MHz DOCSIS 3.1 channels with 16384QAM based on delta-sigma digitization," accepted by *Optical Fiber Communication Conference (OFC)* 2017. (*top score*)

### 2016

- [2] J. Zhang, **J. Wang**, M. Xu, F. Lu, L. Cheng, J. Yu, G.-K. Chang, "Full-duplex mobile backhaul transportation based on fiber-wireless integrated FSO and MMW hybrid links with adaptive signal processing to combat diverse weather conditions," *European Conference on Optical Communication (ECOC)* 2016, paper W.1.E.2.
- [3] **J. Wang**, Z. Yu, K. Ying, J. Zhang, F. Lu, M. Xu, L. Cheng, X. Ma, and G.-K. Chang, "10-Gbaud OOK/PAM4 digital mobile fronthaul based on one-bit/two-bit delta-sigma modulation supporting carrier aggregation of 32 LTE-A signals with up to 256 and 1024QAM," *European Conference on Optical Communication (ECOC)* 2016, paper W.4.P1.

- [4] J. Zhang, **J. Wang**, M. Xu, F. Lu, L. Cheng, and J. Yu, and G.-K. Chang, “Full-duplex asynchronous quasi-gapless carrier-aggregation using filter-bank multi-carrier in MMW radio-over-fiber heterogeneous mobile access networks,” *Optical Fiber Communication Conference (OFC)* 2016, paper Tu2B.2. (*top score*)
- [5] J. Zhang, **J. Wang**, M. Xu, F. Lu, L. Cheng, J. Yu, and G.-K. Chang, “Memory-polynomial digital pre-distortion for linearity improvement of directly-modulated multi-IF-over-fiber LTE mobile fronthaul,” *Optical Fiber Communication Conference (OFC)* 2016, paper Tu2B.3.
- [6] F. Lu, Y.-C. Chi, M. Xu, L. Cheng, **J. Wang**, C.-T. Tsai, G.-R. Lin, and G.-K. Chang, “Cost-effective bi-directional mobile fronthaul employing WRC-FPLD for beyond LTE-advanced services,” *Optical Fiber Communication Conference (OFC)* 2016, paper Tu2B.5.
- [7] **J. Wang**, Z. Yu, K. Ying, J. Zhang, F. Lu, M. Xu, and G.-K. Chang, “Delta-sigma modulation for digital mobile fronthaul enabling carrier aggregation of 32 4G-LTE / 30 5G-FBMC signals in a single- 10-Gb/s IM-DD channel,” *Optical Fiber Communication Conference (OFC)* 2016, paper W1H.2. (*top score*)
- [8] M. Xu, J. Zhang, F. Lu, L. Cheng, **J. Wang**, D. Guidotti, T. Kanesan, S. M. Mitani, and G.-K. Chang, “Multiband OQAM CAP modulation in MMW RoF systems with enhanced spectral and computational efficiency,” *Optical Fiber Communication Conference (OFC)* 2016, paper Tu3B.3. (*top score*)
- [9] L. Cheng, M. Xu, F. Lu, **J. Wang**, J. Zhang, X. Ma, and G.-K. Chang, “Millimeter-wave cell grouping for optimized coverage based on radio-over-fiber and centralized processing,” *Optical Fiber Communication Conference (OFC)* 2016, paper Th2A.17.

## 2015

- [10] **J. Wang**, N. Cvijetic, K. Kanonakis, T. Wang, and G.-K. Chang, “Novel optical access network virtualization and dynamic resource allocation algorithms for the internet of things,” *Optical Fiber Communications Conference (OFC)* 2015, paper Tu2E.3.
- [11] F. Lu, L. Cheng, M. Zhu, **J. Wang**, M. Xu, X. Ma, and G.-K. Chang, “Generalized frequency division multiplexing for photonic-assisted millimeter-wave carrier aggregation,” *Optical Fiber Communications Conference (OFC)* 2015, paper M3E.3.
- [12] J. Zhang, M. Xu, **J. Wang**, F. Lu, L. Cheng, M. Zhu, I. Khalil, J. Yu, and G.-K. Chang, “Carrier aggregation for MMW inter-RAT and intra-RAT in next generation heterogeneous mobile data network based on optical domain band mapping,” *European Conference on Optical Communication (ECOC)* 2015, paper We.4.4.5.

## 2014

- [13] T. Su, J. Zheng, **J. Wang**, M. Zhu, Z. Dong, M. Xu, M. Zhang, X. Chen, G.-K. Chang, "Demonstration of 54.8-GHz radio-over-fiber system with wavelength reuse based on distributed intensity conversion," *IEEE Avionics and Vehicle Fiber-Optics and Photonics Conference (AVFOP)* 2014, paper TuC5, pp.19-20.
- [14] M. Xu, **J. Wang**, M. Zhu, L. Cheng, Y. M. Alfadhli, Z. Dong, and G.K. Chang, "Non-overlapping downlink and uplink wavelength reuse in WDM-PON employing microwave photonic techniques," *European Conference on Optical Communication (ECOC)* 2014, P.7.17.
- [15] **J. Wang**, C. Liu, M. Zhu, M. Xu, Z. Dong, G.-K. Chang, "Characterization and mitigation of nonlinear intermodulations in multichannel OFDM radio-over-fiber systems," *European Conference on Optical Communication (ECOC)* 2014, paper P.7.18.
- [16] F. Lu, **J. Wang**, L. Cheng, M. Xu, M. Zhu and G.-K. Chang, "Millimeter-wave radio-over-fiber access architecture for implementing real-time cloud computing service," *Conference on Lasers and Electro-Optics (CLEO)* 2014, paper STu1J.1.
- [17] M. Zhu, L. Cheng, **J. Wang**, C. Liu, and G.-K. Chang, "Adaptive photonic-assisted M-ary ASK/M-QAM millimeter-wave synthesis in multi-antenna radio-over-fiber system," *Optical Fiber Communications Conference (OFC)* 2014, paper W1J.1.
- [18] L. Cheng, C. Liu, M. Zhu, **J. Wang** and G.-K. Chang, "Centralized optical pre-coding for multi-cell MIMO in millimeter-wave radio-over-fiber system," *Optical Fiber Communications Conference (OFC)* 2014, paper M3D.3.
- [19] L. Cheng, C. Liu, M. Zhu, **J. Wang** and G.-K. Chang, "Optical CoMP transmission in millimeter-wave small cells for mobile fronthaul," *Optical Fiber Communications Conference (OFC)* 2014, paper W2A.43.

## 2013

- [20] M. Zhu, A. Yi, Y.-T. Hsueh, C. Liu, **J. Wang**, S.-C. Shin, J. Yu, and G.-K. G. Chang, "Demonstration of 4-Band millimeter-wave radio-over-fiber system for multi-service wireless access networks," *Optical Fiber Communications Conference (OFC)* 2013, paper OM3D.4.
- [21] **J. Wang**, C. Liu, M. Zhu, A. Yi, G.-K. Chang, "Closed-form analysis of intra/inter-band cross-modulation in multiband radio-over-fiber systems," *IEEE Global Communications Conference (Globecom)* 2013, pp. 2454-2460.
- [22] **J. Wang**, C. Liu, M. Zhu, G.-K. Chang, "Investigation of intra/inter-band cross-modulation in multiband radio-over-fiber systems," *IEEE International Conference on Communications (ICC)* 2013 - workshop on Optical-Wireless Integrated Technology for Systems and Networks, pp. 843-847.



- [23] L. Rao, C. Liu, M. Zhu, **J. Wang**, G.-K. Chang, “A novel full-duplex 60-GHz radio-over-fiber transmission system for next-generation wireless access networks,” *Conference on Lasers and Electro-Optics (CLEO)* 2013, paper CM3G.1.
- [24] **J. Wang**, C. Liu, M. Zhu, A. Yi, G.-K. Chang, “Investigation of intra/inter-band cross-modulation in multi-band radio-over-fiber systems,” *Conference on Lasers and Electro-Optics (CLEO)* 2013, paper CM3G.5.
- [25] M. Zhu, **J. Wang**, C. Liu, L. Chen and G. K. Chang, “Real-time WiFi and gigabit data transmission in multiband 60-GHz radio-over-fiber system for band-mapped broadband wireless services,” *IEEE Photonics Conference (IPC)* 2013, pp. 205-206.

## VITA

Jing Wang was born in 1983 in Shanghai, China. He received the B.E. and M.S.E degrees in Physical Electronics and Optoelectronics from the Department of Electronic Engineering, Tsinghua University, Beijing, China, in 2006 and 2009, respectively. In 2007 and 2009, he was a visiting student at the Italian National Laboratory of Photonic Networks and Scuola Superiore Sant'Anna in Pisa, Italy, where his research include all-optical digital subsystems, optical packet switching, and signal processing. During 2009-2011, he was a graduate research assistant at Massachusetts Institute of Technology, Cambridge, MA. Currently, he is working toward his Ph.D. degree in Prof. Gee-Kung Chang's group at the School of Electrical and Computer Engineering of Georgia Institute of Technology, Atlanta, GA.

He joined Prof. Chang's group since 2011 and have worked on several projects for the National Science Foundation (NSF) Center on Fiber-Wireless Integration and Networking (FiWIN). In 2014, he was a research intern at NEC Labs America, Princeton, NJ; in 2015, he worked as a tech intern at Google, Mountain View, CA; in 2016, he worked as a research intern at Mitsubishi Electric Research Laboratories (MERL), Cambridge, MA; and in 2016, he was as a visiting student at CableLabs, Louisville, CO. His Ph.D. research mainly focuses on nonlinear signal impairments and mitigation technologies for the next generation converged optical-wireless mobile fronthaul networks. His research interests also include optical wireless access networks, mobile fronthaul/backhaul networks, passive optical networks, radio-over-fiber, microwave/millimeter wave photonics, optical signal processing, etc.

He has authored and co-authored more than 50 peer-reviewed journal articles and international conference papers. He was one of the two honorable mention winners of Corning outstanding student paper competition on Optical Fiber Communication

Conference (OFC) 2016, awarded by Optical Society of America. He is a student member of IEEE Photonics Society, Optical Society America, and SPIE. He also serves as an active reviewer for Journal of Lightwave Technology, Journal of Optical Communications and Networking, Optics Letters, Optics Express, Photonics Journal, Applied Optics, Optics Communications, IET Optoelectronics, and Optical Fiber Technology.